# TUDelft

Delft University of Technology

## Influence and Detection of Vacuum Bag Leakages in Composites Manufacturing

Haschenburger, A.I.

**DOI**

**Publication date**
2022

**Document Version**
Final published version

**Citation (APA)**

**Important note**
To cite this publication, please use the final published version (if applicable).
Please check the document version above.

# Influence and Detection of Vacuum Bag Leakages in Composites Manufacturing

## A. Haschenburger

**TU**Delft

DLR
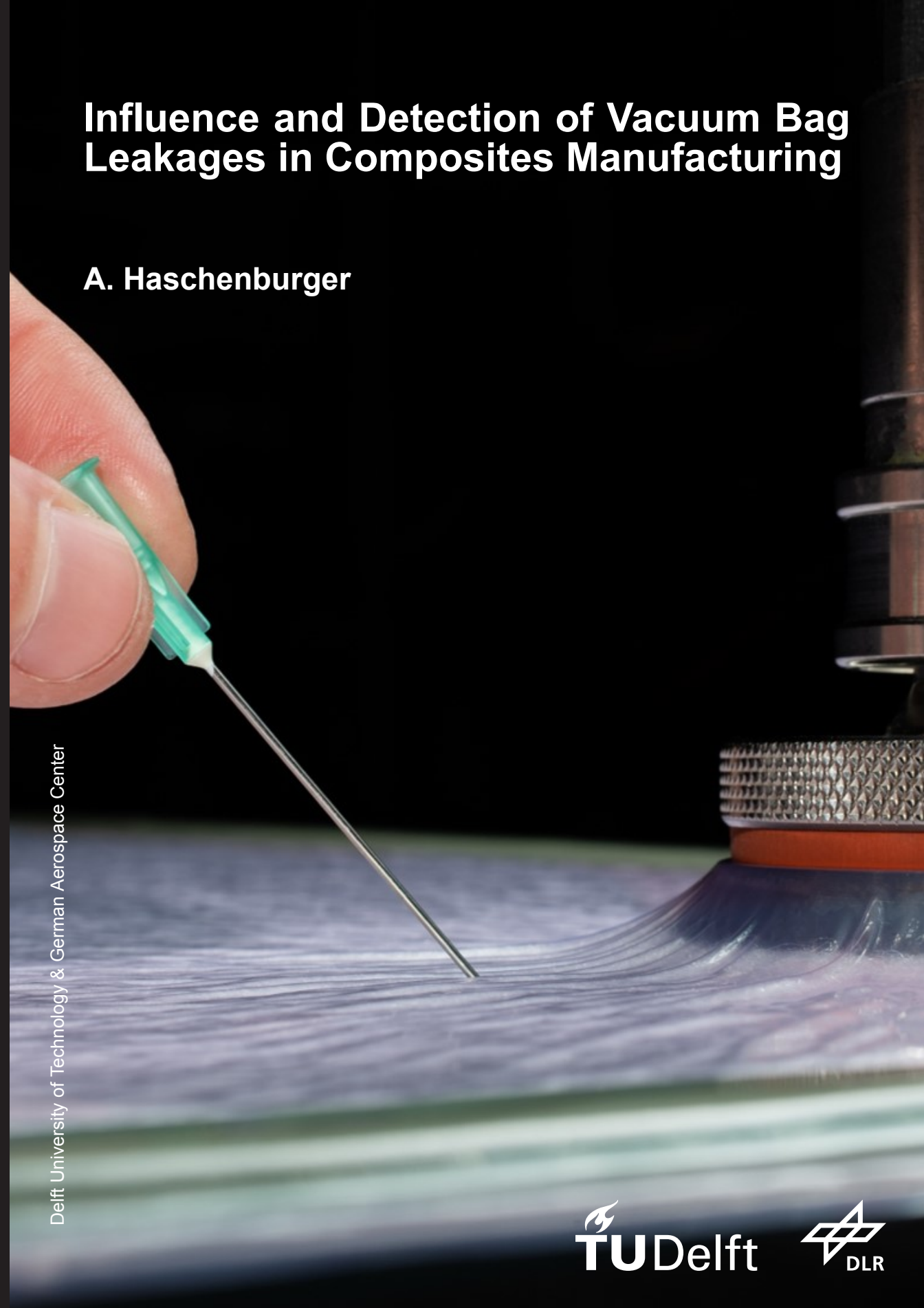
# Propositions

accompanying the dissertation

## Influence and Detection of Vacuum Bag Leakages in Composites Manufacturing

by

## Anja Haschenburger

1.  In the future there will be no open mould process in composites manufacturing without automatic leakage detection. *This proposition pertains to this dissertation.*

2.  Defective vacuum bags in the production of composites have the greatest negative impact on component quality. *This proposition pertains to this dissertation.*

3.  Simulative validation of the vacuum bagging process is the only way to understand leakages holistically. *This proposition pertains to this dissertation.*

4.  Inline inspection methods will replace non-destructive testing of a component in aerospace composite manufacturing entirely in the future. *This proposition pertains to this dissertation.*

5.  The greatest driver of an engineer is not to be satisfied with the given circumstances.

6.  Smarter people don't make you smarter, the curious do.

7.  Science does not matter without art.

8.  Wisdom is of general use only when it is expressed by a question.

9.  Enjoying the disagreement with somebody is the strongest sign of intellectual chemistry. *- Adam Grant*

10. Imposter syndrome about science is an ambivalent trait.

These propositions are regarded as opposable and defendable, and have been approved as such by the promotor prof.dr.ir. R. Benedictus.

# Stellingen

behorende bij het proefschrift

## Influence and Detection of Vacuum Bag Leakages in Composites Manufacturing

door

## Anja Haschenburger

1. In de toekomst zal er geen open matrijs proces in composieten fabricage zijn zonder automatische lekdetectie. *Deze stelling heeft betrekking op dit proefschrift.*

2. Defecte vacuümzakken bij de productie van composieten hebben de grootste negatieve invloed op de kwaliteit van componenten. *Deze stelling heeft betrekking op dit proefschrift.*

3. Simulatieve validatie van het vacuümzakproces is de enige manier om lekkages holistisch te begrijpen. *Deze stelling heeft betrekking op dit proefschrift.*

4. Inline inspectiemethoden zullen in de toekomst het niet-destructief testen van een component in de lucht- en ruimtevaartcomposietproductie volledig vervangen. *Deze stelling heeft betrekking op dit proefschrift.*

5. De grootste drijfveer van een ingenieur is om niet tevreden te zijn met de gegeven omstandigheden.

6. Slimmere mensen maken je niet slimmer, de nieuwsgierigen wel.

7. Wetenschap doet er niet toe zonder kunst.

8. Wijsheid is alleen van algemeen nut als het wordt uitgedrukt in een vraag.

9. Plezier beleven aan onenigheid met iemand is het sterkste teken van intellectuele chemie. *- Adam Grant*

10. Het impostersyndroom over wetenschap is een ambivalente eigenschap.

Deze stellingen worden opponeerbaar en verdedigbaar geacht en zijn als zodanig goedgekeurd door de promotor prof.dr.ir. R. Benedictus.

# Influence and Detection of Vacuum Bag Leakages in Composites Manufacturing

# Influence and Detection of Vacuum Bag Leakages in Composites Manufacturing

## Dissertation

for the purpose of obtaining the degree of doctor
at Delft University of Technology,
by the authority of Rector Magnificus Prof.dr.ir. T.H.J.J. van der Hagen,
chair of the Board of Doctorates,
to be defended publicly on Wednesday 2nd November 2022 at 15:00 o'clock.

by

## Anja HASCHENBURGER

Master of Arts in Management
FOM Hochschule für Oekonomie & Management, Essen, Germany,
born in Stade, Germany.

This dissertation has been approved by the promoters

Composition of the doctoral committee:

| | |
|---|---|
| Rector Magnificus, | Chairman |
| Prof.dr.ir. R. Benedictus | Delft University of Technology, promoter |
| Dr. J. Stüve | Delft University of Technology, copromoter |

*Independent members:*

| | |
|---|---|
| Prof.dr.-ing.habil. B. Fiedler | Hamburg University of Technology |
| Prof.dr.-ing. M. Wiedemann | Technical University of Brunswick |
| Prof. C.A. Dransfeld | Delft University of Technology |
| Dr. S. Hallström | KTH Royal Institute of Technology |
| C. Heim | Airbus Operations GmbH |
| Prof.dr. C. Kassapoglou | Delft University of Technology, reserve member |

An electronic version of this dissertation is available at
http://repository.tudelft.nl/.

*A small leak will sink a great ship.*

Benjamin Franklin

# Contents

# Contents

# Summary

Composites are increasingly used in the aerospace industry due to their lightweight potential and flexible design options. The most widespread manufacturing process for large components made of fibre composites is still the open mould process. In this process, a composite component is placed on a mould and hermetically sealed with a vacuum bag consisting of vacuum film and other auxiliary materials. The function of this vacuum bag is to evacuate possible air inclusions and to transfer the pressure evenly to the component during curing in an autoclave. If the vacuum bag is not tight, the quality of the final product can be affected. Leakages in the vacuum bag lead to porosities and defects in the component and must therefore be avoided by all means.

Even though conventional leakage detection techniques are generally able to detect leakages in vacuum bags, they are usually considered as inaccurate and very time-consuming. Within a market study, performed in this work, it is found that the most promising method for efficient and automated leakage detection is a combination of volumetric flow rate measurement and infrared thermography. The tightness of the vacuum bag is checked with the help of the volumetric flow rate measurement and, in the event of a leak, the affected area can be narrowed down with the help of the flow data. Afterwards, the exact position of the leakage within this area is determined by means of infrared thermography and can thus be remedied.

In order to be able to assess the effects of leakage on vacuum bags, theory, experiment and numeric are subsequently linked to be able to make a valid statement about the condition within the vacuum setup. It is shown that both the volume flow rates and the pressure gradient that occurs as well as the temperature and air velocity in the area of a leakage can be simulated. These effects in turn have an impact on the subsequent component quality. To investigate their influence, various autoclave tests with different types of leakage are carried out and evaluated. It is shown that leakages where there is a direct connection between the laminate and the environment are significantly more critical, regarding porosities, than those where the laminate is still protected from inflowing air by an intact release film. The use of machine learning in leak detection subsequently shows further potential for improving localisation, especially in the case of multiple leaks in the component.

The costs of leakages in the composite component manufacturing process are typically hidden in the overall production costs. To address this, this research also examines the financial impact of leakages and the estimated financial benefits of implementing an advanced leakage detection process. Overall, this research shows that the improved leakage detection, analysis of the impact of leakage in the vacuum bag and on the component, and implementation of machine learning will increase the efficiency, effectiveness, and sustainability of the open mould process.

# Samenvatting

Composieten worden steeds meer gebruikt in de lucht- en ruimtevaartindustrie vanwege hun lichte gewicht en flexibele ontwerpmogelijkheden. Het meest wijdverbreide fabricageproces voor grote onderdelen van vezelcomposieten is nog steeds het open-malproces. Bij dit proces wordt een composietonderdeel op een mal geplaatst en hermetisch afgesloten met een vacuümzak bestaande uit vacuümfolie en andere hulpmaterialen. De functie van deze vacuümzak is het evacueren van mogelijke luchtinsluitingen en het gelijkmatig overbrengen van de druk op de component tijdens het uitharden in de autoclaaf. Als de vacuümzak niet dicht is, kan de kwaliteit van het eindproduct worden aangetast. Lekkages in de vacuümzak leiden tot porositeiten en defecten in het onderdeel en moet daarom met alle middelen worden vermeden.

Hoewel conventionele lekdetectietechnieken over het algemeen in staat zijn om lekken in vacuümzakken op te sporen, worden zij meestal als onnauwkeurig en zeer tijdrovend beschouwd. In een marktstudie, uitgevoerd in dit werk, wordt vastgesteld dat de meest veelbelovende methode voor efficiënte en geautomatiseerde lekdetectie een combinatie is van volumetrische debietmeting en infraroodthermografie. De dichtheid van de vacuümzak wordt gecontroleerd met behulp van de volumetrische debietmeting en in geval van een lek kan het getroffen gebied met behulp van de debietgegevens worden afgebakend. Daarna wordt met behulp van infraroodthermografie de precieze plaats van het lek binnen dit gebied bepaald en kan het worden verholpen.

Om de effecten van lekkage op vacuümzakken te kunnen beoordelen, worden vervolgens theorie, experiment en numeriek aan elkaar gekoppeld om een geldige uitspraak te kunnen doen over de toestand binnen de vacuümopstelling. Aangetoond wordt dat zowel de volumestromen en de drukgradiënt die optreden, als de temperatuur en de luchtsnelheid in het gebied van een lekkage kunnen worden gesimuleerd. Deze effecten zijn op hun beurt weer van invloed op de latere kwaliteit van het onderdeel. Om hun invloed te onderzoeken, worden diverse autoclaaftests met verschillende soorten lekkage uitgevoerd en geëvalueerd. Er wordt aangetoond dat lekkages waarbij er een directe verbinding is tussen het laminaat en de omgeving aanzienlijk kritischer zijn, wat porositeiten betreft, dan lekkages waarbij het laminaat nog beschermd is tegen instromende lucht door een intacte release film. Het gebruik van machine learning bij lekdetectie toont vervolgens verdere mogelijkheden om de lokalisatie te verbeteren, vooral in het geval van meerdere lekken in het onderdeel.

De kosten van lekkages in het fabricageproces van composietonderdelen zijn meestal verborgen in de totale productiekosten. Om dit aan te pakken, onderzoekt dit onderzoek ook de financiële impact van lekkages en de geschatte financiële voordelen van de implementatie van een geavanceerd lekdetectieproces. Over het

algemeen toont dit onderzoek aan dat de verbeterde lekdetectie, de analyse van de impact van lekkage in de vacuümzak en op het onderdeel, en de implementatie van machine learning de efficiëntie, effectiviteit en duurzaamheid van het open mould proces zullen verhogen.

# Preface

This work focuses on the challenges that can be encountered in a vacuum setup for the manufacturing of fibre composite components in an open mould process. Even for large series components in the aerospace industry, vacuum bagging is still a part of the process involving a lot of manual work. Both the execution of the vacuum assembly and the testing of the air tightness are highly dependent on the expertise of the employees and therefore rarely of consistent quality.

My work as a manufacturing engineer at Airbus Operations GmbH in Stade showed me time and again that a majority of quality problems and process uncertainties can be traced back to this supposedly simple process step. In addition, many of the specifications and regulations in force today have grown historically and are based on experience rather than on engineering analysis. It is my ambition not only to perform these analyses, but also to develop tools that help improve the process and prepare it for the future.

This thesis contributes to a better understanding of the vacuum bagging process, the consequences of any undetected leaks and how to fundamentally improve the detection process. This research will enable the open mould process to meet the requirements of sustainable and advanced process technology of the future.

*Anja Haschenburger*
*Delft, September 2022*

# Abbreviations

**ACCEM** *Advanced Composite Cost Estimation Manual*

**AFP** *Automated Fibre Placement*

**AI** *Artificial Intelligence*

**AIPI** *Airbus Process Instruction*

**ANNs** *Artificial Neural Networks*

**ATL** *Automated Tape Laying*

**BCE** *Binary Cross-Entropy*

**CFD** *Computational Fluid Dynamics*

**CFRP** *Carbon Fibre Reinforced Plastics*

**DLR** *German Aerospace Center*

**EP** *Epoxid*

**ETFE** *Ethylene-Tetrafluoroethylene*

**FCNN** *Fully Connected Neural Network*

**FCNNs** *Fully Connected Neural Networks*

**FMEA** *Failure Mode and Effects Analysis*

**FN** *False Negative*

**FP** *False Positive*

**FRP** *Fibre Reinforced Plastics*

**GF** *Glass Fibre*

**IR** *Infrared*

**LCM** *Liquid Composite Moulding*

**LW** *Longwave*

**MAE** *Mean Absolute Error*

**NDI** *Non Destructive Inspection*

**PTFE** *Polytetrafluoroethylene*

**RANS** *Reynolds Averaged Navier-Stokes*

**RTM** *Resin Transfer Moulding*

**SELU** *Scaled Exponential Linear Unit*

**SST** *Shear Stress Transport*

**TN** *True Negative*

**TP** *True Positve*

**UD** *unidirectional*

**VFR** *Volumetric Flow Rate*

**WBCE** *Weighted Binary Cross-Entropy*

**XWB** *Extra Wide Body*

# List of symbols

| Symbol | Description | Unit |
|---|---|---|
| $i, j$ | Universal counting variables | |
| $A_c$ | Parameter for the Reader-Harris/Gallagher Equation | |
| $A_i$ | Area | $m^2$ |
| $a$ | Van-der-Vaals constant | $(Nm^4)/(mol^2)$ |
| $a_i$ | Values for regression function | |
| $a^{[\ell-1]}$ | Activation vector | |
| $a^{[\ell]}$ | Output of the $\ell$-th layer | |
| $a^{[L]}$ | Output of the top layer | |
| $b$ | Van-der-Vaals constant | $m^3/mol$ |
| $b^{[\ell]}$ | Bias vector | |
| $b_p$ | Distance of outer inflection points in the temperature profile | $mm$ |
| $C$ | Discharge coefficient | |
| $C_d$ | Discharge coefficient at leakage | |
| $C_\mu$ | Anisotropy parameter | |
| $c_h$ | Specific heat capacity of substance | $J/(kgK)$ |
| $c_p$ | Specific heat capacity at constant pressure | $J/(kgK)$ |
| $c_{p,m}$ | Van-der-Vaals constant | $J/(molK)$ |
| $c_v$ | Specific heat capacity at constant volume | $J/(kgK)$ |
| $c_{i,j}$ | Flow velocity | $m^3/s$ |
| $D$ | Pipe diameter | $m$ |
| $D_n$ | Needle diameter | $mm$ |
| $D'_n$ | Real needle diameter | $mm$ |
| $D_{vac}$ | Vacuum bag diameter | $m$ |
| $d$ | Orifice diameter | $m$ |
| $d_{vac}$ | Leakage diameter | $m$ |
| $E_b$ | Compression modulus of breather | |
| $E_h$ | Compression modulus of spring | |
| $E_p$ | Compression modulus of prepreg laminate | |
| $f_\theta$ | Defined FCNN function | |
| $g$ | Gravitational acceleration | $m/s^2$ |
| $g^{[\ell]}$ | Activation function | |
| $H$ | Enthalpy | $J$ |

| | | |
|---|---|---|
| $h_{i,j}$ | Specific enthalpy | $J/kg$ |
| $\hat{h}_j$ | Decision function or hypothesis | |
| $h_{tot}$ | Specific total enthalpy | $J/kg$ |
| $K_{Perm}$ | Permeability | $m^3$ |
| $k$ | Lattice fineness | |
| $k$ | Turbulent kinetic energy | $J/kg$ |
| $\ell$ | Number of layer in neural network | |
| $\ell_n$ | Standardized litres | $l$ |
| $L$ | Length | $m$ |
| $L$ | Total number of layers in neural network | |
| $L_1$ | ($= l_1/D$) Distance between the inlet pressure tapping and upstream face of the orifice divided by the pipe diameter | |
| $L'_2$ | ($= l'_2/D$) Ratio of distance between the outlet pressure tapping and downstream face of the orifice to pipe diameter | |
| $M$ | Molar mass | $g/mol$ |
| $M'_2$ | Parameter for the Reader-Harris/Gallagher Equation | |
| $m$ | Mass | $kg$ |
| $m_e$ | $m_e$-element subset of training data | |
| $\dot{m}$ | Mass flow rate | $kg/s$ |
| $n$ | Amount of substance | |
| $n_{leak}$ | Number of leakages in vacuum bag | |
| $n_\ell$ | Dimension of the $\ell$-th layer | |
| $P_v$ | Volume Porosity | |
| $P_i$ | Pressure at pressure taps in orifice plate | $Pa$ |
| $P_{1vac}$ | Ambient pressure | $Pa$ |
| $P_{2vac}$ | Vacuum bag pressure | $Pa$ |
| $p_i$ | Pressure, absolute | $bar$ |
| $p_{app}$ | Applied pressure | $bar$ |
| $p_{Atmo}$ | Atmospheric pressure | $bar$ |
| $p_{eff}$ | Effective pressure onto the laminate | $bar$ |
| $p_{hydro}$ | Hydrostatic resin pressure | $bar$ |
| $\hat{p}_i$ | Pressure profile within the vacuum bag | $bar$ |
| $p_k$ | Probability | |
| $p_{reinf}$ | Pressure of the compact fibre bed | $bar$ |
| $p_{dyn}$ | Dynamic pressure | $bar$ |
| $p_{garvity}$ | Gravitational pressure | $bar$ |
| $p_r$ | Reference pressure | $bar$ |
| $p_{st}$ | Static pressure | $bar$ |
| $p_t$ | Total pressure | $bar$ |

| | | |
|---|---|---|
| $p_{vac}$ | Pressure inside the vacuum bag | $bar$ |
| $p_x$ | Pressure at outlet | $bar$ |
| $p_\infty$ | Absolute ambient pressure | $bar$ |
| $p*$ | Critical value of downstream pressure for chocked flow | $Pa$ |
| $p_0$ | Total upstream pressure | $Pa$ |
| $Q, q_v$ | Volumetric flow rate | $\ell_n/min$ |
| $Q_{calc}$ | Calculated volumetric flow rate | $\ell_n/min$ |
| $Q_{exp}$ | Experimental volumetric flow rate | $\ell_n/min$ |
| $Q_h$ | Heat | $J$ |
| $Q_{in}$ | Incoming airflow through leakage | $\ell_n/min$ |
| $Q_{Leakage}$ | Airflow in the leakage | $\ell_n/min$ |
| $Q_{out}$ | Outgoing flow of the vacuum bag | $\ell_n/min$ |
| $Q_{Pump}$ | Airflow at the vacuum pump | $\ell_n/min$ |
| $Q_{sim}$ | Simulated volumetric flow rate | $\ell_n/min$ |
| $q_{ij}$ | Thermal energy | $J$ |
| $q_L$ | Leakage rate | $mbar \cdot l/s$ |
| $q_m$ | Mass flow rate | $kg/s$ |
| $\dot{Q}_h$ | Heating power | $W$ |
| $R$ | Universal gas constant | $J/(Kmol)$ |
| $R$ | Electrical resistance | |
| $\mathbb{R}$ | Set of real numbers | |
| $Re$ | Reynolds number | |
| $Re_D$ | Reynolds number for pipe diameter | |
| $R^2$ | Determination standard | |
| $r$ | Radius | $mm$ |
| $s_i$ | Vacuum or pressure gauge connection in vacuum bag | |
| $\mathrm{SELU}(z)$ | Scaled Exponential Linear Unit (SELU) activation function | |
| $T_i$ | Temperature at point i | $K$ |
| $T_{atm}$ | Atmospheric temperature | $K$ |
| $T_{obj}$ | Temperature of the object | $K$ |
| $T_{ref}$ | Temperature of the object surroundings reflected toward the camera | $K$ |
| $T_s$ | Sensor temperature | $K$ |
| $T_0$ | Starting temperature $K$ | |
| $t$ | Time | |
| $\bar{U}_{i,j}$ | Mean velocity | $m/s$ |
| $u_{i,j}$ | Fluctuating velocity | $m/s$ |
| $V_{A,eq}$ | Equivalent ridid volume | $\ell$ |
| $V_i$ | Volume | $m^3$ |
| $V_B$ | Volume of the vacuum bag | $l$ |
| $\dot{V}$ | Volumetric flow rate | $m^3/s$ |
| $VFR_{fraction}$ | Volumetric flow rate fraction | |

| | | |
|---|---|---|
| $v$ | Flow velocity | $m/s$ |
| $v_{a,eq}$ | Specific equivalent rigid volume | $\ell_n/m^2$ |
| $W_{atm}$ | Atmospheric radiation | |
| $W_{obj}$ | Object radiation | |
| $W_{ref}$ | Radiation that is reflected from the objects surroundings | |
| $W_{tot}$ | Total radiation | |
| $W^{\ell}$ | Weight matrix | |
| $w_n$ | Weight for weighted binary cross-entropy loss | |
| $w_p$ | Weight for weighted binary cross-entropy loss | |
| $w_{tij}$ | Technical work | $J$ |
| $y$ | Assosiated ground truth | |
| $\hat{y}$ | Model prediction | |
| $Z$ | Compressibility factor | |
| $z_{i,j}$ | Hight of entry and exit level | $m$ |
| $z^{[\ell]}$ | Result for $\ell$-th layer | |
| $\alpha$ | Pre-defined constant for SELU function | |
| $\beta$ | Ratio between orifice and inner pipe diameter | |
| $\gamma$ | Heat capacity ratio $c_p/c_v$ | |
| $\Delta P$ | Pressure difference at orifice plate | $Pa$ |
| $\Delta p$ | Pressure increase in vacuum bag | $mbar$ |
| $\Delta Q_h$ | Absorbed heat | $J$ |
| $\Delta t$ | Measuring time | $s$ |
| $\Delta T_{ij}$ | Temperature difference between point i and j | $K$ |
| $\Delta T_s$ | Temperature increase at sensor | $K$ |
| $\Delta t$ | Time difference between start and end time | $s$ |
| $\epsilon$ | Expansion coefficient | |
| $\varepsilon$ | Turbulent dissipation | |
| $\varepsilon_h$ | Deformation of spring | |
| $\varepsilon_o$ | Emissivity of object | |
| $\varepsilon_v$ | Compression of vacuum bag | |
| $\eta$ | Dynamic viscosity | $Pa/s$ |
| $\theta$ | Parameter vector | |
| $\lambda$ | Pre-defined constant for SELU function | |
| $\mu_{JT}$ | Joules-Thomson coefficient | |
| $\mu_t$ | Eddy viscosity | |
| $\rho_i$ | Density at position i | $kg/m^3$ |
| $\rho_{reg}$ | Regularization strenght | |
| $\sigma$ | Standard deviation | |
| $\sigma_{sbc}$ | Stefan-Boltzmann constant | $W/(m^2K^4)$ |

| | | |
|---|---|---|
| $\sigma(t)$ | External tension on spring | |
| $\sigma(z)$ | Logistic or sigmoid function | |
| $\tau_a$ | Atmosphere transmittance parameter | |
| $\tau_{ij}$ | Deviatoric stress tensor | |
| $\tau_{ml}$ | Threshold decision function | |
| $\tau_t$ | Turbulent stresses (Reynolds Stress) | |
| $\omega$ | Turbulent frequency | |
| $\emptyset_n$ | Nominal diameter of needle | $mm$ |

# 1

## Introduction

**1**

## **1.1.** Background

Fibre-reinforced composites have been used in large civil aircraft construction for several decades. They meet the requirement for high stiffness of a component while maintaining a low structural weight. [1] With increasing development of automated processing, the share of fibre composite structures has grown steadily. In contemporary generation of aircraft, such as the Boeing 787 and the Airbus A350, the application of composite materials is being pushed more and more by the large manufacturers [2, 3], resulting in $54\%$ composites in the Airbus A350 *Extra Wide Body* (XWB) [4] and about $50\%$ of total weight in the Boeing 787 [5].

Composite structures for aerospace applications must meet high quality requirements in terms of fibre volume content and laminate quality. A common production method for high-performance composite components for aerospace structures is prepreg manufacturing. [1, 6] Prepreg materials consist of fibre layers that are preimpregnated with resin. These individual layers are stacked manually or with automated fibre lay up, according to the specification. After the lay up is completed, the part is commonly processed in an open mould under high temperature and pressure, which is referred to as open mould processing. The open mould process is one of the oldest processes for the production of fibre-reinforced composite components. [6] Even though various production processes with closed moulds, such as resin transfer moulding or hot pressing, have been developed since then, the open mould process has proven to be particularly suitable for large high-performance components, while maintaining moderate tool costs. [7] Vacuum bagging is an essential process step in the open mould production and is carried out before the curing in the autoclave, right after the layup of the part is completed. During this production step, the composite layup is hermetically sealed against the environment by auxiliary materials, creating a so-called vacuum bag. [8]

Its function is to distribute the pressure that is applied during the autoclave curing cycle as evenly as possible to the entire component. The pressure difference generated by evacuation of the vacuum bag and pressurisation of the surrounding is a determining factor for the quality of the produced composite part. It hinders the formation of voids or porosities in the laminate by ensuring the evacuation of entrapped air or volatiles. It also keeps the resin pressure high which keeps any dissolved volatiles in solution and enables a homogenous resin flow throughout the laminate. Prior to the curing cycle, the applied vacuum removes entrapped air, consolidates the prepreg layers and debulks the laminate. This can only be ensured if the component, that is sealed between the tool and the vacuum film forms a closed system against the atmosphere inside and outside of the autoclave. [1] A sketch of a vacuum bag and the individual elements is shown in Figure 1.1. Here, also a leakage is included.

Faulty vacuum bags lead to complex repair work and can drastically impair the quality of the composite – in severe cases even inducing scrapping of the entire component. [1, 6, 9–12] As a result of insufficient evacuation of the part and thus low or absent pressure differences between the component and the environment, the formation of cavities and porosities inside the laminate is suspected. [11, 12] Especially for large components, such as wing covers or fuselage segments, the
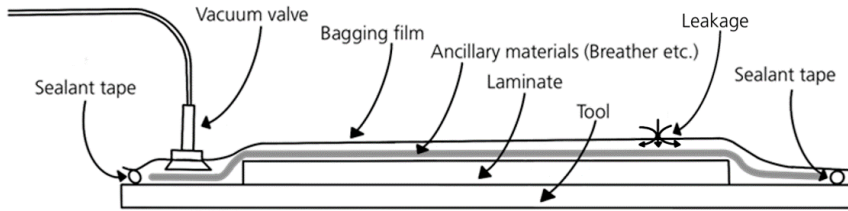
Figure 1.1: Sketch of a vacuum bag, the individual elements and a leakage

construction of a hermetically sealed vacuum bag is challenging and associated with significant manual effort. [13] To avoid vacuum losses, leakage detection methods are applied during various manufacturing steps. Altogether, all technologies available on the market are able to detect leakages in vacuum bagging, but nearly all of them are associated with a high manual and cost intensive effort. None of the existing procedures can detect the leakage with adequate accuracy in a reasonable time and especially not fully automated. [14] Particularly for large components with complex vacuum structures in industrial environments with background noise, especially in the ultrasonic spectrum, e.g. caused by fans and electric motors, the detection becomes more difficult. Under these conditions, the methods are usually very time consuming, inaccurate, and associated with high manual effort.

Leakages can be critical during the processing of open mould prepreg as well as in infusions of composite parts. While it is generally agreed that leakages in vacuum bagging have a negative effect on the part quality, the fundamental mechanisms and the exact influences of leakages on the vacuum bag and the component is limited and have not been fully researched and understood. The contemporary tests and detection methods are extremely dependent on the experience of the user. The thresholds in the given part specifications vary drastically and the processes for detection are usually based on experience or subjective estimates.

## 1.2. Goals and composition of the thesis

To develop an efficient and reliable detection method for leakages in vacuum bagging, it is necessary to understand the effects of different leakages on the physical conditions in the vacuum bag and the laminate. These include the resulting pressure distribution, air flow and temperature if a leakage is present in the vacuum bag, as well as the impact on the final part quality. Furthermore, there is a need to evaluate the current specifications for airtightness in aerospace manufacturing and develop a criterion to quantify and evaluate the severity of a leakage that, in contrast to current specifications, is independent of the component size.

This thesis aims to improve the understanding of the mechanisms inside a vacuum bag during the different production stages. The goal is to assess the influence of leakages on the vacuum bag during the curing process and the final part quality. This includes the identification of a criterion to evaluate the airtightness of

**1**

any part, independent of component size. The development of a fast, reliable and automatable leakage detection is aspired. For this purpose, leakages are investigated from a scientific point of view and a criterion for air tightness is derived that is based on knowledge and not on subjective assessments or experience.

To achieve this, the effects of leakages that appear before and during the autoclave cycle, both inside the vacuum bag and the laminate are examined not only by experiment but also with *Computational Fluid Dynamics* (CFD) simulation and suitable replacement models. Subsequently, the impact of different types of leakage on the final part quality is examined and evaluated. Building on this, different leakage detection methods are investigated and experimentally validated according to their detection and localisation capabilities. Subsequently, the possibility of automating and improving the localisation of leaks through machine learning is investigated and the industrial value is discussed.

The outcome of this thesis is a methodology for the leakage detection process with a uniform evaluation criterion that is based on physical understanding and suitable process models. These developments are especially valuable for manufacturers of high performance composite parts as they enable to improve the vacuum bagging process including the leakage detection and thus the overall part quality of composite components manufactured in the open mould and autoclave processes.

# References

[1] F. C. Campbell, *Manufacturing Processes for Advanced Composites* (Elsevier Science, 2003).

[2] G. Marsh, *Airbus A350 XWB update,* Reinforced Plastics **54**, 20 (2010).

[3] A. McIlhagger, E. Archer, and R. McIlhagger, *Manufacturing processes for composite materials and components for aerospace applications,* in *Polymer Composites in the Aerospace Industry*, edited by P. Irving and C. Soutis (Elsevier, 2020) pp. 59–81.

[4] C. FUALDES, X. JOLIVET, and C. CHAMFROY, *Safe operations with composite aircraft,* Airbus S.A.S (2014), safety First - Magazin.

[5] J. Hale, *Boeing 787 from the ground up,* The Boeing Company - AERO Magazine (2006).

[6] H. Lengsfeld, V. Altstädt, F. Wolff-Fabris, and J. Krämer, *Composite Technologien* (Carl Hanser Verlag, 2014).

[7] R. F. Gibson, *Principles of Composite Material Mechanics*, Mechanical Engineering (CRC Press, 2016).

[8] F. C. Campbell, *Manufacturing Technology for Aerospace Structural Materials*, Aerospace Engineering Materials Science (Elsevier Science, 2011).

[9] G. Fernlund, C. Mobuchon, and N. Zobeiry, *2.3 Autoclave Processing,* in *Comprehensive Composite Materials II* (Elsevier, 2018) pp. 42–62.

[10] T. Centea, L. K. Grunenfelder, and S. R. Nutt, *A review of out-of-autoclave prepregs – Material properties, process phenomena, and manufacturing considerations,* Composites Part A: Applied Science and Manufacturing **70**, 132 (2015).

[11] G. Fernlund, J. Wells, L. Fahrang, J. Kay, and A. Poursartip, *Causes and remedies for porosity in composite manufacturing,* IOP Conference Series: Materials Science and Engineering **139**, 012002 (2016).

[12] F. Y. C. Boey and S. W. Lye, *Void reduction in autoclave processing of thermoset composites,* Composites **23**, 266 (1992).

[13] A. Haschenburger and N. Menke, *Sensor based analysis and identification of leakages in vacuum bagging for high performance composite components,* in *SAMPE Europe Conference* (2018).

[14] A. Haschenburger and C. Heim, *Two-stage leak detection in vacuum bags for the production of fibre-reinforced composite components,* CEAS Aeronautical Journal **10**, 885 (2019).

# 2

# Literature review

*In this chapter, fibre composite materials and their production using prepreg and open mould processes are introduced. The vacuum bag and its components as well as the autoclave curing process are described. Subsequently, an overview of the state of research on vacuum bag leakages is given, where the different types, their consequences as well as detection methods are discussed in detail. Afterwards, fluid dynamics are introduced to describe the physical process inside a leakage, followed by the introduction to machine learning. This literature review provides the fundamental theory for the research in this thesis and serves as the basis for analysing the research and technology gap in order to formulate specific hypotheses.*

---

## **2.1.** Fibre composite materials

**C**omposites are a combination of at least two separate materials that are combined in order to create a new, multi-phase material that is designed to unite favourable characteristics of its constituents. [1, 2] A reinforced composite material usually consists of a reinforcing phase and a matrix, where the reinforcement is usually chosen to be both discontinuous and also stiffer and stronger than the continuous matrix. [1] Fibre-reinforced composites typically result from strengthening a ductile polymer matrix system with a reinforcement of fibrous nature. [3] The most prominent reinforcing fibre types for advanced lightweight applications are glass or carbon fibres. [4] The majority of matrix materials for fibre reinforced composites are thermoset or thermoplastic matrix systems. [5]

Depending on the intended application and production method, different semifinished products are available to be used as reinforcement of a composite material. [2] Beside direct placement of fibre rovings, these can be divided into *unidirectional* (UD) tapes and woven fabrics. The unidirectional arrangement of the fibres inside the UD tape allows for the optimal utilisation of mechanical fibre properties. [3] All semifinished products are available as either dry fabrics or saturated with a resin system (typically epoxy resin) that is subsequently used as the matrix material. [6] These pre-impregnated fabrics are referred to as prepregs and are mostly distributed on rolls with unidirectional or woven reinforcement. Utilisation of prepregs assures an even fiber/resin distribution inside the laminate and allows for high reproducibility with low porosity. [3] Nowadays, prepregs are the most prominent semifinished product used in the aerospace sector. [3, 6]

## **2.2.** The role of consolidation pressure

During the manufacturing of *Fibre Reinforced Plastics* (FRP) the consolidation pressure, that is applied to the laminate plays a crucial role and is part of almost every production process. [7] This pressure is applied at different manufacturing stages and impregnation levels, depending on the chosen material and process. In the prepreg process, the compressive forces are applied to fully impregnated material in order to reduce porosities and voids in the matrix system and obtain the desired fibre volume content. The typical tool used in the autoclave process is the open mould, which is shown in Figure 2.1 on the left. In the open mould process, a hard shaping tool (e.g. made of metal or *Carbon Fibre Reinforced Plastics* (CFRP) is used on the underside and a flexible vacuum structure with a disposable membrane is built up on the top. This vacuum film is tightly sealed on the sides to the bottom tool by means of a sealant tape. [6] In autoclave or out-off autoclave processes the required pressure is obtained at the boundary of this vacuum bag which encloses the part. Autoclave or atmospheric pressure is acting onto the fibre bed beneath the flexible boundary. [8] Depending if a bleeding or zero bleed prepreg material is used, the pressure not only consolidates the laminate and reduces voids but also removes excessive resin to achieve higher fibre volume fractions. [7, 9]

Compared to the autoclave process in the *Liquid Composite Moulding* (LCM) process usually dry reinforcement fibres are consolidated before the infiltration with
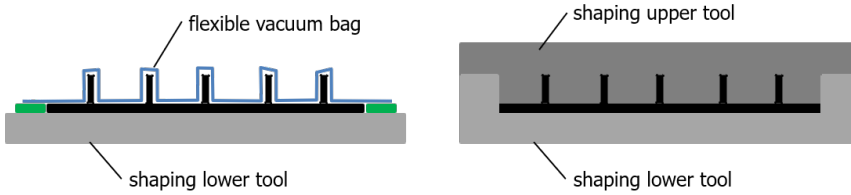
Figure 2.1: Sketch of an open mould (left) and closed mould process (right) [6]

the resin takes place. In the *Resin Transfer Moulding* (RTM) process rigid tooling on both sides of the part as shown in Figure 2.1 is used. The height of the closed mould cavity is predetermined. The preform that is placed inside is compacted by the tool and determines the force on the fibre bed as well as the resulting fibre volume content. In the vacuum infusion process, the dry preform is consolidated by the pressure acting onto the vacuum bag. This pressure has a direct influence on the resulting thickness and fibre volume friction. Furthermore, higher compression of the dry preform results in lower permeability that can influence the infiltration process. [8]

The described consolidation processes are better understood by reference to a mechanical analogy that is shown in Figure 2.2. Under a load the porous medium, like the breather and the laminate, is compressed like a spring. If the voids are filled with a fluid it is compressed or, in case of incompressibility, escapes across the boundaries of the sample. [7, 10] With this Terzaghi principle it is possible to describe the pressure on saturated fabric, where the sum of hydrostatic pressure of the resin ($p_{hydro}$) and compact fibre bed ($p_{reinf}$) corresponds to the applied pressure ($p_{app}$): [10]

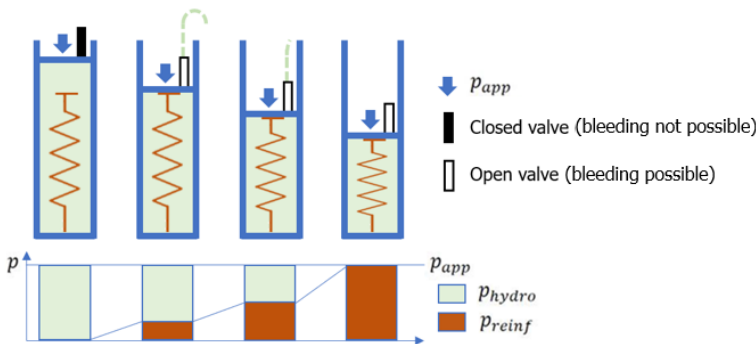$$p_{app} = p_{hydro} + p_{reinf} \tag{2.1}$$



Figure 2.2: Resin flow analogy based on the Terzaghi principle [7, 10]

**2**

Within Figure 2.2 different steps can be described. In the first step, a pressure is applied on the composite consisting of resin and a fibre bed, represented by a piston, spring and valve setup. The valve is closed, so no resin can escape. In this case, the entire load is carried by the resin and no pressure is on the fibre bed. In the next step, the valve is opened and liquid is escaping at a high rate until a portion of the pressure is carried by the spring. The outflow is decreasing as the pressure onto the spring or the fibre bed increases. In a laminate, this can be compared to the bleeding of the resin under the applied pressure of the autoclave. The rate of bleeding is reduced by the lowered hydrostatic resin pressure and the reduced permeability of the reinforcement due to compaction. In the last stage, the hydrostatic pressure drops to zero as all load is carried by the spring. If this happens during composite curing in a state of low resin viscosity, the resin pressure would be to low for pores to collapse and volatiles can no longer be kept in solution, resulting in additional voids inside the laminate. [7, 10, 11]

The prepreg and autoclave process is described in detail in the following Chapter 2.3. Even though the investigations within this thesis are carried out on prepreg and autoclave processes, since this is where the leakage problems are greatest within the aerospace industry, the results can easily be transferred to other open mould processes, e.g. out of autoclave or vacuum infusion processes, as well.

## 2.3. Prepreg/Open mould production process

Figure 2.3 shows the individual production steps for composite parts made of prepreg material. This is the most common manufacturing process used for aerospace parts such as vertical tale planes, wing covers or fuselage shells. [6] In the following sections, the state of the art for fibre composite components and autoclave production will be described.
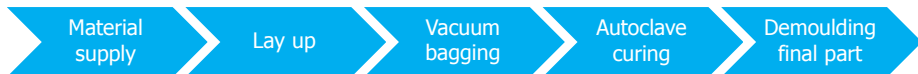


Figure 2.3: Processing sequence for composite parts made of prepreg material

### 2.3.1. Lay up

After the prepreg material is supplied and defrosted, individual plies are stacked onto each other in an orientated manner - manually or with automated lay up processes like *Automated Fibre Placement* (AFP) [6, 12] or *Automated Tape Laying* (ATL) [6]. This is done either on a flat surface such as a laminating table or directly in a mould, which gives the final part its geometry during curing. For the quality of the laminate, it is important that the flat prepreg layers are deposited without wrinkles and under avoidance of air pockets. A good compaction of the lay up is desired and achieved by the compaction rollers and heating systems of the effectors of the automated lay up machines, which apply pressure and heat to the material already laid up. [6] Additional optional debulking steps, during which a vacuum is applied to the laid up laminate, help to further increase its compaction. [11]

### 2.3.2. Vacuum bagging and its components

After the lay up is completed, the laminate on top of the mould needs to be sealed with a vacuum bag. Its primary purpose is to establish a hermetic border between the laminate and the ambient atmosphere to allow an equally distributed application of pressure onto the part during curing. It is also used during the vacuum infusion processes where this border limits the resin flow to the outer part geometry by creating a separate volume around the evacuated component. The forces applied by the pressure difference are distributed uniformly and normal to the component's surface due to the flexibility of the vacuum bag material and the principle of isostatic pressure, even if the part geometry is complex, e.g. reinforced with stiffening elements. For this purpose, the vacuum film must fit the component as accurately and tensionless as possible in order to ensure a uniform pressure at each point. Ideally, the vacuum film lies flat and smoothly on any part geometry to prevent tentering or bridging. [13]

Pressure onto the laminate is desired to compress the fibre bed and in some cases force out excess resin. This is required to gain components with high fibre volume content as needed for high performance composites. With help of the consolidation pressure differential during curing the laminate adapts to the tool geometry. [14] Entrapped air is displaced and reduced from in between fibre layers and the formation of pure resin regions is counteracted, both of which would otherwise result in loss of mechanical properties of the composite structure. Likewise, volatile constituents of the resin system that outgas during curing and could prevent proper bonding of the layers are displaced and transported out of the laminate by the evacuation process. [15] Figure 2.4 illustrates the working principle and pressure related forces of the vacuum bag.
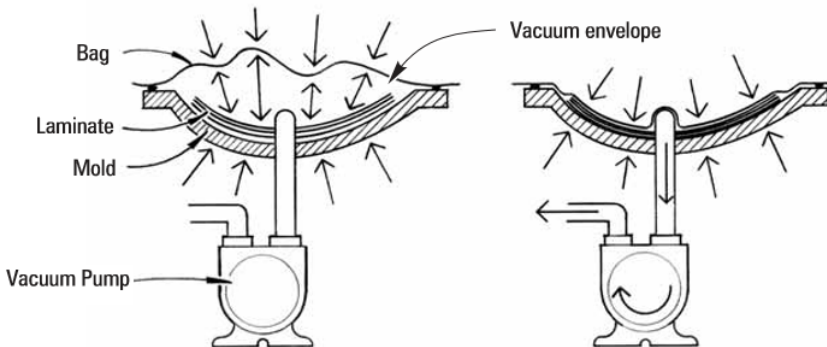


Figure 2.4: Working principle of a vacuum bag [13]

The effective pressure ($p_{eff}$) acting onto the laminate is described by the difference of absolute ambient pressure ($p_\infty$) and absolute pressure inside the vacuum bag ($p_{vac}$).

$$p_{eff} = p_\infty - p_{vac} \tag{2.2}$$

A high degree of evacuation is needed to achieve high forces onto the laminate. During autoclave curing, the pressure acting onto the laminate is further increased by elevating the ambient pressure inside the autoclave. As evident from Equation 2.2 pressure can only act onto the laminate as long as there is an existing pressure difference between the ambient atmosphere and the vacuum bag. Therefore, it is essential that no leakages inside the vacuum bag allow for pressure equalisation between the two volumes.

The elements of commonly used vacuum bagging systems for prepreg materials with zero bleed properties are shown in Figure 2.5 and are individually elaborated in the following.
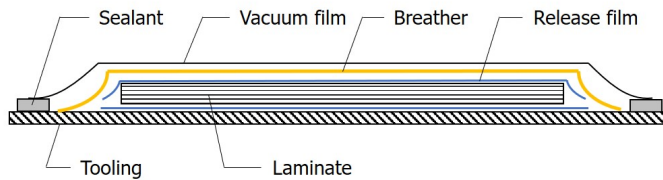


Figure 2.5: Common vacuum bagging setup, cf. [13]

**Vacuum bagging film and sealant tape**   A vacuum bag is hermetically sealed against the ambient atmosphere by the vacuum film as its final layer. It is important that the vacuum film is able to nestle to the contour of the laminate over the course of the entire curing cycle. Therefore, the vacuum film must be flexible during application under standard ambient conditions but also retain sufficient flexibility under elevated temperature. [13] Vacuum films usually consist of *Polytetrafluoroethylene* (PTFE), *Ethylene-Tetrafluoroethylene* (ETFE), polyamide or nylon and have a maximum elongation of up to 500 % at room temperature and a relative humidity of 40 to 60 %. These films are able to adapt to relative humidity. [16] If the humidity drops, the elongation decreases rapidly. Especially during the autoclave cycle, in which the humidity is reduced to about 5 %, the vacuum bag film no longer has any significant elongation properties. [6] For this reason, it is important that the film is not tensioned at any point, lies flat against the component and cannot be forced into any gaps or holes by the vacuum or autoclave pressure. Tears in the vacuum film caused by this effect (vacuum breaks) are one of the most serious causes of quality problems in CFRP components. [17] The vacuum film is sealed onto the tooling by application of sealant tape, commonly a tacky elastomer. [18]

**Release film**   A release film is placed beneath the breather cloth to create a barrier to the peel ply and laminate. This barrier prevents resin from leaking out of the impregnated layers and clogging the overlaying air-carrying breather. It can also be used to prevent demoulding problems and create special surface finishes. [19] Release film can be perforated or non-perforated. For zero bleed prepreg materials usually the non-perforated release film is used in order to avoid resin loss.

**Peel ply**   The uncured laminate can be partially covered with a peel ply. The peel ply is a smooth woven fabric that absorbs excess resin and is peeled off after curing to produce an even and smooth-textured laminate surface. Usually, the resulting surface is activated and can be bonded to or painted without further preparation. Different peel plies are available for different surface qualities which can be chosen dependent on further processing steps. [13]

**Release agent**   A release agent is applied to the tooling surface to prevent adhesion of the laminate resin to the tooling material. Without a release agent, demoulding of the laminate would result in poor surface quality, structural damage of the component or would not be possible at all. Selection of the release agent is dependent on desired surface quality, resin system and tooling material. Films with releasing effect are available as alternative to liquid agents. [13, 20]

**Breather**   The breather, or breather cloth, is a coarse polyester fleece that is used to enable airflow across the entire surface of the laminate during evacuation. The absence of breather cloth can cause the vacuum film to cling to the laminate during evacuation, resulting in sealed-off air volumes that cannot be evacuated properly. Using a breather counteracts the manifestation of entrapped air inside the vacuum. [13, 21] Its function is highly temperature and pressure dependent. The change in air flow rate of various venting materials typically used in the manufacture of aerospace components is shown in Figure 2.6 at a typical process pressure of $7\ bar$ and increasing temperature. From this it can be seen that all breathers exhibit process-dependent permeability.
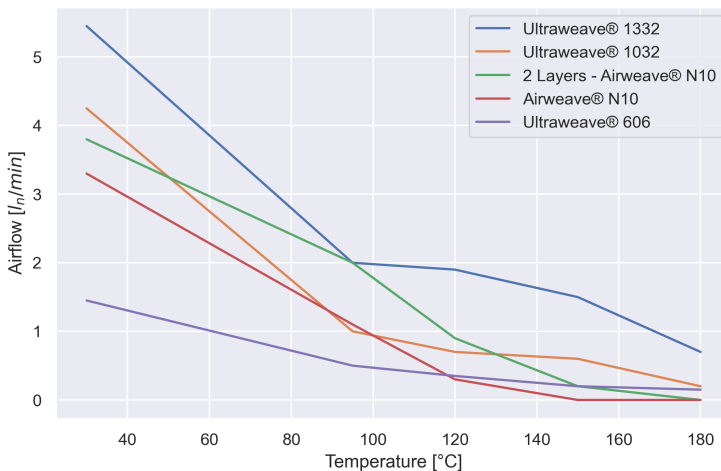


Figure 2.6: Airflow of breathers made by Airtech Europe Salr, Differdange, Luxemburg, at $7\ bar$ and increasing temperature cf. [22]

All elements of a vacuum bag are mostly single use only, which results in considerable amounts of waste, even more so if a vacuum bag is damaged or not suf-

ficiently airtight and must be replaced. This issue increases in severity for large components. Large vacuum bags are more susceptible to leakages due to the large manually sealed circumference and the large leak-prone area of vacuum film. Reusable vacuum bags made of silicone rubber are available to reduce this waste and can be used for over 100 autoclave cycles with temperatures up to $240°C$. [23] These bags are used for smaller components only, as handling and storage issues increase with part size due to larger dimensions and weight of the silicon bag. [17, 24] Since the current state of the industry is that non-reusable vacuum bags are used for large and complex structures and with this thesis a simple and fast transfer of scientific findings from research to industry is to be achieved, silicone bags will not be considered further in this work.

### 2.3.3. Autoclave process

The dominant manufacturing method for composite structures in aerospace applications is the autoclave processing with thermoset prepregs. [11] Autoclaves are of great advantage for the production of components with complex geometries, as the pressure is built up isostatically in the chamber. Thus the component surfaces experience identical pressure conditions, independent of their size or geometry. The size of the autoclave limits the maximum component size that can be produced using this curing technology. [6] A typical autoclave consists of a pressure chamber, electrical and digital controls, a hot gas generator and a vacuum system, schematically shown in Figure 2.7. Single large components or several small components can be accommodated and cured in an autoclave. Autoclaves are therefore highly flexible in their use and are typically designed for process temperatures of up to $200 - 450°C$ and pressures of $1 - 20\ bar$. [6, 11]
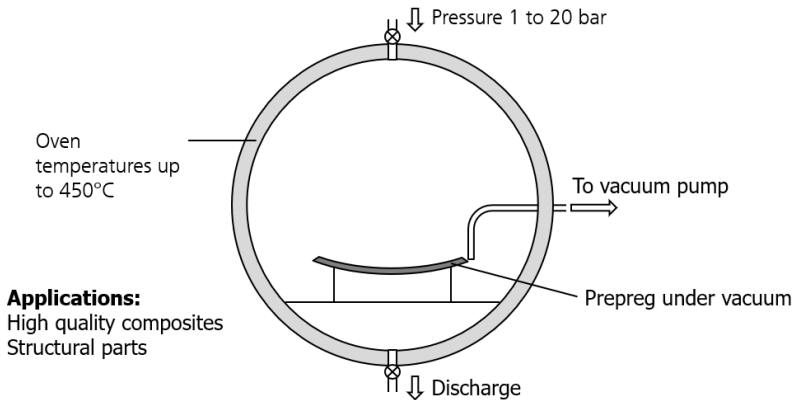


Figure 2.7: Drawing of an autoclave cross section [6, 25]

The pressure inside the autoclave is transferred onto the component at the boundary of the vacuum bag. Since the effective pressure on the part is the difference between ambient and vacuum bag pressure, see Equation 2.2, the higher the

autoclave pressure, the higher the pressure on the laminate. The transfer of auto-
clave pressure to the resin is depending on several factors, including fibre volume
content, laminate composition and the configuration of the vacuum bag.

In classic curing processes, the vacuum pressure is maintained during the first
heating phase. After the first isothermal holding phase, the autoclave pressure is
applied and the vacuum is vented. The idea of this approach is to remove any
volatiles from the resin when the viscosity is reduced, whereas applying autoclave
pressure would cause them to become trapped in the laminate. The pressurisation
following the holding stage ensures good compaction of the laminate before the
resin gels. [6, 17] Since this approach can lead to problems in the production
environment, the recommended curing cycles for newer prepreg generations with
zero bleed properties differ from this. Here, pressure and vacuum are maintained
over the entire length of the cycle. The early pressure increase helps to archive
higher heating rates and to compact and consolidate the prepreg at an early stage.
With increasing heat the viscosity of the resin is reduced and it begins to flow. The
laminate and fibre bed are compacted and trapped air and volatiles are evacuated
or collapsed under the high pressure. [11]

## 2.4. Leakages

The pressure difference between the inside of the vacuum bag and the ambient
atmosphere has significant influence on the quality of the composite component.
To achieve parts of high quality, vacuum loss due to leakages in the vacuum bag or
equipment is not acceptable. [11]

In the following subsections, different leakage types, their consequences as well
as detection methods from the literature are discussed. Finally, the state of the art
in aerospace manufacturing is explained in detail.

### 2.4.1. Leakages in vacuum bagging

Leakages can take multiple manifestations in different parts of the vacuum bag.
Depending on location and type of leakage, their detectability varies and the vacuum
inside the bag is impaired in different ways. [27] Critical types of leakages and their
impact on the quality of composite parts are shown in Figure 2.8 and portrayed in
the following.

**Leakages in vacuum film**   Besides fabrication defects like leaky weld seams in
films of extended width, improper handling in production can result in holes, slots,
perforation and puncture of the vacuum film. Negligent handling of sharp or pointed
objects and tools, as well as stepping onto the vacuum film during application, in-
creases the risk of leakage formation. These leakages can take place in different lo-
cations that might influence the detectability, e.g. under film folds, covered by ex-
ternal tooling or in the area of stiffening elements. [27] Tight application over sharp
edges or sudden thickness increases with small radii leads to local overstraining of
the film, especially in areas that are reinforced by stiffening elements. To prevent
excessive stresses that can lead to failure of the vacuum film, sharp edges must be
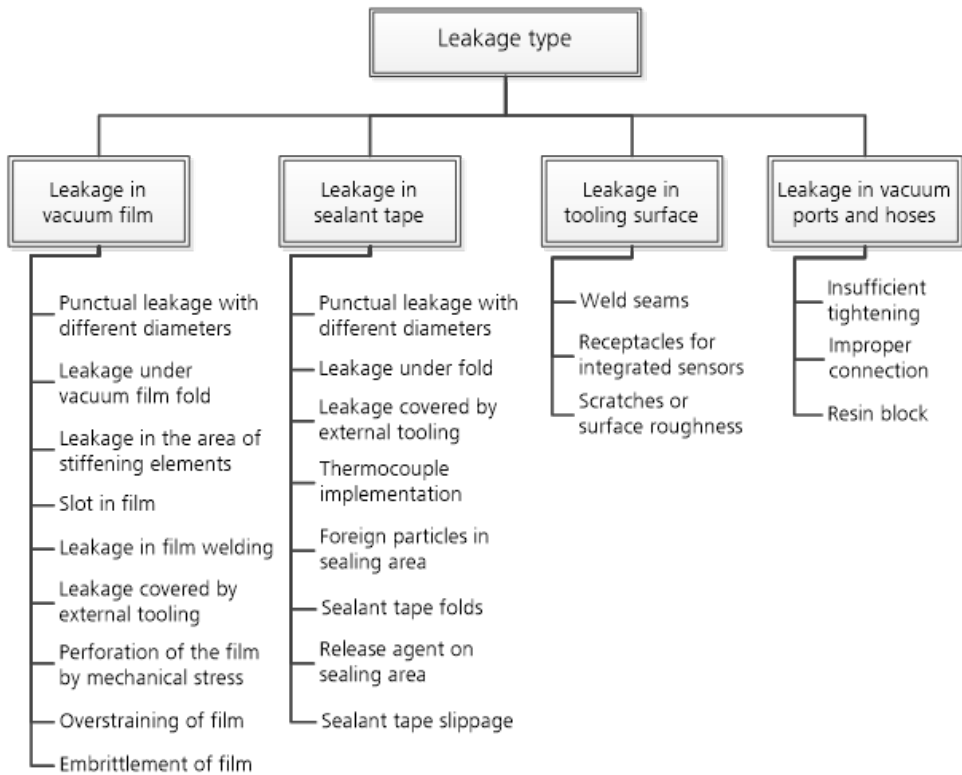
Figure 2.8: Classification of different leakage types, cf. [27]

covered with breather to avoid the formation of holes and punctures. [17] Since the flexibility of the vacuum film is dependent on its moisture content, embrittlement of the film might occur in the dry autoclave environment under elevated temperature. This might lead to failure of the film at improperly placed sections. Embrittlement might also occur if the vacuum film comes in contact with resin which ultimately can also lead to failure. [24]

**Leakages in the sealant tape**  Improper application of the sealant tape is one of the most frequent reasons for leaking vacuum bags. Leakages occur when thermocouples or foreign particles get in between the sealant tape and the tooling or vacuum film and prevent full contact. Besides dust and dirt from the ambient atmosphere, foreign particles can be loose fibres, threads or fluff from components of the vacuum bag such as the breather or peel ply. [28] Like the vacuum film leakages, sealant tape leakages can be located in areas that hinder their detectability (under folds or external tooling). Additionally, vacuum loss occurs when insufficiently pressing the sealant tape against contact surfaces such that airflow between sealant tape and vacuum film or tooling is possible. Grooves in the tooling surface

must be filled completely by the sealant tape and tape crossovers must be sealed by application of sufficient pressure. [6] Since complex geometries require generous application of vacuum film, excess film at the outer perimeter of the vacuum bag leads to formation of folds. The manual application of sealant tape into these folds is very error prone. During the autoclave cycle the strong airstream inside the vessel might lead to flapping of these pleats which can weaken the seal and result in detachment of the film. Release agent on the sealing area reduces the tack of the sealant tape to the tool and prevents secure adhesion. This can result in vacuum loss during curing. If the tension in the bagging film is too high, there is a risk of sealant tape slippage. This usually occurs when the bagging film is too small for the part surface and bridges in some tool areas. In comparison to leakages in vacuum film, leakages caused by improper sealant tape application are considerably easier to locate due to the specific sealant tape circumference as compared to the large surface area of the vacuum film.

**Leakages in tooling surface**   Another leak-prone boundary of the vacuum bagging setup is the surface of the tooling. Scratches in the tool or surface roughness might result in leaky sealing. [6] Weld seams or receptacles for integrated sensors can impair the airtightness of the tooling surface and lead to vacuum loss. [27]

**Vacuum ports and hoses**   Vacuum loss can occur as a result of leaking vacuum hoses or vacuum ports that are tightened insufficiently. Also, the quick connectors of hoses are leak-prone if connected improperly to the vacuum ports. Furthermore, excess resin might block the vacuum lines due to improper bagging. [28]

### 2.4.2. Consequences of leakages in vacuum bagging

The influence of leakages in vacuum bagging on the corresponding composite part quality depends on their location, size and the process step in which they appear. Smaller leaks only lead to low vacuum loss which, to some extent, can be compensated for by large industry vacuum pumps. Larger leaks or fractures of the vacuum film on the other hand result in pressure equalisation between the vacuum bag and the ambient atmosphere. [27]

Figure 2.9 provides an overview of the series of defects that are released when a leak is present in the tool or vacuum bag. It can be seen that a chain of different effects is triggered, which can later manifest themselves as measurable defects in the final component. This defects can be detected during the quality inspection of the finished part. The following gives an overview of the respective literature that considers the individual phenomena.

A high degree of evacuation of the vacuum bag is desired to achieve high forces onto the laminate to gain the desired high fibre volume content and to hinder porosity or void formation. [8, 26] A partial vacuum loss leads to a lower compaction of the laminate layers, while pressure equalisation with the environment results in a total loss of compaction. Due to the lack of compaction and vacuum, trapped air and possible dissolved moisture can not be evacuated from in between the fibre layers and hinder the interlayer bonding of the resin in these areas. The resin
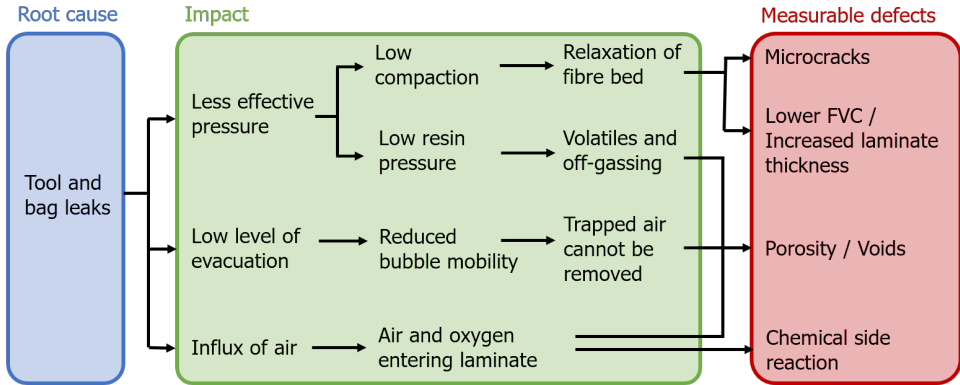
**2**



Figure 2.9: Impacts and measurable defects that are set free due to a leakage in the vacuum bag or tool

pressure becomes too low, to keep volatiles in solution and ensure a sufficient resin infiltration of the fibres in the prepreg laminate. This leads to the formation of porosity and voids inside the cured part which drastically impair the structural performance of the laminate. [29, 30] Figure 2.10 shows an example of voids and porosity in a CFRP laminate as a result of insufficient compaction.
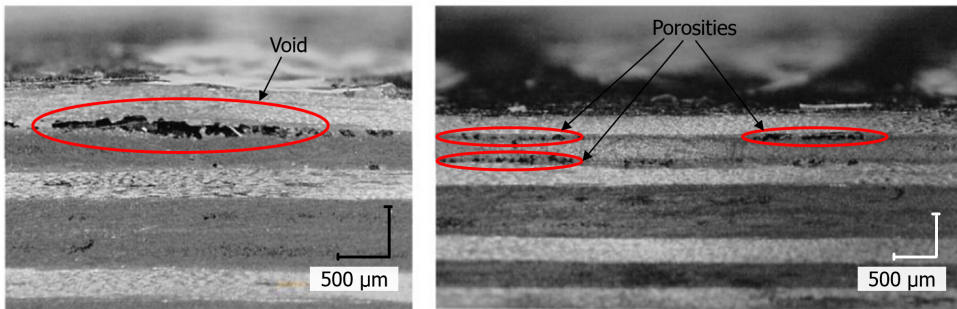


Figure 2.10: Voids and porosity inside a CFRP prepreg component as result of insufficient compaction

Vacuum loss during the autoclave cycle will damage the laminate if the resin is in a stage of the curing cycle during which the resin has started the formation of chemical cross-links but is not completely cured yet. The decrease of pressure onto the laminate causes relaxation of the layers. Since the resin is in a semi-fluid state, the uncured resin can participate in the relaxation while already formed chemical bonds in the cured portions will be broken up. This process leads to the formation of micro cracks which significantly reduce the structural integrity of the component. [28]

In addition to porosity and reduced fibre volume, the penetration of air into the vacuum structure can have other undesirable consequences. It cannot be ruled out that chemical side reactions can take place during curing. One example is the

degradation by oxygen radicals that is observed in epoxy resins from about $100°C$. The oxygen radicals preferentially attack the carbon atom directly adjacent to the nitrogen. A radial chain reaction takes place in several stages and requires an initiation reaction that causes chain branching. After several rearrangements, the bond between the carbon and the nitrogen atom is split and a carbonyl group is formed, see Figure 2.11. [31–34]
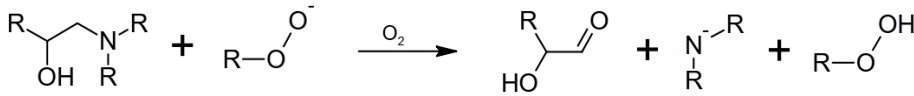


Figure 2.11: Schematic representation of the degradation of an epoxy resin network by oxygen radicals according to [31, 32]

Leakages also impair the quality of parts created by vacuum infusion processes from dry semi-finished products. The inflowing air caused by a leakage not only reduces the level of vacuum but also hinders the resin flow in direction of the leakage area. As a result, an increased number of voids or dry regions of entirely non-wetted fibres occur, leaving the component entirely useless as a worst-case scenario. [11] To reduce the risk of flawed components, vacuum infusion is performed with two stacked, separate vacuum films. This causes increased material usage and while the risk of both vacuum bags being leaky is smaller it is still existent nonetheless. [35]

### 2.4.3. Leakage detection methods

To detect possible leakages before the curing of the component inside the autoclave, the aerospace industry uses leakage detection methods after the vacuum bagging is finalised. In the following, different leakage detection methods from the literature are introduced and discussed.

**Pressure increase test**   The pressure increase test, also known as vacuum drop test, is the most straight forward method of leakage detection and is used in the majority of processes due to its simplicity. The vacuum bag to be tested is connected to a vacuum pump and a vacuum gauge prior to complete evacuation of the setup. Once the desired vacuum level is reached, the vacuum lines are disconnected from the vacuum bag and the pressure increase over a specified time is metered with the pressure gauge. Leakages lead to a pressure increase inside the vacuum bag while no pressure increase indicates an airtight bag. [27, 36]

In industrial processes an acceptable threshold value for pressure increase is commonly given. Typical aerospace manufacturer instructions specify, that a pressure increase in the vacuum bag must not exceed $66\ mbar$ within two minutes so that the component and the vacuum bag can be released for the autoclave process. [36] Should the pressure increase exceed the given threshold, the leakage must be located and repaired. The pressure increase test only allows for the identification of leakages but not for their localisation. Very small leakages might not be captured by the pressure increase test since, due to their constituents, most vac-

uum bags show a high capacitance for inflowing air before the pressure increase reaches the pressure gauge.[27]

The leakage rate can be quantitatively determined from the pressure increase curve according to the following relation: [37]

$$q_L = V_B \frac{\Delta p}{\Delta t} \tag{2.3}$$

with $q_L$ being the leakage rate in $mbar \cdot l/s$, $V_B$ is the volume of the vacuum bag in $l$ and $\Delta p/\Delta t$ is the pressure increase in the vacuum bag $\Delta p$ divided by the measuring time $\Delta t$ in $mbar/s$.

**Ultrasonic sensor**    The flow of air leaking into a vacuum bag contains supersonic turbulent flow that can be detected by an ultrasonic sensor that senses sound generated by escaping gas in a range of $38 - 42 \ kHz$. Ultrasonic leak detection devices convert the recorded ultrasound into frequencies audible to the human ear which the operator can hear through headphones. In addition, the sound level is displayed as a digital output. As the operator moves the device across the vacuum bag the location of the leak is found dependent on the ultrasonic sound levels. Leakage detection with an ultrasonic sensor is comparatively time-consuming since the sensor must be kept within $30 \ mm$ of the vacuum film and moved sufficiently slow for the operator to notice deflection of the digital output. [38] A typical ultrasonic leakage detector is shown in Figure 2.12.



Figure 2.12: Ultrasonic Leakage Detector [38]

**Microphone Array**    Leakage detection using manually placed ultrasonic microphones is already state of the art in the field of compressed-air leakages. In Eret et al. [39] compressed-air leaks are detected using microphone arrays and beam forming, a procedure to identify the position of sources of wave fields, and to locate them over large distances via a generated noise map.

**Infrared Thermography**    The theory of *Infrared* (IR) thermography is based on the fact, that the total radiation $W_{tot}$ that is received by the camera sensor is compiled from three sources: object radiation $W_{obj}$, radiation that is reflected

from the objects surroundings $W_{ref}$ and atmospheric radiation $W_{atm}$. [40–43] This relationship is given as:

$$W_{tot} = W_{obj} + W_{ref} + W_{atm} \tag{2.4}$$

Expanded, the Equation looks as follows:

$$W_{tot} = \varepsilon_o \tau_a \sigma_{sbc} T_{obj}^4 + (1 - \varepsilon_o) \tau_a \sigma_{sbc} T_{ref}^4 + (1 - \tau) \sigma_{sbc} T_{atm}^4 \tag{2.5}$$

where $\sigma_{sbc}$ is the Stefan–Boltzmann constant and equal to $\sigma_{sbc} = 5.67 \times 10^{-8} \frac{W}{m^2 K^4}$, $\varepsilon_o$ being the emissivity of the object, $\tau_a$ specifies the atmosphere transmittance parameter, $T_{obj}$ gives the temperature of the object, $T_{ref}$ denotes the temperature of the object surroundings reflected toward the camera and $T_{atm}$ being the atmospheric temperature.

For the leakage detection, the vacuum bag is scanned with the thermographic camera. Experiments showed, that the vacuum film on top has a transmission for IR-radiation in the spectral range of $7,5 - 13\ \mu m$, which is the sensing spectrum of common IR cameras like FLIR A315 [44], of 60-90% [45], depending on the vacuum film used. The camera is able to detect the temperature on the surface of the vacuum bag and in limits of the breather material beneath and thus shows a temperature deviation due to a leakage. [45]

The thermogram of a leakage and a characteristic temperature profile are shown in Figure 2.13.
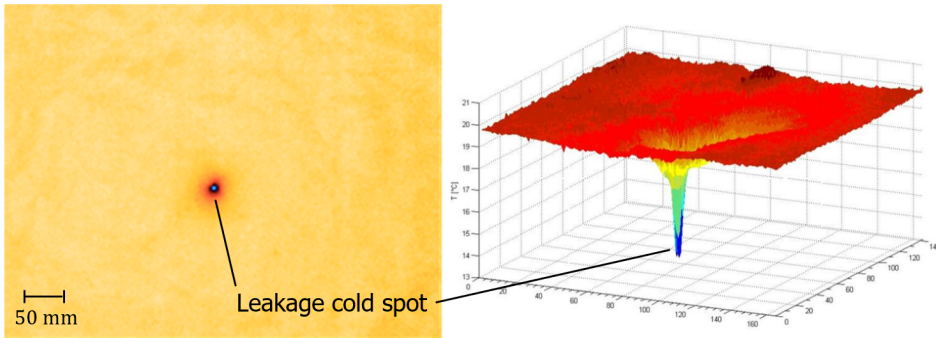


Figure 2.13: Thermogram of a leakage and characteristic temperature profile

The leakage detection system using infrared thermography is based on the Joule-Thomson effect. [46] The effect describes how the air as a non-ideal gas also undergoes changes in temperature during an isenthalpic pressure reduction. Air flowing into the vacuum bag through a leakage expands inside the lower pressurised vacuum bag, thereby cooling itself and the surrounding material down. [47] This local temperature decrease in direct proximity to the leakage can be identified as a cold spot in the image acquired by the thermal camera. To achieve a well-detectable decrease in temperature, it is beneficial to evacuate a faulty vacuum bag to the maximum achievable degree. [27]

This technique is simple to use and a contact-free process meaning its application for leakage detection has no impact on the composite part quality or the vacuum bag. As an imaging method, it allows for quick and exact identification of the leakage position. In addition, leakages have a characteristic temperature profile, which facilitates automated recognition and analysis of the thermal image. [45]

**Sensitive films**    In late 2010 The Boeing Company, Corporation, Chicago (USA) patented an oxygen sensitive film that is placed on the inside face of the vacuum film. [48] The film holds a gas-permeable membrane, which contains oxygen-sensitive material. As soon as a leakage occurs and the material comes into contact with oxygen, its appearance changes and the leakage can be detected visually. [48]

Other sensitive films, including thin planar pressure sensors like the pressure mapping sensor 6077 [49] shown in Figure 2.14, are available from Tekscan Inc. of South Boston, USA. These matrix-based sensors consist of two thin, flexible polyester films on which electrical conductors are printed in stripe patterns. The inside of one sheet has a row pattern, while the inside of the other sheet has columns. The spacing between the stripe patterns varies depending on the sensor application, and a semiconducting coating is applied over the conductors. When the two sheets are placed on top of each other, a grid pattern is formed. The intersections of the strips form individual sensor elements. When a force is applied to these sensor elements, the electrical resistance in the ink changes in inverse proportion to the normal force applied. The sensors are less than $0,1\ mm$ thick and typically have $2.000$ sensor elements. [50] Figure 2.14 shows a typical sensitive film pressure sensor.
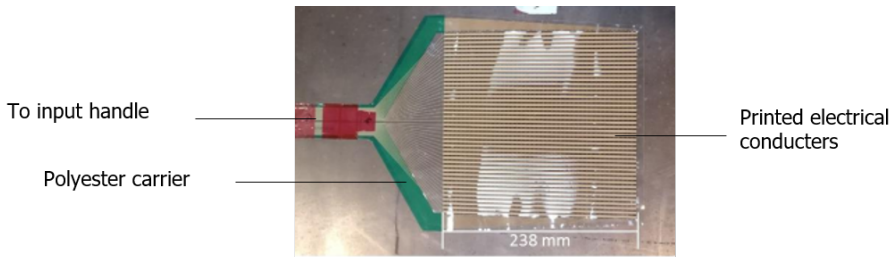


Figure 2.14: Tekscan 6077 pressure sensor

**Piezoelectric sensors**    Research at *German Aerospace Center* (DLR) in Stade has presented piezoelectric sensors as a possible leakage detection technology. [27] For this method, specifically adapted piezoelectric sensors based on standard iMPactXS tactile sensors from iNDTact GmbH, Würzburg (Germany) were used. [51] As shown in Figure 2.15, four of these sensors were used in the tests and placed in the four corners of the vacuum bag. The sensors were covered with the breather cloth and integrated into the structure in a vacuum-tight manner.

To detect a leakage inside a vacuum bag, the sensors make use of the piezo-electric effect which converts deformation – as a result of pressure fluctuations –

into an electrical charge. The progression and the time delay of the individual measurement signals allow for inference on the pressure fluctuation's origin and thus the leakage position. The local pressure change within the vacuum bag produced in the case of a leakage is recorded by the sensors and analysed using a Labview based software. To correctly locate the leakage, the input signals (in $mV$) are compared and the probable position of the leakage is calculated using a multilateral process. The output is an x-y coordinate. [52]
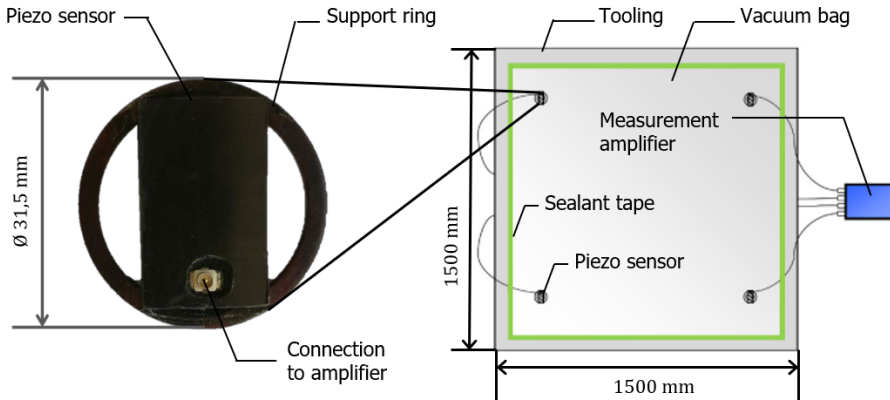


Figure 2.15: Piezo sensor and its integration in the vacuum bag

**Dyes**  A bright yellow fluorescent ink called EpoDye from Struers GmbH, Willich (Germany) is available for detection of cracks and pores in ceramic or metal components. [53] This ink can be used for leakage detection in vacuum bags if mixed with isopropyl alcohol and applied evenly to the outside surface of the vacuum bag. At the location of a leakage the vacuum draws the ink into the vacuum bag where it dyes the breather cloth. The colouration persists when the ink is wiped off the vacuum film and allows for the visual localisation of leakages. The functionality of EpoDye is shown in Figure 2.16.



Figure 2.16: Application of EpoDye for leakage detection

**2**

**Gas detectors**   Helium is the primary gas used in leakage detection with gas detectors. As an inert noble gas, helium will not react with the laminate, resin or cons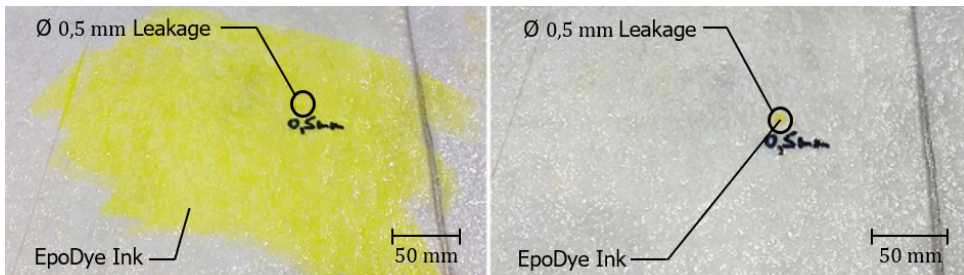tituents of the vacuum bag while also being non-toxic. Sections of the vacuum film are sprayed in sequence or the entire setup is fully submerged into the gas. A mass spectrometer is connected to the vacuum lines such that even smallest amounts of the test gas penetrating through the vacuum bag will be registered. [54] Fully submerging the vacuum bag is less tedious than subsequently spraying sections of the film with test gas but will only indicate the existence of leakages rather than also giving its position. Helium and mass spectrometers have a very high purchase price. Both methods are sketched in Figure 2.17.
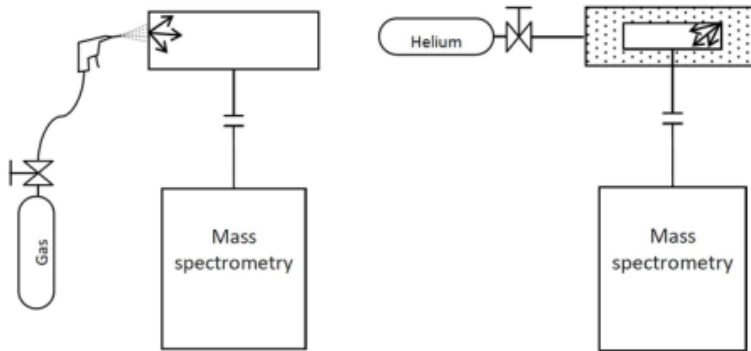


Figure 2.17: Leakage detection methods using test gas. On the left by spraying and on the right by fully submerging the vacuum bag. [54]

**Volumetric flow measurement**   Flow rate is a physical quantity used to quantify bulk fluid movement. It describes the amount of substance or volume of a fluid that passes through an observed tubing per time. [55] Measurement devices used for flow measurements are divided into mass flow meters and volume flow meters based on the respective physical quantity that is used to quantify the flow. The volumetric flow rate is defined by the limit

$$\dot{V} = \lim_{\Delta t \to 0} \frac{\Delta V}{\Delta t} = \frac{dV}{dt} \tag{2.6}$$

and directly correlated to the mass flow rate $\dot{m} = \frac{dm}{dt}$ by the fluid's density $\rho$

$$\dot{m} = \rho \dot{V} \tag{2.7}$$

The SI units for volumetric flow rate and mass flow rate are $[\dot{V}] = \frac{m^3}{s}$ and $[\dot{m}] = \frac{kg}{s}$, respectively. Furthermore, volumetric flow rate is commonly represented by the symbol $Q$.

   In addition to direct measurement, a variety of different physical effects can be used to indirectly determine flow rates by measuring correlated physical quantities

such as particle speed, for instance. [55] Furthermore, in industrial flow measurement it is not uncommon to use Equation 2.7 to convert a measured mass flow rate into volume flow rate that is displayed as a measurement reading. [56]

Thermal flow measurement is an indirect measurement method in which the temperature or a temperature difference is used to determine the mass flow rate via the specific heat capacity of the flowing medium. [57, 58] All design options of thermal mass flow meters consist of a heating unit and one or more points for temperature measurement. [56, 57] Thermal mass flow meters cover a wide measurement range down to small flow rates and show quick response behaviour with only moderate costs. [55] Especially the wide measurement range is of great benefit for leakage detection as the magnitude of volumetric flow rates caused by leakages varies depending on both amount and size of leakages. Additionally, thermal mass flow meters include no moving parts, making them unsusceptible to fatigue and provide a nearly unobstructed flow path. Because volumetric flow rate of the medium is measured via its mass flow rate, the measurement is largely independent of process-related temperature and pressure fluctuations. [55, 56]

Depending on application and magnitude of flow rate, different design options for thermal mass flow meters exist. Figure 2.18 shows a schema of the measurement devices used in the course of this work, a capillary type sensor as used for small flow rates by industrial standards.
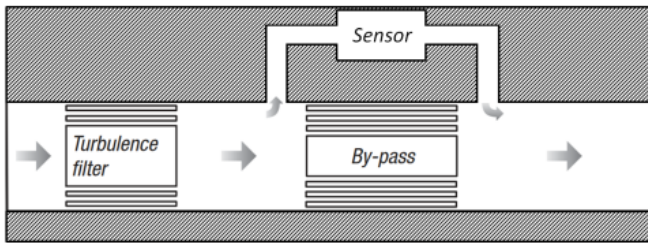


Figure 2.18: Bypass sensor, schematically; cf. [56]

Two temperature measurements are performed in the flume of the sensor, while a heating unit of constant power in between emits a constant amount of heat $Q_h$, not to be confused with the volumetric flow rate as discussed earlier in this chapter, per unit time that is transferred to the flow. The temperature increase $\Delta T_s = T - T_0$ of a substance is correlated to the absorbed heat $\Delta Q_h$ via the specific heat capacity $c_h$ of that substance:

$$\Delta Q_h = c_h \cdot m \cdot \Delta T_s \tag{2.8}$$

Differentiation with respect to time of Equation 2.8 and rearranging yields:

$$\dot{m} = \frac{\dot{Q}_h}{c_h \Delta T_s} \tag{2.9}$$

For constant power of the heating unit $\dot{Q}_h$ the mass flow rate $\dot{m}$ of the fluid can be computed directly based on the temperature increase, the latter being measured

by the temperature sensors adjacent to the heating unit. For small mass flow rates, the molecules of the substance passing through the flume reside in proximity to the heating unit for a longer time, thus absorbing more heat and the measured temperature difference increases. Correspondingly, a high mass flow rate leaves less time for the molecules to absorb heat, thus a smaller temperature increase is measured. A schematic of the sensor and discussed physical quantities is displayed in Figure 2.19.
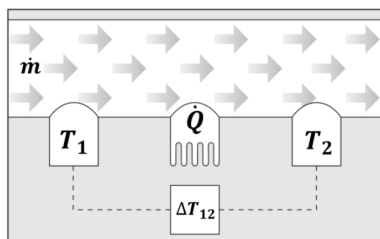


Figure 2.19: Physical working principle of thermal mass flow measurement, cf. [58]

Albeit the physical quantity measured by the thermal measurement principle is the mass flow rate, the sensors need to be calibrated to give volumetric flow rate measures based on Equation 2.7 using a specific gas density at a specific temperature and pressure. The potential deviations, if the gas has e.g. a different humidity or contains evaporations from the resin is around 17%. [56] Presentation of volumetric flow rates in standardised litres ($\ell_n$) per minute is widespread in industry because it makes measurements independent of local process temperature and pressure fluctuations possible.

If a leakage is present in the vacuum bag, a complete evacuation is not possible, due to a constant airflow into the leak. When connecting a vacuum pump, the flawed vacuum bag will be evacuated until equilibrium of incoming leakage flow and outflowing air through the vacuum line. Due to the conservation of mass, in a state of equilibrium the incoming air flow through the leakage $Q_{in}$ must equal the outgoing flow $Q_{out}$, which is shown in Figure 2.20 and stated in Equation 2.10. [26]
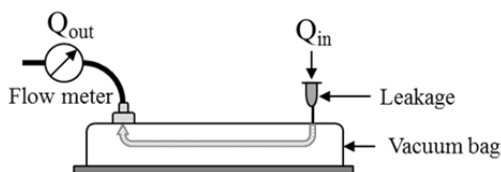


Figure 2.20: Premise: equilibrium of incoming and outgoing flow after sufficient evacuation

$$Q_{Leakage} = Q_{in} = Q_{out} = Q_{Pump} \qquad (2.10)$$

If the vacuum bag is airtight, the volumetric flow rate converges towards zero with progressing evacuation process. After reaching the upper measurement limit,

the volumetric flow rate measurement decreases fast in the initial process. With ongoing evacuation, the decrease of volumetric flow rate per time unit reduces and causes the measurement curve to flatten.

Flow meters for leakage localisation are used in a ready-to-use solution by the name of COHO which is offered by Convergent Manufacturing Technologies, Inc.. [15] COHO is a semi-permanent stand-alone system which connects to the vacuum ports to measure gas flow and off-gassing of constituents within the vacuum bag. An integrated computer algorithm compares gas flows to suggest areas in which leakages may be located. Possible leakage locations are indicated on a computer screen to guide the operator during leakage repair. Besides flow meters for localisation, the system also comprises a vacuum gauge to allow for the performance of vacuum drop tests. [59] At the time of this thesis' submittal, the influence of part geometry and size onto the accuracy of the suggested leakage location were unknown.

### 2.4.4. Leakage detection for aerospace components

The most common leakage detection process on aviation components starts with the application of a sensitive ultrasonic microphone, described in Subsection 2.4.3, to detect small and large leakages along the sealant tape during evacuation of the component. [27] This process step is shown on the left-hand side of Figure 2.21.



Figure 2.21: State of leakage detection technology on vacuum bags in the aircraft industry [27]

After evacuation, a dial pressure gauge as shown on the right-hand side of Figure 2.21 is used to perform the pressure increase test, described in Subsection 2.4.3 and assess the airtightness. [27] If the value is higher than permitted in the relevant specification, the leakage must be located. In older aircraft programmes, this is done using the sensitive microphone that has already been used to check the sealant tape. [27] Newer aircraft programmes additionally use the helium leak test and a test dye to locate leakages. [27] Figure 2.22 shows the flow chart for leakage detection in newer aircraft programs. Here, helium leakage detection is used especially for large composite parts like the A350 wing cover. [60] New developments in research range from volumetric flow rate measurement [15] to

leakage detection with thermographic cameras [46]. All technologies are presented in detail in Subsection 2.4.3.
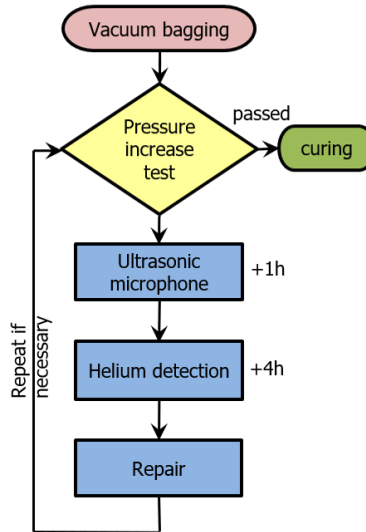


Figure 2.22: Conventional leakage detection process for newer aircraft programs [27]

Once defects are found, they are repaired using adhesive tape or sealant tape. [27] Should defects be unidentifiable, or too large for reworking, the vacuum film must be replaced. This process is very time-consuming and extremely dependent on the experience of the workers. According to Airbus Stade, the costs for a standard vacuum test are approximately € 30-80 per component, but this value is highly dependent on component size. [27] Depending on the production rate, this results in € 25,000-45,000 per component per year for the leakage tests alone. Additional expenditure of approximately € 5,500 per year and component type arises for searching possible leakages or replacing the vacuum bag. In combination with the costs of repairs and scrapping of components due to unidentified leakages, this results in leakage-associated costs of approx. € 50,500-70,500 per year and component type. [27] These extra and avoidable costs strengthen the statement that there is a need for faster and more robust leak detection methods for vacuum bags in the production of fibre composite components. [60] In general the cost factors are strongly dependent on the component size, the experience of the employees and the degree of automation of the process. In order to better understand these influences, the costs are broken down in more detail in Chapter 8 using an example component. In general, it is difficult to estimate the percentage share and these initial figures serve as motivation. The aim is to work through these scientifically and to obtain a detailed breakdown of the hidden costs.

## 2.5. Fluid dynamics

This section provides the theoretical framework of fluid dynamics for calculating the physical quantities within a leakage using the orifice plate model and CFD Simulation. The orifice plate can be used as a substitute model to analytically determine volumetric flow rate and the temperature drop inside a leakage. Later on the fundamental basics for CFD simulation are provided.

### 2.5.1. Orifice Plate

An orifice plate is a thin plate with a milled hole that is installed in a pipe. When flow passes through the hole, a pressure differential is created. This is created by slightly building up pressure upstream and reducing it downstream by forcing the fluid flow to converge through the hole, thereby increasing velocity. [61–64] A typical set up and flow pattern of an orifice inside a piping system is shown in Figure 2.23. Orifices are typically used for flow measurement or flow restriction. While the shape and manufacturing tolerances for orifices used in measurement applications are regulated by international standardisation of for example DIN EN ISO 5167-1 [65], restriction orifices are not defined by these standards.
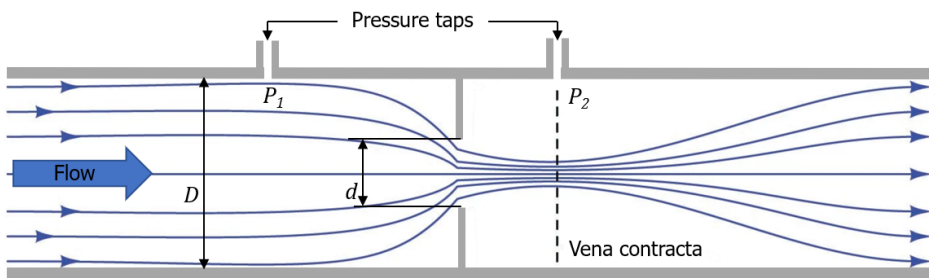


Figure 2.23: Flow through an orifice plate in a piping system cf. [61, 66]

Said et al. [61] calculate the minimum temperature at an orifice due to the Joule-Thomson-Effect using analytical and numerical calculations. As their investigations showed, the minimum temperature can also successfully be modelled with 3D computational simulation achieving very good results. [61]

### 2.5.2. Computational Fluid Dynamics

Computational fluid dynamics are a computer-based tool for simulating the behaviour of systems involving flows, heat transfer, and other physical processes. In this method, the fundamental conservation equations are solved in a particular region for which boundary conditions at the system boundaries are known. The conservation equations for momentum, mass and energy are known as the Navier-Stokes equations established in the early 19th century. [67–69] The *Reynolds Averaged Navier-Stokes* (RANS) equations express the equilibrium between inertial forces, volume pressure and friction forces. These partial differential equations can be solved numerically by discretisation. Due to their non-linear character analyti-

cal solutions are possible only for certain cases, like potential flows, creeping flows and boundary layer flows. Special feature are the additional terms arising from turbulent fluctuations, which complicate the solution of the Navier-Stokes equations. The closure problem is solved using different turbulence models. [67, 68]

$$\text{Continuity Equation} \qquad \frac{\partial \rho}{\partial t} + \frac{\partial (\rho \bar{U}_j)}{\partial x_j} = 0 \qquad (2.11)$$

$$\text{Momentum Equation} \qquad \frac{\partial (\rho \bar{U}_i)}{\partial t} + \frac{\partial (\rho \bar{U}_j \bar{U}_i)}{\partial x_j} = -\frac{\partial \bar{P}}{\partial x_i} + \frac{\partial (\bar{\tau}_{ij} - \rho \overline{u_i u_j})}{\partial x_j} \qquad (2.12)$$

$$\text{With:} \qquad U_i = \underset{\text{Mean velocity}}{\bar{U}_i} + \underset{\text{Fluctuating velocity}}{u_i} \qquad (2.13)$$

$$\bar{U}_i = \frac{1}{\Delta t} \int_{t}^{t+\Delta t} U_i \, dt \qquad (2.14)$$

The total energy is shown in Equation 2.15. The total enthalpy is obtained by adding the enthalpy and the kinetic energy. The viscous work term can be used in CFD simulations if it is applicable. This term can cause a redistribution of energy in the flow, which is not needed in normal applications, but for rotating walls like in turbomachinery it allows the transfer of mechanical work to the fluid (compressor) or its discharge (turbine). In this equation, apart from the viscous work term, there are other "redistributions" of energy. Dissipation in the flow does not increase the total enthalpy, but the kinetic energy decreases and the internal energy (temperature) increases. In an expansion, the velocity and kinetic energy increase and the internal energy decreases. In a compression, the ratios are reversed. [70]

$$\frac{\partial \rho h_{tot}}{\partial t} - \frac{\partial p}{\partial t} + \frac{\partial}{\partial x_j}(\rho U_j h_{tot}) = \frac{\partial}{\partial x_j}(\lambda \frac{\partial T}{\partial x_j} - \rho \overline{u_j h}) + \underbrace{\frac{\partial}{\partial x_j}[U_i(\tau_{ij} - \rho \overline{u_i u_j})]}_{\text{Viscous work term}}$$

$$(2.15)$$

$$\text{Total Enthalpy} \qquad h_{tot} = h \frac{1}{2} U_i U_i + k \qquad (2.16)$$

$$\text{Turbulent Kinetic Energy} \qquad k = \frac{1}{2} \overline{u_i^2} \qquad (2.17)$$

## 2.6. Machine Learning

The study of computer algorithms that can improve automatically through experience and the use of data is called machine learning. An artificial system learns from examples and can generalise these after the learning phase is complete. To do this, machine learning algorithms build a statistical model based on training data. This means that the examples are not simply learned by heart, but patterns and regularities are recognised in the learning data. The approach to machine learning is explained subtly in Figure 2.24. [71]
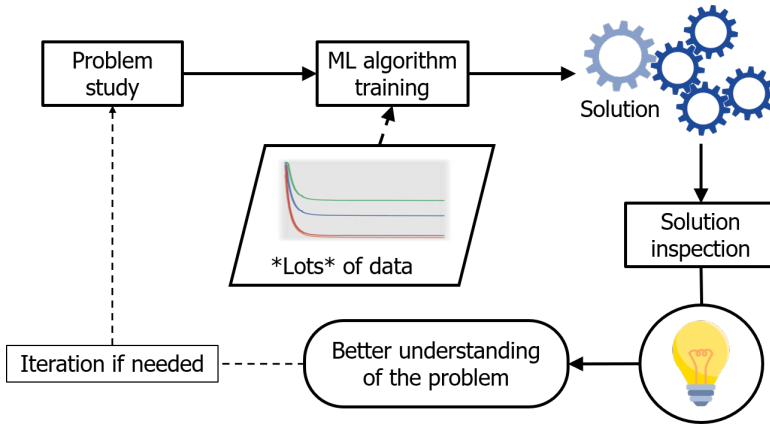
Figure 2.24: Approach to machine learning and data mining, cf. [71]

Deep learning is a machine learning method that uses *Artificial Neural Networks* (ANNs) with numerous hidden layers between the input layer and the output layer to create a rich internal structure to solve the task $T$. The most common tasks that can be solved by machine learning include *Classification* and *Regression*. In the classification task, the algorithm is asked to indicate to which of $k$ categories the input belongs. The regression task is similar to classification but has a different format of output as a numerical value is to be predicted given a specific input. [72]

Based on the kind of training provided, machine learning can be categorised as unsupervised, supervised, semi-supervised and reinforcement learning. [71] In unsupervised learning the algorithm does not receive pre-assigned labels or scores for the training data. In contrast, the supervised learning algorithm experiences a data set where each example includes a label or target. In semi-supervised learning only a portion of examples include a supervision target, while others do not. Reinforcement learning is characterised by having only numerical values for each training pattern instead of detailed tags. [72]

The capability of deep neural networks to generalise to unseen data relies heavily on the availability of sufficient training data. Depending on the application at hand, it is not uncommon to train networks on ten thousands up to millions of examples. Such large quantities of labelled data (i.e., input/output pairs) can be hard to gather, especially in industrial applications. Therefore, data augmentation techniques are frequently used to increase the amount of available training data synthetically. [72]

A *Fully Connected Neural Network* (FCNN) is a mapping $f_{\boldsymbol{\theta}} : \mathbb{R}^{n_0} \to \mathbb{R}^{n_L}$ with parameters $\boldsymbol{\theta}$ that shall be adapted to the data during training. More specifically, $f_{\boldsymbol{\theta}}$ takes an input $\boldsymbol{x} \in \mathbb{R}^{n_0}$ and maps it to an output

$$\hat{\boldsymbol{y}} \coloneqq f_{\boldsymbol{\theta}}(\boldsymbol{x}) \in \mathbb{R}^{k^2} \tag{2.18}$$

where the circumflex indicates that $\hat{\boldsymbol{y}}$ is a model prediction rather than the associated ground truth $\boldsymbol{y}$, that represents the reality.

A FCNN is usually considered a stack of *layers* each of which carries out a linear transformation of its inputs followed by a non-linear function. The general scheme is as follows:

$$
\begin{aligned}
\boldsymbol{a}^{[0]} &:= \boldsymbol{x} \\
\boldsymbol{z}^{[\ell]} &:= \boldsymbol{W}^{[\ell]} \boldsymbol{a}^{[\ell-1]} + \boldsymbol{b}^{[\ell]} \\
\boldsymbol{a}^{[\ell]} &:= g^{[\ell]}(\boldsymbol{z}^{[\ell]})
\end{aligned} \left.\vphantom{\begin{aligned} z \\ a \end{aligned}}\right\} \; \ell = 1, \dots, L
$$

$$
f_{\boldsymbol{\theta}}(\boldsymbol{x}) := \boldsymbol{a}^{[L]}
$$

(2.19)

The total number of layers $L$ is called the *depth* of the network. The $\ell$-th layer receives as input the *activation* vector (or simply output) $\boldsymbol{a}^{[\ell-1]} \in \mathbb{R}^{n_{\ell-1}}$ of the preceding layer which then undergoes a linear transformation by means of an $n_\ell \times n_{\ell-1}$ *weight matrix* $\boldsymbol{W}^{[\ell]}$ and an $n_\ell$-dimensional *bias vector* $\boldsymbol{b}^{[\ell]}$. The result $\boldsymbol{z}^{[\ell]}$ is further passed through a nonlinear *activation function* $g^{[\ell]} : \mathbb{R}^{n_\ell} \to \mathbb{R}^{n_\ell}$ to generate the output $\boldsymbol{a}^{[\ell]}$. Finally, the function value $f_{\boldsymbol{\theta}}(\boldsymbol{x})$ is defined as the output $\boldsymbol{a}^{[L]}$ of the top layer, see Figure 2.25.
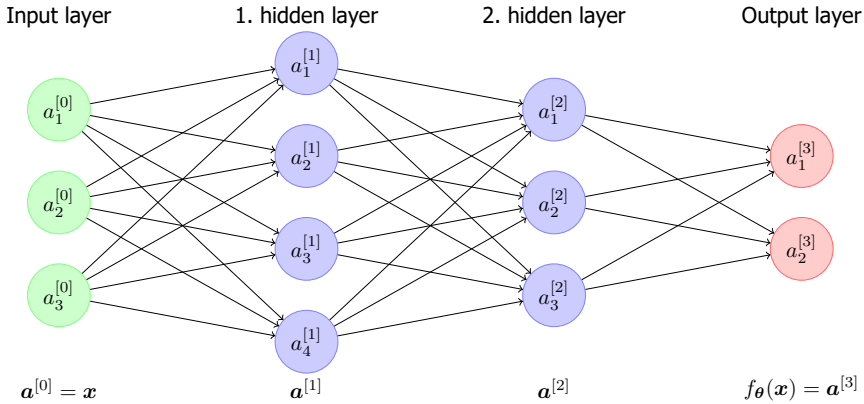


Figure 2.25: FCNN architecture. All layers of the neural network are fully connected with each other.

To compute the hidden layer values, the activation functions are used, that need to be chosen. The *Scaled Exponential Linear Unit* (SELU) activation function [73]

$$
\text{SELU}(z) = \begin{cases} \lambda z & \text{if } z > 0 \\ \lambda \alpha (\mathrm{e}^z - 1) & \text{if } z \le 0 \end{cases}
$$

(2.20)

can be seen in Figure 2.26 on the left. Therein, $\alpha$ and $\lambda$ are pre-defined constants ensuring a so-called *self-normalisation* property of the network layers which mitigates typical issues that can arise during training. The no less common logistic (or sigmoid) function [72]

$$
\sigma(z) = \frac{1}{1 + \mathrm{e}^{-z}}
$$

(2.21)

can be seen in Figure 2.26 on the right. Both are applied component wise to vector-valued inputs.

Figure 2.26: Activation functions

Different metrics are used to assess and compare the performance of different models. The *Mean Absolute Error* (MAE) [72]

$$\text{mae} = \frac{1}{m_e k^2} \sum_{i=1}^{m_e} \sum_{j=1}^{k^2} |\hat{y}_j^{(i)} - y_j^{(i)}|$$ (2.22)
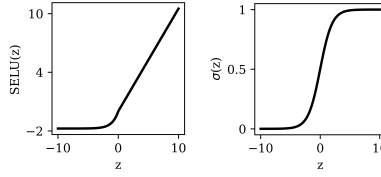
measures the mean absolute difference between predicted leakage probabilities and ground truths. Hence, model outputs are directly taken into account. However, the ultimate goal is rather to obtain a binary decision (zero or one) than a probability. To that end, it is common practice to introduce a threshold $\tau_{ml} \in [0, 1]$ which is then used to derive a decision function (or *hypothesis*) as follows:

$$\hat{h}_j = \begin{cases} 1 & \text{if} \quad \hat{y}_j \geq \tau_{ml} \\ 0 & \text{else} \end{cases}$$

The total count of *True Positve* (TP) and *False Positive* (FP) predictions on an entire dataset (training, validation or test) is used to compute the *precision* [72]

$$\text{precision} = \frac{\#TP}{\#TP + \#FP}$$ (2.23)

of a classifier. Vice versa, with the *False Negative* (FN) the *recall* [72]

$$\text{recall} = \frac{\#TP}{\#TP + \#FN}$$ (2.24)

denotes the probability that a positive prediction is a true positive. Both precision and recall must obviously lie in the interval $[0, 1]$ while a value close to one is obviously preferable in both cases. However, there is a trade-off: A model that performs only positive predictions would have perfect recall and low precision, while a model that is rather restrained in making positive predictions would have lower recall and higher precision. For that reason, and to obtain a single number evaluation metric, one often considers the so-called *F-score* [72]

$$\text{f-score} = \frac{2}{\frac{1}{\text{precision}} + \frac{1}{\text{recall}}}$$ (2.25)

which is simply the harmonic mean of precision and recall.

# References

[1] I. M. Daniel and O. Ishai, *Engineering Mechanics of Composite Materials* (Oxford University Press, 2007).

[2] R. M. Jones, *Mechanics Of Composite Materials* (CRC Press, 2018).

[3] M. Flemming, G. Ziegmann, and S. Roth, *Faserverbundbauweisen: Halbzeuge und Bauweisen*, Faserverbundbauweisen (Springer, 1996).

[4] M. Flemming, G. Ziegmann, and S. Roth, *Faserverbundbauweisen: Fasern und Matrices* (Springer Berlin Heidelberg, 2012).

[5] M. Flemming, G. Ziegmann, and S. Roth, *Faserverbundbauweisen: Fertigungsverfahren mit duroplastischer Matrix*, Faserverbundbauweisen (Springer Berlin Heidelberg, 2013).

[6] H. Lengsfeld, V. Altstädt, F. Wolff-Fabris, and J. Krämer, *Composite Technologien* (Carl Hanser Verlag, 2014).

[7] Z. Cai and T. Gutowski, *Consolidation techniques and cure control, Handbook of Composites*, , 576 (1998).

[8] A. Yong, A. Aktas, D. May, A. Endruweit, S. Lomov, S. Advani, P. Hubert, S. Abaimov, D. Abliz, I. Akhatov, M. Ali, S. Allaoui, T. Allen, D. Berg, S. Bickerton, B. Caglar, P. Causse, A. Chiminelli, S. Comas-Cardona, M. Danzi, J. Dittmann, C. Dransfeld, P. Ermanni, E. Fauster, A. George, J. Gillibert, Q. Govignon, R. Graupner, V. Grishaev, A. Guilloux, M. Kabachi, A. Keller, K. Kind, D. Large, M. Laspalas, O. Lebedev, M. Lizaranzu, A. Long, C. López, K. Masania, V. Michaud, P. Middendorf, P. Mitschang, S. van Oosterom, R. Schubnel, N. Sharp, P. Sousa, F. Trochu, R. Umer, J. Valette, and J. Wang, *Experimental characterisation of textile compaction response: A benchmark exercise,* Composites Part A: Applied Science and Manufacturing **142**, 106243 (2021).

[9] Y. Gu, C. Xin, M. Li, Y. Cheng, and Z. Zhang, *Resin pressure and resin flow inside tapered laminates during zero-bleeding and bleeding processes,* Journal of Reinforced Plastics and Composites **31**, 205 (2012).

[10] R. Dave, J. L. Kardos, and M. P. Duduković, *A model for resin flow during composite processing: Part 1—general mathematical development,* Polymer Composites **8**, 29 (1987).

[11] G. Fernlund, C. Mobuchon, and N. Zobeiry, *2.3 Autoclave Processing,* in *Comprehensive Composite Materials II* (Elsevier, 2018) pp. 42–62.

[12] D. Maass, *Automated dry fiber placement for aerospace composites,* in *Danobat* (2012).

[13] West System Inc., *Vacuum Bagging Techniques*, West System, 7th ed. (2010).

[14] T. Centea, L. K. Grunenfelder, and S. R. Nutt, *A review of out-of-autoclave prepregs – Material properties, process phenomena, and manufacturing considerations,* Composites Part A: Applied Science and Manufacturing **70**, 132 (2015).

[15] M. D. Lane, A. Poursartip, G. Fernlund, A. M. Floyd, D. A. V. Ee, and M. E. J. Hibbert, *Detection, monitoring, and management of gas presence, gas flow and gas leaks in composite manufacturing,* (2018).

[16] Airtech Europe Sarl, *Ipplon® DP1000 Data Sheet - Soft nylon film with an excellent elongation* (2020).

[17] F. C. Campbell, *Manufacturing Processes for Advanced Composites* (Elsevier Science, 2003).

[18] Airtech Europe Sarl, *GS-213 Data Sheet - Industry standard vacuum bag sealant tape for metal and composite tools* (2015).

[19] G. W. Becker and D. Braun, *Duroplaste - Kunststoff Handbuch 10* (Carl Hanser Verlag, 1987).

[20] G. Lubin, *Handbook of Composites* (Springer US, 2013).

[21] Airtech Europe Sarl, *Ultraweave® 606 Data Sheet – Medium weight nylon breather / bleeder* (2018).

[22] Airtech Europe Sarl, *Breathers & Bleeders Section Guide* (2018).

[23] A. Harper, *Why consider reusable vacuum bags?* Reinforced Plastics **57**, 40 (2013).

[24] F. C. Campbell, *Manufacturing Technology for Aerospace Structural Materials*, Aerospace Engineering Materials Science (Elsevier Science, 2011).

[25] Hexcel Corporation, *HexPly® Prepreg Technology*, Hexcel Cooperation (2013), Publication No. FGU 017c .

[26] A. Haschenburger, N. Menke, and J. Stüve, *Sensor-based leakage detection in vacuum bagging,* The International Journal of Advanced Manufacturing Technology **116**, 2413 (2021).

[27] A. Haschenburger and C. Heim, *Two-stage leak detection in vacuum bags for the production of fibre-reinforced composite components,* CEAS Aeronautical Journal **10**, 885 (2019).

[28] K. Kumar, M. Safiulla, and K. Ahmed, *Analysis of vacuum failures during curing of CFRP composites,* International Journal Of Scientific & Technology Research **2**, 220 (2013).

**2**

[29] G. Fernlund, J. Wells, L. Fahrang, J. Kay, and A. Poursartip, *Causes and reme-dies for porosity in composite manufacturing,* IOP Conference Series: Materi-als Science and Engineering **139**, 012002 (2016).

[30] F. Y. C. Boey and S. W. Lye, *Void reduction in autoclave processing of thermoset composites,* Composites **23**, 266 (1992).

[31] D. Fata and W. Possart, *Aging behavior of a hot-cured epoxy system,* Journal of Applied Polymer Science **99**, 2726 (2005).

[32] S. Wiebel, *Untersuchung zur thermischen Langzeitstabilität von Epoxidharzen-der elektrischen Isoliertechnik in Abhängigkeit von oxidativen Umgebungsein-flüssen*, Ph.D. thesis, Technische Universität Darmstadt (2012).

[33] C. Damian, E. Espuche, and M. Escoubes, *Influence of three ageing types (thermal oxidation, radiochemical and hydrolytic ageing) on the structure and gas transport properties of epoxy–amine networks,* Polymer Degradation and Stability **72**, 447 (2001).

[34] G. W. Ehrenstein and S. Pongratz, *Beständigkeit von Kunststoffen* (Hanser, 2007).

[35] A. Hindersmann, *Confusion about infusion: An overview of infusion processes,* Composites Part A: Applied Science and Manufacturing **126**, 105583 (2019).

[36] Airbus Operations GmbH, *AIPI03-02-019 Issue A3. Airbus Process Instruction – Manufacture of Monolitihic Parts with Thermoset Prepreg Materials* (2016).

[37] H. Rottländer, W. Umrath, and G. Voss, *Leybold - Grundlagen der Lecksuch-Technik*, Leybold GmbH (2016).

[38] Hilger und Kern GmbH, *Leak Detect - Leckage-Suchgerät für Druckluftnetze und Pneumatiksysteme in Maschinen und Anlagen*, Hilger und Kern (2013).

[39] P. Eret and C. Meskell, *Microphone arrays for compressed air leakage detec-tion,* in *4th Berlin Beamforming Conference* (2012).

[40] M. Vollmer and K.-P. Möllmann, *Infrared thermal imaging: fundamentals, re-search and applications* (John Wiley & Sons, 2017).

[41] FLIR Systems Inc., *The ultimate infrared handbook for R&D professionals,* Boston: FLIR AB (2010).

[42] N. Zobeiry, J. Park, and A. Poursartip, *An infrared thermography-based method for the evaluation of the thermal response of tooling for composites manufacturing,* Journal of Composite Materials **53**, 1277 (2018).

[43] R. Usamentiaga, P. Venegas, J. Guerediaga, L. Vega, J. Molleda, and F. Bulnes, *Infrared Thermography for Temperature Measurement and Non-Destructive Testing,* Sensors **14**, 12305 (2014).

[44] FLIR Systems, Inc., *FLIRA315 / A615 - Thermal Imaging Cameras for Machine Vision* (2014).

[45] H. Uçan, J. Bölke, C. Krombholz, H. Gobbi, and M. Meyer, *Robotergestützte Leckageerkennung an Vakuumaufbauten mittels Thermografie,* in *DLRK - Deutscher Luft- und Raumfahrtkongress* (2011).

[46] J. Bölke, H. Ucan, D. Stefaniak, and C. Krombholz, *Leckageerkennung,* (2012).

[47] P. Atkins, P. W. Atkins, and J. de Paula, *Atkins' Physical Chemistry* (OUP Oxford, 2014).

[48] M. E. Benne and F. B. Miller, *Leak detection in vacuum bags,* (2010).

[49] Tekscan Inc., *Pressure Mapping Sensor 6077* (2015).

[50] Tekscan Inc., *I-Scan Product Selection Guide* (2020).

[51] iNDTact GmbH, *iMPactXS Data Sheet - High-performance acoustic emission and dynamic load sensor* (2021).

[52] R. Petricevic, O. Radestock, C. Launer, and D. Kuhn, *Messvorrichtung und Verfahren zur Ermittlung und Ortung von Undichtkeiten beim Vakuumsackver-fahren,* (2015).

[53] Struers GmbH, *EpoDye Safety Data Sheet* (2019).

[54] Pfeiffer Vacuum Technology AG, *Lecksucher - Das breiteste Angebot an Lö-sungen für die Lecksuche mit Helium und Wasserstoff* (2016).

[55] H. R. Tränkler and E. Obermeier, *Sensortechnik: Handbuch für Praxis und Wissenschaft* (Springer Berlin Heidelberg, 2013).

[56] C. Mahrer and D. Walliser, *Instruction manual red-y smart series*, Aesch (2007).

[57] K. W. Bonfig, *Technische Durchflussmessung: unter besonderer Berücksichti-gung neuartiger Durchflussmessverfahren* (Vulkan-Verlag, 2002).

[58] Institut für Füge- und Schweißtechnik, *Berührungslose Durchflussmessung hochviskoser Klebstoffe,* Braunschweig (2008).

[59] Convergent Manufacturing Techonolgies Inc., *Coho gas flow and vacuum leakdetection system,* (2021).

[60] A. Haschenburger and N. Menke, *Sensor based analysis and identification of leakages in vacuum bagging for high performance composite components,* in *SAMPE Europe Conference* (2018).

[61] M. M. Said, *Analytical and Numerical Calculation of the Orifice Minimum Tem-perature Due to Joule - Thomson Effect,* Fluid Mechanics **3**, 33 (2017).

[62] A. Linford, *Flow Measurement and Meters*, Mechanical engineering series (Spon, 1961).

[63] M. Reader-Harris, *Orifice Plates and Venturi Tubes*, Experimental Fluid Mechanics (Springer International Publishing, 2015).

[64] R. W. Miller, *Flow Measurement Engineering Handbook* (McGraw-Hill Education, 1996).

[65] DIN EN ISO 5167-1, *Durchflussmessung von Fluiden mit Drosselgeräten in voll durchströmten Leitungen mit Kreisquerschnitt - Teil 1: Allgemeine Grundlagen und Anforderungen,* (2004).

[66] DIN EN ISO 5167-2, *Durchflussmessung von Fluiden mit Drosselgeräten in voll durchströmten Leitungen mit Kreisquerschnitt - Teil 2: Blenden,* (2003).

[67] P. M. Gerhart, A. L. Gerhart, and J. I. Hochstein, *Munson, Young and Okiishi's Fundamentals of Fluid Mechanics* (Wiley, 2016).

[68] G. Alfonsi, *Reynolds-averaged navier–stokes equations for turbulence modeling,* Applied Mechanics Reviews **62** (2009), 10.1115/1.3124648.

[69] H. Oertel, *Prandtl - Führer durch die Strömungslehre: Grundlagen und Phänomene*, Prandtl - Führer durch die Strömungslehre (Springer Fachmedien Wiesbaden, 2017).

[70] E. Krause, H. Schlichting, H. J. Oertel, and K. Gersten, *Grenzschicht-Theorie* (Springer, 2006).

[71] A. Géron, *Hands-On Machine Learning with Scikit-Learn and TensorFlow: Concepts, Tools, and Techniques to Build Intelligent Systems* (O'Reilly Media, 2017).

[72] I. Goodfellow, Y. Bengio, and A. Courville, *Deep Learning*, Adaptive Computation and Machine Learning series (MIT Press, 2016).

[73] G. Klambauer, T. Unterthiner, A. Mayr, and S. Hochreiter, *Self-normalizing neural networks,* in *Proceedings of the 31st international conference on neural information processing systems* (2017) pp. 972–981.

[74] Y. S. Aurelio, G. M. de Almeida, C. L. de Castro, and A. P. Braga, *Learning from imbalanced data sets with weighted cross-entropy function,* Neural Processing Letters **50**, 1937 (2019).

# 3

# Research gap and hypotheses

*The vacuum bagging is an essential process step during the manufacturing of high-performance composite components. Leakages can hinder full evacuation of the part and may lead to drastic defects in the final component. Therefore, the need for a reliable and fast leakage detection process in the industry is high, although the impact of a leak onto the final part is not fully investigated and understood. With the help of the state of the art, this chapter identifies the research and technology gaps and defines the goal of the thesis. The approach leads to the definition of a principle hypothesis and five hypotheses which affect the outline of the research performed in this work. The outline and structure of the present thesis are summarised at the end of this chapter.*

## **3.1.** Research and technological gap

Leakages are a concern in processing of open mould prepreg and infusion of composite parts. The literature and understanding of fundamental mechanisms is limited in this field and the processes for leakage detection are usually based on subjective estimates or empirical values.

Literature describes a need for high vacuum and pressure during the curing process. [1–6] A loss in vacuum or even pressure equalisation can lead to insufficient consolidation and voids inside the part which impair the quality and mechanical properties of the component. The reason for void formation is complex and has been studied in a few researches, especially for out of autoclave materials. [5, 6] Fernlund et al. [5] describe void sources that increase the risk of porosity, like entrapped air, leaks and volatiles, and void sinks that counteract this risk, like high evacuation level, elevated resin pressure and bubble mobility. Kumar et al. [7] investigate the effect of vacuum loss during the cure process on the mechanical properties of the component while focusing on the process time during which the vacuum loss takes place.

While it is generally agreed that leakages in vacuum bagging have a negative effect on the part quality, the exact influences of leakages on the vacuum bag and the component have not been fully researched and understood. The contemporary tests and detection methods are extremely dependent on the experience of the user. The thresholds in the given part specifications vary drastically due to the lack in automation and engineering analysis.

Altogether, all technologies available on the market are able to detect leakages in vacuum bagging, but nearly all of them are associated with a high manual and cost intensive effort. None of the existing procedures can detect the adequate position of a leakage in an adequate time and especially not fully automated on large components.

A major problem in the detection of leaks in the aerospace industry is that the detection methods used in series production and their limit values defined in specifications are valid independent of the component size, see Subsection 2.4.4. While in other leakage detection applications for overpressure and vacuum leaks, leakage rates are usually given in $mbar \cdot l/s$ [8] where the individual volume is taken into account, this is not the case for the threshold value specified in the *Airbus Process Instruction* (AIPI) [9]. The specified value of $66\ mbar$ per $120\ s$ is already exceeded after $66\ s$ for a $1\ l$ vacuum bag and a $0.1\ mm$ leakage, whereas a $2\ l$ vacuum bag requires $132\ s$ and would therefore be accepted with the same leakage size. The leakage rate of $1\ mbar \cdot l/s$ however is the same in both cases as the leakage size stays the same.

To develop an efficient and reliable detection method for leakages in vacuum bagging, it is necessary to understand the effects of different leakages on the physical conditions in the vacuum bag and the laminate. This includes pressure distribution, air flow and temperature as well as the impact on the final part quality. So far, there is no suitable substitute model that adequately describes the interrelationships between the effects of a leakage and the listed parameters. In literature, substitute models from geology are used for composite materials, but have never

been applied to describe a leakage case. [10] Furthermore, there is a need for a criterion in aerospace production to quantify and evaluate the severity of a leakage that is independent of the component size.

## 3.2. Research objectives

As can be seen from the literature review and the research gap derived from it, there is a large discrepancy between leakage detection in general and leakage detection in composite processing, especially in aerospace. The aim of the thesis is to better understand leakages in vacuum bags as well as their consequences and to derive uniform requirements for detection from the newly gained knowledge. From this, a new approach for the aerospace industry will be developed in which new technologies and sensors will be used and tested for their suitability. The localisation of the leaks, which is hardly possible in an adequate time with the methods currently used in series production and on large parts, is also investigated as part of the work. Various methods, such as machine learning, are used to draw conclusions from the sensor data about the position of the defect in the vacuum bag.

The outcome of this thesis, in addition to an improved understanding of the effects of leakages in vacuum bags, is a method for leakage detection and localisation based on the new requirement of a unified volume-based leakage criterion that not only simplifies leakage detection, but also makes it more robust, reliable, and cost-effective. These findings are particularly valuable for the aerospace industry as they ensure a stable process and enable higher automation of the vacuum bagging process in CFRP part manufacturing.

Based on the previously described deficits and the objectives of the thesis, below the hypotheses are formulated, which will be answered in this thesis and ideally close or reduce the knowledge and technology gaps described above.

## 3.3. Hypotheses

The literature review in Chapter 2 and the explanations in Section 3.1 and Section 3.2 are based on state of art and research in the field of vacuum bagging, leakages and leakage detection. The following principle hypothesis and individual hypotheses are based on the previous assumptions. They summarise the questions which need to be answered in order to determine the main factors for leakage detection and the influence of leakages in vacuum bagging on the part quality. At the same time, the hypotheses address areas in which further research may be taken up.

**Principle hypothesis:**  There is a method to characterise the influence of leakages in vacuum bagging on component quality in terms of size, type and location.

- **Hypothesis 1:** The influence of leaks on temperature, pressure distribution and velocity can be mapped and predicted with the help of flow simulation.

- **Hypothesis 2:** The impact of a leakage on the part quality in terms of porosity and voids can be physically explained and characterised.

- **Hypothesis 3:** There is a flow-dependent criterion for the exact quantification and evaluation of the airtightness.

- **Hypothesis 4:** With the help of a two-step process, it is possible to determine the exact location of the leak and thus achieve a significant time saving in leak detection (>30%).

- **Hypothesis 5:** With the help of machine learning and Neural Networks it is possible to achieve higher precision when identifying leak prone areas with flow measurement compared to a naive model based approach.

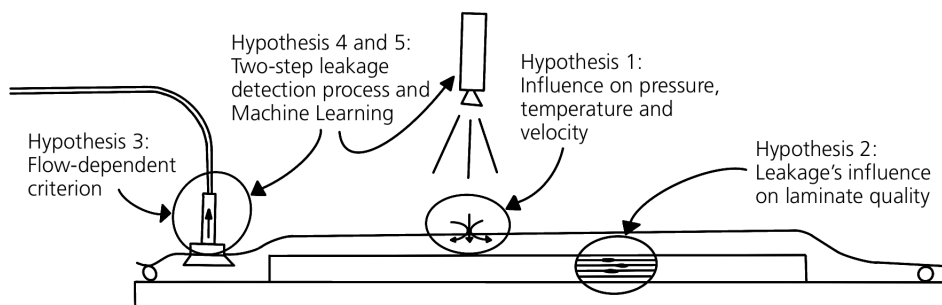The hypotheses 1-5 are shown schematically on a cross section of a vacuum bag in Figure 3.1.



Figure 3.1: Schematic affiliation of all hypotheses shown on a vacuum bag cross section

## **3.4.** Outline

The outline of this thesis aspires to a clear composition with regard to chapters and hypotheses, see Figure 3.2. The scientific approach is to first understand the problems associated with leakages in vacuum bags and their consequences on laminate quality before identifying appropriate detection and localisation methods and evaluating the industrial benefits.

After the introduction and literature review in Chapter 2, the research gap, objective of the thesis and the resulting hypotheses are presented in Chapter 3.

The first hypothesis is addressed in Chapter 4 of the thesis. To determine the influence of leakages on temperature, pressure distribution and airflow, and to create deeper understanding in the complex interactions inside the vacuum bag, an analytical model and a flow simulation is set up in Chapter 4. Furthermore some tests are carried out to validate the findings and flow simulation results.

In Chapter 5 of this thesis the impact of leakages on the resulting part quality is evaluated. Therefore a couple of tests need to be carried out to investigate the main factors of influence of leakages on porosity, voids and other possible quality issues. Hypothesis two relates to this topic and is discussed in this chapter.

Hypotheses three and four are addressed in Chapter 6 by an investigation of possible leakage detection methods. After narrowing down these methods the two-stage leakage detection process, its advantages and especially the volumetric flow rate measurement are described in a more detailed consideration within this chapter.

Chapter 7 of this thesis investigates the potential of machine learning and neural networks to further improve the leakage localisation with volumetric flow measurement. Model and data based approaches are compared in their accuracy and the fifth hypothesis is reviewed.

Finally the industrial value of the leakage detection process and the technologies assessed in this thesis are discussed in Chapter 8. Chapter 9 concludes with the results of this research and indicates where further work can be continued.
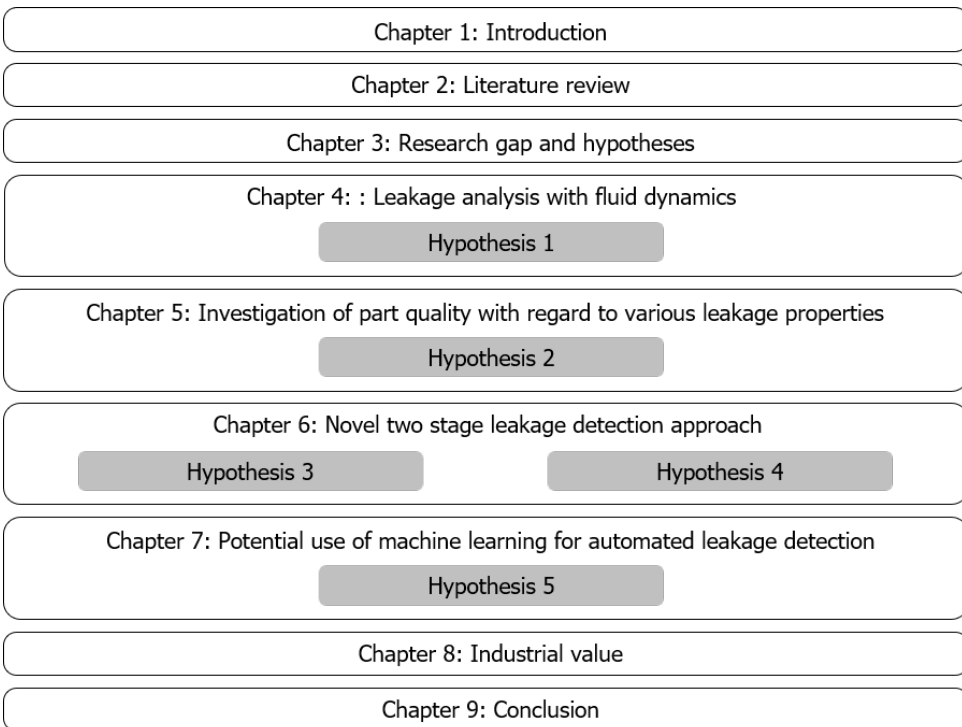
Chapter 1: Introduction

Chapter 2: Literature review

Chapter 3: Research gap and hypotheses

Chapter 4: : Leakage analysis with fluid dynamics
Hypothesis 1

Chapter 5: Investigation of part quality with regard to various leakage properties
Hypothesis 2

Chapter 6: Novel two stage leakage detection approach
Hypothesis 3          Hypothesis 4

Chapter 7: Potential use of machine learning for automated leakage detection
Hypothesis 5

Chapter 8: Industrial value

Chapter 9: Conclusion

Figure 3.2: Thesis outline and affiliation of hypotheses

# References

[1] G. Fernlund, C. Mobuchon, and N. Zobeiry, *2.3 Autoclave Processing,* in *Comprehensive Composite Materials II* (Elsevier, 2018) pp. 42–62.

[2] H. Lengsfeld, V. Altstädt, F. Wolff-Fabris, and J. Krämer, *Composite Technologien* (Carl Hanser Verlag, 2014).

[3] T. Centea, L. K. Grunenfelder, and S. R. Nutt, *A review of out-of-autoclave prepregs – Material properties, process phenomena, and manufacturing considerations,* Composites Part A: Applied Science and Manufacturing **70**, 132 (2015).

[4] F. C. Campbell, *Manufacturing Processes for Advanced Composites* (Elsevier Science, 2003).

[5] G. Fernlund, J. Wells, L. Fahrang, J. Kay, and A. Poursartip, *Causes and remedies for porosity in composite manufacturing,* IOP Conference Series: Materials Science and Engineering **139**, 012002 (2016).

[6] F. Y. C. Boey and S. W. Lye, *Void reduction in autoclave processing of thermoset composites,* Composites **23**, 266 (1992).

[7] K. Kumar, M. Safiulla, and K. Ahmed, *Analysis of vacuum failures during curing of CFRP composites,* International Journal Of Scientific & Technology Research **2**, 220 (2013).

[8] H. Rottländer, W. Umrath, and G. Voss, *Leybold - Grundlagen der Lecksuch-Technik*, Leybold GmbH (2016).

[9] Airbus Operations GmbH, *AIPI03-02-019 Issue A3. Airbus Process Instruction – Manufacture of Monolitihic Parts with Thermoset Prepreg Materials* (2016).

[10] R. Dave, J. L. Kardos, and M. P. Duduković, *A model for resin flow during composite processing: Part 1—general mathematical development,* Polymer Composites **8**, 29 (1987).

# 4

# Numerical analysis of leakages

*If there are leaks in a vacuum bag, the airflow, the volumetric flow rates, the pressure conditions and the local temperature in the vacuum bag will be affected. In order to understand the governing relationships, the influences are investigated analytically, experimentally and numerically in this chapter. This knowledge can be used to improve the detection and localisation of leaks, as well as to assess the effects on component quality.*

## 4.1. Introduction

To develop an efficient and reliable detection method for leakages in vacuum bags, it is necessary to understand the effects of different leakages on the physical properties of the vacuum bag and the laminate. This includes pressure distribution, airflow and temperature in the vicinity of the leak as well as the entire vacuum set up. Since all these properties are due to the airflow inside the vacuum bag, complex flow models need to be solved. [1]

Figure 4.1 shows the three disciplines of fluid mechanics and the structure of the chapter at hand. First, an attempt is made to find an analytical solution for the calculation of the physical conditions within the leakage using substitute models. Subsequently, these results are compared with experiments and further insights into the conditions in the entire vacuum structure are gathered. As these are complex relationships that are difficult and costly to reproduce, suitable simulation models are then created and CFD simulations carried out to determine the effects on pressure, velocity and temperature. By evaluating all three methodological approaches, a coherent picture of the effects of leakages on the conditions within the vacuum bag is obtained. This is important to better understand and interpret the resulting defects in the laminate in Chapter 5 as well as to develop suitable detection methods for leaks and limit the measuring ranges of the sensors used in Chapter 6.
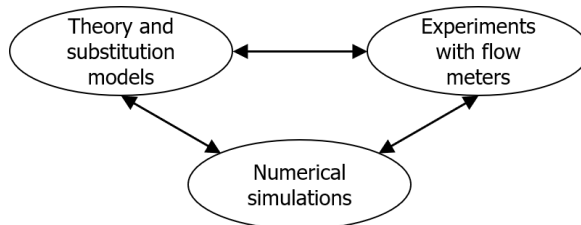


Figure 4.1: Structure of this chapter orientated on the three disciplines of fluid mechanics cf. [1]

## 4.2. Methodology

To better understand the mechanisms that occur inside a vacuum bag during a leak, a surrogate model and a simulation have been created. The following subsections describe the model creation as well as the boundary conditions for both approaches. The methodological procedure for the experiments that were subsequently carried out to verify the analytical calculation and CFD simulation are also presented below.

### 4.2.1. Orifice plate model creation

The chosen model to analytically calculate the mass and volume flow rate present in the area of the leakage has been the orifice plate, see Subsection 2.5.1. This model has been chosen because it represents the conditions within a leakage very well. Figure 4.2 shows a sketch of the transferred orifice plate model onto a vacuum bag. Unlike the Laval nozzle, in which the cross section narrows gradually,

the orifice plate, like the leakage, represents an abrupt change in cross-section encountered by an air flow. If the physical conditions within the vacuum bag can be successfully calculated by the orifice plate model, the effects of leakages of different sizes can be determined analytically. This can be helpful when creating leakage simulations, e.g. in order to be able to impose the correct mass flow on the inlet (the leakage) in a simplified 2D model. A reliable simulation in turn allows to evaluate the influence of a leakage or to perform data augmentation for *Artificial Intelligence* (AI) approaches.
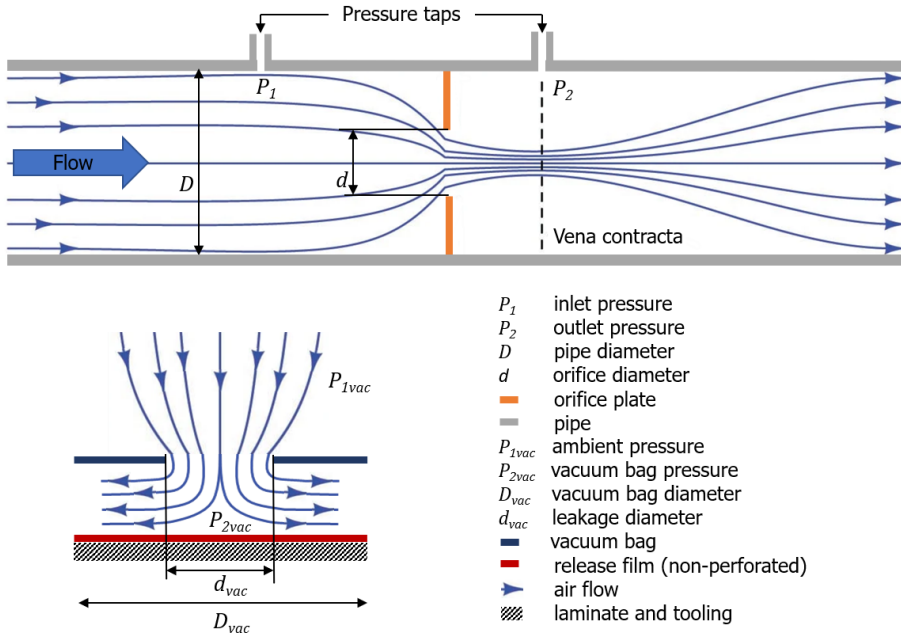


Figure 4.2: Transfer of the orifice model to a vacuum assembly

**Volumetric flow rate**   The sizing of orifice plates for gas applications is mainly determined by a formula described as the "Basic Compressible Sizing Equation", expressed below: [2, 3]

$$q_m = \frac{C}{\sqrt{1-\beta^4}} \epsilon \frac{\pi}{4} d^2 \sqrt{2\Delta P \rho_1} \tag{4.1}$$

With $q_m$ being the mass flow rate and $C$ the discharge coefficient. The discharge coefficient represents the relationship between the actual and the ideal, frictionless mass flow rate through the orifice. $\beta$ represents the ratio between orifice and inner pipe diameter, $d$ is the orifice diameter, $\rho_1$ is the density of the fluid upstream of the orifice plate and $\epsilon$ the expansion coefficient, where $\epsilon = 1$ if the fluid is considered

incompressible (liquid) and $\epsilon < 1$ if it is compressible (gaseous). [2] As shown in Figure 4.2, $P_1$ is the static inlet pressure measured at $1D$ upstream of the orifice plate, $P_2$ is the static outlet pressure measured at $\frac{1}{2}D$ downstream of the orifice plate, thus in Equation 4.1 $\Delta P = P_1 - P_2$.

Accordingly, the volumetric flow rate $Q$ is calculated:

$$Q/60000 = \dot{V} = \frac{q_m}{\rho} \tag{4.2}$$

Where $\rho$ is the density of the fluid at the temperature and pressure to which the volume is referenced.

For smaller values of $\beta$, e.g. restriction plates with $\beta$ less than $0.25$ and not covered by DIN EN ISO 5167-2 [3], the flow rate for compressible fluids depends on whether the flow is choked. For vacuum bags with leakage, the $\beta$ ratio is very small, e.g. a vacuum bag with a diameter of $1\ m$ already has a $\beta$ ratio of $< 0,001$ for a leakage of $< 1\ mm$. It needs to be checked whether the flow is choked. If this is the case, then the flow can be calculated as such.

Assuming ideal gas behaviour, a steady-state, choked flow occurs when the downstream pressure falls below a critical value $p*$. This critical value can be calculated from the dimensionless equation for the critical pressure ratio: [4, 5]

$$\frac{p*}{p_0} = \left(\frac{2}{\gamma + 1}\right)^{\frac{\gamma}{\gamma-1}} \tag{4.3}$$

Where $\gamma$ is the heat capacity ratio $c_p/c_v$ of the heat capacity at constant pressure $c_p$ to heat capacity at constant volume $c_v$ and $p_0$ is the total upstream pressure. With $P_2$ for downstream pressure and $P_1$ for upstream pressure the equation can be modified.

$$P_2 \leq P_1 \left(\frac{2}{\gamma + 1}\right)^{\frac{\gamma}{\gamma-1}} \tag{4.4}$$

This states that the downstream pressure becomes irrelevant if it is less than a multiple of the upward pressure. If Equation 4.4 is satisfied, the flow will be "choked" to a velocity of Mach 1.

Ideal gas behaviour has been assumed as air at ambient conditions of $1\ bar$ and $298\ K$ has a compressibility factor of $Z \approx 1$. As, in case of a vacuum bag, the upstream pressure $P_{1vac}$ is the atmosphere and the gas is air with a heat capacity ratio of $\gamma = 1.4$ the equation can be solved to $P_{2vac} \leq 0.535\ mbar$. Consequently it can be stated, that if the pressure inside the vacuum bag ($P_{2vac}$) falls below $0.535\ mbar$ the flow through the leakage is choked.

For choked flow conditions the following Equation can be used to calculate the mass flow rate $q_m$: [6]

$$q_m = C_d A_o \sqrt{\gamma \rho_1 P_1 \left(\frac{2}{\gamma+1}\right)^{\frac{\gamma}{\gamma-1}}} \qquad (4.5)$$

To calculate the volumetric flow rate $Q$, the equation can be converted as follows:

$$Q = C_d A_o \sqrt{\gamma \frac{P_1}{\rho_1} \left(\frac{2}{\gamma+1}\right)^{\frac{\gamma}{\gamma-1}}} \qquad (4.6)$$

Where $C_d$ is the discharge coefficient and $A_o$ is the orifice or leakage area. The coefficient of discharge can be calculated with the following Reader-Harris/Gallagher Equation with the given parameters: [3]

$$\begin{aligned}
C_d =&\, 0,5961 + 0,0261\beta^2 - 0,216\beta^8 + 0,000521\left(\frac{10^6\beta}{Re_D}\right)^{0,7} + (0,0188 + 0,0063A_c) \\
&\beta^{3,5}\left(\frac{10^6}{Re_D}\right)^{0,3} + (0,043 + 0,080e^{-10L_1} - 0,123e^{-7L_1})(1 - 0,11A_c)\frac{\beta^4}{1-\beta^4} \\
&- 0,031(M'_2 - 0,8M'^{1,1}_2)\beta^{1,3}
\end{aligned}$$

$$(4.7)$$

Where $Re_D$ is the Reynolds Number for the pipe diameter. $L_1$ $(= l_1/D)$ is the distance between the inlet pressure tapping and upstream face of the orifice divided by the pipe diameter. Accordingly, $L'_2$ $(= l'_2/D)$ is the ratio of distance between the outlet pressure tapping and downstream face of the orifice to pipe diameter ($L'_2$ indicates the reference of the distance to the backside of the orifice plate, $L_2$ would refer to the distance from the face of the orifice plate). As well as $M'_2 = \frac{2L'_2}{1-\beta}$ and $A_c = \left(\frac{19000\beta}{Re_D}\right)^{0,8}$. [3]

Since the ratio of leakage to vacuum bag is very small, $\beta \approx 0$, the value for $C_d$ can be assumed to be $0.5961$.

The volumetric flow rate of leakages of different sizes has been determined experimentally with volumetric flow rate measurement described in Subsection 4.2.6, so that the accuracy of this analytical model could be verified with the experimental data.

**Temperature**   The cooling in the area of a leakage, which can be observed by means of infrared thermography, is assumed to be caused by the relaxation of inflowing air to a lower pressure level. To analytically describe the conditions in the area of the leakage and determine the resulting temperature drop the Joule-Thomson principle is used.

Figure 4.3 shows the thermodynamic principles of the Joule-Thomson expansion. Air with the ambient pressure $p_1$ and the ambient temperature $T_1$ flows through the throttle. The air flowing in behaves like a piston, which delimits the volume $V_1$. On the other side of the throttle, the pressure level $p_2$ is lower and the air occupies a correspondingly larger volume $V_2$. A temperature $T_2$ is established.
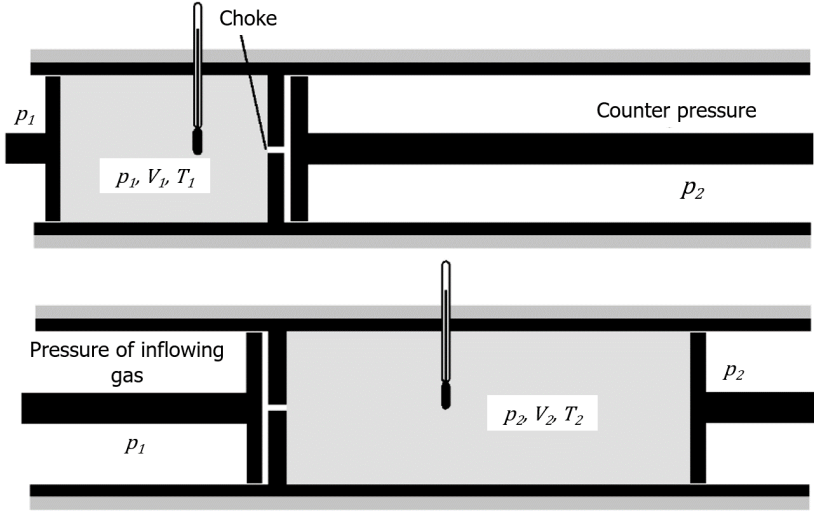


Figure 4.3: Illustration of the thermodynamic principles of Joule-Thomson expansion. The position of the pistons indicates the gas flowing in and out; the pistons provide a constant pressure on each side of the throttle. The transition from the upper to the lower diagram, which corresponds to the average of a given amount of gas through the throttle, occurs without enthalpy change, cf. [7]

According to the first law of thermodynamics for stationary flow processes the following applies: [8]

$$q_{12} + w_{t12} = h_2 - h_1 + \frac{1}{2}(c_2^2 - c_1^2) + g(z_2 - z_1) \qquad (4.8)$$

Where $q_{12}$ is the thermal energy, $w_{t12}$ is the technical work, $h_{1,2}$ are the specific enthalpies, $c_{1,2}$ are the velocities and $z_{1,2}$ are the heights of the entry and exit level.

As the gas flow is initiated due to the differences in pressure levels, no technical work is performed on the system $w_{t12} = 0$. The system is considered as adiabatic, as there is no significant heat exchange with the environment $q_{12} = 0$, and the change in potential energy from inlet to outlet is negligible, resulting in: [8, 9]

$$h_1 + \frac{c_1^2}{2} = h_2 + \frac{c_2^2}{2} \qquad (4.9)$$

Although velocities near the orifice can be relatively high and might cause extra temperature change, measurements upstream and downstream of the reduced flow area show in most cases that the change in fluid specific kinetic energy between these locations can be neglected, which reduces Equation 4.9 to: [9]

$$h_1 = h_2 \tag{4.10}$$

This is therefore an isenthalpic throttling of the gas. However, these assumptions only apply at a sufficiently large distance from the throttling point. [8]

For ideal gases, enthalpy depends only on temperature and not on pressure, so $T_1 = T_2$. If, on the other hand, air is consider to be a real gas, the enthalpy also depends on the pressure. In this case, a temperature $T_1 \neq T_2$ is established. This effect is also known as the Joule-Thomson effect. [8]

The effect can be explained by the fact that in real gases, in contrast to ideal gases, forces of attraction or repulsion occur between the molecules. Which of the two forces predominates depends on the medium under consideration and the state variables pressure and temperature. For air at ambient temperature and ambient pressure, the attractive forces predominate. If the pressure is now reduced, the average particle distance increases in the opposite direction to the attractive force. The energy required for this is taken from the kinetic energy of the particles. The gas consequently cools down. [10]

The relationship between the temperature change and the pressure gradient is described by the Joule-Thomson coefficient $\mu_{JT}$. [10]

$$\mu_{JT} = \left(\frac{\partial T}{\partial p}\right)_H \tag{4.11}$$

The coefficient $\mu_{JT}$ can be calculated using Van der Waals constants with the following equation:

$$\mu_{JT} \approx \frac{\left(\frac{2a}{RT}\right) - b}{c_{p,m}} \tag{4.12}$$

Following Van der Waals constants for air have been used: [11]

$$a = 0.136 \frac{Nm^4}{mol^2} \tag{4.13}$$

$$b = 3.657 \cdot 10^{-5} \frac{m^3}{mol} \tag{4.14}$$

$$c_{p,m} = 29.11 \frac{J}{molK} \tag{4.15}$$

This results in the following value for $\mu_{JT}$ at a temperature of $293\ K$ of:

$$\mu_{JT} \approx 2.58 \cdot 10^{-6} \frac{K}{Pa} = 0.258 \frac{K}{bar} \tag{4.16}$$

The calculations of the temperature inside the leakage have been evaluated with thermographic imaging in Subsection 4.3.2. However, the largest temperature difference is expected in the immediate vicinity of the leakage due to the increased flow velocity. The Joule-Thomson effect does not take this cooling into account, so that the calculations might be adapted for this particular case in Subsection 4.3.2.

**Pressure**   Once a state of equilibrium of the vacuum inside the bag is reached, a constant static pressure is established in a vacuum bag. Due to the presence of leakages, the gas remaining inside the vacuum bag or the constantly inflowing gas is not at rest, but is subject to flow processes due to the evacuation. For the quality of a vacuum setup, the remaining static absolute pressure in the setup is decisive. According to the Bernoulli equation in the field of gravity, the total pressure $p_t$ is composed of the static pressure $p_{st}$ and the dynamic pressure $p_{dyn}$. [12]

$$p_t = p_{st} + p_{dyn} + p_{gravity} \tag{4.17}$$

$$= p_{st} + \frac{\rho}{2}c^2 + \rho g z \tag{4.18}$$

Pressure and velocity are linked at each point of the velocity field.

In case of a vacuum bag the gravitational field can be neglected, as the flow is mostly horizontal, i.e. $z \approx 0$ and the density of gases is usually much lower than that of liquids so that the dynamic pressure together with the static pressure yields the total pressure inside of the bag. Following the dynamic pressure inside the leakage can be calculated with:

$$p_{dyn} = \frac{\rho}{2}c^2 \tag{4.19}$$

The calculation of the static pressure for compressible fluids is only possible numerically so that this will be carried out using CFD simulation.

### 4.2.2. Spring damper analogy model creation

To visualise the effects of a leakage in a vacuum bag and the corresponding changes of the pressure inside the bag, a spring damper analogy has been used, as described in Subsection 2.4.2. In Figure 4.4 springs and dampers have been used to represent the compression and reset behaviour of the breather material and the prepreg laminate (grey).

Figure 4.4 shows the pressure profile $\hat{p}_i$ within the vacuum bag for the individual states during the production process and if a leakage is present. The effective pressure $p_{eff}$ acting onto the laminate can be calculated with Equation 4.20 and is symbolised in Figure 4.10 by the small black arrows on top of the vacuum bag.

$$p_{eff} = p_{Atmo} - \hat{p}_i \tag{4.20}$$

In Figure 4.4a the initial state of the vacuum bag is shown. The prepreg laminate is layed up on top of a hard tooling and is shown in grey. Within the laminate air is entrapped during the layup process, which is represented by small inclusions. A non perforated release film is placed over the laminate, shown in red. Above this the breather material is placed which is intended to ensure uniform evacuation of the component. The vacuum bag is hermetically sealed by a vacuum film, illustrated in blue. The restoring forces of the laminate and the breather are represented by springs. During the initial state, before the evacuation of the bag, the pressure

$\hat{p}_a$ inside the bag is the same as the atmospheric pressure $p_{Atmo}$. The effective pressure $p_{eff}$ is zero.



Figure 4.4: Schematic representation of the pressure inside the vacuum bag. a) Initial state without vacuum $\hat{p}_a = p_{Atmo}$ (light blue line), b) During evacuation of the vacuum bag $\hat{p}_b < p_{Atmo}$ (purple line), c) Fully evacuated $\hat{p}_c << p_{Atmo}$ (green line), d) Vacuum bag with leakage $\hat{p}_c < \hat{p}_d \le p_{Atmo}$ (orange line)

During the evacuation process from Figure 4.4b, the remaining air inside the breather and the laminate is removed, which is represented by the blue arrows. The laminate and the breather are compressed. The internal pressure $\hat{p}_b$ is reduced and the effective pressure $p_{eff}$ rises. $p_{eff}$ is represented by the black arrows.

When the vacuum bag is fully evacuated, a state of equilibrium is established in Figure 4.4c. If the assembly is tight, the internal pressure $\hat{p}_c$ drops to almost zero $bar$. The effective pressure $p_{eff}$ on the laminate reaches its maximum. This

pressure can only be further increased by raising the ambient pressure, as is the case in an autoclave process.

Figure 4.4d illustrates the case of a leakage. The vacuum foil is damaged, which leads to a leak in the structure. Air from the environment flows through the leak and spreads out, shown by blue arrows. Since the release film is still intact, the air can not flow into the laminate. It spreads out in the breather and is then evacuated via the vacuum port and the vacuum pump. A constant air flow inside the bag is formed. In the vicinity of the leakage the internal pressure $\hat{p}_d$ increases and even reaches the ambient pressure $p_{Atmo}$ in the direct area of the leak. A pressure gradient builds up around the leakage. The effective pressure on the laminate $p_{eff}$ decreases locally which is shown in the graphic by the reset of the springs and dampers. Due to the local pressure difference, the resin also starts to flow preferentially into this area as soon as it reaches the lowest viscosity during the curing cycle and becomes fluent. This resin flow is represented by the thick black arrows.

In the experimental evaluation in Subsection 4.2.6, the magnitude of the pressure gradient around the leakage has been investigated. The effect of the leakage onto the final part quality will be subject to the trials in Chapter 5.

### 4.2.3. CFD simulation setup

Two simulations have been set up in order to investigate the influence of leakages in a vacuum bag. For both 3D and 2D simulation the ANSYS CFD software has been used. The following gives an overview about the simulation setup. The used models are all based on the basics of CFD described in Chapter 2.5.2.

ANSYS CFD uses the finite volume technique as the numerical solution method. The region is divided into individual control volumes, depending on the modelled grid. The conservation equations are discretised spatially and temporally for each control volume and solved iteratively. The result consists of approximated values for each variable at specified points in the computational domain. Evaluation in the post-processor allows the visualisation of the flow using the result values of the variables in the discretised points.

For calculations, ANSYS CFD uses iterative multigrid procedures. With the help of this procedure, the conservation equations are linearised. Coarser and finer grids are used to which the results are interpolated. This can speed up the solution, for example, long wavelength errors disappear faster on a coarser grid than on a finer grid. If necessary, a coarser grid would be used first and then the results are interpolated to a finer grid.

Most commonly the $k$-$\varepsilon$-turbulence model is used. It is a two-equation model in which two transport equations are solved for $k$ (kinetic energy of turbulence $\sim L^2/t^2$, $L$: length scale, $t$: time) and $\varepsilon$ (turbulent dissipation $\sim L^2/t^3$). An eddy viscosity $\mu_t$ is introduced, which depends on the turbulent parameters:

$$\mu_t = \rho C_\mu \frac{L^2}{t} = \rho C_\mu \frac{k^2}{\varepsilon} = \rho C_\mu L^2 \omega \tag{4.21}$$

In the case of turbulent viscosity, it is assumed that, analogous to viscous stresses, turbulent stresses are proportional to velocity gradients:

$$\tau_t = \mu_t \frac{\partial U}{\partial y} \tag{4.22}$$

The length scale $L$ (size of the turbulence elements / large eddies) is determined in the two-equation models using the transport equation:

$$L = \frac{k^{3/2}}{\varepsilon} = \frac{k^{1/2}}{\omega} \tag{4.23}$$

Where $\omega$ is the turbulent frequency ($\sim 1/T$), which is used as a turbulence parameter in the $k$-$\omega$-turbulence model. Two-equation models are a good compromise in terms of accuracy and economy for many flows. Unlike the $k$-$\varepsilon$-model, the $k$-$\omega$-model does not need special viscosity-dependent functions in the viscous sublayer near the wall. The $k$-$\omega$-model provides better results for delayed boundary layers and detached flows but stronger sensitivity to external turbulence parameters.

The *Shear Stress Transport* (SST)-model is a mixture of the $k$-$\varepsilon$- and $k$-$\omega$-turbulence model, with $k$-$\omega$ near the wall and $k$-$\varepsilon$ in the exterior and the external flow. It provides an additional modification of $C_\mu$ for accurate calculation of flows with pressure gradients and detachment. As the SST-model uses the advantages of both models, it is used in the following simulations.

### 4.2.4. 3D simulation

For the detailed investigations of the flow and physical effects inside a vacuum bag with a leakage, a 3D simulation has been set up in ANSYS CFX 19 [13]. In this model, a square vacuum bag including the surrounding ambient atmosphere has been generated.

**Simulation model**   Within this model, two domains have been created, the ambient atmosphere (fluid domain) and vacuum bag (porous domain), see Figure 4.5. The vacuum bag has been modelled as a volume, defined as a porous medium. Since the main flow occurs in the breathing material and the laminate itself is separated from this layer by a non perforated release film, the laminate itself is not part of the model. This simplifies the simulation and the observed effects can be transferred to the underlying laminate using, for example, the spring analogy from Subsection 4.2.2.

The vacuum bag film has been described by a membrane that separates the porous medium from the environment or fluid domain. There are four outlets in the corners of the vacuum bag representing the vacuum connection to the pump. These outlets can be individually assigned a pressure and thus different combinations can be simulated. The leakage itself is represented by a hole in the vacuum bag, where an interface between the porous medium and the ambient atmosphere has been created. Only the size of the surface has an influence on the flow, the shape of the leakage is secondary. Since round leakages with a constant area can be reproduced well in the experiments with the help of hypodermic needles, this shape has also been chosen for the simulation.
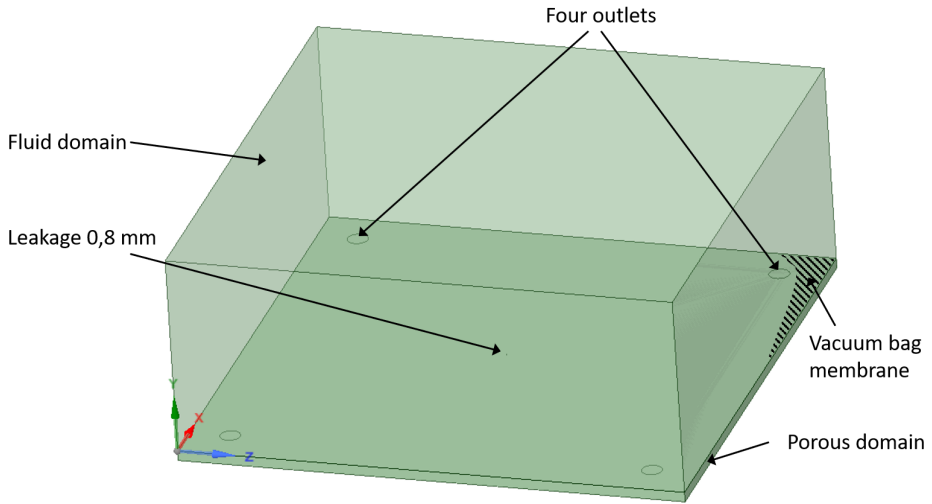
Figure 4.5: Main elements of the ANSYS 3D simulation model

Even though the breather and the vacuum bag are a flexible system that is subject to a change in volume due to evacuation of the entrapped air, it can be represented as a rigid volume in the simulation. As described in the spring analogy from Subsection 4.2.2 when the vacuum is applied, the breather is compressed to a maximum and at a certain vacuum level behaves like a container with a fixed volume. Since the simulated leakages are expected to cause only local pressure changes and that the pressure only rises above a critical value within the leakage itself, the vacuum structure has been modelled in the simulation as a porous medium with a fixed volume. To verify these assumptions further tests regarding the behaviour of the breather will be carried out in Subsection 6.3.3.

The vacuum bag has a base area of $500 \times 500 \ mm^2$ and a height of $10 \ mm$. The leakage is located in the centre of the part and has a diameter of $0.8 \ mm$. The outlets or vacuum connections are located in the four corners of the part with a distance of $60 \ mm$ to the edge and have a diameter of $20 \ mm$. The upper environment or fluid domain has been modelled on top with the same size as the vacuum bag and a height of $200 \ mm$. This model is presented in Figure 4.5. The ratio of leak size to vacuum bag had to be chosen due to a limitation in the ANSYS software that prevents smaller leaks from being resolved and meshed. A workaround to avoid these constraints is presented in the 2D simulation in Subsection 4.2.5.

**Meshing**  The meshing of the model has been performed with the ANSYS 19.3 Workbench [13] meshing tool. An unstructured mesh with tetrahedra has been created, as this type of mesh creation is easy to automate. The mesh of the vacuum bag and the ambient atmosphere need to be connected through an interface in the leakage area. The walls of a model require special consideration. Due to the

circumstances that the velocity at a fixed wall ("no-slip" in CFX) is zero, certain velocity profiles are formed. Therefore, the grids at the walls, i.e. in this boundary layer region, should be provided with a certain resolution to be able to represent them adequately. [1, 14] The inflation function, is an ANSYS feature which allows thin element stacking in the direction normal to the boundary to correctly capture the velocity and temperature gradients near no-slip walls. Within the model it has been used to create the boundary layers within the porous medium of the vacuum bag. The mesh statistics show that the whole mesh consists of 1,235,693 nodes and 4,670,545 elements. The mesh and the inflation prism layers are shown in Figure 4.6. As can be seen, the mesh refinement has been chosen according to the part features. A potential mesh convergence study would have to be designed to increase the number of cells relative to their size. Since the biggest influence comes from which fineness was chosen at which position, a mesh convergence study is not used in this thesis. In future work, however, such a study could make sense in order to reduce computational time and costs.
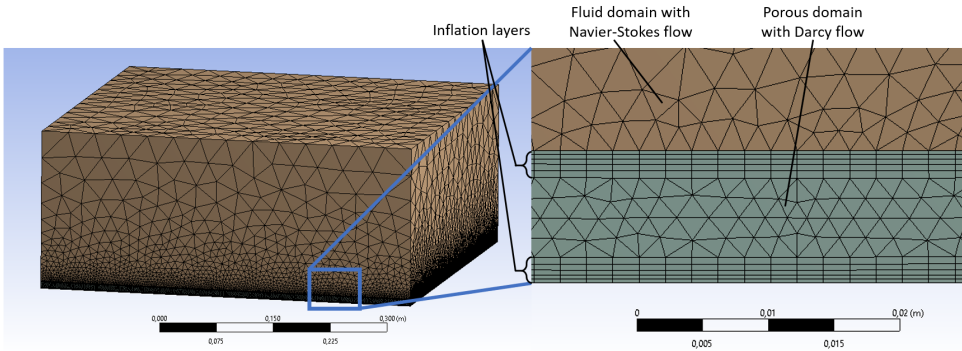


Figure 4.6: Meshing of the 3D simulation model with detail view of inflation layers

**Boundary conditions**  The fluid has been defined as air ideal gas and the five outer surfaces of the fluid domain are defined as openings, such that it is not a closed system. The pressure has been set to $101,325\ Pa$ ambient pressure and the temperature of the inflowing air is $20°C$. For the vacuum bag, a uniform (isotropic) volume porosity of $0.5$ and an isotropic permeability of $2.73^{-10}\ m^2$ has been defined. Both values for a typical breather material, that is used in the serial production, under full vacuum pressure are derived from the studies of Arafath et al [15] which investigates the gas transport in prepregs and breather material.

When using a permeability, the pressure drop is calculated as follows [16]:

$$\frac{\Delta p}{\Delta x} = \frac{P_v v \eta}{K_{Perm}} \tag{4.24}$$

Where $K_{Perm}$ is the permeability, $P_v$ is the volume porosity, $v$ is the flow velocity and $\eta$ is the dynamic viscosity. It follows that the smaller the permeability, the

greater the pressure drop. The pressure gradient and the permeability determine the magnitude of the velocity and the velocity curve, respectively. With smaller permeabilities, the pressure loss is greater and the velocities smaller, which leads to less cooling of the air. It is therefore essential to define the exact permeabilities for the breathers used.

An interface within the area of the leak has been created between the ambient fluid domain and the porous domain of the vacuum bag. Here both meshes have been connected to ensure a continuous flow between both domains. The pressure on the outlets has been set to $p_x = -0.9\ bar$ as the reference pressure $p_r$ has been defined as $p_r = 1\ bar$ atmosphere. Different combinations of outlets and leakages have been tested in the simulation. All simulations are steady state simulations calculated with the SST turbulence model, as it blends the advantages of the $k$-$\varepsilon$-turbulence and the $k$-$\omega$-turbulence model, see 4.2.3. In this model the Navier-Stokes equation is used to calculate the flow within the fluid domains. In the porous domain, the flow is calculated by means of the Darcy equation, a special solution of the Navier-Stokes equation. The heat transfer has been calculated by the total energy equation, described in Subsection 2.5.2.

Altogether, four 3D simulations with different configurations for outlet and leakages have been carried out. During the simulation run it could be observed that there is a better convergence of the continuity and momentum equation, compared to energy and turbulence. Only from an iteration number of approx. 10000 the mass flows from the leak and the outlets are approximately constant. It showed that the simulations are very time-consuming.

### 4.2.5. 2D simulation

Since the 3D simulation is very time-consuming and the leakage sizes in the selected simulation models are limited, a 2D simulation has been set up. ANSYS 19.3 Fluent [17] has been used for this purpose. The advantage of this simulation reduces the calculation time from seven days to a couple of minutes and that there is no longer any limitation regarding the sizes of the leakage and the vacuum bag. However, this is at the expense of the level of detail in terms of the exact values within the leakage.

**Simulation model and meshing**   Compared to the 3D simulation the 2D simulation model consists solely of a plate with the dimensions of the vacuum bag. Two dimensions for the simulated vacuum setups have been chosen: one to correspond to the dimensions of the vacuum setup that was simulated in the 3D simulation and one that has the same size as the experiments for the machine learning performed in Chapter 7.

As shown in Figure 4.7 the sizes are $500 \times 500\ mm^2$ and $1500 \times 1500\ mm^2$ with vacuum connections in all four corners. These are shown in the model as round cutouts with a diameter of $10\ mm$. The distance of the outlets to the vacuum bag edge is $20\ mm$ for the smaller and $70\ mm$ for the larger part. The leakage itself is implemented in the model as a round cutout as well. As only the area is The size for the leakage cutout has been chosen to be of $0.4\ mm$ radius for the smaller bag

and of $1\ mm$ radius for the larger setups to ensure a ratio of leakage to vacuum bag dimension that is still possible to process with the ANSYS software. Through the boundary conditions, these leakage cutouts have been defined as mass flow inlets with different mass flow rates to simulate different sized leakages.

The meshing has been performed with the ANSYS 19.3 Workbench meshing tool. The maximum element size has been set to $10\ mm$ for the larger geometry. The mesh for the $500 \times 500\ mm^2$ geometry consists of 3460 nodes and 3361 elements, whereas the $1500 \times 1500\ mm^2$ mesh consists of around 24500 nodes and roughly 24000 elements depending on the leakage number and position. Figure 4.8 shows the meshes in comparison. With the feature of named selections, the elements have been named: the hole component as the vacuum bag, the edges of the vacuum connection cutouts as Outlet 1-4 and the edge of the cutout for the leakage named as Inlet.
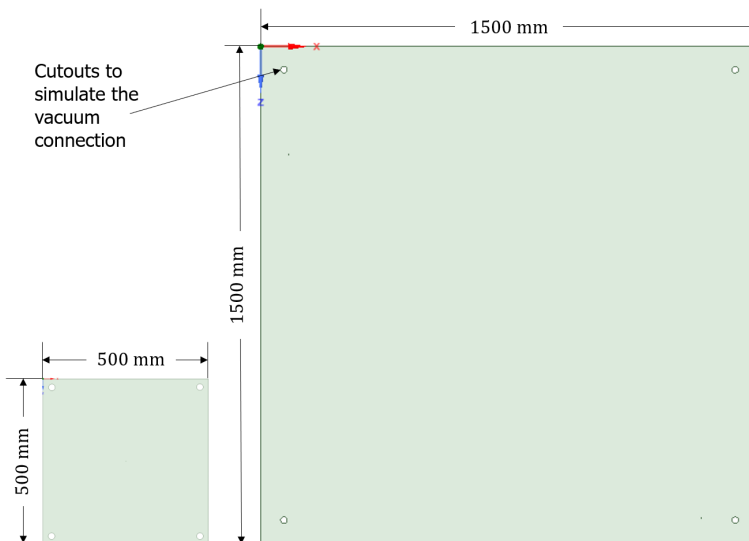


Figure 4.7: Model geometries for 2D simulation

**Boundary conditions**  As already introduced above, the mesh has been loaded into the ANSYS 19.3 Fluent software and the 2D space and steady state has been chosen. As calculation models, the viscous transition SST model as well as the energy equation has been selected. The fluid is air at room temperature. The cell zone has been defined as a porous medium with a uniform (isotropic) volume porosity of $0.5$ and an isotropic permeability of $2.73^{-10}\ m^2$, determined by Arafath et al. [15], so that a Darcy flow is present.

The outlets have been defined as pressure outlets with a gauge pressure of $p_x = -950\ mbar$ as the reference ambient pressure is defined as $p_r = 0\ bar$ by default. The leakage has been defined as a mass-flow inlet where the mass flow in $kg/s$
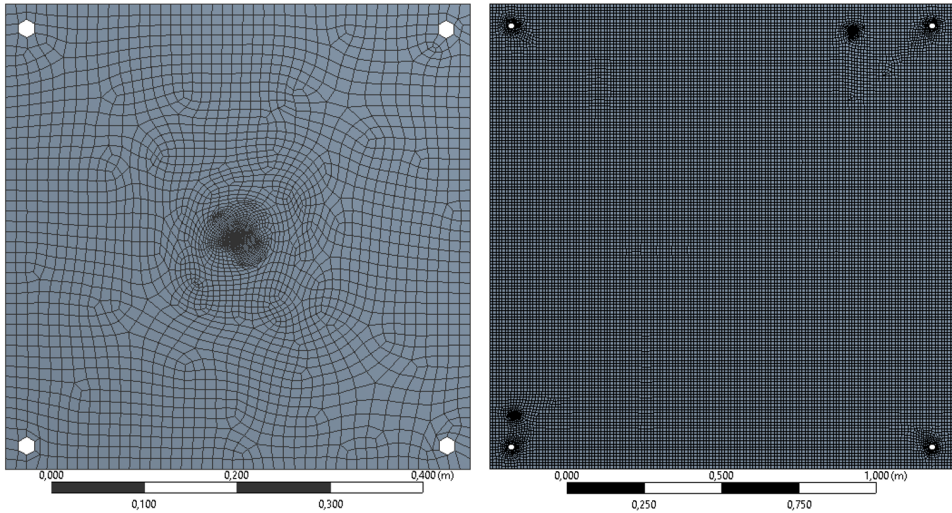
Figure 4.8: Meshes for 2D simulation

is specified as a function of the respective leakage size. The respective value has been determined by the calculations from Subsection 4.2.1. In this way, different leakage sizes can be simulated in the vacuum setup, even if this had not been possible before due to software restrictions. Within the performed trials it needs to be checked if the inaccuracy caused by the fact that the modelled leakage has a constant size of $1\ mm$ radius is negligible if the mass flow fits the actual leakage size.

Four 2D simulations on the $1500 \times 1500\ mm^2$ vacuum bag have been carried out and the flow rates are compared to experiments performed in Chapter 7 with the same methodology as described in Subsection 4.2.6. The leakage position can be seen in Figure 4.9 and were randomly defined. Sample 0, 3, 4 and 9 were chosen because they contained one or two leakages. The final results for the comparison with the experiments are shown in Subsection 4.3.1.

### 4.2.6. Experimental setup

In order to obtain basic knowledge about the influences of leakages on the pressure distribution and the local temperature in the vacuum bag, as well as to verify the theory and simulation models, different tests have been carried out on differently sized setups. A validation table made of stainless steel with a flat surface has been used as a tool for the setups. Pressure gauges, thermal mass flow meters, pressure-sensitive films and a thermography system have been used for the measurements.

**Measurement technology**    The used pressure gauge has been a *Thermovac TM 101* manufactured by Oerlikon Leybold Vacuum GmbH, Köln (Germany) [18] and the flow meters were *Hi-Performance Smart Meters* from the *red-y smart series* by Vögtlin Instruments GmbH, Muttenz (Switzerland) [19]. In contrast to the pres-

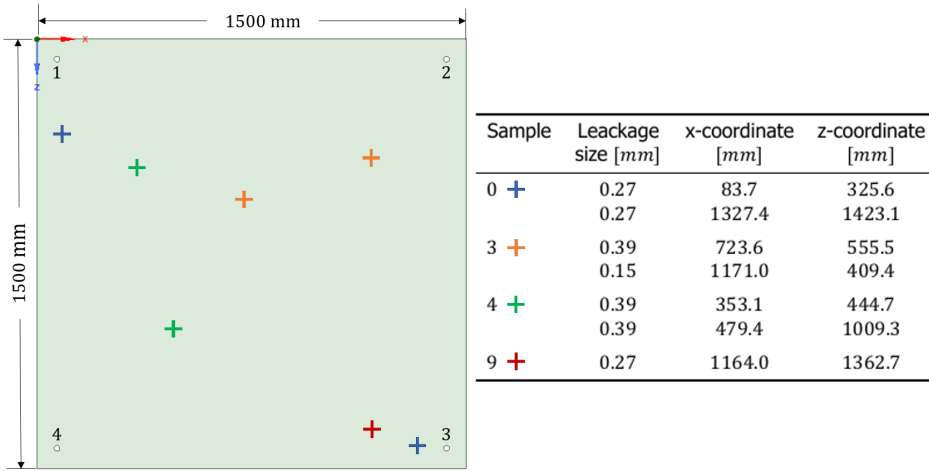| Sample | | Leackage size [mm] | x-coordinate [mm] | z-coordinate [mm] |
|---|---|---|---|---|
| 0 | + | 0.27 | 83.7 | 325.6 |
| | | 0.27 | 1327.4 | 1423.1 |
| 3 | + | 0.39 | 723.6 | 555.5 |
| | | 0.15 | 1171.0 | 409.4 |
| 4 | + | 0.39 | 353.1 | 444.7 |
| | | 0.39 | 479.4 | 1009.3 |
| 9 | + | 0.27 | 1164.0 | 1362.7 |

Figure 4.9: Leakage size and positions of the conducted experiments and simulations

sure gauge, the flow meters are available with different measurement ranges. Two types of thermal mass flow meters have been chosen to sufficiently cover a measurement range of 0 $\ell_n/min$ to 20 $\ell_n/min$ for all relevant leakage sizes. The first flow meter has a small measurement range to accurately take measurements for small leakages while the second flow meter is dimensioned to take measurements for larger leakages. The used measurement technology is shown in Figure 4.10, measurement ranges and errors are listed in Table 4.1.
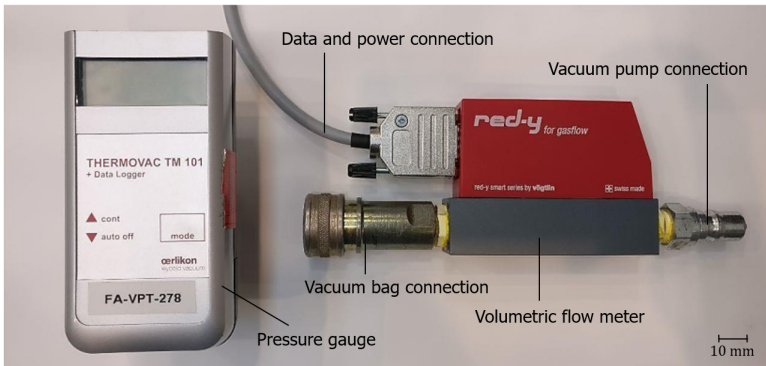


Figure 4.10: *Thermovac TM 101* and *red-y smart GSM*

In addition, two-dimensional pressure sensors from the company Tekscan Inc., South Boston (USA) have been used, like described in Subsection 2.4.3. Depending on the selected sensor, the sampling rate is up to 100 $Hz$ with a resolution of 8 $bit$. Thus $2^8 = 256$ different values ($0 - 255$) can be coded. Calibration converts

Table 4.1: Measurement technology [18, 19]

| Instrument | Measurement range | Error |
|---|---|---|
| Oerlekin Leybold *Thermovac TM 101* | $1200 - 5 \cdot 10^{-4}\ mbar$ | $200 - 10\ mbar$ 0.3% of full scale $10 - 2 \cdot 10^{-3}\ mbar$ 10% of reading $< 2 \cdot 10^{-3}\ mbar$ < factor 2 |
| Vögtlin Instruments GSM-C3TA-BN00 | $0\ \ell_n/min - 20\ \ell_n/min$ | $\pm$0.3% of full scale $+ \pm 0.5\%$ of reading |
| Vögtlin Instruments GSM-C3TA-BN00 | $0\ \ell_n/min - 1\ \ell_n/min$ | $\pm$0.3% of full scale $+ \pm 0.5\%$ of reading |

these raw values into pressure units. [20, 21] For the performed trials, sensors of the types 6077 and I-Scan 210 have been used and are described in Table 4.2. Dimensions and areas refer to the active area provided with sensor points. The linearity is $< \pm 3\%$ and the repeatability is $< \pm 3.5\%$. [21]

Table 4.2: Pressure sensors used and their characteristics [20, 21]

| Sensor | Dimension x $[mm]$ | Dimension y $[mm]$ | Area $[mm^2]$ | Resolution $[points/mm^2]$ | Sensor points |
|---|---|---|---|---|---|
| 6077 | 95.3 | 53.3 | 5080 | 0.276 | 1400 |
| I-Scan 210 | 238 | 238 | 56640 | 0.0034 | 1936 |

The main component of the measurement system used for IR-based leakage detection is the FLIR A615® IR camera [22] from the manufacturer FLIR Systems Inc., Wilsonville (USA). The camera has an uncooled thermal receiver which is equipped with a microbolometer matrix. The optical resolution is $640\ x\ 480$ pixels, resulting in a 4:3 image. The thermal sensitivity is $50\ mK$ at a temperature of $30\ °C$. The resolution of such low temperatures places the highest demands on the consideration of interfering influences such as atmospheric radiation and reflections. In the context of this work, a value of $0.1 - 0.3\ K$ is specified for the consideration of the measurement noise due to the low consideration of the disturbance influences. The measurement range of the camera is in the IR-*Longwave* (LW) range with wavelengths between $7.5 - 13\ \mu m$ and the frame rate is a maximum of $50\ Hz$. [22]

**Volumetric flow rate**    To evaluate the analytical and numerical volumetric flow rate calculations, flow rate measurements on different sized vacuum bags have been carried out. Three sizes of vacuum bags with the dimensions of $620 \times 910\ mm^2$, $1160 \times 1160\ mm^2$ and $1450 \times 1460\ mm^2$ have been created. The setup of three differently sized vacuum bags was intended to allow for findings concerning the influence of the vacuum bagging area onto the volumetric flow rate.

All leakage investigations were conducted with a simplified vacuum bagging setup. Inside the vacuum bag, nearly all airflow takes place within the breather cloth whose primary function is the distribution of airflow across the vacuum bag. Air flowing through other layers of the bagging is mostly hindered by the resin and would in fact cause harm to the composite part which is why the release film is included as a barrier. Since most relevant airflow caused by a leakage is travelling through the breather, the simplified vacuum bag as used for all conducted experiments was constructed with only a layer of breather and without laminate, peel ply, and release film. Furthermore, the tooling was not treated with a release agent. The term vacuum bag used in subsequent experiment descriptions refers to this simplified version of the vacuum bag. The used materials are listed in Table 4.3. All experiments were performed in an air-conditioned environment at 22°C.

Table 4.3: Vacuum Bagging Materials

| Material | Manufacturer | Product |
|---|---|---|
| Vacuum film | Airtech Europe Salr, Differdange, LUX | Ipplon DP 1000 [23] |
| Breather | Airtech Europe Salr, Differdange, LUX | Ultraweave 1332 [24] |
| Sealant tape | Airtech Europe Salr, Differdange, LUX | GS-213-3 [25] |
| Adhesive tape | Nitto Denko Corp., Osaka, Japan | PS-1 [26] |

Leakages have been introduced into the vacuum bag under consistent conditions to ensure comparability and repeatability of conducted experiments. It showed that leakages created by puncture of the vacuum film differ in shape, presumably due to deviations during puncture, in needle geometry, or local quality deviations of the film. Furthermore, it seemed that the vacuum would pull the film together again over time such that leakages would decrease in size while vacuum lines were connected. To avoid these phenomena, leakages have been created by using the needle channel of single-use hypodermic needles of different sizes according to DIN EN ISO 7864 [27] shown in Figure 4.11 as leakage area. After insertion, the needles remained inside the vacuum film to ensure a constant, reproducible leakage area with only minimal deviations due to the puncture process. After measurements, leakages were repaired with adhesive tape.

Differently sized leakages have been introduced consecutively at four evenly spaced locations along the centre line of the vacuum bags. Hypodermic needles of seven sizes have been used to create one leakage at every location after evacuation. Standard sizes of hypodermic needles were chosen up to a size where the created leakage would emit a hissing noise which was detectable by ear without effort. Combinations of needles were used to create leakage areas which filled in gaps in the measurement series due to the standard sizes of the injection needles. Used hypodermic needles and combinations are listed in Table 4.4.

The vacuum bag has been repaired and evacuated prior to every leakage introduction. After every puncture of the vacuum film, the volumetric flow rate has been measured until equilibrium was reached. A total of twelve measurements has been taken for each needle diameter.
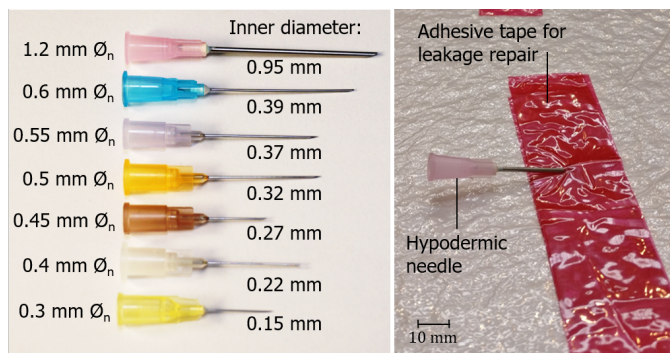
Figure 4.11: Hypodermic injection needles used for leakage creation, cf. [28] and created leakage in a vacuum bag

Table 4.4: Leakage size characterisation results

| Nominal diameter $\varnothing_n$ $[mm]$ | Inner diameter $[mm]$ | Leakage area $[mm^2]$ |
|---|---|---|
| 1.2 | 0.95 | 0.7088 |
| 0.9 | 0.65 | 0.3318 |
| 0.8 | 0.57 | 0.2552 |
| 0.6 | 0.39 | 0.1195 |
| 0.45 | 0.27 | 0.0573 |
| 0.4 | 0.22 | 0.0573 |
| 0.3 | 0.15 | 0.0177 |
| $1.2 \times 2$ | N/A | 1.4176 |
| $0.8 \times 2$ | N/A | 0.5104 |
| $1.2 + 0.8$ | N/A | 0.9640 |
| $1.2 + 0.8 \times 2$ | N/A | 1.2192 |

**Temperature**    To evaluate if the results from the calculations and simulation regarding the temperature inside the leakage hold true experiments with different leakage diameters have been carried out. Three needles with different diameters have been used in this experiment. As they would be visible in the thermograph they had to be removed in order to measure the temperature drop in the centre of the leakage. To avoid a change in the leakage diameter, all leaks have been measured with a microscope after creation. Table 4.5 shows the resulting leakage area for all experiments. The three different diameters have been used 10 times each. And the static pressure inside the vacuum bag has been measured.

During a second experiment, the continuous recording of a thermogram sequence and the parallel measurement of the pressure level in the test set-up have been carried out with the aid of a digital pressure gauge. A leakage of $0.55$ $mm$ diameter is implemented in the vacuum membrane. The pressure level in the vacuum bag is continuously increased by disconnecting the vacuum pump. The recorded thermogram sequences are used for subsequent linear temperature measurements

Table 4.5: Leakage size characterisation results

| Needle diameter $D_n$ [$mm$] | 0.33 | 0.65 | 0.95 |
|---|---|---|---|
| Hole # | Area measured [$mm^2$] | Area measured [$mm^2$] | Area measured [$mm^2$] |
| 1 | 0.045 | 0.156 | 0.717 |
| 2 | 0.061 | 0.231 | 0.366 |
| 3 | 0.072 | 0.239 | 0.356 |
| 4 | 0.063 | 0.214 | 0.548 |
| 5 | 0.055 | 0.229 | 0.328 |
| 6 | 0.073 | 0.238 | 0.456 |
| 7 | 0.065 | 0.243 | 0.295 |
| 8 | 0.067 | 0.212 | 0.402 |
| 9 | 0.078 | 0.217 | 0.370 |
| 10 | 0.052 | 0.240 | 0.497 |
| Average area [$mm^2$] | 0.063 | 0.222 | 0.434 |
| Standard deviation $\sigma$ | 0.010 | 0.024 | 0.124 |
| Real diameter $D'_n$ [$mm$] | 0.28 | 0.53 | 0.74 |

with an orientation of $90°$ to the vertical axis of the thermogram. The measurement length of the implemented axis is $200$ pixels, resulting in an actual length in the field of view of $28.48\ mm$ at a measurement distance of $110\ mm$. Based on the recorded pressure and temperature data, the respective differential pressure level between the vacuum bag and the atmosphere can be assigned to the individual images of the thermogram sequence. The atmospheric pressure is determined to be $1017\ mbar$. The ambient temperature is $22°C$.

**Pressure distribution**    For the first test, a vacuum setup has been created with an inserted pressure-sensitive film. The setup is only slightly larger than the sensor, so that pressure values are available for the majority of the area. In this way, basic effects are to be made visible and, if necessary, their expression and direction was investigated. In contrast to conventional vacuum bags with breather material, the venting fabric has been replaced by a peel ply in this setup. The increased flow resistance of this setup is intended to slow down the flow processes in order to increase any pressure gradients that may occur and also to draw conclusions about larger components. The vacuum bag for the test is shown in Figure 4.12.

After ensuring the airtightness of the vacuum bag, a leakage is introduced $100\ mm$ in front of the sensor with a $0.5\ mm$ hypodermic needle (see Figure 4.11).

According to the principle of operation of the foil sensors, the determined pressure values correspond to the effective pressure to be calculated according to $p_\infty - p_{vac} = p_{eff}$ that a component would experience in a vacuum bag. The sensor used delivers 1936 pressure values on an area of $238 \times 238\ mm^2$. By process-
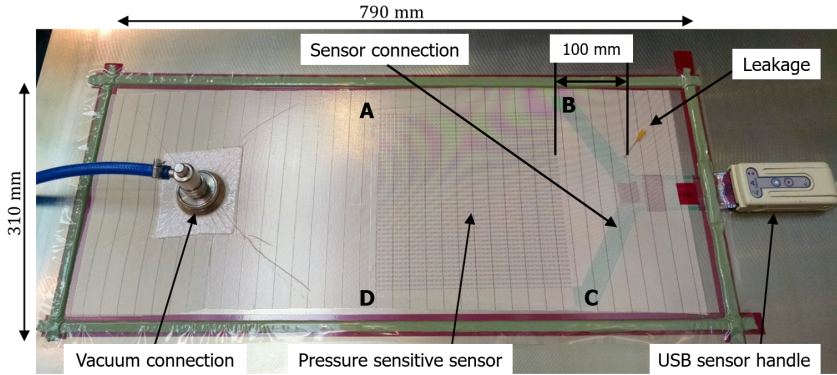
Figure 4.12: Trial setup for pressure sensitive films inside the vacuum bag

ing the data into three-dimensional representations, a quick overview of the spatial distribution of the pressure can be obtained.

To evaluate the findings from the trial with the pressure sensitive sensor, larger trials with absolute pressure gauges have been carried out. A square vacuum setup with a side length of $3000\ mm$ has been used for this experiment. One vacuum connections $s_1$ and two pressure gauges $s_2 - s_3$ have been integrated to carry out the measurements. A schematic representation and a picture of the experimental setup can be seen in Figure 4.13.
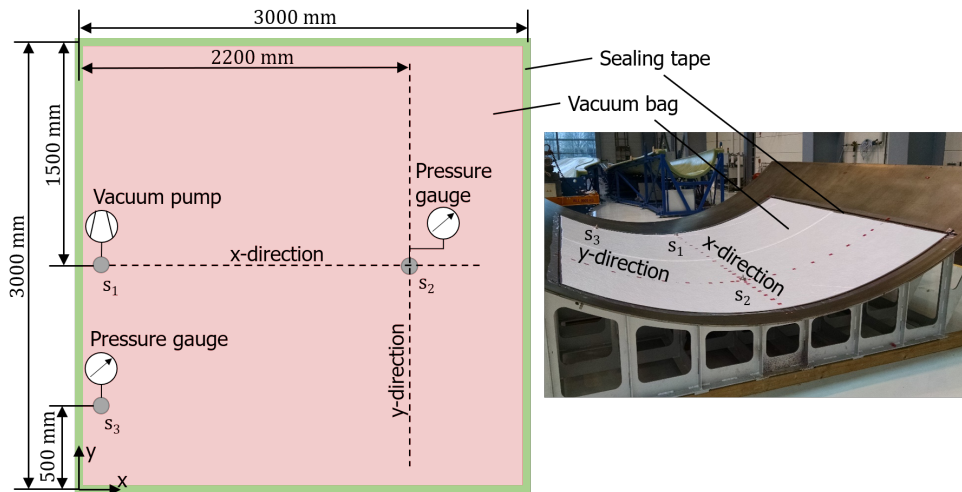


Figure 4.13: Schematic representation and picture of the experimental setup, the leakages are generated on the dashed lines shown

To determine the pressure gradients, the gas pressure had to be determined at numerous points along at least two axes. However, since determining the gas

pressure requires a vacuum port and so many ports are practically impossible to integrate, a fixed vacuum port has been used instead to measure the pressure of different leakages. This allows the pressure to be measured at different distances from the leakage. The expected pressure gradients are relatively small, so that errors due to leakages of different sizes must be eliminated. For this purpose, the pressure is additionally recorded at a second point, the measuring point $s_3$. The pressure values measured at point $s_2$ are corrected with the pressure values of this remote point, which is only slightly affected by the local gradients. The obtained value also represents the dynamic pressure inside the bag $p_{dyn} = s_2 - s_3$.

## 4.3. Results

In this section, the results for the volumetric flow rate, the temperature inside the leakage as well as the pressure distribution are presented. All evaluations are based on the analytical calculation with the substitute model as well as the numerical simulation and are verified with the results from the experiments.

### 4.3.1. Volumetric flow rate

The values for the volumetric flow rate results are listed in Table 4.6 and Figure 4.14. The calculated values $Q_{calc}$ using Equation 4.6 and the boundary, including a constant $C_d = 0.5961$ discussed in Subsection 4.2.1 are compared with the 3D Simulation results described in Subsection 4.2.4 and experimental data from trials described in Subsection 4.2.6. The leakage diameter and area is given by the available inner diameters of the hypodermic needles. $Q_{exp}$ is the average volumetric flow rate of twelve readings per needle diameter. The values are compared by calculating the maximal percentage deviation $Q_{exp/sim}$ ($error$) between analytical volumetric flow rate $Q_{calc}$ and experimental $Q_{exp}$ or simulated volumetric flow rate $Q_{sim}$:

$$Q_{exp/sim} \ (error) = 100 \cdot \frac{(Q_{calc} - Q_{exp/sim})}{Q_{calc}} \tag{4.25}$$

The $Q_{calc/csim}$ ($error$) describes the deviation from the calculated $Q_{calc}$ or simulated volumetric flow rate $Q_{sim}$ to the experimental $Q_{exp}$:

$$Q_{calc/esim} \ (error) = 100 \cdot \frac{(Q_{exp} - Q_{calc/sim})}{Q_{exp}} \tag{4.26}$$

For the comparison of experimental and analytical volumetric flow rate it can be seen that the maximum percentage error is $33.33\%$ for the smallest leak size. In general, the deviation increases with decreasing leakage diameter and area. With the exception of the $0.71 \ mm^2$ leakage, the calculated flow values are higher than the measured ones. The reasons for this may lie in the determination of the inner diameter. This is subject to manufacturing tolerances and can vary from needle to needle. In addition, dust or lint from the breather material can clog the needle and further reduce the diameter and flow, especially in the small needle sizes.

The mass flow of the simulated ø $0.8 \ mm$ leakages is the same in all examples with $1.11 \cdot 10^{-4} \ kg/s$ which results in a volumetric flow rate of approximately

Table 4.6: Comparison between experimental, analytical and simulated volumetric flow rate

| Leakage ⌀ [mm] | Leakage area [mm²] | $Q_{exp}$ [ℓ$_n$/min] | $Q_{calc}$ [ℓ$_n$/min] | $Q_{exp}$ (error) [%] | $Q_{calc}$ (error) [%] | $Q_{sim}$ [ℓ$_n$/min] | $Q_{sim}$ (error) [%] | $Q_{esim}$ (error) [%] |
|---|---|---|---|---|---|---|---|---|
| 1.34 | 1.42 | 9.83 | 10.00 | 1.70 | 1.73 | | | |
| 1.25 | 1.22 | 8.10 | 8.60 | 5.81 | 6.17 | | | |
| 1.11 | 0.96 | 6.55 | 6.80 | 3.68 | 3.82 | 8.80 | 29.41 | 34.35 |
| 0.95 | 0.71 | 5.39 | 5.00 | 7.80 | 7.24 | | | |
| 0.81 | 0.51 | 3.33 | 3.60 | 7.47 | 8.08 | 5.55 | 54.21 | 66.67 |
| 0.65 | 0.33 | 2.32 | 2.34 | 0.85 | 0.86 | | | |
| 0.57 | 0.26 | 1.70 | 1.80 | 5.56 | 5.88 | | | |
| 0.39 | 0.12 | 0.75 | 0.84 | 10.71 | 12.00 | | | |
| 0.27 | 0.06 | 0.31 | 0.40 | 22.50 | 29.03 | | | |
| 0.22 | 0.04 | 0.24 | 0.27 | 11.11 | 12.50 | | | |
| 0.15 | 0.02 | 0.09 | 0.12 | 25.00 | 33.33 | | | |
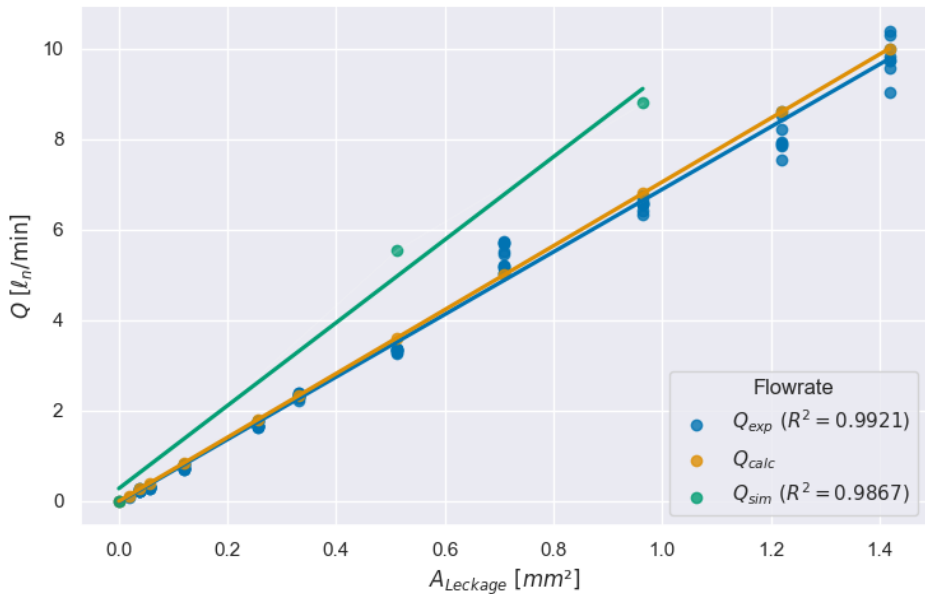


Figure 4.14: Comparison of the experimental, simulated and analytical flow rate from Table 4.6

$5.55\ l/min$ when using Equation 2.8 and an air density of $1.20\ kg/m^3$. The the calculated value of $3.33\ l/min$ is significantly lower than the simulated one, see Figure 4.14. The same holds true for the two leakage case in which the simulated volumetric flow rate is approximately $8.8\ l/min$ compared to the experimental $6.55\ l/min$ for a $0.96\ mm^2$ leakage area. Even if the order of magnitude is correct, this deviation is most likely due to discrepancies between reality and simulation model. It may be, that the volume porosity, which was assumed to be $0.5$ in the boundary conditions, is too high for the breather as a porous medium. Furthermore, it is also possible that there are deviations in the air density, so that the simulated volumetric flow rate is falsified.

The experimental, analytical and simulated flow rates are compared within the plot in Figure 4.14. It can be seen that the difference between the experimental and calculated values is very small. The non-significant random experimental scatter of the determined flow rates for individual leakage sizes is in some cases significantly higher. This comparison proofs, that it is possible to calculate the volumetric flow rate for different leakage size with Equation (4.6). It needs to be noted, that at a leakage size smaller than approx. $0.39\ mm$ in diameter the error is higher than $10\%$, but the smaller the leakage is, the less critical it is for production processes. In addition, the flow calculation shows higher values than the measured flow rate, so that the calculation would rather calculate too much flow than too little flow and is therefore on the safer side.

In addition, the results of the 3D simulations showed that in the case of a central leak, the mass or volume flow is evenly distributed among the activated outlets. In the case of the two leaks, the flow is unevenly distributed with respect to the distance between the outlet and the leak. The outlet closest to the leaks has the highest flow, and as the distance to the leakages increases, the flow decreases. The same can be seen in the 2D simulation.

The comparison of the four 2D simulations on the $1500 \times 1500\ mm^2$ vacuum bag and the experiments for sample 0, 3, 4 and 9 described in Subsection 4.2.5 and Table 4.9 are shown in Table 4.7 and Figure 4.15. It shows the simulated and experimental volumetric flow rates for each outlet as well as the percentage share. In contrast to the velocity and temperature, the mass flow rate at the outlets is calculated according to the experimentally determined values. In particular, for the simulation of the $1500 \times 1500\ mm^2$ sized component, the values of the mass flow rates at the outlets for decentralised leakage are in agreement with the values measured in reality with only small deviations in the order of magnitude of the value. Figure 4.15 shows, that the percentage or fraction of the total flow at the individual outlets matches the experiments. The deviation of the absolute values can be explained by fluctuations within the experiments. In this case, the injection needles are inserted manually into the vacuum bag. It can happen that the size of the hole deviates from the specified size due to the insertion process or clogging of the needle channel.

Table 4.7: Simulated and experimental flow rate and percentage per outlet

| Sample | Outlet | Simulation | | Experiment | |
|---|---|---|---|---|---|
| | | Flow rate $[l_n/min]$ | Percentage % | Flow rate $[l_n/min]$ | Percentage % |
| 0 | 1 | 0.206 | 32.5 | 0.426 | 30.8 |
| | 2 | 0.069 | 10.9 | 0.160 | 11.5 |
| | 3 | 0.277 | 43.8 | 0.613 | 44.3 |
| | 4 | 0.081 | 12.8 | 0.186 | 13.4 |
| 3 | 1 | 0.210 | 27.6 | 0.222 | 27.6 |
| | 2 | 0.227 | 29.9 | 0.241 | 30.0 |
| | 3 | 0.162 | 21.4 | 0.163 | 20.3 |
| | 4 | 0.160 | 21.1 | 0.178 | 22.1 |
| 4 | 1 | 0.433 | 32.8 | 0.481 | 32.0 |
| | 2 | 0.247 | 18.7 | 0.287 | 19.0 |
| | 3 | 0.252 | 19.0 | 0.286 | 19.0 |
| | 4 | 0.390 | 29.5 | 0.451 | 30.0 |
| 9 | 1 | 0.030 | 11.6 | 0.032 | 12.3 |
| | 2 | 0.038 | 14.6 | 0.043 | 16.3 |
| | 3 | 0.147 | 56.4 | 0.138 | 52.6 |
| | 4 | 0.045 | 17.4 | 0.050 | 18.8 |
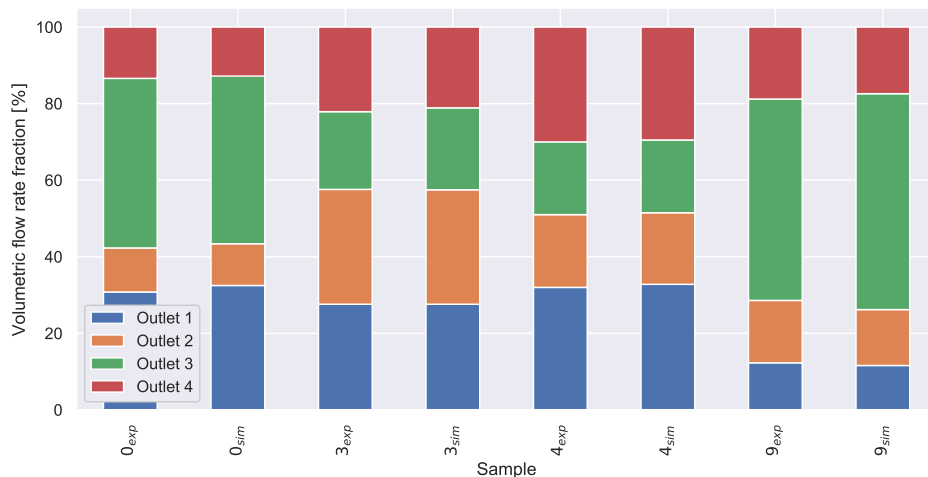


Figure 4.15: Comparison of the experimental and simulated volumetric flow rate fraction of the individual outlets from Table 4.7

### 4.3.2. Temperature

Within the following, the results for the temperature inside the leakage are presented. The analytical results are followed by simulation and experimental evaluation.

**Analytical results**   With a Joule-Thomson coefficient of $\mu_{JT} = 0.258\frac{K}{bar}$ calculated in Subsection 4.2.1 and the usual pressure conditions at a tight vacuum bag with very small leakage, a pressure drop of maximum $1\ bar$ is observed. This should result in a temperature drop of about $0.258\ K$. In previous tests, however, a temperature drop of up to $7\ K$ was observed.

The reason for this deviation is that the assumptions made in Equation 4.10 only apply at a sufficiently large distance from the leakage. The IR image of a leakage shows, however, that the largest temperature drop occurs in the area of the leakage itself. The low Joule-Thomson coefficient and the resulting small temperature drop also confirm that the assumption that air behaves like an ideal gas under the given conditions made in Subsection 4.2.1 is correct.

To estimate the temperature drop at a leakage the assumptions made in Equation 4.10 need to be adapted. Very high flow velocities occur in the cross-section of the leakage. Assuming that the ambient air is at rest ($c_1 = 0$), the following results from Equation 4.9:

$$h_2 = h_1 - \frac{1}{2}c_2^2 \tag{4.27}$$

With $h = c_p T$ gives:

$$T_2 - T_1 = -\frac{c_2^2}{2c_P} \tag{4.28}$$

In the cross-section of the leakage, the enthalpy decreases due to the acceleration of the air and there is a larger temperature drop than due to the ideal Joule-Thomson effect.

The air velocity inside the leakage can be calculated through the previously determined volumetric flow rate ($Q_{calc}$):

$$c_2 = \frac{Q_{calc}}{A} = 118\ m/s \tag{4.29}$$

The corresponding temperature drop calculated through the decreased enthalpy in Equation 4.28 results in a temperature difference of $\Delta T = -7\ K$. In the following this results are compared to the the minimum temperatures occurring inside the leakage in the 3D numerical simulation and are experimentally validated with an IR camera.

**Simulation results**   It is hard to determine the velocity of air and the temperature drop inside the leakage through the simulation, as in the 3D simulation this is

the interface between the ambient atmosphere and the porous medium which resembles a limiting case. The velocity and temperature around the leak shows almost the same values for the three cases with one central leakage. When looking at the simulated velocity further downstream the leak it can be seen, that higher values than the calculated ones in Subsection 4.3.2 are reached. Figure 4.16a shows a velocity contour for the four vacuum connection case on a plane with $0.26\ mm$ offset from the vacuum film where the velocity is at a maximum.

The temperature drop in the area of the leakage is similar. The simulation gives much higher temperature differences at a surrounding temperature of $20°C$ than the analytically determined temperature gradients of $\sim 7\ K$. Figure 4.16b shows the contour plot of the temperature profile around the leakage for the four vacuum connections case on a plane with $0.1\ mm$ offset from the vacuum film. It can be seen that the change in temperature, like the change in velocity, is concentrated in the immediate vicinity of the leakage. In difference to the velocity, the minimum temperature is reached directly inside the leak and not further downstream. Even though the magnitudes of the simulation agree with those of the theory and the experiment, it is also clear from the results that fine tuning is still necessary in the 3D simulation. Nevertheless, the conditions inside a vacuum bag can be explained and represented on a qualitative level with the help of the established simulation model.

Within the 2D simulation the velocity and temperature are not shown in the right order of magnitude, which is not surprising since the maximum values occur in the direct centre of the leak. Due to the cut-outs in the simulation model this area is not part of the 2D simulation, as described in Subsection 4.2.5.

**Experimental results**  The previously calculated temperature difference in the leakage centre was $-7\ K$ for an air velocity of $118\ m/s$, see Equation 4.29. This theoretical velocity is valid for all leakage sizes calculated and tested in Subsection 4.3.1. The local cooling in the area of the leakage can be made visible with a thermographic camera, since the area of the leakage emits less radiant energy due to the temperature reduction. Figure 4.17 shows a 2D thermogram of a leakage as well as its three-dimensional representation with corresponding temperature distribution. The position of the leakage is clearly indicated by the maximum temperature difference of $6\ K$. The effect of the temperature in the centre of the leak and the static vacuum bag pressure is shown in the Table 4.8 and Figure 4.18. The results are from one hole in the entire vacuum bag, and the experiment is carried out ten times for each leakage size, see Subsection 4.2.6.

The results of the trials show, that a cold spot is created in the centre of the leakage. The $\Delta T$ is the ambient temperature during the experiment minus the temperature of the leak. For smaller diameter holes ($D_1'$), the resulting $\Delta T$ is larger ($7.2\ K$) than for the lager diameter $D_2'$ or $D_3'$ leaks ($5.0$ and $3.8\ K$, respectively), see Figure 4.18 . This shows that the calculated temperature difference of $7\ K$ is valid only for small leakages and high pressure differences. With increasing leakage size and increasing pressure inside the vacuum bag, the temperature difference decreases. This phenomenon corresponds to the observations in the Joule Thomson effect, which state that for real gases a change in pressure is proportional to a
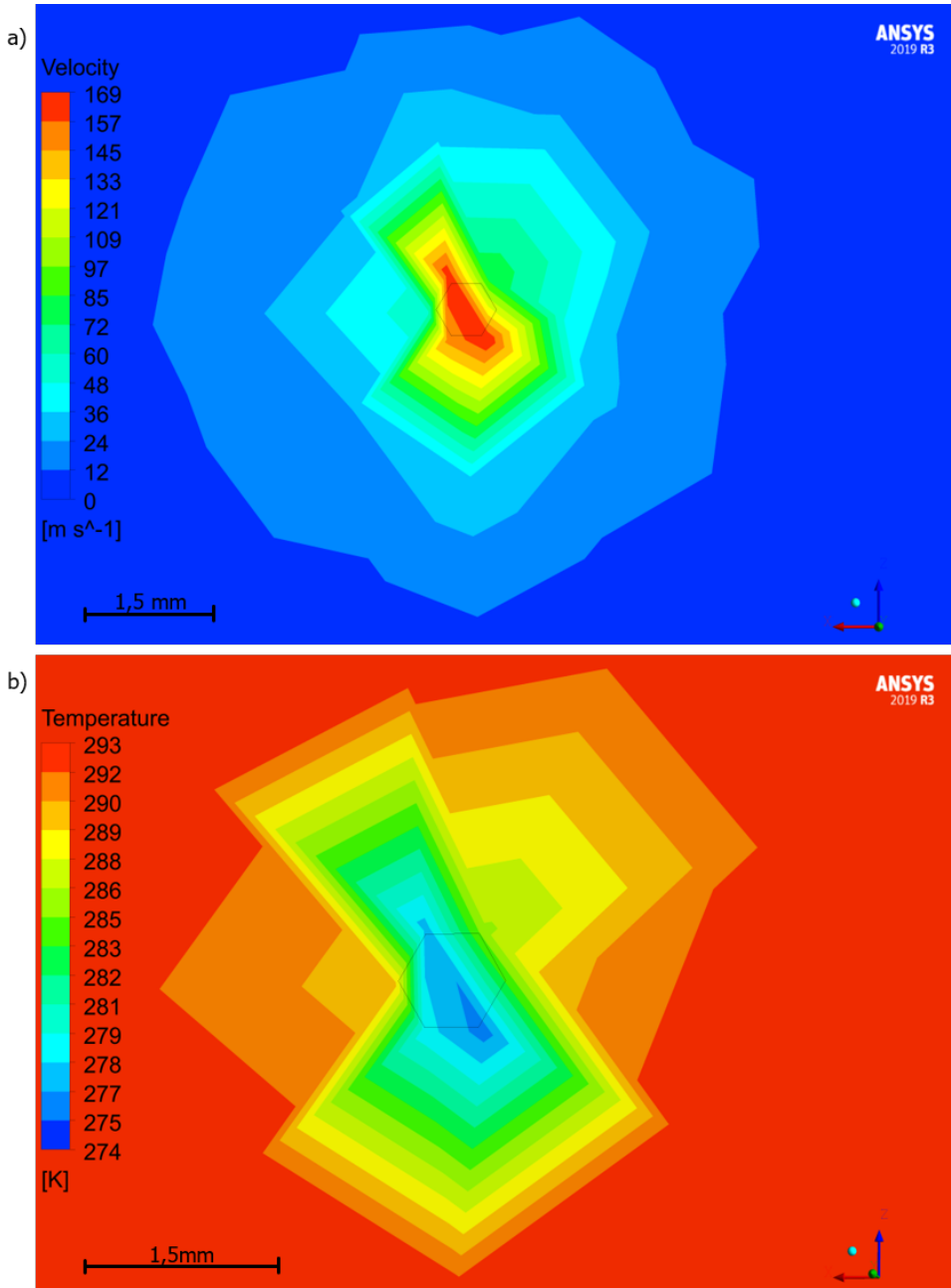
Figure 4.16: 3D Simulation results for a) velocity and b) temperature around the leakage for the sample with four vacuum connections and one central leakage
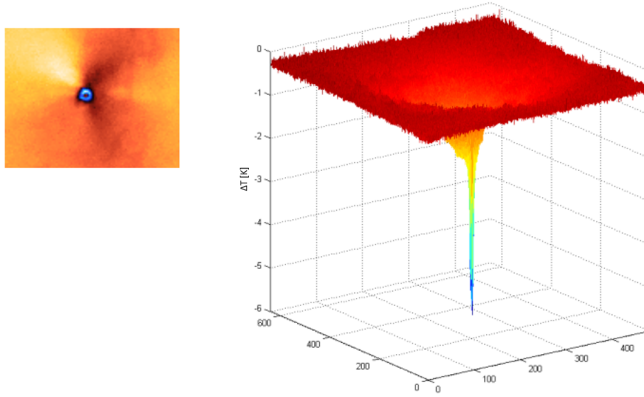
Figure 4.17: Thermogram and three-dimensional representation of a leakage

Table 4.8: Results for $\Delta T$ and $p$ of a single hole in the vacuum bag set-up

| Hole # | $D_1'$ (0.28 mm) | | $D_2'$ (0.53 mm) | | $D_3'$ (0.74 mm) | |
|---|---|---|---|---|---|---|
| | $\Delta T$ [K] | $p$ [mbar] | $\Delta T$ [K] | $p$ [mbar] | $\Delta T$ [K] | $p$ [mbar] |
| 1 | 7.1 | 23.3 | 5.2 | 48.7 | 3.9 | 62.8 |
| 2 | 7.3 | 26.2 | 5.3 | 52.6 | 3.8 | 56.6 |
| 3 | 6.8 | 25.5 | 4.8 | 44.9 | 4.1 | 64.5 |
| 4 | 7.2 | 26.8 | 5.2 | 51.9 | 4.2 | 72.8 |
| 5 | 7.1 | 27.5 | 4.9 | 49.6 | 3.2 | 60.2 |
| 6 | 7.8 | 32.1 | 5.0 | 53.2 | 3.7 | 58.6 |
| 7 | 7.5 | 25.4 | 5.4 | 51.9 | 3.5 | 67.9 |
| 8 | 6.9 | 27.4 | 4.8 | 48.0 | 3.6 | 75.7 |
| 9 | 7.3 | 28.6 | 4.6 | 48.2 | 3.5 | 68.0 |
| 10 | 7.4 | 28.4 | 4.7 | 48.5 | 4.2 | 66.3 |
| Average | 7.2 | 27.1 | 5.0 | 49.8 | 3.8 | 65.3 |
| Standard deviation $\sigma$ | 0.276 | 2.236 | 0.259 | 2.469 | 0.316 | 5.770 |
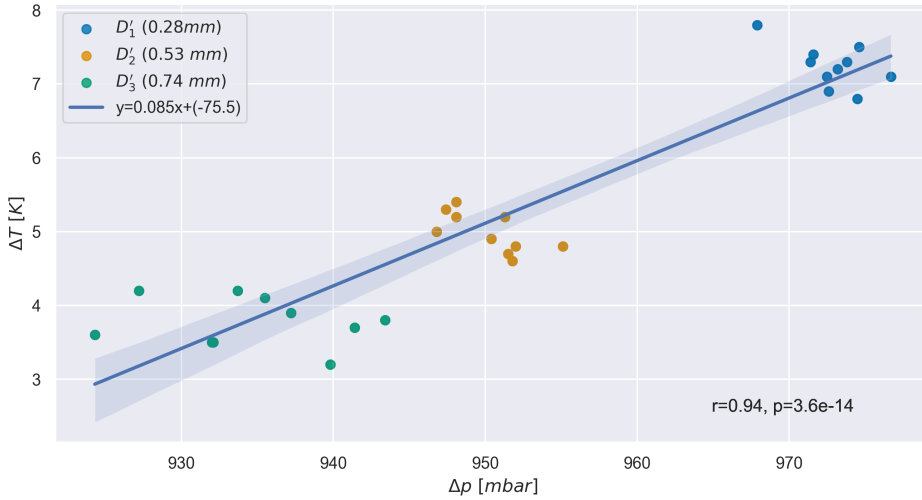
Figure 4.18: $\Delta T$ versus $\Delta P$ correlation for three different leakage diameter from Table 4.8

change in temperature. As the calculated Joule Thomson effect is much lower than the observed changes some other effects might play a role, for example the breather inside the vacuum bag, which has not been considered in the calculations but causes a disturbance to the incoming airflow. There is no freedom from friction and in addition, due to the formation of vortices, the change of state is no longer quadratic, which means that no simple thermodynamic statement can be made and the calculations only give a guidance value for the ideal state.

These observations have also been verified in a second experiment. The curves of the determined temperature differences for a constant leakage size and decreasing pressure level are shown in Figure 4.19. The arrow indicates the direction of increasing differential pressure for the respective curves. Like seen in the experiments before, the measurable temperature difference increases with increasing differential pressure. The distance $b_P$ of the outer inflection points in the temperature peak remains constant at about $2\ mm$. Both experiments show that the calculation of the temperature with the analytical model described in Subsection 4.3.2 is accurate only when the leak is of a small size (ø< $0.5\ mm$) and the pressure difference corresponding to the leakage size is maximum, so that a high velocity of the inflowing air is obtained.

### 4.3.3. Pressure

Within the following, the results for the pressure distribution inside a vacuum bag with a leakage are presented. The analytical results are followed by simulation and experimental evaluation.
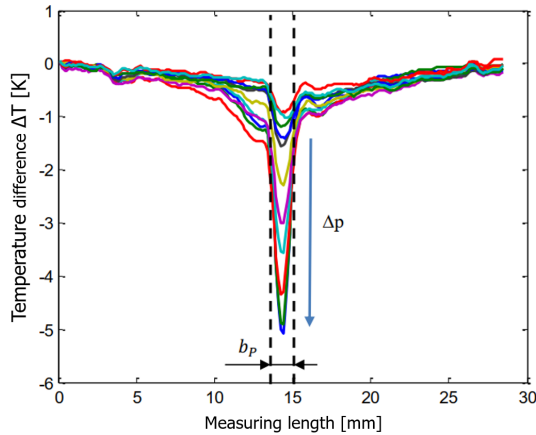
Figure 4.19: Temperature profiles for varying differential pressure and constant leakage size of ⌀0.55 $mm$

**Analytical results**   With the previously calculated velocity of $c_2 = 118\ m/s$ in Equation (4.29) and the boundary described in Subsection 4.2.1 a local dynamic pressure for the location of the leakage is obtained.

$$p_{dyn} = \frac{\rho}{2}c^2 = 8702.5\ Pa = 870.25\ mbar \tag{4.30}$$

This dynamic pressure together with the static pressure yields the total pressure inside of the bag and in this case at the direct location of the leak. In the simulation and the experimental evaluation this value will be checked and validated.

**Simulation results**   Figure 4.20 shows the pressure ratios for all four simulated configurations of the 3D Simulation, described in 4.2.4. In 4.20a there is only one vacuum connection and one central leakage. The resulting pressure gradient along two lines crossing the leakage is shown Figure 4.21.

In Figure 4.20b there are two vacuum connections in opposite corners and a central leak. The total pressure level in this vacuum bag is lower than in 4.20a due to the two vacuum ports. The area of higher pressure is formed around the leak and in the area between the outlets.

In 4.20c there are four vacuum connections in all corners of the vacuum bag. The leakage is positioned in the centre of the part, that the pressure gradient is almost circular around the leak. The overall pressure level in this simulation is the lowest of all four tests due to the large number of vacuum ports. Therefore it is the vacuum set up with the highest effective pressure acting on the laminate.

Figure 4.20d also has four vacuum connections and is the only simulation where two leakages are positioned in the part. Both leakages have the size of $0.8\ mm$. One is positioned in the middle of the part and the other one towards the upper edge of the setup. Within this trial it can be seen that the overall pressure is lower
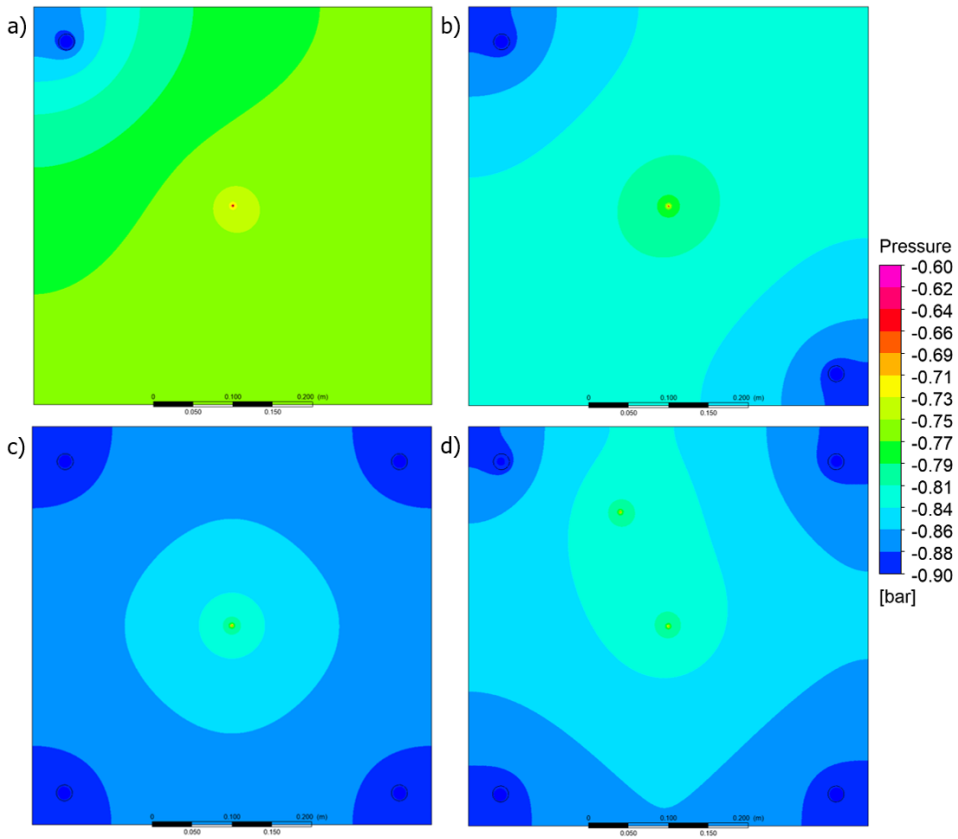
Figure 4.20: Simulated pressure distribution for different vacuum bags and leakage setups. a) One vacuum connection and one central leakage, b) two opposite vacuum connections and a central leakage, c) vacuum connections in all four corners of the vacuum bag and one central leakage, d) four vacuum connections in the conners and two leakages, one central and one towards the upper edge of the figure
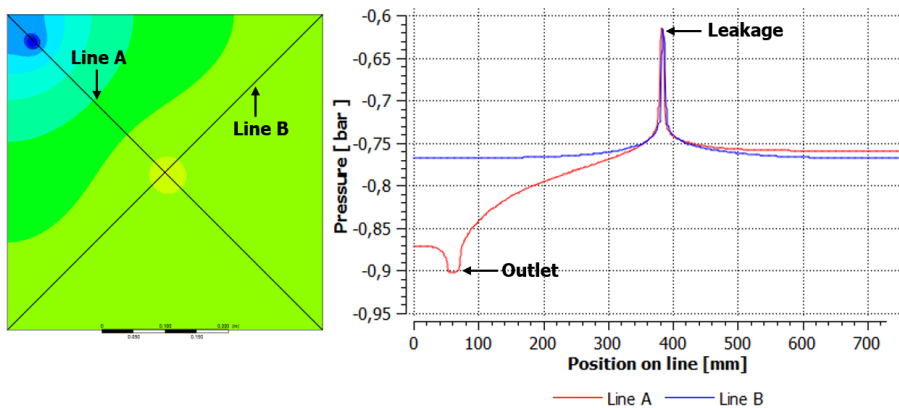


Figure 4.21: Detailed pressure distribution within the vacuum bag along two lines crossing the leakage

than presented in Figures 4.20a and 4.20b due to the higher amount of vacuum ports. It is not as low as in Figure 4.20c as an additional leak is present.

The results show that the more vacuum ports are used, the lower the pressure in the vacuum bag and the higher the effective pressure on the laminate, even or especially when leakages are present. The area affected by the leakage reduces as the number of vacuum connections increases.

The resulting pressure levels for the 2D simulations can be seen in Figure 4.22.
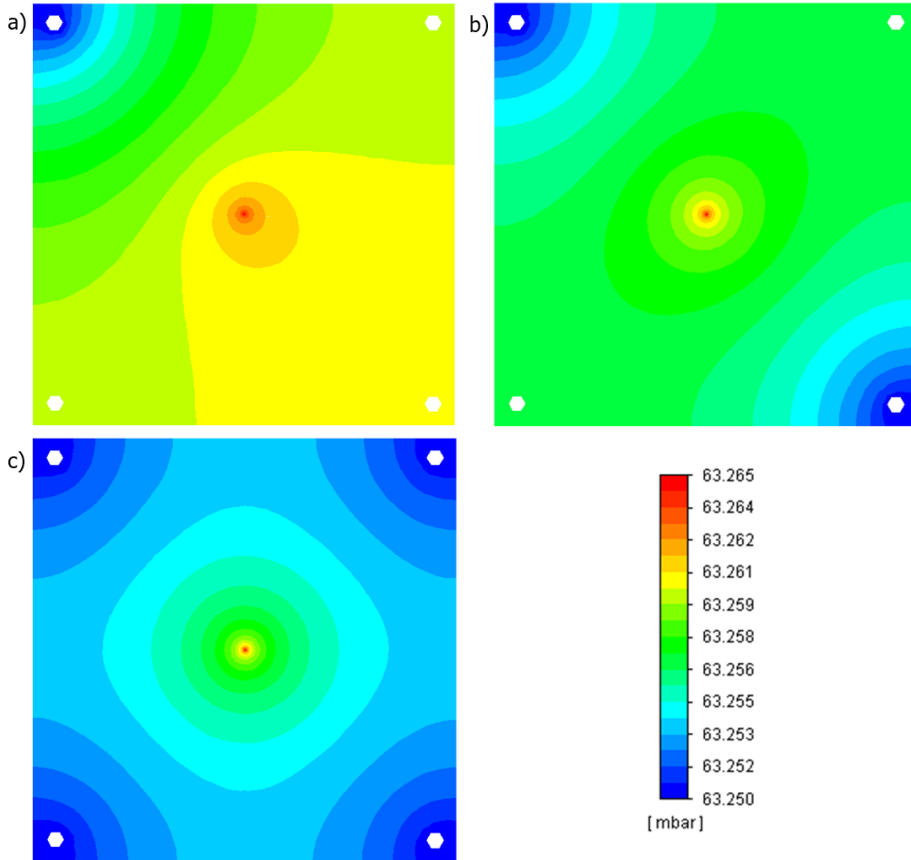


Figure 4.22: Resulting pressure distribution for the $500 \times 500 \ mm^2$ 2D simulation

When comparing the results of the $500 \times 500 \ mm^2$ 2D simulation to the results of the 3D simulation it can be concluded, that the pressure distribution of the two simulations is comparable, although the absolute values differ considerably.

Only a very small value of pressure change can be observed throughout the vacuum bags in Figure 4.22, the dominant pressure is close to the set outlet pressure of $-950 \ mbar \ relative$ or $50 \ mbar \ absolute$ respectively. The reason for this might be the definition of mass flow inlets in which ANSYS Fluent ignores the initial gauge pressure whenever the flow is subsonic, which is the case in the sur-

rounding area of the leakage. As stated in the user guide, a mass-flow inlet is usu-
ally used when it is more important to match a prescribed mass flow rate than to
match the total pressure of the inflow stream. [17]

**Experimental evaluation**   Figure 4.23 shows a representation of the pressure
distribution obtained with the sensitive film.  The leakage is located $100\ mm$ in
front of the sensor and opposite to the vacuum connection.  The pressure values
are colour-coded in the unit millibar.
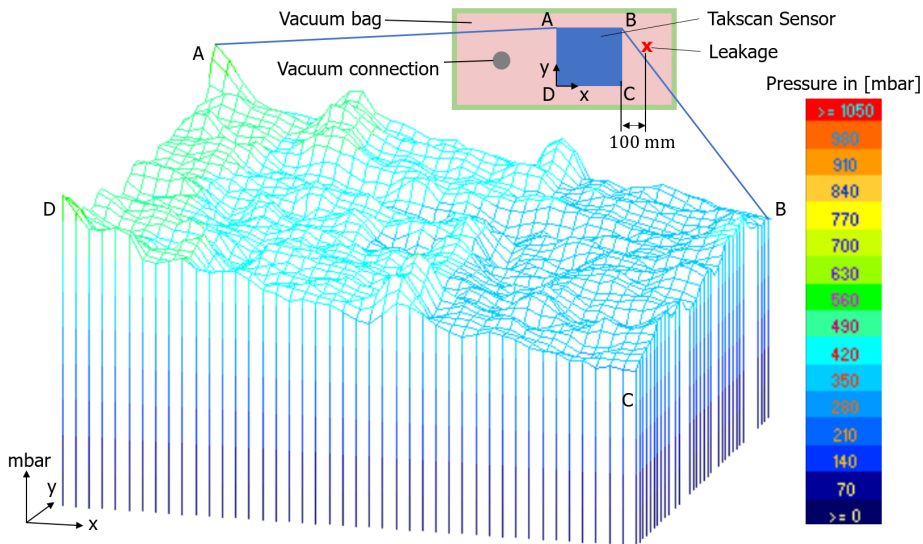


Figure 4.23: Three-dimensional representation of the pressure distribution of a vacuum setup with peel
ply; the leakage is located $100\ mm$ right to the sensor and figure.  The letters indicate the position of
the sensor, see sketch and Figure 4.12.

It is easy to see that a significantly higher pressure ($p_{eff} \approx 521\ mbar$ to $p_{eff} \approx
380\ mbar$) is acting on the vacuum connection side.  There is also a pressure
gradient of a similar magnitude along the entire length of the sensor, in x-direction.
In y-direction, however, no gradient can be seen with the bare eye.
A line-by-line evaluation of the data in y-direction shows a significantly lower
gradient than in x direction. This is made more visible by an additional calculation
and application of the difference to the arithmetic mean. Here it was evaluated that
the effective pressure decreases towards the leakage and increases slightly towards
the edges of the vacuum bag.
According to these data shown in 4.23, there is a pressure gradient in both
expansions of the surface of the vacuum assembly, whereby this appears to have
a larger amount in an axis with leakage and vacuum connection.  The pressure
gradient transversely decreases on both sides of the leakage, while longitudinally
the effective pressure increases steadily in the direction of the vacuum connection.

The results from the larger trials described in Subsection 4.2.6 and Figure 4.13 are shown in Figure 4.24 and Figure 4.25. These validate that the corrected dynamic values $p_{dyn}$ show an almost symmetrical curve along the y-axis towards the leakage, see green curve in Figure 4.24. Where $p_{dyn} = s_2 - s_3$ and the distance between these two pressure gauges is $2400\ mm$. The gas pressure within the structure increases with decreasing distance to the leakage. As the values can not be measured in the direct area of the leakage, the nearest measurement is taken $50\ mm$ next to the leakage, at the location of $s_2$. The values measured are $p_{dynmax} = 52.7\ mbar$. The maximum calculated dynamic pressure in the direct area of the leak is $87.0\ mbar$, see Subsection 4.3.3. This seems to be a plausible value related to the Gaussian distribution of the resulting pressure gradient for $p_{dyn}$.
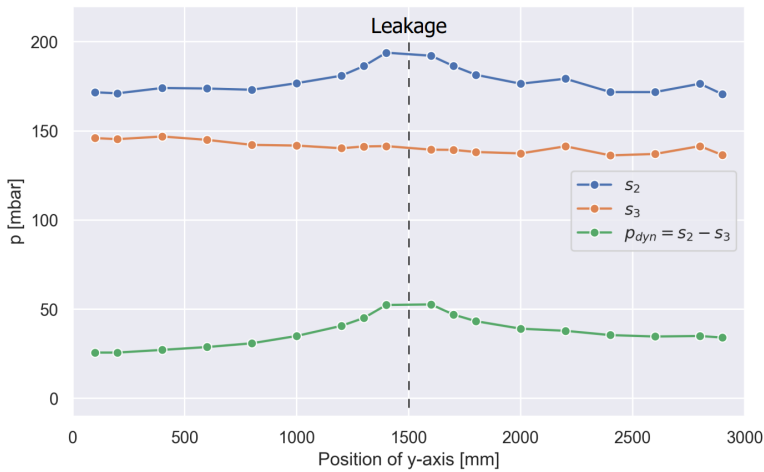


Figure 4.24: Determined pressure curve along the y-axis with distance between $s_2$ and $s_3$ $2400mm$, see Figure 4.13

The fact that the course of $p_{dyn}$ shows a deviation from the expected symmetry is due to the decreasing pressure values at the measuring point $s_3$. The reason for this is the larger distance between the leakages on this side and the point $s_3$.

The procedure when evaluating the pressure gradient in x-direction is similar to that described above for the y-axis. The course of the graph, seen in Figure 4.25, is clearly different having no global symmetry. The pressure values show an increase towards the leakage only from a distance of approx. $1500\ mm$. Up to a distance of approx. $500\ mm$ a linear increase with a gradient of $1 - 2\ mbar/100\ mm$ can be observed. This gradient increases from then up to about $7\ mbar/100\ mm$. Behind the leakage, against the direction to the suction, the gas pressure decreases more slowly than in the opposite direction. In addition, the gradients that occur are lower and drop to only $0.6\ mbar/100\ mm$ at a distance of about $500\ mm$. This results in a higher overall pressure level on the side of the vacuum assembly facing away from the vacuum connection. Like on the y-axis the maximum calculated dynamic pressure of $87.025\ mbar$ seems possible for $p_{dyn}$ in the direct area of the leak.

The results obtained in this test confirm the knowledge gained in the analytical consideration and the preliminary test about the pressure distributions in vacuum setups (Section 4.2) and supplement them by the respective orders of magnitude.
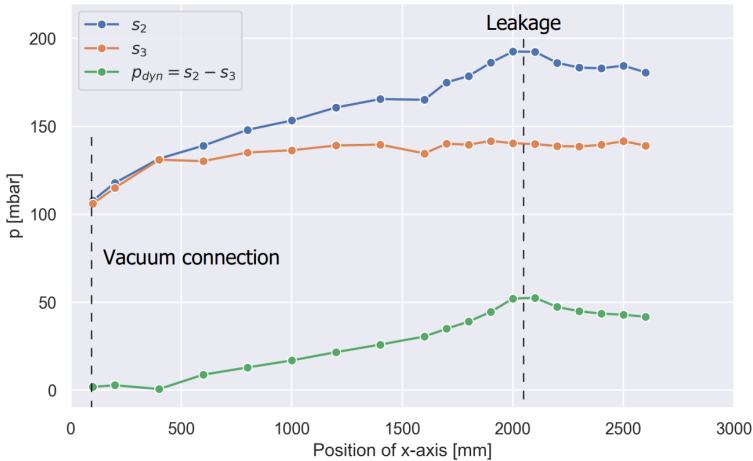


Figure 4.25: Determined pressure curve along the x-axis with distance between $s_2$ and $s_3$ $2400mm$, see Figure 4.13

The results for the x and y-axis can be compared with the simulation results shown in Figure 4.21. It can be seen that the course of the graph is the same and differs only in the absolute values. This can be explained by the different dimensions of the vacuum bags. While a large set up was used in the experiment, the set up in the simulation is smaller due to the boundary conditions, resulting in a higher pressure gradient in the simulation. Furthermore, the maximum values within the leakage and the vacuum connection or outlet could not be shown in the experiment but show high peaks in the simulation. These seem to correlate with the calculated dynamic pressure inside the leak of $87\ mbar$.

Finally, the pressure gradient caused by a leakage was observed to be dependent on the distance of the leakage from vacuum gauge and vacuum port. The pressure reading fell as the leakage position was moved away from the vacuum gauge and rose as the leakage position was moved away from the vacuum port. The observable fact and a potential explanation are schematically sketched in Figure 4.26.

The pressure at the exact location of a leakage is about the same as the ambient pressure. In the vicinity of a leakage, a pressure gradient occurs within a distinct radius. A leakage introduced at position 1 has the same radius of pressure gradient as a leakage introduced at position 2 because both positions share an equal distance to the vacuum port. When the position of a leakage is moved away from the vacuum gauge, as in Figure 4.26a, the area of pressure gradient is shifted accordingly. Thus, the vacuum gauge is moved into a region of the pressure gradient that results in a lower pressure reading.
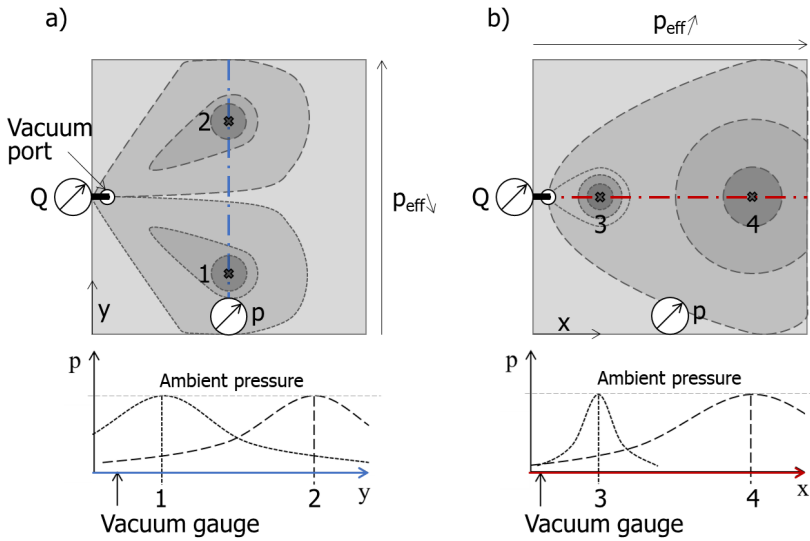
Figure 4.26: Progression of pressure dependent on leakage position (schematic sketch). 1, 2, 3 and 4 indicating different leakage positions and their resulting pressure gradient inside the vacuum bag. $p$ showing the pressure progression at the vacuum gauge as the leakage is shifted in direction indicated.

The size of the areas of the pressure gradient defined by isobaric curves around a leak depends on the distance to the vacuum port. In proximity of the vacuum port (position 3), the inflowing air is aspirated without significant diversion, resulting in a small area of the occurring pressure gradient. In contrast, a large area of pressure gradient occurs for leakages far away from the vacuum port (position 4) because the inflowing air distributes across a larger area before it is aspirated by the vacuum line. Due to the increasing area of the pressure gradient around a leakage, the vacuum gauge falls into higher pressurised regions when the leakage position is shifted away from the vacuum port, thus giving a higher pressure reading.

**Spring damper analogy**    The results for the pressure gradient can also be transferred to the spring damper model. As there is a correlation of the pressure acting onto the vacuum bag and the restoring force of the spring. If an external tension $\sigma_t$ is applied and maintained, the spring deforms elastically, but is slowed down by the damper, also known as the Newton element, so that the deformation occurs with a time delay. Over time, the deformation approaches the value given by the spring or Hooke element. If the external force disappears, the body gradually springs back to its original position. The deformation of the Kelvin body in the spring damper model is thus limited and reversible. [29] Since the deformation $\varepsilon_h$ is only delayed by the damper, it approaches the value of the pure elastic element after a certain time, resulting in: [30]

$$\varepsilon_h = \frac{\sigma_t}{E_h} \tag{4.31}$$

Where $E_h$ is the compression modulus of the breather $E_b$ or the prepreg laminate $E_p$. When putting the elements in series, as it is the case in the described surrogate model for the vacuum bag the compression of the vacuum bag $\varepsilon_v$ under a tension $\sigma_t$ results in: [31]

$$\varepsilon_v = \frac{\sigma_t}{E_p} + \frac{\sigma_t}{E_b} \tag{4.32}$$

As the compression modulus of the breather material or prepreg is hard to identify and subject to a lot of influences and scatter [32, 33], the model is used to qualitatively illustrate the influence of a leakage on the compression of the materials and the resulting consequences for the laminate. When comparing the model to the results for the pressure distribution, it becomes evident, that the area with the less effective pressure acting onto the vacuum bag is the area in the direct vicinity of the leakage. Here the compression of the springs in the model and the material in reality is the lowest, resulting in higher laminate thickness and possible accumulations of porosities in this area after curing.

The radius of the pressure gradient around the leakage and thus the compression of the springs or material is depending on the distance between the leakage and the vacuum connection. For leakages near to the vacuum port the radius of the pressure gradient and thus the resulting area with lower compression is relatively small compared to the area for leakages further away from the vacuum connection, see also Figure 4.26. Furthermore, it can be seen in Figure 4.20, that the more vacuum connections are used, the higher the overall pressure level inside the vacuum bag and the smaller the radius of the pressure gradient.

## **4.4.** Discussion of hypothesis addressed

The influence of leaks on temperature, pressure distribution and velocity is evaluated within the present chapter. Theory, experiments and numerical calculations are used to map the conditions that occur in a leakage and in a vacuum bag. By comparing the methodological approaches, the individual results are verified and the most suitable method identified.

The orifice approach shows the possibility to calculate the volumetric flow rate for different leakage sizes within a high accuracy of $< 10\%$ regarding leakages larger than $0.39mm$. This proved to be helpful to simulate the resulting volumetric flow rate at multiple vacuum connections inside a vacuum bag in the 2D simulation. Only two leakages sizes have been simulated within the 3D simulation. These showed deviations of around $30 - 66\%$ from the calculated and experimental values. Even though, the magnitude of these values is in the correct order there is still a need to fine tune the simulation regarding the permeability and porosity of the porous medium.

It has been found that detailed 3D simulations are best suited for the qualitative representation of the effects of leakages on temperatures, pressures, and ve-

locities. These enable two-dimensional evaluations of the parameters and could be validated by the preceding experiments and analytical considerations especially for the pressure gradient inside the vacuum bag. Here it becomes evident that both the total number of vacuum connections and their individual distance from the leak play a decisive role in the resulting pressure gradient in the vacuum bag. It was found that the more vacuum ports used, the smaller the affected area around the leak. Regarding the distance, the results show that the further away the leak is from the vacuum port, the larger the affected area and the more critical the pressure gradient for the component.

When looking at the velocity and temperature in the direct area of the leakage there is a higher deviation to the experimental and analytical data. As stated in [34] the velocity and temperature become maximum further downstream the leak which can also be seen in the simulation data. The maximum temperature drop in the experiments and calculations is $\sim 7\ K$ whereas the maximum in the simulation is $\sim 20\ K$ but only for a small area below the resolution range of the thermographic camera. When comparing with the area average, the deviation decreases and the order of magnitude becomes comparable with deviations similar to those that could already be observed with the volumetric flow.

The computational costs could be optimised by fine tuning the mesh for the simulation. To reduce computational time within this thesis, the complexity of the model is reduced to a 2D simulation. With the help of the previously analytically calculated boundary conditions, it is possible to simulate the mass flows at the vacuum connections in terms of the percentages with an average accuracy of $2\%$ and, within limits, also in terms of the absolute values with an average accuracy of $37\%$. This enables the rapid simulation of various leakages in components and the resulting measured values. In addition, the process can be automated via scripts, which can be used e.g. for synthetic data generation for machine learning, described in Chapter 7.

The spring analogy explains the pressure distribution inside a vacuum bag with and without a leakage. This theory could be supported by the experiments and the simulation and can be used when evaluating the effects of leakages on the laminate quality in Chapter 5.

The present chapter shows, that hypothesis 3 holds true and that the influence of leaks on temperature, pressure distribution and velocity can be mapped with the help of flow simulation, as well as calculated analytically with the aid of the adapted orifice plate model.

# References

[1] S. Lecheler, *Numerische Strömungsberechnung: Schneller Einstieg in ANSYS CFX 18 durch einfache Beispiele* (Springer Fachmedien Wiesbaden, 2017).

[2] DIN EN ISO 5167-1, *Durchflussmessung von Fluiden mit Drosselgeräten in voll durchströmten Leitungen mit Kreisquerschnitt - Teil 1: Allgemeine Grundlagen und Anforderungen,* (2004).

[3] DIN EN ISO 5167-2, *Durchflussmessung von Fluiden mit Drosselgeräten in voll durchströmten Leitungen mit Kreisquerschnitt - Teil 2: Blenden,* (2003).

[4] M. Potter, D. Wiggert, and B. Ramadan, *Mechanics of Fluids* (Cengage Learning, 2011).

[5] D. Simpson, *Practical Onshore Gas Field Engineering* (Elsevier Science, 2017).

[6] DIN EN ISO 9300, *Durchflussmessung von Gasen mit Venturidüsen bei kritischer Strömung,* (2005).

[7] I. Marić, *The Joule–Thomson effect in natural gas flow-rate measurements,* Flow Measurement and Instrumentation **16**, 387 (2005).

[8] H. D. Baehr, *Stationäre Fließprozesse,* in *Thermodynamik: Eine Einführung in die Grundlagen und ihre technischen Anwendungen* (Springer Berlin Heidelberg, Berlin, Heidelberg, 1988) pp. 223–283.

[9] M. J. Moran, H. N. Shapiro, D. D. Boettner, and M. B. Bailey, *Fundamentals of Engineering Thermodynamics* (Wiley, 2010).

[10] W. Demtröder, *Experimentalphysik 1* (Springer Berlin Heidelberg, 2015).

[11] E. Hering, R. Martin, and M. Stohrer, *Physik für Ingenieure*, 12th ed. (Springer Berlin Heidelberg, 2016).

[12] G. Cerbe and G. Wilhelms, *Technische Thermodynamik: Theoretische Grundlagen und praktische Anwendungen* (Carl Hanser Verlag GmbH & Company KG, 2013).

[13] ANSYS, Inc., *ANSYS 2019 R3 - Capabilities* (2019).

[14] J. Matsson, *An Introduction to ANSYS Fluent 2019*, Better Textbooks. Lower Prices (SDC Publications, 2019).

[15] A. Arafath, G. Fernlund, and A. Poursartip, *Gas transport in prepregs: Model and permeability experiments,* in *Proceedings of International Conference on Composite Materials* (2009).

[16] M. Flemming, G. Ziegmann, and S. Roth, *Faserverbundbauweisen: Fertigungsverfahren mit duroplastischer Matrix*, Faserverbundbauweisen (Springer Berlin Heidelberg, 2013).

**4**

[17] ANSYS, Inc., *Fluent User's Guide*, 2019 R3 ed. (2019).

[18] Oerlikon Leybold Vacuum GmbH, *THERMOVAC TM101,* (2021).

[19] C. Mahrer and D. Walliser, *Instruction manual red-y smart series* (2007).

[20] Tekscan Inc., *Pressure Mapping Sensor 6077* (2015).

[21] Tekscan Inc., *I-Scan Product Selection Guide* (2020).

[22] FLIR Systems Inc., *User's manual FLIR A6xx series* (2016).

[23] Airtech Europe Sarl, *Ipplon® DP1000 Data Sheet - Soft nylon film with an excellent elongation* (2020).

[24] Airtech Europe Sarl, *Ultraweave® 1332 Data Sheet – Heavy weight nylon breather / bleeder* (2018).

[25] Airtech Europe Sarl, *GS-213 Data Sheet - Industry standard vacuum bag sealant tape for metal and composite tools* (2015).

[26] Nitto Denko Corporation, *PS-1 Data Sheet - High temperature / high tensile silicone flash masking tape* (2020).

[27] DIN EN ISO 7864:2016-12, *Sterile hypodermic needles for single use - Requirements and test methods,* (2016).

[28] B. Braun SE, *Präzision in der Injektion und Applikation - Mit B. Braun Einmalspritzen und Einmalkanülen* (2018).

[29] M. Pahl, W. Gleißle, and H. M. Laun, *Praktische Rheologie der Kunststoffe und Elastomere* (VDI-Verlag, 1991).

[30] W. Rust, *Nichtlineare Finite-Elemente-Berechnungen* (Vieweg+Teubner Verlag, 2011).

[31] M. Wolff, M. Böhm, S. Bökenheide, and N. Kröger, *Two-Mechanism approach in thermo-viscoelasticity with internal variables,* Technische Mechanik **32**, 608 (2012).

[32] Q. Govignon, S. Bickerton, and P. Kelly, *Simulation of the reinforcement compaction and resin flow during the complete resin infusion process,* Composites Part A: Applied Science and Manufacturing **41**, 45 (2010).

[33] A. Yong, A. Aktas, D. May, A. Endruweit, S. Lomov, S. Advani, P. Hubert, S. Abaimov, D. Abliz, I. Akhatov, M. Ali, S. Allaoui, T. Allen, D. Berg, S. Bickerton, B. Caglar, P. Causse, A. Chiminelli, S. Comas-Cardona, M. Danzi, J. Dittmann, C. Dransfeld, P. Ermanni, E. Fauster, A. George, J. Gillibert, Q. Govignon, R. Graupner, V. Grishaev, A. Guilloux, M. Kabachi, A. Keller, K. Kind, D. Large, M. Laspalas, O. Lebedev, M. Lizaranzu, A. Long, C. López, K. Masania, V. Michaud, P. Middendorf, P. Mitschang, S. van Oosterom,

R. Schubnel, N. Sharp, P. Sousa, F. Trochu, R. Umer, J. Valette, and J. Wang, *Experimental characterisation of textile compaction response: A benchmark exercise,* Composites Part A: Applied Science and Manufacturing **142**, 106243 (2021).

[34] M. M. Said, *Analytical and Numerical Calculation of the Orifice Minimum Temperature Due to Joule - Thomson Effect,* Fluid Mechanics **3**, 33 (2017).

**4**

# 5

# Experimental analysis of leakages

*In order to assess the criticality of leaks, it is important to know their influence on the quality of a part. In this chapter, the effects of leaks that have been introduced in a defined manner into a vacuum bag are investigated. The physical processes that occur during curing within the leaking vacuum structure are analysed optically as well as by means of ultrasonic testing and thickness measurement and a better understanding of the effects on laminate quality is generated. It is found that there is a difference between leakages in the vacuum bag only and leakages that affect both the vacuum and release film.*

## **5.1.** Introduction

Within this chapter a number of different trials is performed to investigate if the impact of a leakage on the part quality in terms of porosity and voids can be physically explained and characterised. The tested leakages can be divided in leakages that only appear in the vacuum bag and leakages in the vacuum bag and release film with direct contact to the laminate. The focus of the tests is to assess the amount of porosity and void increase in relation to the leakage position and size. It is not a question of assessing the extent of these defects. The effect (porosities) of the defect (leakage) is examined, the evaluation of the effect, i.e. the porosities, is out of scope. No investigations are carried out into the altered mechanical characteristics caused by the defects in the laminate. The investigations focus on drawing conclusions about which defects leakages of a certain size and position cause in certain areas of the laminate.

## **5.2.** Methodology

In the context of this chapter and the performed tests, the consequences of leakages in the vacuum bag on the laminate quality are investigated. For this purpose, a series of autoclave trials has been performed. The investigations have been carried out on flat components where various leakages have been introduced into the vacuum bag before the autoclave process.

### **5.2.1.** Laminate and vacuum bag composition

The material that has been used for the experiments was Hexcel M21/45%/120 [2], a *Glass Fibre* (GF)-reinforced prepreg system. A GF-reinforced material has been chosen to make it easier to detect the resulting porosities in the component due to its transparent properties. Porosities in CFRP components can only be detected with the help of additional tests such as ultrasound or X-rays, whereas in the case of GF components, visual inspection can detect the defects.

The maximum component size in the tests was approx. $500 \times 500 \ mm^2$, in order to be able to handle the final components, to realise several tests at once and to carry out further quality checks. The laminates each consisted of $1$, $10$ or $20$ equally orientated layers of M21/45%/120 material which corresponds to a final component thickness of approx. $0.1$, $1$ or $2 \ mm$ respectively. The single layer test has been chosen to determine if there is a preferred direction of leakage propagation in the satin fabric of the prepreg material. The prepreg material consists of a 4HS satin weave reinforcement structure and the 45% depicts the resin content of the material by weight. [2] The vacuum bagging has been carried out according to Figure 2.5 and consisted of the materials listed in Table 5.1.

### **5.2.2.** Leakage insertion

The leaks have been inserted into the vacuum bag in three different ways and can be divided into leakages in the vacuum film and leakages in the vacuum and release film. While the first case is the most common, the case where the vacuum and the release film is damaged is more critical. It can happen if very sharp objects, e.g.

Table 5.1: Vacuum bagging materials

| Material | Manufacturer | Product |
|---|---|---|
| Prepreg | Hexcel | M21/45%/120 [2] |
| Release film | Airtech International Inc. | Wrightlon WL5200 [3] |
| Breather | Airtech International Inc. | Ultraweave 1332 [4] |
| Vacuum film | Airtech International Inc. | Ipplon DP1000 [5] |
| Sealant tape | Airtech International Inc. | GS-213-3 [6] |
| Adhesive tape | Nitto Inc. | PS-1 [7] |

scissors, drop onto the finished bag. Furthermore, the direct connection of the leak to the laminate can simulate the case of a leakage in the mould, e.g. at weld seams or at integrated sensors.

**Leakage in vacuum bag and release film**   To simulate leaks in vacuum bag and release film single-use hypodermic needles have been inserted. This procedure can be seen in Figure 5.1 and has been used in different leakage studies like. [8, 9] The size of the needles varies between $0.15\ mm$ and $0.95\ mm$ inner diameter. To ensure a constant leak size, the needles have been left in the vacuum setup throughout the curing process. The needles have been wrapped and secured with extra sealing tape to prevent the needles from slipping out or moving during the autoclave process due to air movement, see Figure 5.1 right-hand side. All plastic components of the needle had to be removed before curing to prevent melting and clogging of the needles.
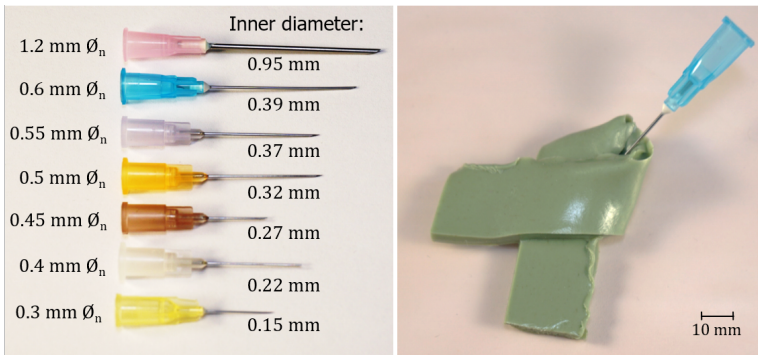


Figure 5.1: Hypodermic injection needles used for leakage creation and the created leakage in a vacuum bag

It should be noted that the size of the leaks, especially if they are pierced with a metal needle is subject to certain temperature fluctuations due to the thermal expansion of the materials. However, due to the small size of the leaks, these variations are negligible as they are lower than the variations due to the piercing

process itself. Former investigations showed that this variation is up to 7% of the volumetric flow rate due to a side flow that may enter the vacuum bag at the outer sides of the inserted needle. [8]

**Leakage in vacuum film only**   To replicate leakages only in the vacuum bag, two different methods have been used. The first approach to the artificial creation of leaks is the insertion by drilling into metallic plates. Figure 5.2 shows one of the aluminium plates used in which holes of different sizes have been drilled. The theoretical hole size varies between $0.1\ mm$ and $0.35\ mm$. Examination under the microscope showed that the real hole size is much larger due to manufacturing tolerances.
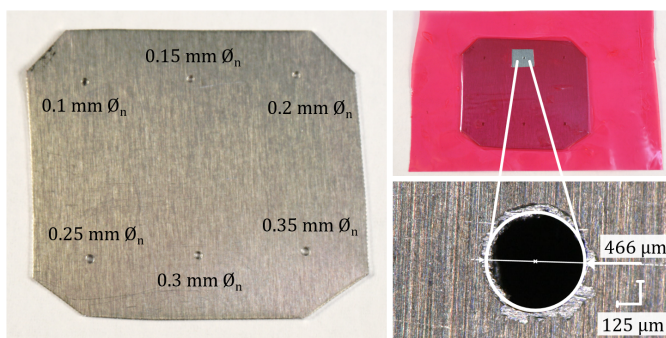


Figure 5.2: Aluminium plates with different size holes to simulate leakages

The real leakage sizes varied between $0.34\ mm$ and $0.73\ mm$ and have been determined individually by microscope measurement and by evaluating the resulting flow rate before the tests. On the right-hand side of Figure 5.2 it is shown, how the plates have been integrated into the vacuum bag. The vacuum bag has been cut and replaced by the plate in the area where the leakage was intended. It was placed airtight on the vacuum bag and fixed with adhesive tape. Only the leakage size used for the test had been cut out of the adhesive tape and thus represented the artificial leakage. It is possible that the stiffness of the plate may have an influence on the compaction of the breather and laminate in the direct area, therefore holes have been also made in an alternative way and the influence of the metal plate and the limitations of the results have been examined.

The second method of simulating leaks has been to punch the holes in the vacuum bag in predefined areas with a punching device. Figure 5.3 shows the tools and the resulting hole in the vacuum bag. To prevent the film from being torn out in the area of the hole, a strip of adhesive tape has been applied in the area of the leakage. This strengthened the film locally and also simplified the insertion of the hole. The theoretical hole size has been $0.5\ mm$ and $0.8\ mm$ and the real leakage size $0.57\ mm$ and $0.83\ mm$ respectively.
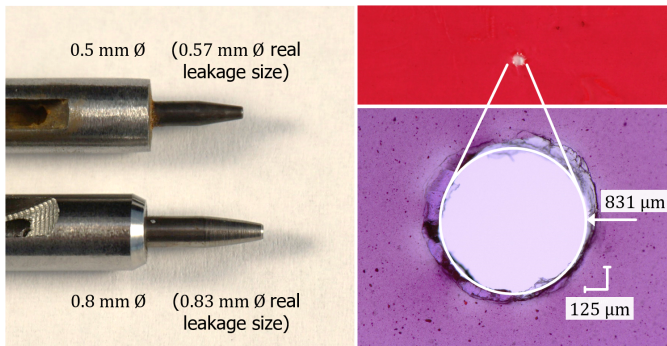
Figure 5.3: Punching tools and resulting artificial leakage in vacuum bag

### 5.2.3. Autoclave set up

All together three autoclave trials have been performed to evaluate the influence of leakages on the laminate quality. Within these tests, the autoclave cycle, described in Subsection 5.2.4 was kept the same, only different configurations of leakages, plate sizes and superstructures have been tested. The three autoclave cycles have been necessary because of the limited tool size. Table 5.2 provides an overview of the tests.

Table 5.2: Overview of the configurations of the performed trials

| Autoclave cycle | Laminate size | Plys | Leakage type | Leakage size |
|:---:|:---:|:---:|:---:|:---:|
| 1st | $500 \times 500\ mm^2$ | 20 | none | none |
| | $500 \times 500\ mm^2$ | 20 | needle | Ø 0.15 $mm$ |
| | $500 \times 500\ mm^2$ | 20 | needle | Ø 0.39 $mm$ |
| | $500 \times 500\ mm^2$ | 20 | needle | Ø 0.95 $mm$ |
| | $300 \times 150\ mm^2$ | 20 | no vacuum | |
| 2nd | $500 \times 500\ mm^2$ | 1 | needle | Ø 0.39 $mm$ |
| | $500 \times 500\ mm^2$ | 20 | plate | Ø 0.33 $mm$ |
| | $500 \times 500\ mm^2$ | 20 | needle | Ø 0.39 $mm$ |
| | $250 \times 250\ mm^2$ | 20 | needle | Ø 0.22 $mm$ |
| | $250 \times 250\ mm^2$ | 20 | needle | Ø 0.27 $mm$ |
| | $120 \times 120\ mm^2$ | 20 | plate | Ø 0.47 $mm$ |
| | $120 \times 120\ mm^2$ | 20 | plate | Ø 0.42 $mm$ |
| 3rd | $500 \times 500\ mm^2$ | 20 | needle | Ø 0.32 $mm$ |
| | $500 \times 500\ mm^2$ | 20 | needle | Ø 0.37 $mm$ |
| | $500 \times 500\ mm^2$ | 20 | punch | Ø 0.57 $mm$ |
| | $500 \times 500\ mm^2$ | 20 | punch | Ø 0.83 $mm$ |
| | $120 \times 120\ mm^2$ | 20 | needle | Ø 0.39 $mm$ |
| | $120 \times 120\ mm^2$ | 10 | needle | Ø 0.39 $mm$ |
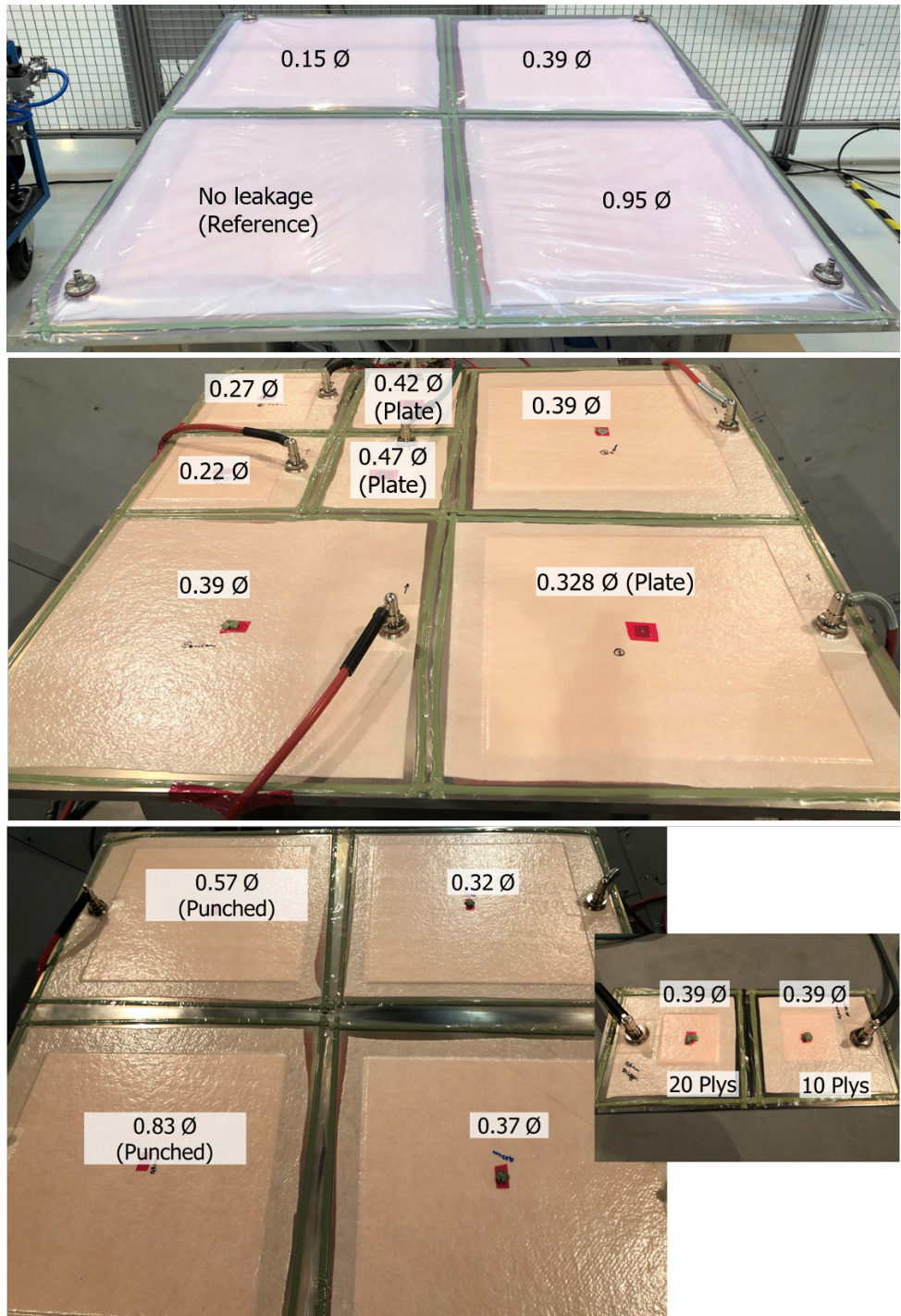
Figure 5.4: Setup of the three autoclave trials and the introduced leakages

Figure 5.4 shows the autoclave setups and the introduced leakages for each trial. Before the autoclave cycle, both the volumetric flow rate measurement and a pressure increase test have been performed to evaluate the airtightness of the vacuum bags.

### 5.2.4. Curing

The autoclave cycle used for curing was the cycle specified for Hexcel M21 materials in the data sheet. [2] The autoclave cycle includes a $180$-minute hold at the temperature of $150°C$ and the final cure at $180°C$ held for $120$ minutes. The pressure in the autoclave is $7\ bar\ relative$ (where $0\ bar\ relative$ is equivalent to approximately $101,325\ Pa \cong 1\ bar\ absolute$) over the complete curing cycle. After the pressure is applied the vacuum is reduced to $-0.2\ bar$ in the cycle specified by Hexcel. In the tests carried out, the vacuum has been kept at $-1\ bar$ for the entire cycle in order to be able to better investigate the effects of the artificially introduced leaks. In addition, flow meters have been integrated into four of the vacuum ports on the autoclave side in order to monitor the flow values during the autoclave cycle.

### 5.2.5. Testing methods

After the specimens have been cured in the autoclave, they have been examined and evaluated in various ways. One of the most important tests is the visual inspection of the laminates for porosity. In order to check whether a visual inspection of the glass laminates is sufficient to detect all porosities, additional ultrasonic tests in the form of a c-scan have been carried out on two plates. The tests have been carried out according to the Airbus test specifications AITM 6- 4010 [10] and AITM 6-4012 [11] which state that the inspection of fibre composites is to be carried out by ultrasonic phased-array technique and for glass fibre reinforced plastics the ultrasonic pulse-echo inspection is used. The evaluation of the results has been carried out according to the Airbus standard AITM 6-0011 [12], which establishes the general requirements applicable to non-destructive inspections and the classification for reporting. These tests have been supplemented by micrographs and thickness measurement. To investigate the influence of leakage on the laminate thickness, thickness measurements have been carried out on some of the test panels. Figure 5.5 shows the measuring clamp used and the test plate with the measuring points drawn in. The leakage (if any) is located at the origin of the coordinate system used.
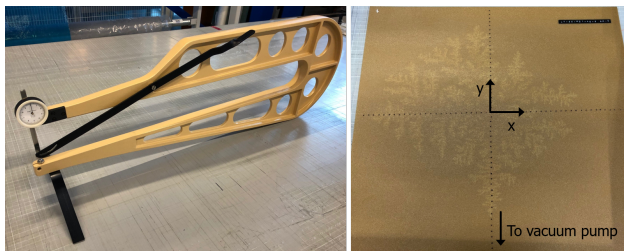


Figure 5.5: Thickness gauge and test grid on a test plate with the leakage at the origin. The black dots represent the measuring points.

### 5.2.6. Spring damper model

In order to understand the cause and background of the test results, the findings are compared with the surrogate model, described in Subsection 4.2.2 and 4.3.3. In Figure 5.6 the four different test configurations are shown with the help of the replacement model.
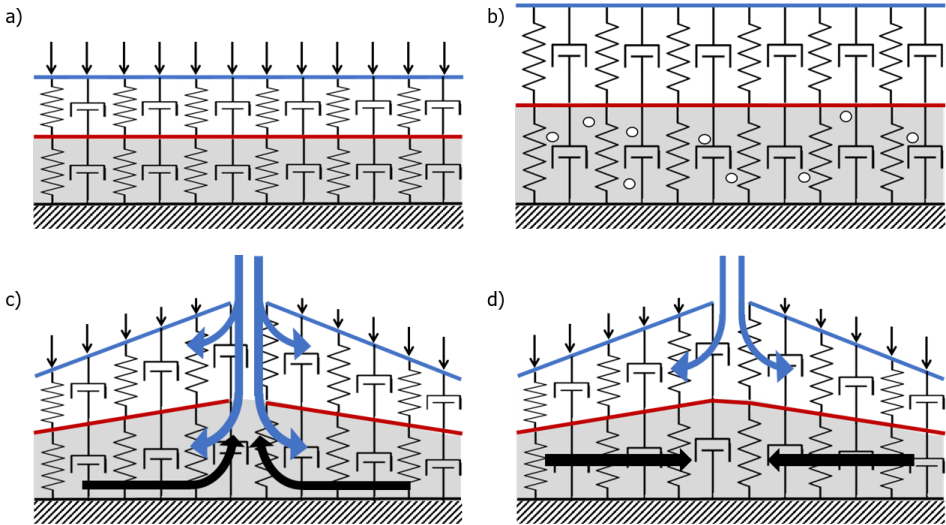


Figure 5.6: Schematic representation of the pressure inside the vacuum bag during curing. a) Reference without a leakage and full vacuum, b) Reference without vacuum and compaction, c) Vacuum bag with leakage in vacuum film and release film, d) Vacuum bag with leakage in vacuum bag only

Figure 5.6a shows the reference case where there is no leakage in the vacuum setup. The black arrows symbolise the ambient pressure in the autoclave acting on the vacuum bag and compressing both the breather and the laminate. Air trapped in the assembly during the manufacturing process has been evacuated and the part can cure without porosity or voids caused by leakages.

If no pressure difference can be built up between the laminate and the environment, e.g. because a pressure equalisation takes place due to a large tear in the film, no compression of the laminate takes place. Figure 5.6b shows that entrapped air could not be removed from in-between the layers and that the laminate cures without any applied forces.

The leakage artificially introduced into the vacuum assembly by a needle has locally damaged not only the vacuum bag but also the release film, like shown in Figure 5.6c. In this case, the ambient air can enter the vacuum setup. It spreads both in the breather and in the laminate. The blue arrows symbolise the air flow. The effective pressure on the laminate and the breather decreases locally and there is a resetting of the materials in this area. The resin flow, represented by black arrows, is orientated towards the leakage, as the pressure on the laminate is lowest here.

Figure 5.6d shows the substitute model with a leak only in the vacuum film. This has been realised in the tests by punching the vacuum bag. The ambient air can penetrate the vacuum bag and spreads out in the breather material. The effective pressure on the laminate drops in the vicinity of the leakage which results in a relaxation of the breather and laminate in this area and an increased laminate thickness in this region. The resin beneath the release film flows into the area with the lowest effective pressure on the vacuum setup, which is in the area of the leak.

## 5.3. Results

In the following, the results of the tests are presented and analysed. In addition to the expected porosities and defects in the final component, further effects are observed in the laminate, which will also be discussed in the following subsections. These include the leakage test, colour changes, porosity, thickness changes and resin flow.

### 5.3.1. Leakage test

Before the autoclave cycle, both the volumetric flow rate measurement and a pressure increase test is performed. The corresponding values can be taken from Table 5.3.

Table 5.3: Volumetric flow rate measurement and pressure increase test for the performed trials. The * marks measurements where the upper measurement limit of the used sensor is exceeded.

| Leak size | Volumetric flow rate $[l_n/min]$ | Vacuum value at start $[bar\ relative]$ | Vacuum value after 2 min $[bar\ relative]$ |
|---|---|---|---|
| None | 0.010 | −1.01 | −1.00 |
| Ø 0.15 $mm$ | 0.086 | −1.00 | −0.96 |
| Ø 0.22 $mm$ | 0.196 | −1.01 | −0.87 |
| Ø 0.27 $mm$ | 0.251 | −0.99 | −0.87 |
| Ø 0.32 $mm$ | 0.444 | −1.00 | −0.73 |
| Ø 0.33 $mm$ (Plate) | 0.597 | −0.99 | −0.77 |
| Ø 0.37 $mm$ | 0.545 | −0.97 | −0.77 |
| Ø 0.39 $mm$ | 0.545 | −0.97 | −0.75 |
| Ø 0.39 $mm$ | 0.770 | −1.00 | −0.73 |
| Ø 0.39 $mm$ (1 Ply) | 0.773 | −0.99 | −0.74 |
| Ø 0.39 $mm$ (10 Plys) | NA | −0.93 | −0.67 |
| Ø 0.39 $mm$ (20 Plys) | NA | −0.93 | −0.71 |
| Ø 0.42 $mm$ (Plate) | 0.836 | −0.94 | −0.37 |
| Ø 0.47 $mm$ (Plate) | 0.755 | −0.96 | −0.56 |
| Ø 0.57 $mm$ (Punch) | 1.080* | −0,94 | −0.77 |
| Ø 0.83 $mm$ (Punch) | 3.700 | −0,94 | −0.03 |
| Ø 0.95 $mm$ | 1.080* | −0.91 | −0.03 |

It can be seen that the vacuum bag with no leakage has almost no volumetric flow rate and the pressure increase can be neglected. The limit relevant for aerospace manufacturing of $66\ mbar$ in two minutes is exceeded for leakage sizes bigger than $0.15\ mm$. Only the vacuum bag without a leakage and the vacuum bag with the $0.15\ mm$ leakage meet the criterion with a pressure increase of $10\ mbar$ and $40\ mbar$ respectively. The other vacuum bags have a higher pressure increase and would therefore not be approved for the autoclave process in the series production process. The measured volumetric flow rate of the $0.5\ mm$ and $0.95\ mm$ leakage is the upper limit of the applied flow meter. The true flow rate at these leak size should be higher. In previous trials in Subsection 4.3.1 a volumetric flow rate of $\approx 1.8\ l_n/min$ and $\approx 5\ l_n/min$ was determined for the needle sizes used.

## 5.3.2. Colour gradation of laminates and vacuum bags

During the debagging of the experiments of the first trial, discolouration of the vacuum bags can be detected. Figure 5.7a shows the vacuum setups of the first test directly after the autoclave. It can be seen that the vacuum bag without leakage has the lightest colour. The greater the leakage, the darker the colour of the corresponding vacuum bag. The same can also be seen in the respective breather materials. These have darkened accordingly depending on the size of the leak, shown in Figure Figure 5.7b.
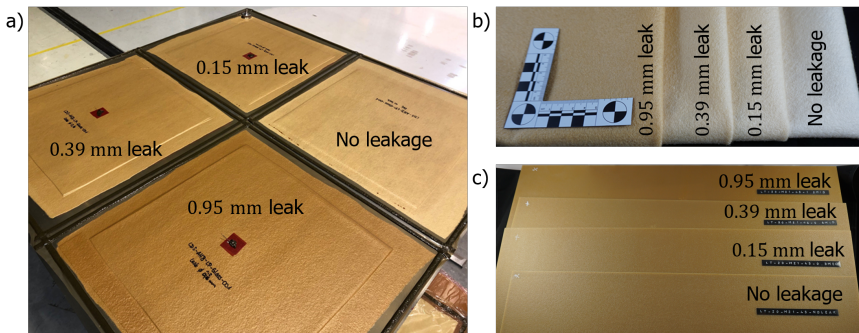


Figure 5.7: Colour gradation of a) vacuum bags, b) breather and c) laminate right after autoclave cycle

In addition to the breather, the laminate also shows increasing discolouration with increasing leakage size, see Figure 5.7c. An explanation for this seems to be a side reaction of volatile, short-chain constituents of the *Epoxid* (EP) resin with the residual oxygen, causing the discolouration, like described in Subsection 2.4.2. Since this is a chemical reaction, it may also be progressing under the film and in the laminate. This also fits with the increasing hole size: more air ingress leads to more side reaction. Even if the autoclave is filled with nitrogen during the process for safety reasons, a certain amount of residual oxygen will remain inside the pressure vessel. This seems to be sufficient to cause a side reaction with the epoxy resin.

### 5.3.3. Porosity and voids

The simulated leakages and tests carried out can be divided into two categories, those in which the leakage extends through the release film into the laminate and those in which the release film remains intact and the leakage only occurs in the vacuum film. Since the results of the two leakage types are very different in terms of porosities, the following evaluations are divided into the two categories leakages in vacuum and release film as well as leakages in vacuum film, only.

**Leakages in vacuum and release film**   When a leakage is inserted with a hypodermic needle, the release film on the laminate is always damaged as well. This means that the incoming air can penetrate not only the breather but also the laminate. A first indicator for this is a resin accumulation in the breather in the immediate vicinity of the leakage. The resin has the opportunity to flow through the damaged release film into the breather; at the same time, the air has the opportunity to flow through the leak into the laminate.

Figure 5.8 shows the results of the first series of tests. It can be seen that there is a clear formation of porosity around the leakage at the needle size of $0.39\ mm$ and $0.95\ mm$. The flaws form in a branch shape starting from the leakage into the laminate. It appears that the spread of the $0.95\ mm$ needle is somewhat greater than that of the $0.39\ mm$ needle. With the $0.15\ mm$ needle, only a slight shadow can be seen in the area of the puncture.
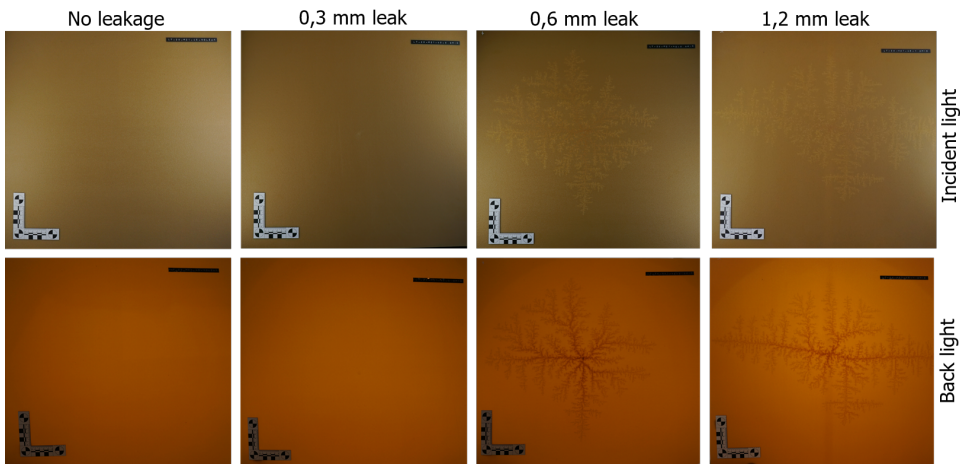


Figure 5.8: Leakage size and resulting laminate quality of the first trial (upper row with incident light and lower row with back light)

The non-uniform pattern in the x and y directions can be explained by the fact that no attention was paid to the warp and weft direction of the individual layers of the 4HS fabric during the production of the laminates for the first test series. It can be assumed that the air can spread more easily in the weft direction due to the lower undulations of the fibres.

The micrographs in Figure 5.9 show that in the uncured prepreg material, the resin has predominantly settled on the undulated weft threads. This additionally blocks the air flow. In the following tests, care was taken to align the plies evenly in order to confirm the phenomenon.
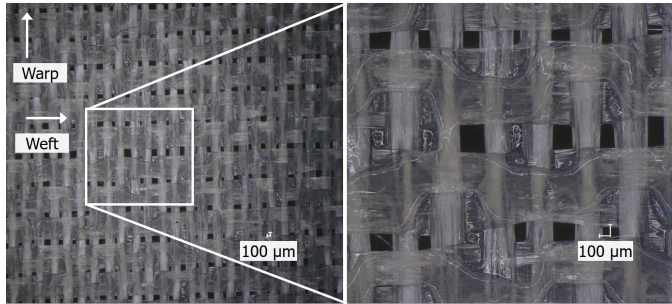


Figure 5.9: Microscope image of the uncured prepreg material with 30x and 100x magnification

The branch like forming of the porosities is related to the fingering flow that results inside the laminate. The viscous fingering was first observed during sugar refining operations and studied in numerous experiments in the fields of science ever since. [13–15] In the field of composites manufacturing this kind of flow has been observed and studied especially in resin injection and infiltration processes. [16, 17] Viscous fingering is a phenomenon that describes multiphase-fluid flow through porous media. The term "viscous fingering" comes from the fact that in most, but not all cases, the mechanism of this instability is closely related to the viscosity difference between two phases. [18] This could also be observed in an other experiment where the breather material has been infused with blue coloured water as shown in Figure 5.10.
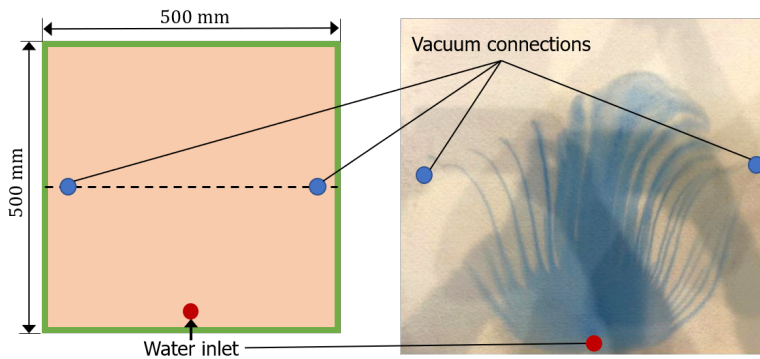


Figure 5.10: Experiment for viscous fingering effect using blue coloured water and breather material

The water that is infused to the breather has a lower viscosity than the remaining air inside the vacuum bag, so that an instability occurs since the water has a greater

mobility than the air. The same applies for the tests with leakages in vacuum and release film where the inflowing fluid, in this case nitrogen at $180°C$ and $7\ bar$, has lower viscosity than the composites resin.

In order to find out from which needle or leakage size porosities arise, the leakage diameter range between $0.15\ mm$ and $0.39\ mm$ is further resolved. In the tests with $0.22\ mm$ and $0.27\ mm$ needles, no defects were found in the laminate. Only from a size of $0.32\ mm$ do the typical branch-like, fingering flaws appear. In the case of the $0.32\ mm$ needle size, porosities form within a $40\ mm$ radius around the injection point, see Figure 5.11.
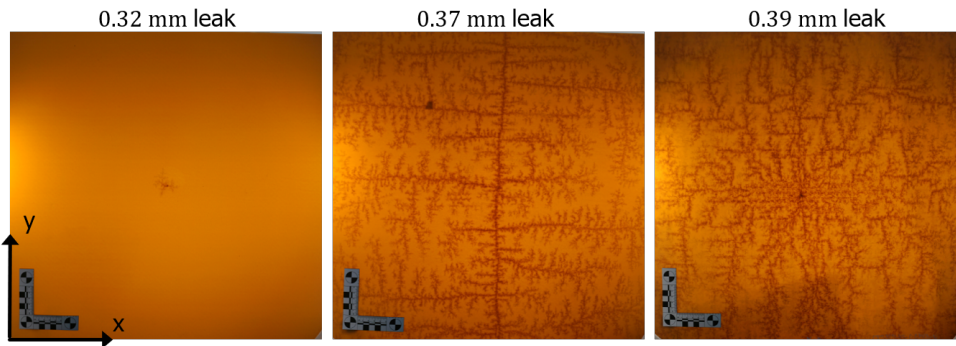


Figure 5.11: Leakage size and resulting laminate quality for $0.32\ mm$, $0.37\ mm$ and $0.39\ mm$ needle size

The results for the $0.37\ mm$ and $0.39\ mm$ leaks show significantly more porosity than the results from the first trial. The reason for this is the extent of the damage to the release film in the different tests. While in the first test the release film is only slightly damaged, in the second test the damage is much more severe, as confirmed by microscopic examination of the release film after curing. Figure 5.12 shows that the film in the first test shows one tear, while the release film in the second test shows several punctures and holes. This can be explained by a possible movement of the hypodermic needle during curing in the autoclave. The strong air flow can set the needle in motion and damage the release film in several areas. More damage to the release film therefore means more air entering the laminate.

The plates with the $0.15\ mm$ and $0.95\ mm$ leakage are selected for ultrasonic inspection via c-scan. The $0.15\ mm$ leakage plate shows only a little shadow so the ultrasonic test can validate if a real defect can be detected. The $0.95\ mm$ specimen shows large porosity areas so that a comparison between visual inspection and ultrasonic scan can be made.

Figure 5.13 shows the ultrasound results. It can be seen that the visual and ultrasonic inspection provide consistent results. In the case of the $0.15\ mm$ leakage, a slight shadow was detected in the final laminate in the area of the injection point. However, the evaluation of the ultrasonic inspection could not detect any porosities here. The porosities of the $0.95\ mm$ plate also show up in the ultrasonic scan exactly as they can be seen in the visual inspection. The evaluation according to
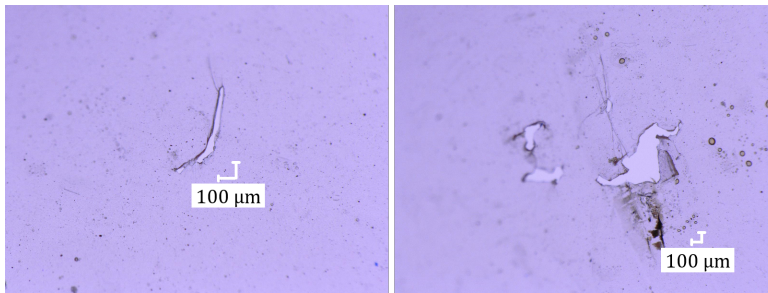
Figure 5.12: Damage of release film for the $0.39\ mm$ leakage in the first (left side) and second trial (right side)

the Airbus criteria (AITM 6-0011 [12]) shows the framed red area $1$ as a defect with an extension of $554 \times 349.7\ mm^2$ and a resulting area of $193,733.8\ mm^2$.

Additional micrographs are taken from the plates with leakage sizes of $0.22\ mm$ and $0.37\ mm$ and from the reference plate without vacuum in order to check the depth of the leakage. Figure 5.14 shows a comparison of the micrographs of the three laminates.

It can be seen that the laminate with the $0.22\ mm$ leakage has no defects. The laminate with the $0.32\ mm$ leakage shows some porosities and voids. A determination of the percentage of voids over the cross-section through image analysis results in approximately $10\%$. The porosities are found across the entire thickness of the laminate and are mostly located in the voids of the fabric, next to the intersections. As expected, the laminate cured without vacuum shows the highest percentage of porosity with about $30\%$ across the cross section. The defects are distributed over the entire thickness of the laminate as well. In addition, it can be seen that the laminate has a significantly higher thickness than the other two laminates due to the high proportion of porosities and the lack of compression during curing.

The tests show a high agreement with the spring model described in Subsection 5.2.6. In case of the continuous leak through the vacuum and release film, described by Figure 5.6c, the resin may leak out and spread in the breather material, as observed in the trials. It can also be seen, that the air is flowing not only into the breather but also into the laminate, forming the fingering porosity seen in Figure 5.11 and 5.13. In case of the non vacuum test panel the laminate thickness is very high and volatiles released during curing remain in the laminate and form additional voids, like seen in Figure 5.6b and 5.14.

**Leakages in vacuum film**   For the leakage insertion with the metal plate, no defects were found in the laminate but it showed that the plate and the underlying breather in this area were imprinted into the laminate. This can be explained by the higher stiffness of the plate compared to a flexible vacuum bag. The metal plate, even though it is very thin, imprints the underlying breather more into the laminate compared to the flexible vacuum bag. Since it cannot be ruled out that the locally
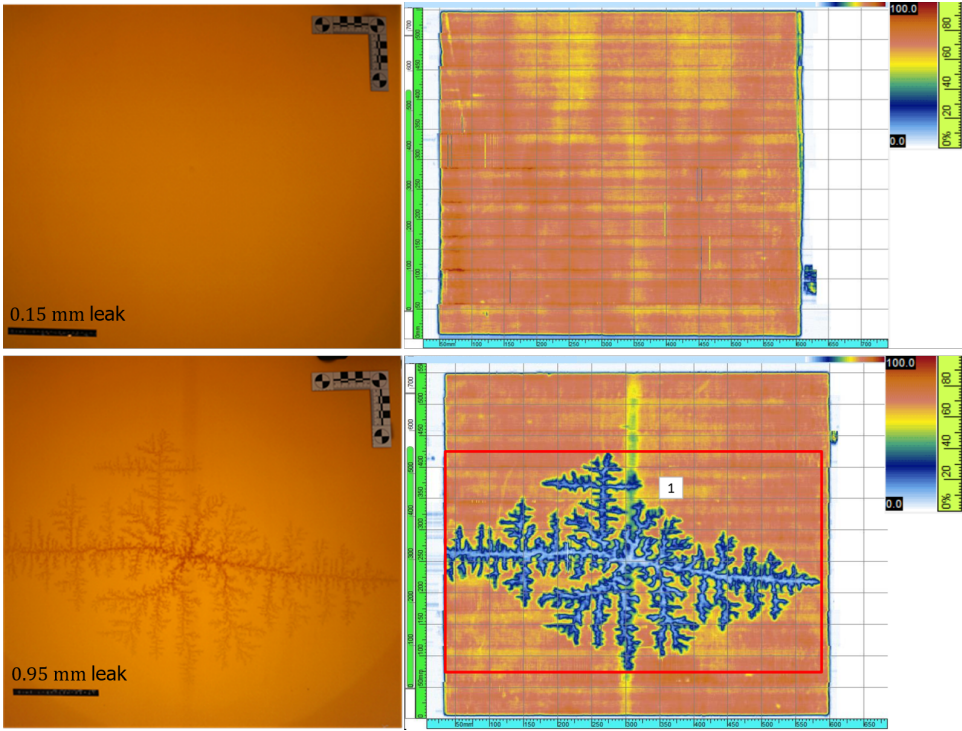
Figure 5.13: Original laminate and c-scan results for the $0.15\ mm$ and $0.95\ mm$ needle leakage
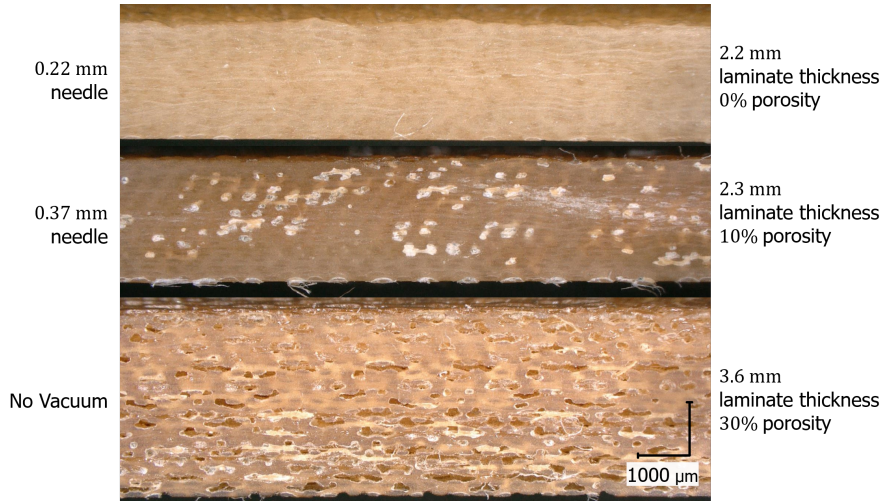


Figure 5.14: Micrographs of the laminates with a $0.22\ mm$ and $0.37\ mm$ leakages, and without vacuum. The void percentage has been quantified through image analysis.

altered stiffness of the film due to the metal plate has an influence on the effects of the leakage, the punching method is used in the other trials.

Two sizes are tested with the punching tool: $0.57\ mm$ and $0.83\ mm$. Figure 5.15 shows the laminate with a $0.83\ mm$ leakage. No defects are visible in both of the laminates. A subsequent ultrasonic examination also revealed no porosities in the component (see Figure 5.15).
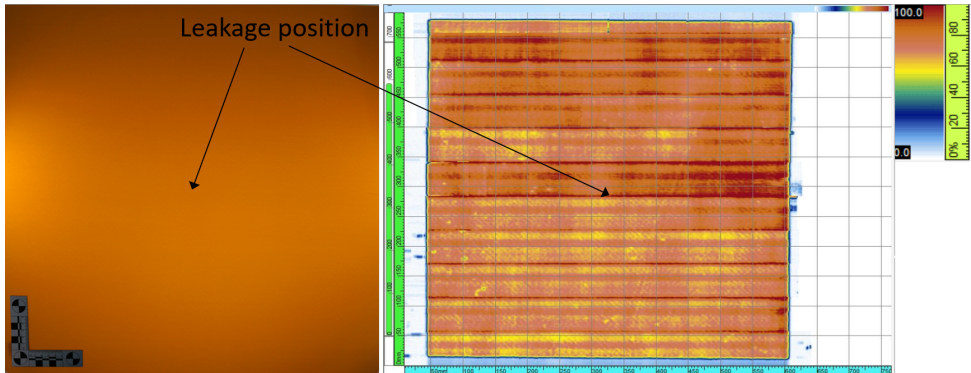


Figure 5.15: Original laminate and c-scan results for the $0.83\ mm$ punched leakage

Both tests show that a release film hermetically seals the laminate and that the air flowing in through the leakage cannot enter the component. The air flows through the breather and is evacuated by the vacuum pump. These results are also supported by the spring analogy described in Subsection 5.2.6. Figure 5.6d shows the case where the leakage is only in the vacuum film. Here, no air may enter the laminate and no porosities were found in the tests, like seen in Figure 5.15.

Even though no porosities were found in the laminates, a higher flow of resin to the suction unit was detected in the tests in which only the vacuum bag showed a leak. In some cases, the resin flow was so high that accumulations formed in the area of the vacuum connection. In all tests, the vacuum connections were positioned at the same distance from the leakage. The higher resin flow towards the pump was not observed in the tests with the hypodermic needles. Here, only the resin flow into the breather in the area of the leakage was noticeable.

## 5.3.4. Laminate thickness

As can be seen in the micrographs in Figure 5.14, there are large differences in thickness between a laminate cured under pressure and vacuum and one cured without pressure. Table 5.4 shows the results of the thickness measurement and in Figure 5.16 and 5.17 these are shown for several laminates in x and y direction like described in Subsection 5.2.5. It can be seen that the thickness of the reference plate without leakage has an almost constant thickness of $2.2\ mm$. The reference plate, which was cured without vacuum, shows a significantly higher thickness of $3.6\ mm$ and is thus much thicker than all other test plates. The test plates with the highest porosities, such as the plates with the $0.6\ mm$ and $1.2\ mm$ needles, show

a higher thickness of $2.3 - 2.4\ mm$ in the area of the leak and the propagation zone of the porosities.

Table 5.4: Average, minimum and maximum laminate thickness of test panels as well as laminate thickness in the area of the leakage

| Leakage size and type | Average laminate thickness [$mm$] | Min. laminate thickness [$mm$] | Max. laminate thickness [$mm$] | Laminate thickness at leak [$mm$] |
|---|---|---|---|---|
| None | 2.20 | 2.19 | 2.25 | NA |
| 0.15 $mm$ needle | 2.20 | 2.20 | 2.25 | 2.25 |
| 0.32 $mm$ needle | 2.21 | 2.15 | 2.3 | 2.25 |
| 0.39 $mm$ needle (first trial) | 2.27 | 2.20 | 2.30 | 2.30 |
| 0.39 $mm$ needle (second trial) | 2.33 | 2.30 | 2.40 | 2.40 |
| 0.95 $mm$ needle | 2.27 | 2.20 | 2.30 | 2.30 |
| 0.60 $mm$ plate | 2.20 | 2.15 | 2.30 | 2.25 |
| 0.57 $mm$ punch | 2.20 | 2.10 | 2.25 | 2.25 |
| 0.83 $mm$ punch | 2.20 | 2.10 | 2.30 | 2.30 |
| No vacuum | 3.60 | 3.50 | 3.60 | NA |

The test component with the metal plate shows only a small change in thickness directly in the area of the leakage. The variation in thickness of the plates with the punched leaks is particularly interesting. Here it can be seen that an increased thickness occurs in the direct area of the leakage, even without porosities in the laminate. In the y-direction, the laminate thickness visibly decreases to $2.1\ mm$ towards the vacuum pump and increases to $2.25-2.3\ mm$ in the area of the leakage, before it returns to a normal level of $2.2\ mm$ opposite the vacuum pump.

## 5.4. Discussion of hypothesis adressed

The research by Fernlund et al. [19] and Boey et al. [20] illustrate the reasons for void formation in laminates. They mention that leakages are a source for porosities in laminates but do not explain to which degree. The investigations performed in this thesis complement this research and focus on the explanations why and to which extend leakage cause voids and porosities in the final composite part.

The most important finding of the investigation carried out is that a distinction must be made between leaks that only affect the vacuum membrane and are separated from the laminate by an intact, non-perforated release film, and those where the release film is also damaged or perforated. The latter proved to be significantly more critical. The results for the continuous leakages in vacuum and release film show that the air enters not only the breather but also the laminate. Since air
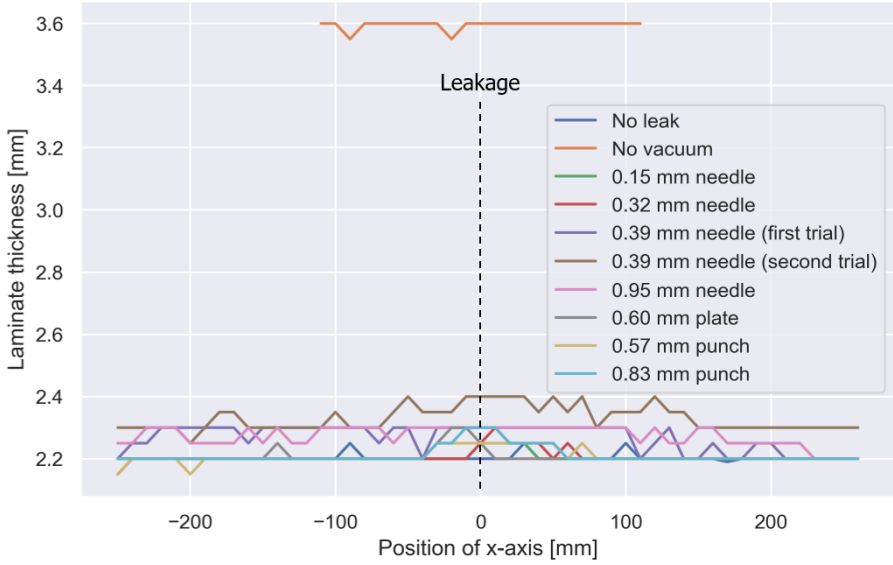
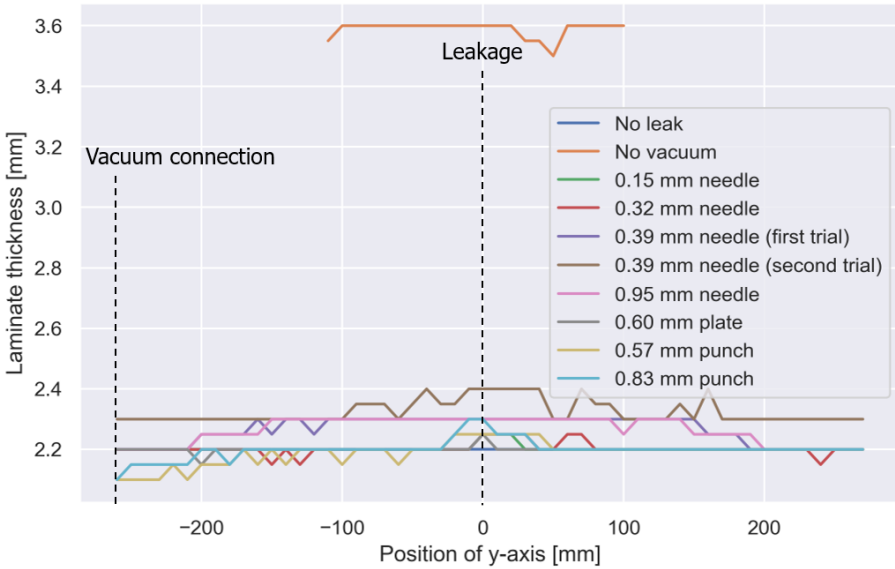Figure 5.16: Laminate thickness of test specimens in x-direction



Figure 5.17: Laminate thickness of test specimens in y-direction

chooses the path of least resistance, the first consideration would be that it flows primarily through the breather to the vacuum pump, since this should offer particularly good flow properties and low air resistance. The test results show, however, that the air also spreads in the laminate during the curing process if there is a possibility to do so. This indicates that during curing, heat and pressure cause compression of the breather, which adversely affects permeability. Figure 2.6 shows the permeability of different breather materials under $7\ bar$ pressure and different temperatures. It can be seen, that the airflow at $180°C$ for all breather materials is reduced drastically, with some even dropping to zero. The breather used in the experiments shows the best airflow capabilities at all temperatures but sees a reduction of $86\%$ from $20°C$ to $180°C$. With decreasing permeability of the breather, the air escapes into the interstices of the laminate and spreads out in a circular, fingering pattern starting from the leakage. At some point in the process, with increasing temperature onto the vacuum bag and component the permeability of the laminate appears to be greater than or at least equal to that of the breather, allowing the air to spread through the laminate and create the observed porosities.

In the tests carried out with leakages only in the vacuum film, the resin flows towards the leakage, as this is the area with the lowest effective pressure. This corresponds with the findings of the thickness measurement. As described in Section 2.2 and in Figure 2.2 by the Terzaghi principle, the consolidation pressure is divided onto the resin and the fibre bed. In the area, where the pressure onto the component lowered, the pressure onto the reinforcement is reduced and like a spring the fibre bed relaxes creating space that is filled by resin from higher pressure areas. This is also illustrated in the spring damper model in Figure 5.6 .

The decrease in laminate thickness towards the vacuum connection can be explained by the strong air flow in the breather. This causes not only the air to be evacuated but also the resin to flow towards and into the vacuum connection, thus reducing the laminate thickness in this area. No porosities were found in the laminate in this leakage case. This may be related to good evacuation of the trapped air before the autoclave cycle. If this air is not fully evacuated, potential air pockets would accumulate together with the resin flow towards the leakage and the area with the lowest effective pressure, like shown in the spring damper model in Figure 5.6. Evacuation of trapped air becomes more difficult with increasing component size and complexity, and the likelihood of porosity accumulating in areas of lower pressure increases.

Considering the results mentioned above, the Hypothesis 5 holds true. The possibility to demonstrate the physical processes that occur inside a leaky vacuum bag by a surrogate model based on spring damper analogy, also used by Dave et al. [21] is shown.

The tests carried out in this chapter have shown the effects that undetected leaks can have on component quality. A distinction must be made between two types of leakages: those in which there is a direct connection between the atmosphere and the laminate, and those which are located only in the vacuum film with a laminate that is still sealed off by a release film.

While the first case is much more critical because the air flows directly into the laminate and creates porosities, it is very unlikely for this to happen in production when using non perforated release film. However, it can be transferred to leakages in tools, e.g. at welding seams, where a solution could be to use additional release film between tool and component.

If the leakage is only in the vacuum bag, no defects could be detected in the laminate even with leakage sizes of up to $0.83 \ mm$. This leakage type proved to be hardly critical and only led to slight local changes in thickness, even if the pressure increase was well above the aircraft manufacturers regulations. The results indicate, that this type of defect only leads to defects in the laminate in combination with increasing component size and complexity as well as insufficient evacuation before the process.

5

# References

[1] A. Haschenburger and J. Stüve, *Influence of leaky vacuum bags on the quality of composite parts made from prepreg material,* Zeitschrift Kunststofftechnik / Journal of Plastics Technology **4**, 204 (2021).

[2] Hexcel Corporation, *HexPly® M21 Data Sheet,* (2020).

[3] Airtech Europe Sarl, *Wrigthlon® WL5200 Data Sheet - High performance fluoropolymer release film* (2019).

[4] Airtech Europe Sarl, *Ultraweave® 1332 Data Sheet – Heavy weight nylon breather / bleeder* (2018).

[5] Airtech Europe Sarl, *Ipplon® DP1000 Data Sheet - Soft nylon film with an excellent elongation* (2020).

[6] Airtech Europe Sarl, *GS-213 Data Sheet - Industry standard vacuum bag sealant tape for metal and composite tools* (2015).

[7] Nitto Denko Corporation, *PS-1 Data Sheet - High temperature / high tensile silicone flash masking tape* (2020).

[8] A. Haschenburger, N. Menke,  and J. Stüve, *Sensor-based leakage detection in vacuum bagging,* The International Journal of Advanced Manufacturing Technology **116**, 2413 (2021).

[9] A. Haschenburger and C. Heim, *Two-stage leak detection in vacuum bags for the production of fibre-reinforced composite components,* CEAS Aeronautical Journal **10**, 885 (2019).

[10] Airbus Operations GmbH, *AITM 6-4010 Issue 6. Inspection of fibre composites by ultrasonic phased array technique* (2013).

[11] Airbus Operations GmbH, *AITM 6-4012 Issue 4. Ultrasonic puls-echo inspection of glass fibre reinforced plastics* (2015).

[12] Airbus Operations GmbH, *AITM 6-0011 Issue 9. Non Destructive Inspection of Composite Parts* (2016).

[13] S. Hill and F. P, *Channeling in packed columns,* Chemical Engineering Science **1**, 247 (1952).

[14] D. Hillel and R. S. Baker, *A descriptive theory of fingering duringinfiltration into layered soils,* Soil Science **146**, 51 (1988).

[15] A. Pinilla, M. Asuaje,  and N. Ratkovich, *Experimental and computational advances on the study of viscous fingering: An umbrella review,* Heliyon **7**, e07614 (2021).

5

[16] S.-J. Liu and S.-P. Lin, *Study of 'fingering' in water assisted injection molded composites,* Composites Part A: Applied Science and Manufacturing **36**, 1507 (2005).

[17] R. Matsuzaki, M. Naito, D. Seto, A. Todoroki, and Y. Mizutani, *Analytical prediction of void distribution and a minimum-void angle in anisotropic fabrics for radial injection resin transfer molding,* Express Polymer Letters **10**, 860 (2016).

[18] G. M. Homsy, *Viscous fingering in porous media,* Annual review of fluid mechanics **19**, 271 (1987).

[19] G. Fernlund, J. Wells, L. Fahrang, J. Kay, and A. Poursartip, *Causes and remedies for porosity in composite manufacturing,* IOP Conference Series: Materials Science and Engineering **139**, 012002 (2016).

[20] F. Y. C. Boey and S. W. Lye, *Void reduction in autoclave processing of thermoset composites,* Composites **23**, 266 (1992).

[21] R. Dave, J. L. Kardos, and M. P. Duduković, *A model for resin flow during composite processing: Part 1—general mathematical development,* Polymer Composites **8**, 29 (1987).

5

# 6

# Leakage localisation and quantification approach

*Commercially available methods are suitable for identifying leakages in vacuum bags; however their application is predominantly associated with high outlay in labour and time, and thus high costs. The first scope of this chapter is the qualitative evaluation of the different available leakage detection technologies presented in Chapter 2. This shows that the combination of volumetric flow rate measurement and infrared thermography is the most promising concept for quick, reliable and automated identification of leakages in vacuum bags for large components. Hereby the fourth hypothesis is addressed and it is analysed, if it is possible to significantly reduce the process time for leak location by using a two-step procedure.*

*Subsequently, the measurement of the volumetric flow rate is described and evaluated in more detail in order to further improve the possibility of leakage localisation. It is tested if a flow-dependant criterion for the exact quantification and evaluation of airtightness can be identified and thus hypothesis 3 verified.*

## **6.1.** Introduction

The existence of a leakage in a vacuum bag can have a substantially impact on the final part quality. The standard procedure for the leakage detection performed in the aerospace industry was described in Subsection 2.4.4 and consists mainly of a pressure increase test and a position localisation with the help of an ultrasonic microphone. Within this chapter the different available leakage detection methods presented in Subsection 2.4.3 are analysed, compared and assessed.

## **6.2.** Methodology

Within this section the methodology of the performed tests is described. To improve the leakage detection for composite components a technology assessment is performed and afterwards a novel leakage detection approach developed. For this process, the volumetric flow rate measurement seemed to be the most promising technology which is later on described and investigated in more detail in Subsection 6.2.3.

### **6.2.1.** Technology assessment

To evaluate all technologies available on the market and in research, the different detection methods are summarised and then compared with each other using a test matrix. The conducted market analysis identified a total of nine leakage detection methods that are presented in detail in Subsection 2.4.3:

- Pressure increase test
- Ultrasonic sensor testing
- Infrared thermography testing
- Sensitive films testing
- Microphone array testing
- Piezoelectric sensors measurement
- Dye testing
- Gas detector test
- Volumetric flow measurement

To compare the different technologies, different test assemblies were used to model various boundary conditions. To ensure a comparison of all methods, first tests were performed on a small scale. A table-top tool $1500 \times 1500 \; mm^2$ in size was used. As shown in Figure 6.1, an optical metering cell including a thermographic camera attached to a linear drive was installed.

The most promising detection technologies were subsequently tested on a larger scale to test the transferability of the small scale results. An A350 fuselage shell tool with double-curved geometry was used for this purpose. Vacuum bags $4300 \times 1500 \; mm^2$ and $2000 \times 2000 \; mm^2$ in size were constructed. In a further series of tests, stiffening elements and film folds were integrated into the vacuum bags to check the effects of these interfering factors on the various detection methods.

Leakages were artificially introduced into the vacuum bag using hypodermic needles of different diameters or box cutters, depending on the desired leakage type.

**6**
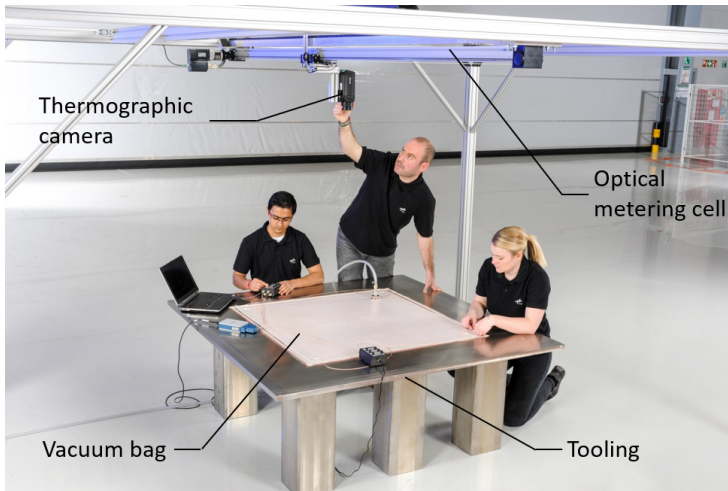
Figure 6.1: Table-top tool with optical metering cell

To ensure isolated existence of artificial leakages, the vacuum bag was checked for leakages using the pressure increase method prior to each trial.

Different types of leakages in vacuum bags had to be addressed within the trials. To this end, a list containing the various leakage types was generated in cooperation with the aerospace industry. The list is shown in Figure 6.2 and shows the chosen leakage types from the complete list that was presented in Figure 2.8. In order to evaluate the severity, occurrence and detectability of the different leakage types that can occur in a vacuum bagging, the quality department of a European aircraft component manufacturer performed a *Failure Mode and Effects Analysis* (FMEA) which can be found in Appendix A, Table A.1.

The considered leakage types are the primary leakages that occur within the vacuum film and the sealant tape and are the most critical during composite manufacturing. Other leakages can occur in the mould or at the vacuum ports. These cases were not considered in the scope of this tests.

Considering the various test assemblies and leakage types, a test matrix was generated in which all available detection technologies could be compared with one another. The following evaluation criteria have been agreed with a European aircraft component manufacturer and were used:

- Automated or manual
- Duration
- Handling
- Autoclave compatible
- Minimum size of detectable leakage
- Maximum component size
- Cost
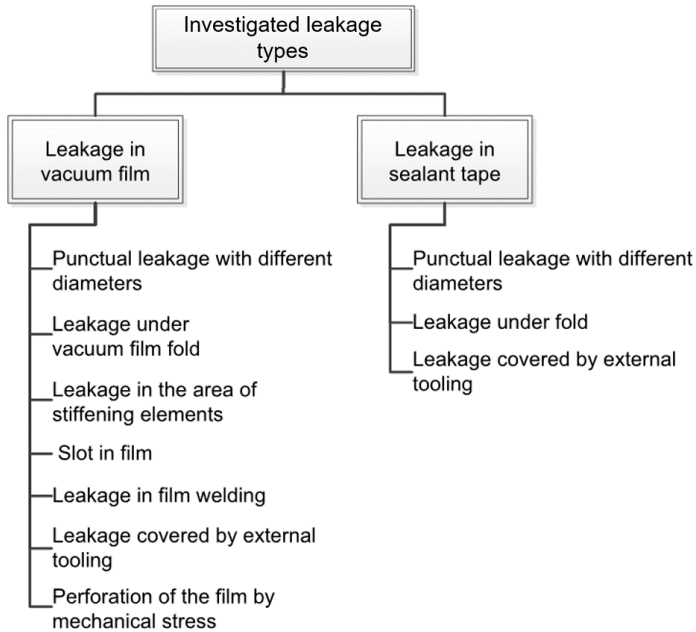
Figure 6.2: Classification of the different leakage types tested within the trials

A weighting factor was assigned to each assessment point to produce a final overall assessment for each method. This factor has been agreed with the manufacturing engineering at the European aircraft component manufacturer and is also a conclusion from the performed FMEA. The test matrix with the weighting factor can be found in Table A.2 in Appendix A.

### 6.2.2. Improved leakage detection

Since it could not be assumed that one leakage detection method fulfils all the criteria examined, it has been possible to combine different technologies in a meaningful way. The technologies are thus able to compensate for their respective detection limitations and can significantly reduce the time required. A possible concept for this kind of detection and the improvement compared to the state of the art (see Subsection 2.4.4)can be seen in Figure 6.3.

With the two-stage process it has been possible to improve detection times and automate the procedure for the composite part manufacturing. Right after the vacuum bag was finished, a sensor system has been used during the evacuation process to check if a leakage is present in the part. In opposition to the pressure increase test the system does not add any extra time to the process and an exact criterion for the evaluation of the airtightness has been used. If a leak will be detected, the sensor system calculates the area in the vacuum film where the leakages are presumably located. In the second step, a thermographic camera will be
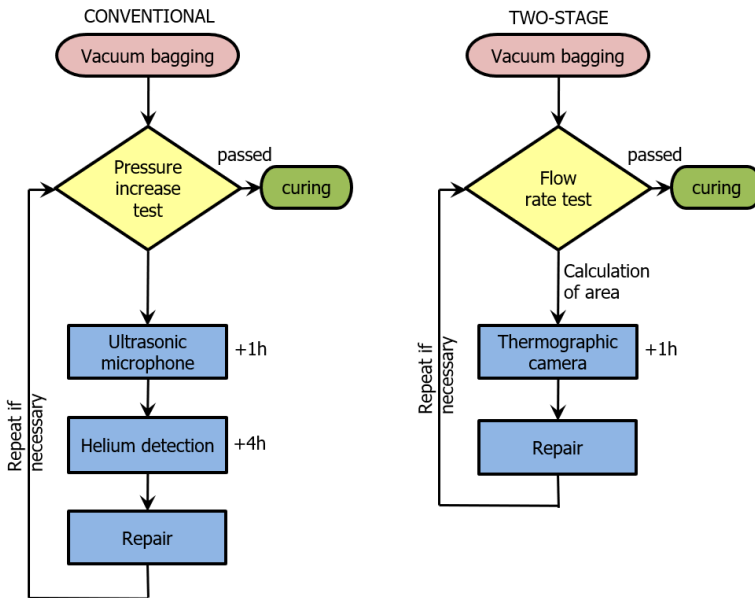
Figure 6.3: Comparison of flow charts for the current technique and the new process

used only in the determined areas and indicates the exact position of the leak. This process was expected to deliver considerable time savings and has a high potential for automation.

Instead of multiple independent leakage detection methods that have been used in sequence without taking each other into account, both methods in the two-stage process are interlinked. After identification of a leakage during evacuation, the severity of the leakage should be clear. Should the measurement exceed part specifications, an area for thermographic inspection will be identified using multiple flow meters. Subsequently, a thermographic camera would be applied to locate the leakage position exactly.

### 6.2.3. Volumetric flow rate measurement investigation

To evaluate the volumetric flow rate measurement of the two-stage leak detection process in more detail and the feasibility of its three main applications, three groups of experiments have been performed. Figure 6.4 gives an overview about the three classifications and the corresponding trials. The execution of the individual tests is described in detail in the following chapters. The used measurement technology and the experiment setup is the same as described in Subsection 4.2.6.

**Identification of leakages**   The first field of application of the volumetric flow meters was the identification of leakages through the flow rate. If the flow rate measurement could be used for the identification of leakages in a vacuum bag, it would mean, that it is possible to identify leaks during the evacuation process. This
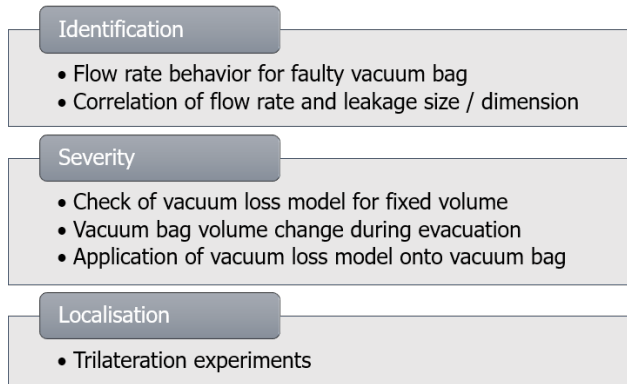
Figure 6.4: Experiment sequence for volumetric flow rate measurement

was the prerequisite for the aforementioned elimination of the pressure increase test in order to reduce production time.

To evaluate if the flow rate measurement is capable of identifying leaks a more precise understanding of its progression during evacuation of a vacuum bag with and without leakages has been necessary. Flow rates from the evacuation of airtight and leaky vacuum bags, where the leaks have been introduced before and after evacuation, were recorded with the experimental setup and equipment described in Subsection 4.2.6. Different sizes of leakages have been investigated to create a possible correlation between the flow rate measurement and the leakage dimension. Furthermore, different vacuum bag sizes ($910 \times 620~mm^2$, $1160 \times 1160~mm^2$ and $1450 \times 1450~mm^2$) and leakage positions have been investigated to evaluate, if the flow rate changes with different dimensions and positions. These tests were carried out to assess whether a leakage in the vacuum bag could be identified and if the volumetric flow rate would give an indication of the size of the leakage.

**Severity of leakages and creation of a model**   On the basis of the first tests and the fast convergence of the volumetric flow rate towards a tight or flawed level, as described in Section 2.4 and Subsection 4.3.1, a reasonable time saving has been expected by replacing the current leakage detection method. To substitute the common pressure increase test described in Subsection 2.4.3, the severity of a leakage needs to be known. As the common test is based on the pressure increase over a defined time it was necessary to convert the current specifications into flow rates. A correlation between the two parameters had to be found.

In order to evaluate leakages appropriately, some leakage calculation principles are necessary. Since the air inside the vacuum bag can be treated as an ideal gas, see Subsection 4.2.1, the pressure inside the bag is directly dependent on the amount of air gas inside the vacuum bag. The two values are connected by the ideal gas law:

$$pV_A = nRT \tag{6.1}$$

Where $n$ is the amount of air gas taking the volume $V_A$ inside the vacuum bag. $T$ and $p$ are temperature and pressure, respectively, and $R$ is the universal gas constant.

A pressure increase over time within a fixed volume at constant temperature is only possible if the number of molecules of the gaseous substance increases simultaneously.

$$\frac{\Delta p}{\Delta t} V_A = \frac{\Delta n}{\Delta t} RT \tag{6.2}$$

The left hand side of Equation 6.2 is commonly defined as the so-called leakage rate $q_L = \frac{\Delta p}{\Delta t} V; [q_L] = \frac{(mbar*\ell)}{s}$. [5] With the introduction of the leakage rate it is possible to quantify leakages in evacuated or pressurised containers. A leakage rate of $q_L = 1 \frac{(mbar*\ell)}{s}$ causes the pressure inside an evacuated or pressurised volume of one litre to increase or decrease by one millibar in one second, respectively.

Using the relation of mass, amount of substance and molar mass $n = \frac{m}{M}$ and rearranging yields the mass of air that has to be introduced into the vacuum bag to cause a given pressure increase.

$$\frac{\Delta m}{\Delta t} = \frac{\Delta p}{\Delta t} \cdot \frac{V_A M}{RT} \tag{6.3}$$

The connection of mass to volume by the density $\rho$ allows the reformulation of the Equation 6.3 in terms of volume that is to be added to cause a given pressure increase inside the vacuum bag over time.

$$\frac{\Delta V}{\Delta t} = \frac{\Delta p}{\Delta t} \cdot \frac{V_A M}{RT\rho} \tag{6.4}$$

The volume of air that is flowing into the vacuum bag through a leakage is measured by the volumetric flow rate $Q$. Approximating $Q$ to be constant throughout the process, $Q = \frac{dV}{dt} = \frac{\Delta V}{\Delta t}$, then a correlation of volumetric flow rate and pressure increase is given as:

$$Q = \frac{\Delta p}{\Delta t} \cdot \frac{V_A M}{RT\rho} \tag{6.5}$$

An evacuated vacuum bag of volume $V_A$ will experience a pressure increase of $\Delta p$ per time $\Delta t$ if a constant volumetric flow rate of air $Q$ enters through a leakage. The accuracy of this pressure increase model was estimated to be $f_{aim} = \pm 10\%$, see Appendix B, which would be acceptable for manufacturing purposes.

The functionality of the model has been verified experimentally for a rigid container. The purpose of this experiment was the controlled introduction of a leakage into a rigid vessel and the measurement of the occurring volume flow and the associated pressure increase inside this container. The rigid container tested to prove the functionality of the model was chosen to be a resin trap (see Figure 6.5a) with a volume of $29\ l$ with a volumetric flow meter inserted at the connection to the vacuum pump.

Unlike a rigid container, a vacuum bag as shown in Figure 6.5b has flexible borders and changes its volume during the evacuation process, presumably resulting in a non-linear progression of the pressure increase over time.
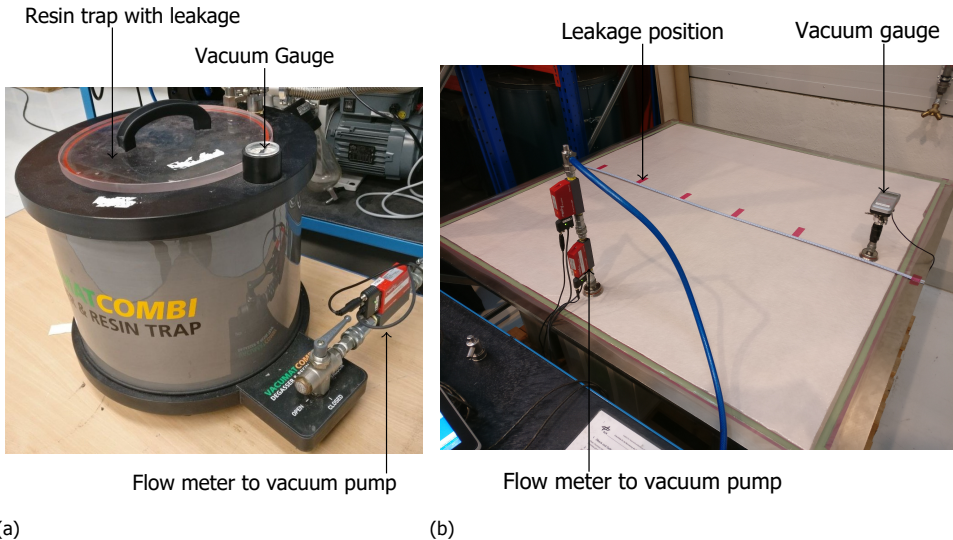


Figure 6.5: Resin trap - experimental setup (a) and Vacuum bag - experimental setup (b)

The initially derived equation for pressure increase required the volume as a constant physical quantity which was not given in the case of vacuum bags. Thus, more profound knowledge about the volume contained in a vacuum bag and its change with progressing evacuation or aeration had to be obtained in order to make adjustments to the equation if necessary. A second experiment has been performed to prepare the use of the pressure increase model for vacuum bags of variable size. The out flowing volume of a vacuum bag has been measured for evacuation from different absolute pressures, to evaluate the equivalent rigid volume of the vacuum bag and breather.

To verify the correlation between the volumetric flow rate and the pressure increase over time, a third experiment has been performed. Different sized vacuum bags were punctured with hypodermic needles of various nominal diameters to introduce controlled leakages. The resulting pressure increase has been logged to calculate pressure differences over distinct time periods. With the knowledge gained from the previous tests, it has been possible to calculate the resulting volumetric flow rates on the basis of the given pressure increase over time and vice versa.

**Localisation of leakages**  To speed up the detection process, the localisation of the leakage when using multiple volumetric flow meters has been desired. If the incoming air flow through the leak is divided in a certain pattern into separate vacuum lines, depending on their distance to the leakage, it would be possible to draw conclusions about its location. To achieve this, it has been necessary to

measure and compare the individual volumetric flow rates at several distributed vacuum connections.

The position of a point in two-dimensional space is sufficiently described by its distance to three fixed reference points. This method of localisation is called multilateration and depicted in the left image of Figure 6.6. [6] The leakage is located in the intersection of the resulting radii. The more accurate the measurements, the smaller the resulting area.
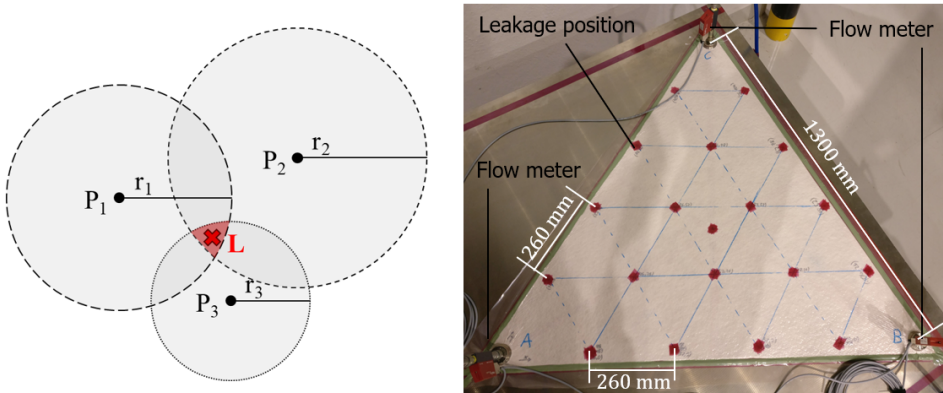


Figure 6.6: Principle of multilateration and experimental setup with triangular vacuum bag

Based on the multilateration localisation principle, a vacuum bag in the shape of an equilateral triangular has been used for the first trial, as shown in the right image of Figure 6.6. Since conservation of mass holds true, the incoming flow through the leakage equals the sum of the individual sub flows for an equilibrium state:

$$Q_{in} = Q_{Leakage} = Q_1 + Q_2 + \dots + Q_n = Q_{out} \tag{6.6}$$

If only one flow meter is used, the leakage position should be irrelevant for the output of the flow meter. If several flow meters are used, the flow is divided among the different sensors, since the materials in the vacuum form a flow resistance and thus a resistance network has been considered for this measuring principle.

A qualitative comparison of the flow rate distribution at different leakage positions enabled the triangle to be divided into twelve sectors, as shown in Figure 6.7. The affected area with the leakage can be identified and investigated with further detection methods.

In order to check the approaches, a larger vacuum setup was created with the side lengths of $1500\ mm$ x $1500\ mm$. Four vacuum connections were placed in the four corners of the vacuum setup, like shown in Figure 6.8.

A total of $300$ experiments with different random leakage positions have been performed and the data recorded. The leaks were created with hypodermic needles of different diameters. The key condition was the equidistant placement of the vacuum connections. This allows for the bagged area to be symmetric and comply
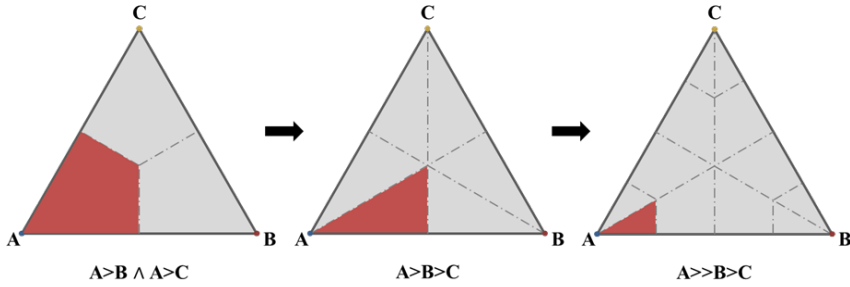
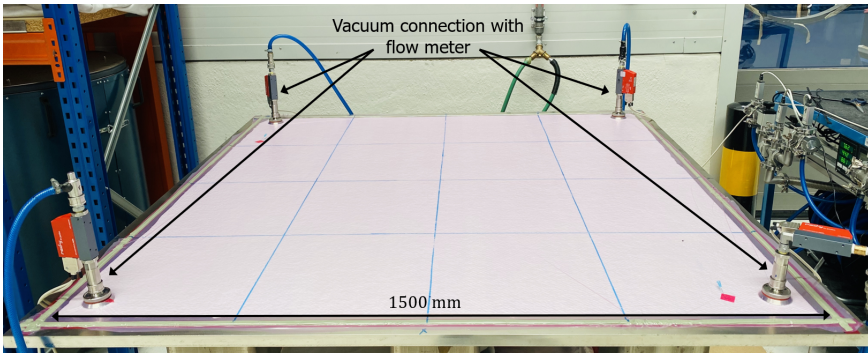Figure 6.7: Qualitative partitioning approach for determination of leakage area on triangular vacuum bag



Figure 6.8: Vacuum bag setup for the performed trials

to the norms of the principle of localisation. The concept of leakage localisation for a four flow meter setup has been similar to that with a three flow meter setup. Based on illustration of the experimental setup in Figure 6.9, the area in which the leak is present can be narrowed down.
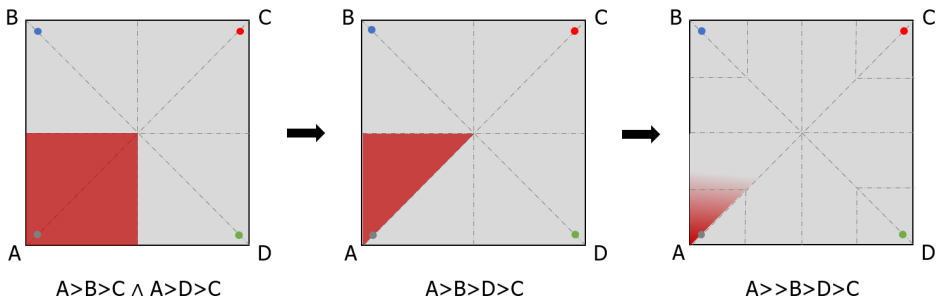


Figure 6.9: Qualitative partitioning approach for determination of leakage area on square vacuum bag

Since it is assumed that the total *Volumetric Flow Rate* (VFR) is evenly distributed among the connected vacuum ports depending on the distance of each port to the

leak, a numerical regression is used to find a relationship between the distance from the leak to the vacuum port and the $VFR_{fraction}$ flowing through that vacuum port. This relation was then used to make a prediction on the location of the leakage. A plot of the relevant data is shown in 6.10.
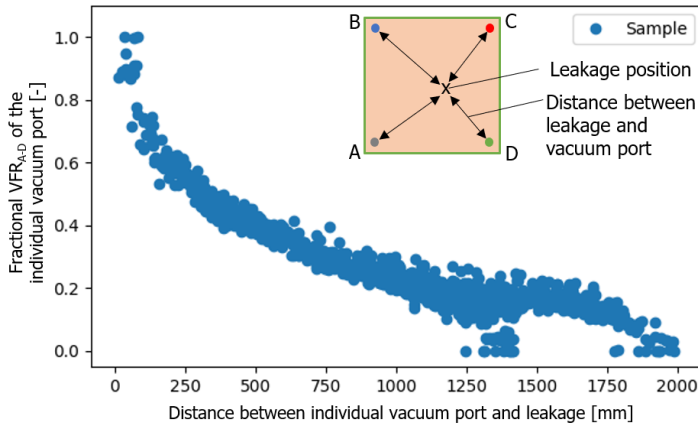


Figure 6.10: In this plot of the single leakage experiments, each point is defined by a distance of the leakage to the individual vacuum port A-D (horizontal axis) and a VFR fraction of the individual vacuum port A-D (vertical axis). There is a point for each of the four vacuum connections of every experiment. For each experiment, the horizontal component is obtained calculating the distance between a specific vacuum connection and the leakage of the experiment, the vertical consists in the $VFR_{A-D}$ fraction measured in that corresponding vacuum port A-D. The points seem to suggest a relation similar to an inverse proportionality.

The pattern created by the data points along a curve suggests a relation between the two variables (pump-leakage distance and VFR fraction) similar to an inverse proportionality. The regression that used the distance from vacuum port as an independent variable and the fractional VFR as dependent variable. The basis functions of the regression were obtained starting from a high number of functions, such as powers of $x$, $1/x$, trigonometric functions, the exponential function, and the natural logarithm. Equation 6.7 represents the relation between $VFR_{fraction}$ and the distance from the leakage to the pump, $r$, as a combination of the basis functions and their coefficients, where $a_i$ represents a to be determine value.

$$VFR_{fraction} = a_1 + a_2 \cdot r + \frac{a_3}{r} + \frac{a_4}{r^2} + \frac{a_5}{r^3} + a_6 \cdot \tan(r) + a_7 \cdot e^r + a_8 \cdot \ln(r) \quad (6.7)$$

The regression has been performed several times in order to reject basis functions that do not provide a meaningful contribution. That is when they have a negligibly small coefficient assigned to them. Finally, the regression function was inverted and applied simultaneously to the fractional VFRs of the four vacuum ports. This resulted in the estimated distance between each port and the leakage, visualised as circles around the vacuum ports. Since the radii of all four circles were estimations, the circles do not intersect in one and the same point, which would be

the case if an exact relation was known. Hence, the prediction for the leakage lo-
cation was the point which is closest to all four circles. To find this point, Newton's
method for optimisation [7] was applied to minimise the sum of the squares of the
distances from the prediction to the circles. An example of the circles and the pre-
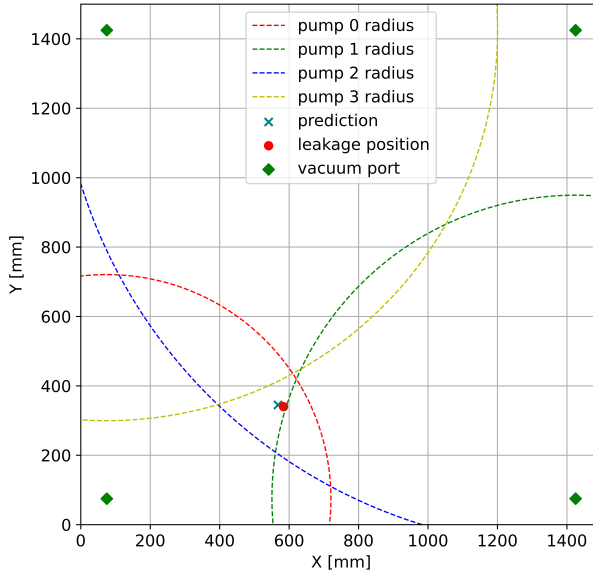diction is shown in Figure 6.11.



Figure 6.11: Graphical representation of the quadrilateration step in the prediction of the leakage position
using the numerical regression from Equation 6.7 and quadrilateration method. The arches represent
the expected leakage location based solely on one VFR fraction, with the use of the four VFR fractions,
quadrilateration can be utilised; Newtons method allows to localise the point with the shortest distance
from each of the arches, thus producing a single point as the prediction of the leakage

## 6.3. Results

Within this section, the results of the tests are presented and analysed. The tech-
nology assessment is followed by the development of a two-stage leakage detec-
tion system and the detailed evaluation of the volumetric flow rate measurement
and its capability to detect, assess and locate leakages in a vacuum bag.

### 6.3.1. Technology assessment

In the course of the preliminary tests, all available technologies are examined and
the most promising methods are preselected in order to test them on a larger scale.
A detailed test matrix is generated and the results can be found in Table A.2 in
Appendix A.

**Preliminary trials** Within the small scale trials it could already be seen that not all technologies were equally suited for reliable leakage detection and localisation. The *pressure increase test*, described in Subsectuion 2.4.3, which is currently being used in production, is only suited for determining the existence of a leak, but does not enable its localisation. With increasing component size, the detectability of a leak becomes less explicit, since detection time and the positioning of the metering device play a crucial role.

Some preliminary trials are being carried out using *ultra-sonic microphones*, described in Subsection 2.4.3, to detect leakages in different vacuum bags. Here, it is apparent that the distance between the microphone and the vacuum bag should not exceed $30\ cm$. The greatest disadvantage, however, is that not every leakage appears to emit sufficient sound in the ultrasonic range. Apparently, some leakages have a predominantly laminar flow, such that hardly any high-frequency sound is generated. On the other hand, sounds in the ultrasonic range that are detected by the microphones may also be produced at obstacles to the flow or structural transitions without there being leakages, for example, between individual sheets of the breather layer or close to the vacuum connection, thus misdirecting the microphone operator. On the other hand, better results were achieved on the vacuum sealing tape, as only linear sections had to be inspected. It must also be noted that larger leakages are already perceived by human hearing, and the handset is intended for smaller leakages. Due to the described problematic results, this technology is not considered any further in this thesis.

Leakage detection using *sprayed helium*, described in Subsection 2.4.3 is state of the art in newer aircraft programmes. During production, some disadvantages of this method have become apparent. On one hand, the test is very time-consuming, as only small areas can be tested. On the other hand, the test can only identify the area and not the exact position, quantity or type of leakage. Furthermore, it has been observed that vacuum films can become permeable to helium atoms over time. In this case, a leakage would be indicated as a false-positive. Due to these drawbacks, no further trials were carried out within the thesis.

Leakage detection using *ink or dye*, described in Subsection 2.4.3 especially showed problems in case of film folds and around stringers. Reliable application and removal of the dye is associated with a greater expenditure of time. The detection of leakages is also made more difficult by folds. As expected, it became evident that leakage detection is absolutely dependent on the presence of a white breather cloth. CFRP stringers that are already cured are generally not covered with breather cloth, such that leakages in these areas are almost impossible to identify due to the poor visibility of the relatively thin, yellow dye on the black CFRP stringers.

The detection of leakages with *oxygen sensitive films*, described in Subsection 2.4.3 could not be performed, as of 2022, no such film has ever been commercially available. However, it must be noted that this film would represent an additional auxiliary material within the vacuum bag. On one hand, this increases cost and time outlay in construction of the vacuum bag, and on the other hand an increased volume of waste if it is not possible to integrate this material into a vacuum film.

Investigations of *pressure sensitive films* showed that local pressure deviations caused by leakages are detectable with these sensors and that an inference on the position of a leakage is possible, see Chapter 4. However, the sensors are not available in large dimensions and need to be applied to the inside of the vacuum bag where they would adhere to the resin and leave marks on the component surface. Additionally, the sensor cables need to be lead through the vacuum bag which is leak-prone.

In the above described preliminary trials, *infrared thermography*, *piezoelectric sensors*, and the *volumetric flow rate measurement* appeared to be the most suitable with regard to the assessment criteria and were examined on a larger scale. The results are shown individually below.

**Large scale trials**   Leakage detection using **IR thermography**, described in Subsection 2.4.3 has turned out to be a very reliable method. Especially leakages in the vacuum film on top of breather cloth are easily identified by thermography. As expected, the leakage location stands out very clearly as a cold spot. Perforations in the film can be identified in this way. A drop in temperature can be detected in the immediate vicinity of the leakage, as shown in Figure 6.12. This is of particular significance if the position of the leakage itself cannot be imaged directly by the camera lens, as may occur when there are folds in the vacuum film. The temperature drop in the wider surroundings of the leakage still allows it to be roughly located.
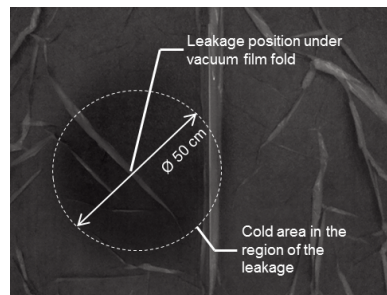


Figure 6.12: Thermal image of a leakage under a film fold. A drop in temperature in the area around the leakage can be identified.

Leakages on the upper side of a fold, i.e. in places where the airflow has to travel some distance before reaching the breather cloth, are particularly hard to identify. The temperature difference of the air presumably reduces along the route of the flow, such that the breather layer experiences little to no cooling. Leakages at stiffening elements that are not covered with a breather layer are also hard to identify. The reason for this is likely the high thermal capacity of the material or its high coefficient of thermal conductivity.

One additional advantage is that leakage detection by thermography has already been carried out successfully in an autoclave. For this purpose, a thermography system inside a water-cooled pressure vessel has been integrated in the research

autoclave at DLR in Stade. [8] And the detection can be automated using image processing algorithms.

*Piezoelectric sensors*, described in Subsection 2.4.3, were able to detect almost all types of leakages unless several leakages occurred in a single vacuum bag. Further development of the analysis software would be required for this.

As expected, improved accuracy of the identified leakage location occurred during the large-scale trials, since the signal propagation times also increased. The data recorded in this test is shown in Figure 6.13. It must be noted that stiffening elements were incorporated into the vacuum bag during this test, which are represented as black lines in the figure. The size of each examined field, in the centre of which the test leakage was introduced, is $200\ mm$ by $200\ mm$. Within the diagram, the respective deviation between the real and the determined leakage position (euclidean distance) is given for each field and indicated by colour. The average deviation between actual and calculated leakage positions is $471\ mm$.

| x → \ y ↓ | 150 | 350 | 550 | 750 | 950 | 1150 | 1350 | 1550 | 1750 [mm] |
|---|---|---|---|---|---|---|---|---|---|
| 150 | 862 | 366 | 516 | 194 | 1063 | 1123 | 1084 | 564 | 1123 |
| 350 | 686 | 677 | 976 | 780 | 26 | 417 | 634 | 483 | 417 |
| 550 | 306 | 788 | 314 | 251 | 16 | 171 | 553 | 127 | 171 |
| 750 | 527 | 220 | 289 | 63 | 220 | 138 | 109 | 240 | 138 |
| 950 | 418 | 90 | 211 | 297 | 388 | 286 | 462 | 92 | 286 |
| 1150 | 196 | 33 | 118 | 488 | 418 | 782 | 366 | 437 | 782 |
| 1350 | 548 | 467 | 495 | 144 | 759 | 593 | 499 | 622 | 593 |
| 1550 | 360 | 589 | 392 | 247 | 756 | 858 | 691 | 618 | 858 |
| 1750 [mm] | 677 | 623 | 323 | 231 | 885 | 787 | 773 | 201 | 787 |

Figure 6.13: Leakage detection using piezoelectric sensors described in Subsection 2.4.3. Four sensors are integrated into the four corners of the vacuum bag. The deviation between the real and the determined position is given in $mm$. Deviation is indicated as acceptable by green colouration; yellow indicates marginal deviation; red indicates an unacceptable result.

It is easy to see that the reliability of the calculation procedure is not equal at all points, but its distribution is not chaotic either. It is evident that the values obtained close to the edges are more unreliable. A positive aspect is that a negative influence of the procedure by the stiffening elements is not observed.

The trials show that the technology is essentially suitable for narrowing down the location of a leakage, but an accurate determination of the position is not yet possible. For this method to work properly, a set of raw data must be taken for each piezoelectric sensor for a given part geometry. Due to the sensitivity of the sensors, the measurement is very susceptible to vibrations coming from the surrounding. It was proposed to integrate the sensors into the tooling as future work; however, at the time of this thesis' submittal the intool sensor integration had not yet been technically realised, leaving problems for the usage of piezoelectric sensors unsolved. Since the sensors are embedded into the vacuum bag, they are in contact with the laminate and will leave marks on the component surface. Furthermore, the sensor cables must be routed through the vacuum bag which is leak-prone, and the sensors cannot currently withstand the elevated temperatures inside the autoclave.

**Volumetric flow measurement** is the most promising method for leak detection as it is the only method to detect all possible leakages inside the vacuum bag. Implemented in the vacuum lines connected to a vacuum bag, both leakage detection and localisation are conceivable applications. Since the flow meters are integrated into the vacuum lines, there is no contact with the composite part, leaving its mechanical properties and surface unimpaired. Depending on which end of the vacuum line the flow meter is integrated, the integrity of hoses and quick connectors can also be checked. The tests proved that three main conclusions can be drawn from the volume flow measured during vacuum bag evacuation. These three conclusions are:

- The existence of a leakage (Identification)

- The vacuum loss caused by a leakage (Severity)

- The position of the leakage (Localisation)

The connected vacuum lines can continuously extract and remove the air flowing in through a leak. After sufficient evacuation time, this equilibrium leads to a sustained increased flow rate and thus the presence of a leakage is indicated. Furthermore, a correlation of volume flow and leakage area could also be demonstrated.

The quality of a vacuum bag can be quantified by the occurring pressure increase per time unit. The correlation of the measured volumetric flow rate in the case of an existing leakage to the occurring increase of pressure after disconnecting the vacuum lines could be determined. The severity of a leakage and its effect on the vacuum bag could be estimated from the measured volumetric flow rate. In the future, the volumetric flow rate could serve as a criterion for vacuum bag quality that would be independent of leak location and part size.

It also proved possible to locate the position of a leakage by using several volumetric flow meters. Since the incoming flow is distributed among the individual vacuum lines in a regular pattern depending on the respective distance to the leakage, it is possible to draw conclusions about the location of the leakage. For this purpose, it is necessary to measure and compare the individual volume flow rates at several distributed vacuum connections.

As the flow meters can be integrated in the vacuum lines, an implementation inside the autoclave is possible as well. The sensors are installed outside the pressure vessel in the individual vacuum lines leading to the vacuum pump. In this case they are not exposed to high temperatures and pressures and are still able to identify leakages that occur during the curing cycle. All these findings are described in detail in Section 6.2.3.

**Summary of findings**   The comparison in Subsection 6.3.1, the conducted trials in Subsection 6.3.1 and the results of the test matrix that can be found in Table A.2 in Appendix A show that the best results are achieved using infrared thermography and volumetric flow rate measurement of all tested methods for leakage detection. Figure 6.14 shows the results of the trials from the test matrix of A.2 in a radar chart. Infrared thermography is very accurate and can determine the exact position of the leakage, which make it stand out among the other methods. Volumetric flow rate measurement, on the other hand, can quickly identify the presence of a leak and narrow down the area of a leakage but cannot determine its exact position. All other tested procedures require more time and/or higher manual effort, as for example piezo sensor, dye and ultrasound microphone procedures.
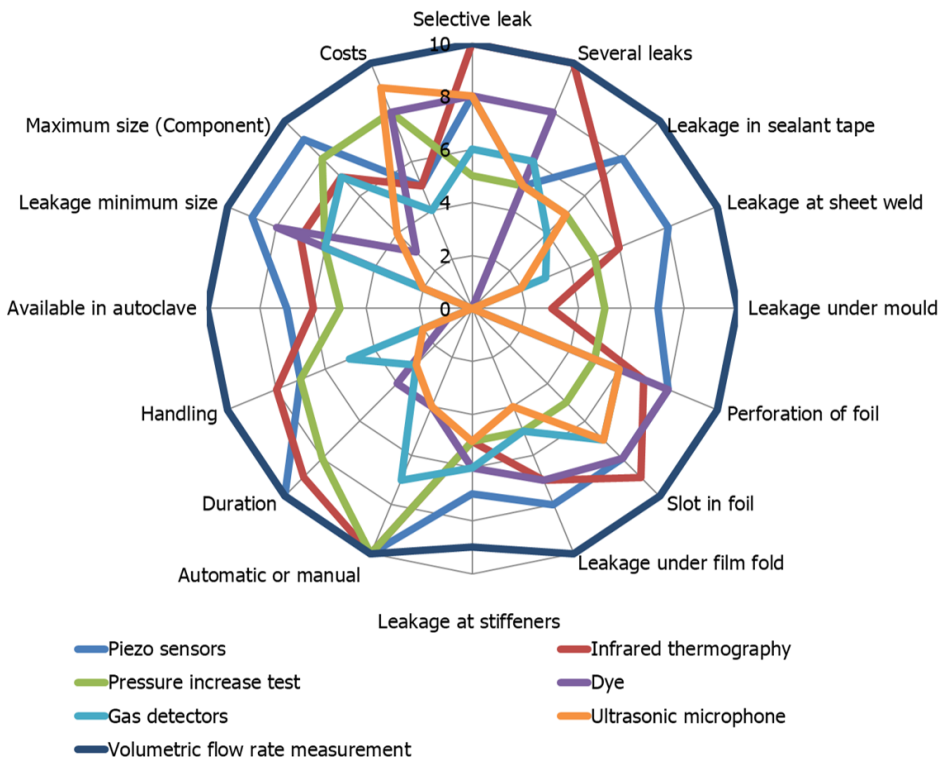


Figure 6.14: Analysis of the trial results in a radar chart. On a scale from 0 to 10, 0 stands for particularly bad and 10 for very good.

An additional advantage of leakage detection using thermography and volumetric flow rate measurement is its option to be used during the autoclave cycle. The technologies have been successfully transferred to larger, more complex components for fuselage geometries.

### 6.3.2. Two-stage leakage detection

The findings obtained in the trials in the previous Subsection 6.3.1 showed that all of the technologies available on the market may be potentially suitable for identifying leakages in vacuum bags but they each have individual detection limits or are associated with high time and cost outlays. Overall, leakage detection using thermography and volumetric flow rate measurement perform the best in the test matrix considering their individual properties. However, both technologies also have their respective disadvantages when it comes to speed (thermography) or accuracy (volumetric flow rate measurement). This has resulted in the idea of linking both procedures to obtain a two-stage, robust leakage detection system, see also Subsection 6.2.2.

The direct comparison of the conventional and the two-stage process in Figure 6.3 shows that the pressure increase test as decision basis for whether the component can be passed on to the next process stage is exchanged for the flow rate test. If the pressure increase test is not passed, the different detection procedures are used. Using current leakage detection technology, this may mean an additional time requirement of up to five hours. The implementation of volumetric flow meters for leakage detection offers a high savings potential. By interlinking the detection and localisation methods in the two-stage leakage detection, the process time is reduced from about $5$ hours to only $1$ hour conservatively calculated for a $60\ m$ large part, see also Figure 6.3. This results in a process time reduction of up to $80\%$ compared to the state of the art process shown in Figure 2.22.

### 6.3.3. Volumetric flow measurement

As the flow rate measurement is an essential part of the novel leakage detection approach and may potentially replace the pressure increase test, it is investigated in more detail. The evaluations can be found within this subsection and are divided into the three main categories: identification, severity and localisation.

**Identification of leakages**  The progression of the magnitude of the volumetric flow rate for an airtight and flawed bag is shown in Figure 6.15 for an exemplary test configuration.

As can be seen in Figure 6.15 a leakage in a vacuum bag causes a notably elevated volumetric flow rate compared to an airtight bag. It makes no difference if the leak is created before or after evacuation, the volumetric flow rate converges towards the same value if the leakage is of the same size. This finding confirms that existing leakages as well as leakages that occur during the vacuum bagging process or handling of the auxiliary materials can be identified and distinguished based on the volumetric flow rate progression. Furthermore, the time required
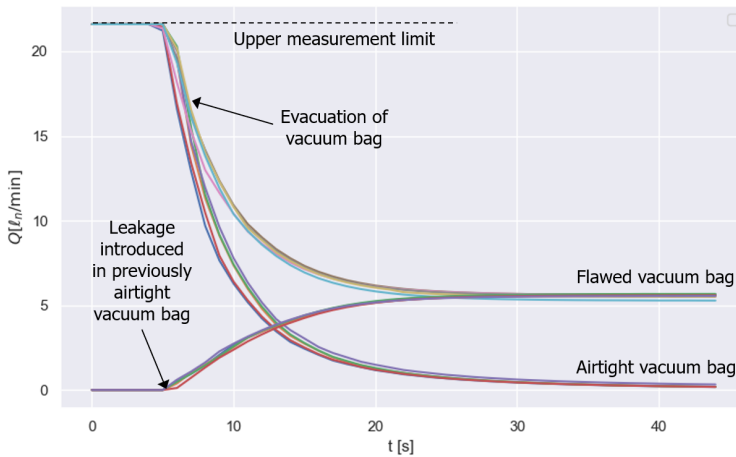
Figure 6.15: Flow rate progression with and without leakage and after leakage introduction with a Ø 0.95 $mm$ hypodermic needle as an example. Different colours represent different measurements

to identify a flawed vacuum bag with this method is significantly lower than the common pressure increase test that is performed after evacuation of the bag.

In the test performed in Subsection 4.3.1 it can be seen, that different leakage sizes in the vacuum bag cause volumetric flow rates of distinct values. A linear correlation is resulting when plotting the equilibrium flow rate values over the leakage area like shown in Figure 4.9. The performed experiments also show that the resulting volumetric flow rate is independent of the vacuum bag size and leakage position, see Figure A.1 in Appendix A.

**Severity of leakages and creation of a model**   The functionality of the model created in Subsection 6.2.3 is verified experimentally for a rigid container within the expected accuracy. It can be seen in Figure 6.16a that with disconnection of the vacuum pump, the pressure inside the resin trap started to increase. Initially, the rise showed linear behaviour in lower pressure regions while the rate of pressure gradually declined towards the end of the aeration. Hypodermic needles of larger diameter resulted in steeper curves and faster aeration of the resin trap than those of smaller diameter. Using Equation 6.5 volumetric flow rates are calculated from pressure increases over different times which are taken from the measured pressure data. Subsequently, the calculated volumetric flow rates are compared to the values that are measured during the experiment. Within the range of pressure increase which is common for vacuum bag specifications, the linear approximated pressure increase is proven to correlate with the leakage volumetric flow rate and resulting pressure increase for a rigid container within an acceptable margin of error. The basis for reformulation of current quality specifications from permitted pressure increase into volumetric flow rate is therefore established. From Figure 6.16b it becomes apparent that the progression of pressure increase over time inside a

vacuum bag is non-linear due to its flexible borders and changes of volume during the evacuation process.



(a)                                                        (b)
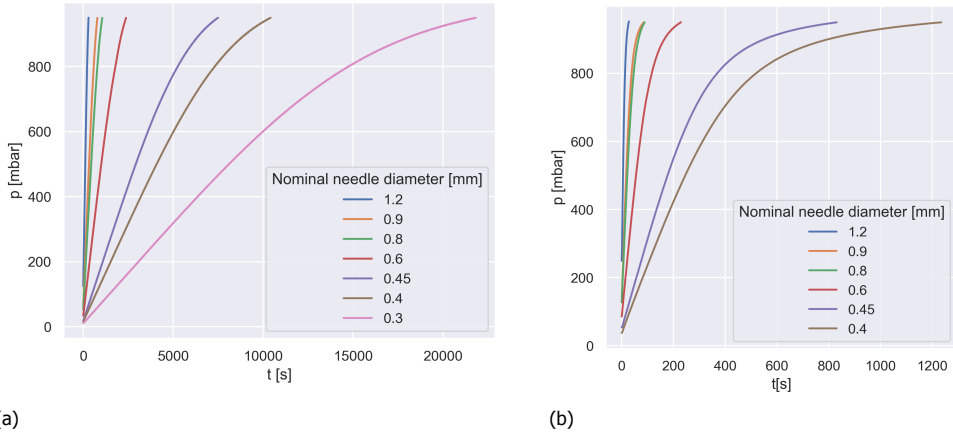
Figure 6.16: Progression of pressure inside the resin trap (a) and progression of pressure inside the vacuum bag (b); leakages created with different hypodermic needle diameter

In the subsequent experiments to determine the respective volume in the rigid container and in the vacuum bag, this is again clarified. By comparison of the air contents of vacuum bags and resin trap, it could be concluded that a vacuum bag constructed with an Ultraweave 1332 breather [9] – after initial compression – behaves analogous to a rigid container below an absolute pressure of $600\ mbar$. Typical system pressures for vacuum bags are significantly lower than $600\ mbar$ such that air which leaks into a vacuum bag will find a pseudo-rigid container and cause an equal vacuum loss as would occur for a true rigid container. Past an internal pressure of $600\ mbar$, the effective pressure onto the vacuum bag is no longer larger than the elastic restoring force of the breather causing the latter to relax. Vacuum loss above $600\ mbar$ must never arise during manufacturing of high performance composites and is beyond regular vacuum loss specifications. To correlate a volumetric flow rate and the resulting pressure increase within the pseudo-rigid region of a vacuum bag, an equivalent rigid volume $V_{A,eq}$ must be used. The equivalent rigid volume represents the theoretical volume of air that a vacuum bag would contain at ambient pressure if no elastic relaxation of the breather occurred. Equivalent rigid volumes of all measured vacuum bags were obtained from the experimental data by extrapolation of the linear section to ambient pressure, thus neglecting the elastic relaxation of the breather. The equivalent rigid volumes of all tested vacuum bags are compiled in Table 6.1.

Division of the equivalent rigid volumes by the area of the respective vacuum bag yielded the specific equivalent rigid volume $v_{A,eq}$ for each vacuum bag. The specific equivalent rigid volume was introduced as a means of accounting for vacuum bags of arbitrary size. Evaluation of the specific equivalent rigid volumes of all measured
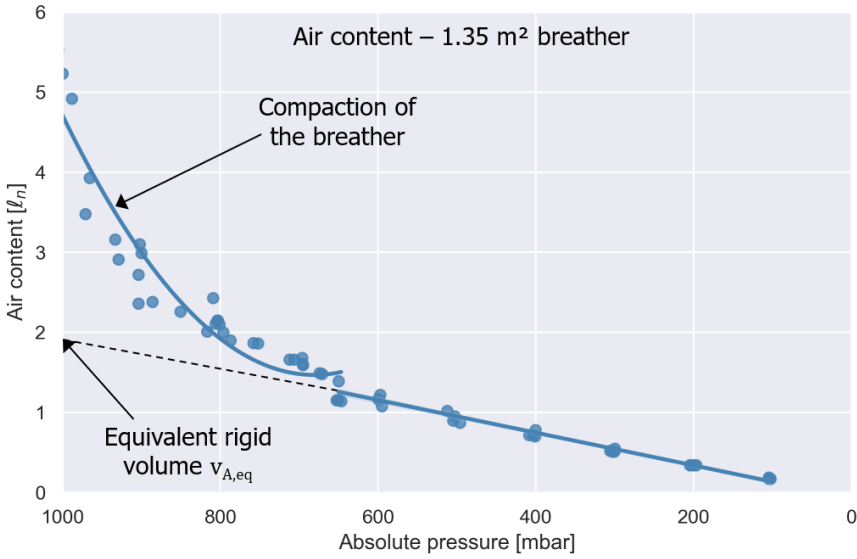
Figure 6.17: Vacuum bag air content throughout evacuation process measured at a $1.35\ m^2$ vacuum bag with Ultraweave 1332 breather
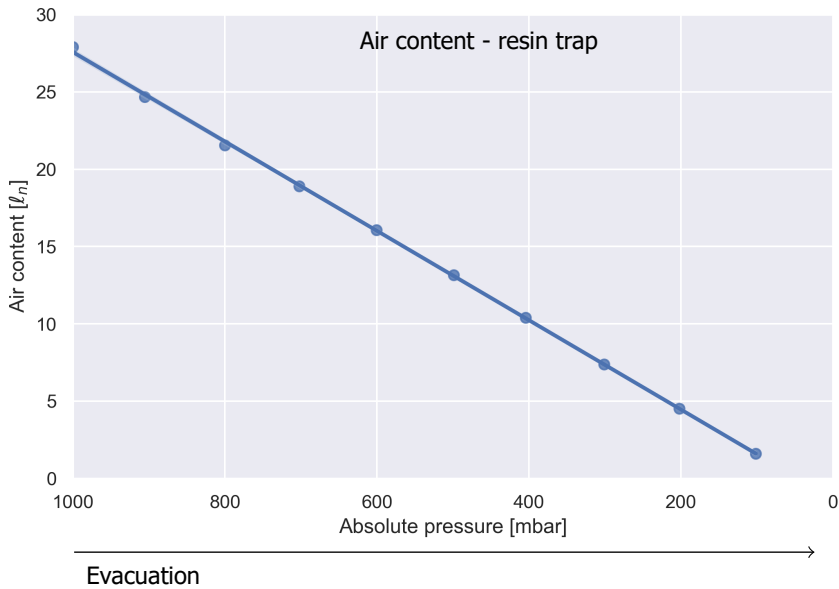


Figure 6.18: Resin trap, or rigid container air content throughout evacuation process

vacuum bags yielded an average of $1.3\ \ell_n$ per square meter of Ultraweave 1332 breather.

$$\bar{v}_{A,eq} = \frac{1}{5} \sum_{i=1}^{5} v_{A,eq,i} = 1.3 \frac{\ell_n}{m^2} \tag{6.8}$$

follows, that a vacuum bag with Ultraweave 1332 breather has a volume of $1.3\ \ell_n$ for every square meter of breather inside the vacuum bag. For different breather types, this specific equivalent rigid volume needs to experimentally evaluated.

Table 6.1: Equivalent rigid volumes measured at different sized vacuum bags with Ultraweave 1332 breather

| $i$ | $A\ [m^2]$ | $V_{A,eq}\ [\ell_n]$ | $v_{A,eq}\ [\ell_n/m^2]$ |
|---|---|---|---|
| 1 | 4.80 | 6.45 | 1.34 |
| 2 | 3.24 | 3.98 | 1.23 |
| 3 | 2.12 | 2.47 | 1.17 |
| 4 | 1.35 | 1.86 | 1.38 |
| 5 | 0.56 | 0.76 | 1.36 |

**6**

Here, too, an accuracy of $\pm\ 10\%$ below an absolute pressure of $600\ mbar$ can be achieved under special conditions:

- Consideration of remaining volumetric flow rate for small leakages during evacuation

- Prevention of pressure gradient formation in large vacuum bags by using vacuum channels or flow aids

No influence of the vacuum bag size on the functionality of the pressure increase model can be detected, with the exception of small vacuum bags with large leaks. The rapid aeration does not allow the formation of a linear pressure rise in the available measurement resolution and the pressure increase model is not applicable. The position of a leak in a vacuum bag does not affect the functionality of the model.

The results show that the volumetric flow rate measurement is a valid replacement of the commonly used pressure increase test. The current part specification for the acceptable pressure increase over a certain period of time can be converted into an acceptable volumetric flow rate. By measuring the flow rate during evacuation, it can be checked whether the pressure inside the vacuum bag would exceed the allowable pressure threshold. With this model, all sizes and shapes of vacuum bags are covered, if specific equivalent rigid volumes are used. For serial production it is advisable to measure the actual equivalent rigid volume of the part to be tested with a volumetric flow meter totaliser, like performed with the Ultraweave 1332 breather.

**Localisation of leakages**   It is observed, that the volumetric flow rate caused by
a leakage is divided among the three vacuum connections in a distinct pattern. As
seen in Figure 6.19 in a triangular setup, the distribution is related to the respective
distance of leakage to the vacuum ports. The leakage size has no influence on the
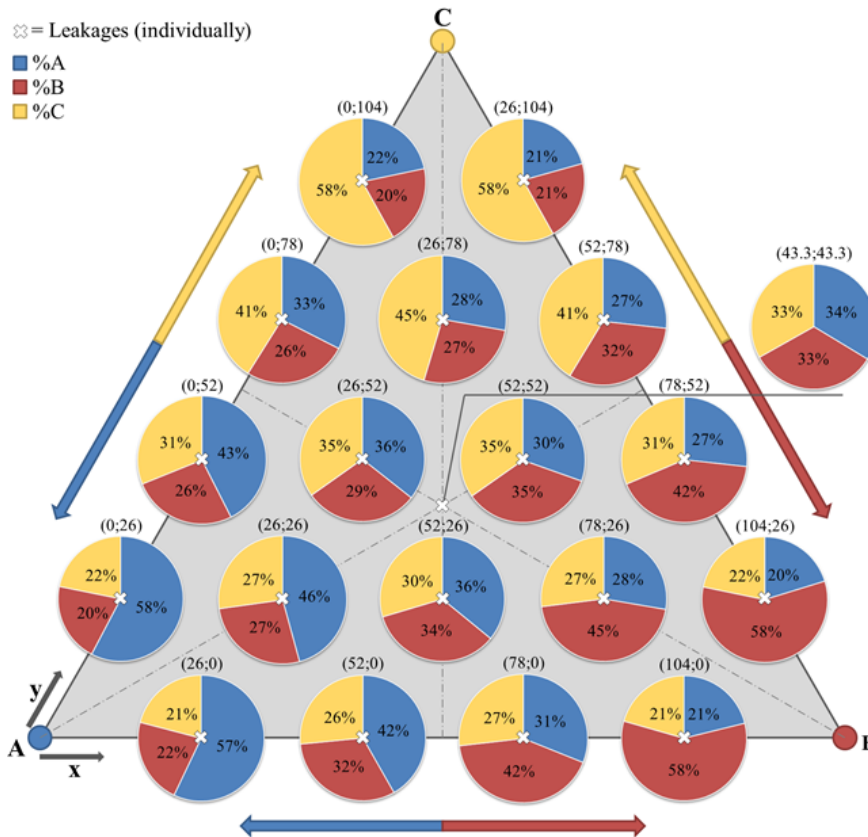resulting pattern, as the flow rate fraction stays the same and only the total value
changes.



Figure 6.19: Distribution of volumetric flow rate fractions for the three vacuum ports A,B and C for a
single $\varnothing_n$ 0.8 mm leakage at different locations (x;y)

   All experiments on the triangular vacuum bag setup with different hypodermic
needle sizes show the same following regularities:

1. The closer a leakage is introduced to a vacuum port, the higher is the per-
   centage of total flow that was aspirated by the associated vacuum line.

2. The volumetric flow rate of a leakage introduced at the centre of the triangle
   split evenly among all three vacuum lines.

3. For rotation in increments of $120°$ around the centre position, coinciding leakage positions show equivalent distribution of volumetric flow rate.

4. For leakages that are introduced at the same distance around separate vacuum ports, the distribution of volumetric flow rate is observed to be equivalent.

5. For leakages that are introduced at the same distance around separate vacuum ports, the distribution of volumetric flow rate is observed to be equivalent.

6. When shifting a leakage on a straight line between two vacuum ports, the share of the first vacuum line decreases in favour of the second vacuum line's share. The share of the third vacuum line stays constant for leakages on the same radius around the associated vacuum port.

7. Shifting a leakage away from a vacuum port along the angle bisector, results in a decreased share of volumetric flow rate for that vacuum. The remaining volumetric flow rate is evenly split among the two vacuum ports which do not lie on the angle bisector.

The findings from the square experiment, shown in Figure 6.20, correlate with the findings of the triangular setup and are stated in the following:

1. The distribution of the airflow is equal at the centre, when the flow meters are equidistant from the leakage.

2. Along the diagonal, the flow is evenly distributed to the vacuum ports located next to the dominant flow meter.

3. Along the central horizontal and vertical line, the flow is distributed equally to a set of two flow meters exactly opposite to one another.

4. At any point of the vacuum bag, the principle of localisation fulfils the requirement to identify and locate the reduced search area.

5. When a random leakage point is flipped or rotated on the board with respect to the data collected based on the current orientation, the new data coincides with the flipped or rotated data. This stands true because of the symmetric nature of the board and current arrangement of the flow meters on the vacuum bag.

The numerical regression from Equation 6.7 resulted in the relation shown in Equation (6.9).

$$VFR_{fraction} = 0.497672 - 0.000254 \cdot r + \frac{13.93866}{r} \tag{6.9}$$

Where $r$ is the distance between leakage and a particular vacuum port in $mm$ and VFR$_{fraction}$ is the fraction of the total VFR flowing through that vacuum port.
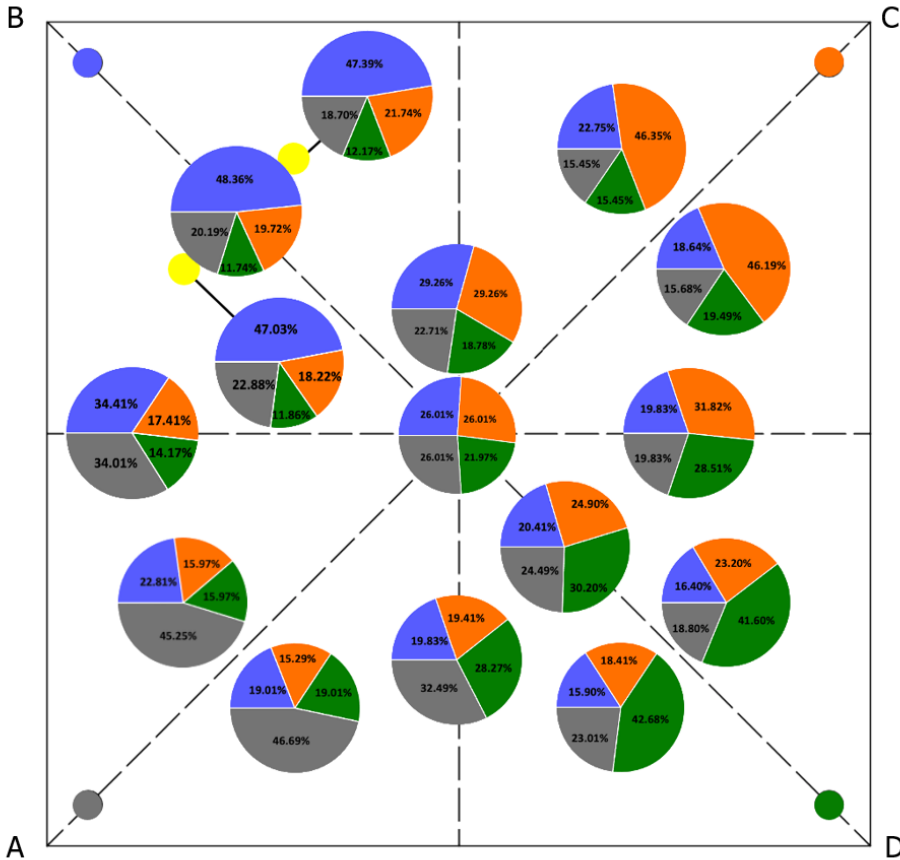
Figure 6.20: Distribution of volumetric flow rate for a single $\varnothing_n$ 0.6 mm leakage at different locations in a sqaure vacuum setup with four vacuum lines

The regression function is visualised in 6.21 compared to the data for the square vacuum bag. As 300 experiments have been carried out, and four vacuum connections have been used this results in 400 data points. It can be seen, that especially with increasing distance between leakage and vacuum port and decreasing fractional VFR the noise in the measurement data increases.

Predictions for three general cases are presented in Appendix A Figure A.2. In the first case, shown in Figure A.2a, the method is able to predict the leakage position around the centre with reasonable accuracy. In Figure A.2b, a case is depicted where the leakage is on the boundary and the prediction is less accurate. In the third case, the leakage is located towards the boundary but not in the immediate vicinity, as can be seen in Figure A.2c. The accuracy of the prediction is in between the accuracies for the two previously mentioned cases. In general, the closer the
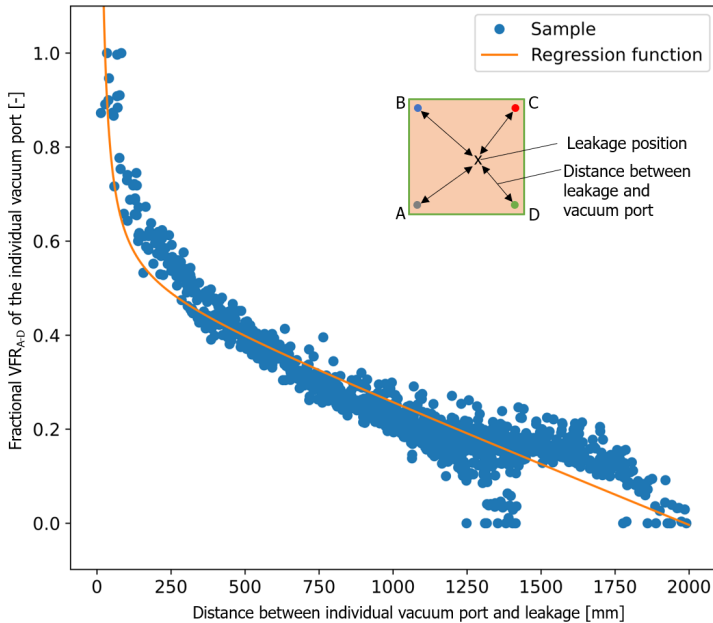
Figure 6.21: The image shows the same distribution of data points related to one-leakage experiments in the square vacuum bag as in 6.10 together with the regressor function found (Equation 6.9), orange line. The found regressor function approximates the distribution of the points better for middle range distances rather than for extremes (both large and small distances)

leakage is located to the boundary, the more difficult it is for the method to accurately predict the leakage location. The numerical regression method was based on single-leakage cases only. Therefore, this method is not able to capture the complexity that occurs when multiple leakages with varying diameters are present. Newton's method converges fairly well towards the actual leakage position when the leakage is not near one of the vacuum ports. Whenever the leakage is located close to a vacuum port, Newton's method has the tendency to diverge. Hence, the leakage is assumed and predicted to be in vicinity of the vacuum port with the highest fractional VFR, whenever the method diverges. On assessment, this assumption yields desirable results. 6.22 shows the distribution of the error between the prediction and the actual location.

In case there is only one leakage in the vacuum structure, both localisation approaches, the partitioning approach presented in Subsection 6.2.3 as well as the regression and multilateration approach work very well and can reliably limit the affected area. However, if there are several leaks in the vacuum assembly, this localisation is only partially successful. The VFR of the individual leaks at the individual vacuum connections add up and an incorrect position is indicated. This is particularly the case if the leakages are of a similar size. If one of the two leaks is significantly larger, the prediction of the position will point slightly more in the
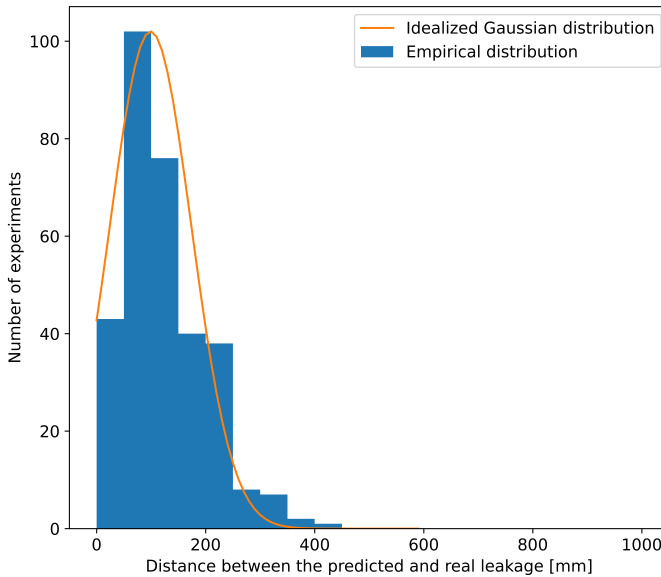
Figure 6.22: Distribution of error between experiment and leakage position prediction determined by the numerical regression Equation 6.9 and mutilateration method, using the VFR from the experiments (blue histogram). In the great majority of cases, the value of the error is lower than $200\ mm$

direction of that leak. Nevertheless, in the presence of multiple leaks, it becomes rather complex to rely on the presented approach since for any combination of flow ratios with respect to the flow meters, a single leak with a definite size can be represented on the vacuum bag.

To refine the localisation with multilateration, further trials are required, especially for geometries with irregular distribution of flow meter. Nevertheless, combined with the partitioning approach, it can be used to further define the position of the leakage in a previously narrowed down area. Once a section with a potential leakage position has been identified, the multilateration approach can be used to obtain a radius around the nearest vacuum port. In this way, the possible leak position is reduced to a radius segment limited by the section borders.

A novel approach for leakage localisation utilising machine learning is discussed in Chapter 7. The machine learning approach bears the same goal i.e. to localise a leak but into a much smaller area on a vacuum bag and further find a concept to detect multiple leaks. Flow distribution data over a time span is acquired to use the concept of deep learning techniques, to teach the machine to detect the area where the leak(s) are possibly located.

## 6.4. Discussion of hypotheses addressed

As discussed at the beginning, this chapter aims to refer to the first two hypotheses.

Referring to **Hypothesis 3** *"There is a flow-dependent criterion for the exact quantification and evaluation of the airtightness."* the aim is to replace the pressure increase testing with a new method that can determine the tightness of the vacuum bag independently of the component size and the measurement location. The performed tests show that the volumetric flow rate measurement is able to meet these conditions. The equilibrium flow rate reading of one or multiple measurement points combined can give an exact information about the leakage area inside the vacuum bag. The component size and measurement location has no significant influence on the final volumetric flow rate. The tests also showed that the measurement can take place during the evacuation of the part and will need no further time to perform a specific test procedure, which may shorten production times.

Furthermore, a correlation of constant volumetric flow rate and pressure increase inside a rigid container is found with Equation 6.5. It was furthermore found that below an absolute pressure of $600\ mbar$, vacuum bags that were constructed with an Ultraweave 1332 breather behave like a rigid container that has a volume of $1.3\ \ell_n/m^2$ of breather inside the vacuum bag. Equation 6.5 enables the conversion of the given pressure increase limits of existing specifications into volumetric flow rate thresholds and vice versa.

The results show that volumetric flow meters are not only able to detect the presence of a leakage in a vacuum bag, but can also provide information on the severity and location of the leakage. Hence, it is proven that there is a flow-dependent criterion for the exact quantification and evaluation of the airtightness of vacuum bags.

Referring to **Hypothesis 4** *"With the help of a two-step process, it is possible to determine the exact location of the leak and thus achieve a significant time saving in leak detection (>30%)."*, originally, volume flow measurement is intended exclusively for the identification of defective areas of a vacuum bag in preparation for thermographic leak detection. However, further investigations show that the interpretation of volume flow measurements offers additional application possibilities. In addition to leakage localisation, volume flow meters have proven to be useful as a replacement for the usual pressure increase test after appropriate preparatory work.

In combination with infrared thermography, a complete leak location process can be realised, as shown in Figure 6.23.
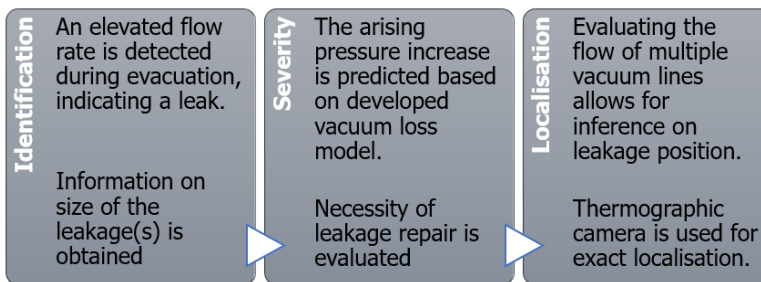


Figure 6.23: Conceivable application of volumetric flow measurement in automated leakage detection

The implementation of volumetric flow meters for leakage detection is expected to offer a high savings potential. As the flow rate is measured directly during the evacuation process, the time for the pressure increase test can be eliminated. The process effort for leak detection and localisation can be reduced, whereby the latter can even be skipped depending on the assessed severity of the leakage. In combination with an evaluation algorithm and thermographic leakage localisation, volume flow measurement is a promising sensor system for fully automatic leakage detection.

By interlinking the detection and localisation methods in the two-stage leakage detection, the process time for the leakage detection of vacuum bagas can be reduced from about $5$ hours to only $1$ hour conservatively calculated, see Figure 6.3. This results in a process time reduction of up to $80\%$ and proves that hypothesis four holds true.

**6**

# References

[1] A. Haschenburger and C. Heim, *Two-stage leak detection in vacuum bags for the production of fibre-reinforced composite components,* CEAS Aeronautical Journal **10**, 885 (2019).

[2] A. Haschenburger, N. Menke, and J. Stüve, *Sensor-based leakage detection in vacuum bagging,* The International Journal of Advanced Manufacturing Technology **116**, 2413 (2021).

[3] A. Haschenburger and N. Menke, *Sensor based analysis and identification of leakages in vacuum bagging for high performance composite components,* in *SAMPE Europe Conference* (2018).

[4] A. I. Haschenburger, L. Onorato, M. S. Sujahudeen, D. S. Taraczky, A. Osis, A. R. S. Bracke, M. D. Byelov, F. I. Vermeulen, and E. H. Q. Oosthoek, *Computational methods for leakage localisation in a vacuum bag using volumetric flow rate measurements,* Production Engineering (2022), 10.1007/s11740-022-01129-8.

[5] B. Gu and X. Huang, *Investigation of leak detection method by means of measuring the pressure increment in vacuum,* Vacuum **80**, 996 (2006).

[6] S. Schelkshorn, *Multisensorielle Positionsbestimmung aus Dopplersignalen* (Logos Verlag Berlin GmbH, 2008).

[7] B. Polyak, *Newton's method and its use in optimization,* European Journal of Operational Research **181**, 1086 (2007).

[8] H. Uçan, D. Akin, and A. Tripmaker, *Einsatzmöglichkeiten von Thermografiemessungen im Autoklaven zur Prozessüberwachung und Qualitätskontrolle,* in *DLRK – Deutscher Luft- und Raumfahrtkongress* (2015).

[9] Airtech Europe Sarl, *Ultraweave® 1332 Data Sheet – Heavy weight nylon breather / bleeder* (2018).

# 7

# Utilisation of machine learning for automated leakage detection

*In contrast to knowledge based approaches like trilateration, deep learning approaches do not require hand-crafted rules to predict even multiple leakage positions from flow measurements. However, adapting the parameters of a data driven model to an intended task requires the availability of a sufficiently large amount of training data of a certain quality. In this chapter an integrated approach covering data acquisition, data augmentation, architecture design of the neural network as well as model training and evaluation is presented. It is shown that neural networks can achieve high speed leakage detection and localisation.*

---

## 7.1. Introduction

Within this chapter the applicability of deep learning techniques [2] to the task of leakage localisation based on multiple volumetric flow rates is investigated. The aim is to train machine learning models to determine the position of one or multiple leakages in a square vacuum bag with four volumetric flow rate sensors that has already been presented in Chapter 6. A total number of 1000 different random leakage positions and combinations of leakage diameter and number inside the vacuum bag is generated and the flow rate measurement carried out experimentally. Within this experiments, three different leakage sizes and a maximum number of three leakages inside the part is examined. The investigation of the volumetric flow rate measurements includes the evaluation of the equilibrium data as well as the time series data during the evacuation of the vacuum assembly. The experimental workpiece and the data acquisition process are described in Subsection 7.2.1. Afterwards, a symmetry-based approach to augment the real data with additional synthetic examples in Subsection 7.2.2 is introduced and the data preprocessing is described in Subsection 7.2.3. Utilised neural network architectures and the training procedure are presented in Subsection 7.2.4. Evaluation metrics and experimental variables are subject of Subsections 7.2.7 and 7.2.6, respectively. Experimental results are reported subsequently in Section 7.3.

## 7.2. Methodology

In the following the training data acquisition, the data augmentation and preprocessing as well as the model architectures and training procedure are presented.

### 7.2.1. Training data acquisition

A flat panel of $1500 \times 1500\ mm$ has been selected for the training data acquisition, the same as used for the experiments in Chapter 6. Figure 7.1 shows the experimental setup before and during data recording.
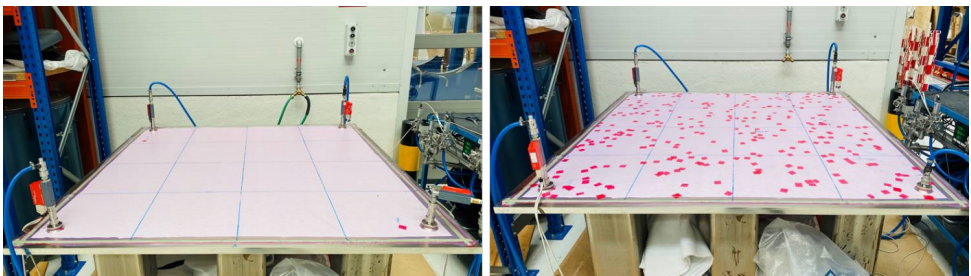


Figure 7.1: Experimental set up of the vacuum bag before and during the data recording. The red dots are adhesive tape to cover up the inserted leakages for the training data recording.

For each experimental set-up that has been generated, first of all a random integer between 0 and 3 was drawn, which represented the number of leaks that have been placed in a previously airtight vacuum bag. The respective probabilities were

0.1 for no leakage and 0.3 for each remaining case so that in the end there were approximately 100 leakage-free setups as well as roughly 300 setups for each case of one, two or three introduced leakages. Afterwards, one of $4 \times 4$ quadratic subregions for each leakage has been chosen, ensuring that none of the subregions contained more than one leakage. Finally, random horizontal and vertical coordinates inside each chosen subregion were generated and randomly one of three possible needle diameters (0.3, 0.45 or 0.6 $mm$) was assigned to each leakage. An exemplary setup is displayed in Figure 7.2.
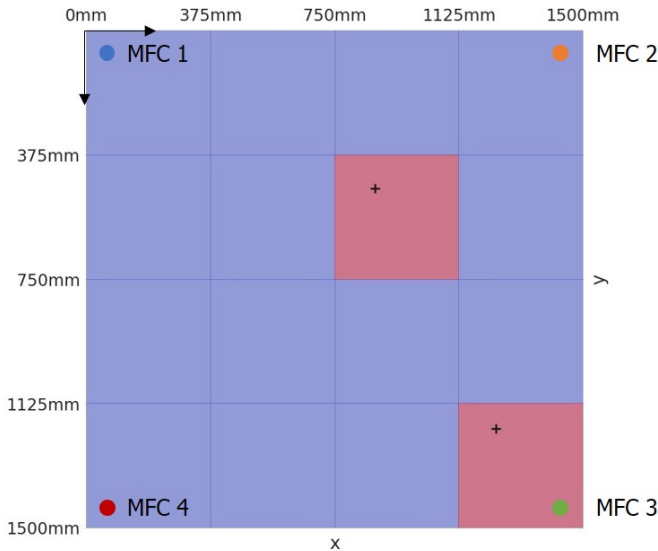


Figure 7.2: Exemplary experimental setup with two leakages, one leakage located at $(x, y)$ = (872.3 mm, 475.0 mm) with needle diameter 0.45 mm and another one at $(x, y)$ = (1237.6 mm, 1199.8 mm) with needle diameter 0.6 mm, indicated with a +

Before each experimental run, the vacuum bag has been ventilated and leakages were placed in the specified positions by means of hypodermic needles, as described in Chapter 6. The recording of a sample started with the evacuation of the bag and ended a few seconds after the equilibrium for all four flow sensors was reached. Recorded flow rates associated with the setup from Figure 7.2 are displayed in Figure 7.3. After each run, all introduced leakages have been patched to restore airtightness of the vacuum bag.

### 7.2.2. Data augmentation

To increase the amount of the available training data synthetically, an approach that exploits the symmetric placement of the four vacuum connections at each corner of the quadratic workpiece has been used. Figures 7.4a and 7.4f illustrate the subset of the original experimental set-ups including examples with exactly one leakage. Data augmentation has been applied only to the training data in Figure 7.4a while the test data in Figure 7.4f will contain only real examples further on.
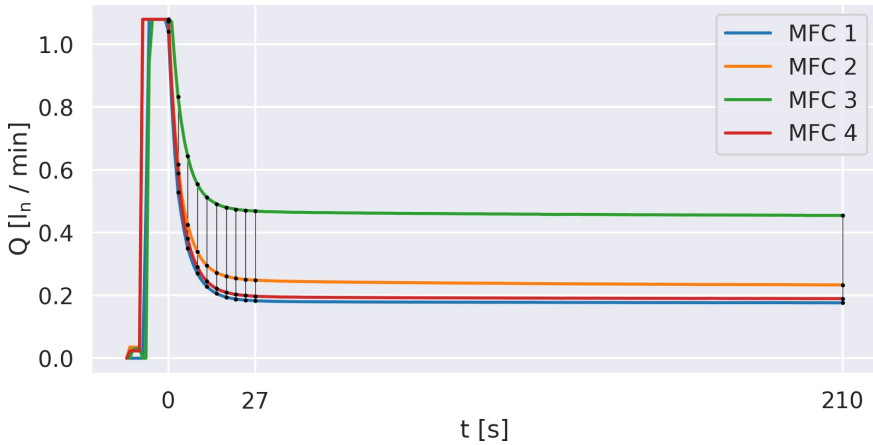
Figure 7.3: Exemplary recorded flow rates (input data) showing the equilibrium flow data at $t = 210\ s$ used as input data for the equilibrium flow rate numerical experiments and the extensions for the time series data at $t = 0,\ 3, \ldots,\ 24,\ 27\ s$

As a first step, all experimental setups from the training data were rotated clockwise by $90$ degrees. Due to the inherent symmetry of the vacuum connections it is clear that a rotated leakage position should cause flow rate measurements that resemble an accordingly transposed version of the original flow rate measurements, up to noise. Hence, there was no need for a new physical measurement but the data has been augmented synthetically by means of a few simple numerical calculations. Figure 7.4b shows all original experimental setups together with their $90$ degree rotated versions. The same procedure has been applied twice more by rotating all original setups by $180$ and $270$ degrees. The entire training data after two and three subsequent $90$ degree rotations is illustrated in Figures 7.4c and 7.4d, respectively. Finally, all setups from Figure 7.4d have been flipped once (horizontally or vertically both yield identical results after three preceding rotations) and a data set eight times larger than the original was created.

Figure 7.4 is restricted to examples with at most one leakage for illustrative purposes. However, exactly the same sequence of augmentation techniques has been applied to all examples with more than one up to the maximum of three leakage. After the conventional split [3] into training and test data ($90\%$ vs. $10\%$ of the $1000$ original recordings) a training set consisting of $900$ original examples was available. These were augmented in the described way to obtain a total of $7200$ training examples.

### 7.2.3. Data preprocessing

As stated above, the goal is to train deep learning models for leakage localisation. In this thesis, *Fully Connected Neural Networks* (FCNNs) were considered which are basically parametrised mappings $f_{\boldsymbol{\theta}} : \mathbb{R}^{n_0} \to \mathbb{R}^{n_L}$. Thus, the input dimension $n_0$ and the assembly of feature vectors $\boldsymbol{x} \in \mathbb{R}^{n_0}$ from recorded flow rates as well as

(a) original training data

(b) + 1 rotation

(c) + 2 rotations

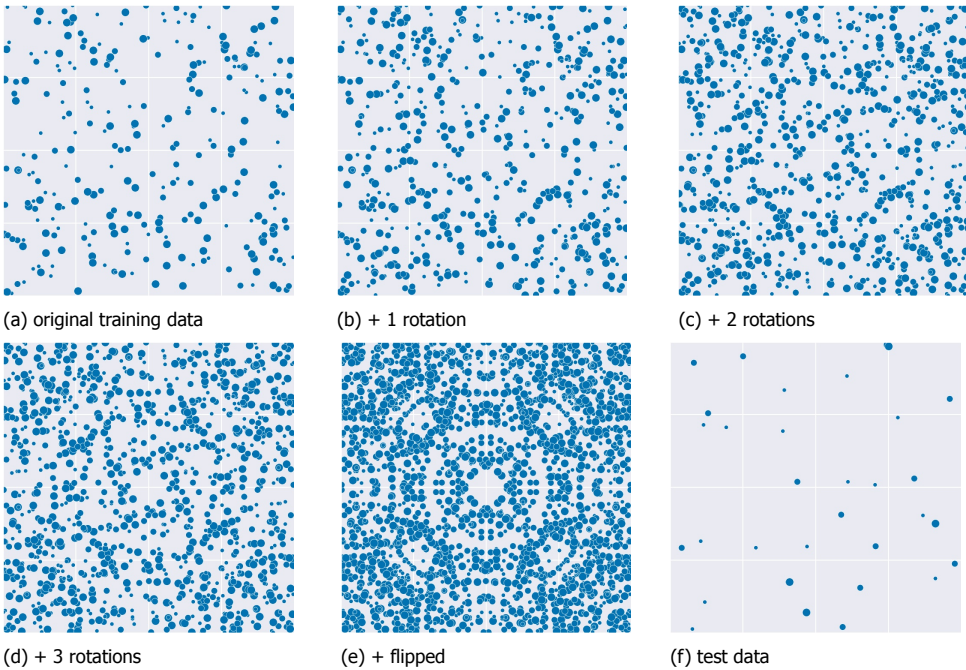(d) + 3 rotations

(e) + flipped

(f) test data

Figure 7.4: Augmented training data and test data using the example of single-leakage samples. The blue dots indicate the individual leakage positions and the different different sizes correspond to the three different diameters used in the experiments.

the output dimension $n_L$ and the assembly of label vectors $\boldsymbol{y} \in \mathbb{R}^{n_L}$ from leakage positions need to be specified first.

Two different types of input data were distinguished that have both been considered in our numerical experiments: First, only flow rates in the very last time step of each record (equilibrium flow rates) have been considered. The corresponding data in Figure 7.3 are the four points in the flow rate measurements at the respective location at $t = 210$. Thus, the input dimension in this case was $n_0 = 4$. Second, the equilibrium values have been extended by flow rates from ten additional time steps at the beginning of each time series every 3 seconds, namely $t = 0, \ 3, ..., \ 24, \ 27 \ s$ as also depicted in Figure 7.3. Consequently, the input dimension in this case was $n_0 = 4 \cdot 11 = 44$. Note that $t = 0$ was consistently chosen as the time step where the first flow rate dropped from the maximum flow level (approximately $1.08 \ \ell_n/min$) after opening of the valves at the beginning of each evacuation.

Regarding the output data, the situation was slightly complicated by the fact that the number of leakages $n_{leak}$ in the vacuum bag is unknown when the readily trained network is supposed to make predictions on unseen data. In case it is aimed to predict exact horizontal and vertical positions per leak, the model needed to output two coordinates $x/y$ per leakage. Still assuming a maximum number of three leakages $n_{leak} = 3$ inside the vacuum bag, it would hence not be clear

whether the output dimension $n_L$ should be 0, 2, 4 or 6, as $n_L = 2n_{leak}$. A remedy might be the introduction of objectness scores [4]. The idea of the objectness score is that you do not know the exact number of leaks and therefore keep a certain number in stock and create dummies. Each dummy is then assigned a probability, the objectness, which has a value between 0 and 1, where 0 means there is no leakage and 1 means there is. Although this constitutes a possible workaround to account for an unknown number of leakages, a different approach has been chosen here. Namely, the regression problem (predicting coordinates) was turned into a classification problem. To that end, the experimental workpiece has been subdivided into a number of $k^2$ quadratic subregions and a label was assigned to each single subregion depending on whether at least one leakage has been included (label 1) or not (label 0). As a consequence, a fixed output dimension $n_L = k^2$ was obtained that does not depend on the number of leakages $n_{leak}$ but only on an a priori fixed lattice fineness $k$. Exemplary labels associated with the example from Figures 7.2 and 7.3 are displayed in Figure 7.5.
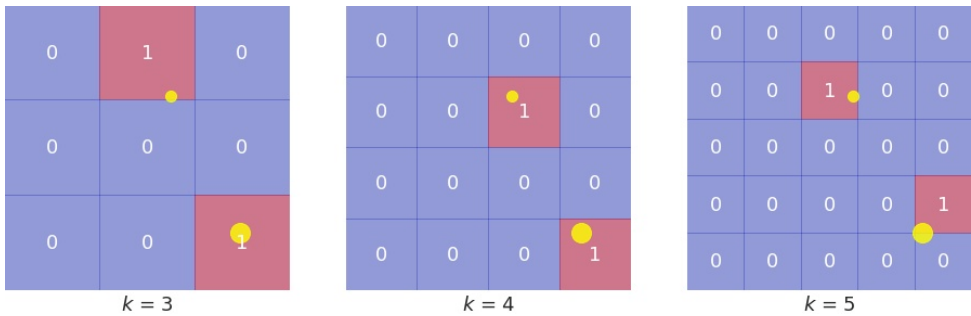


Figure 7.5: Examples of subregion classification approach (output data). The leakages are shown as yellow dots and the workpiece was divided in 9, 16 and 25 subregions respectively. The output label 0 or 1 indicates the presence of a leakage in the corresponding subregion.

## 7.2.4. Model architectures and training

From here on, the aim is to investigate the suitability of FCNNs like described in Section 2.6 for predicting leakage-prone areas from volumetric flow rates, especially in the presence of multiple leakages.

In the subsequent experiments, a constant depth $L = 6$ of the FCNN has been used, i.e., all models feature an input layer ($\ell = 0$), five so-called *hidden layers* ($\ell = 1, \ldots, 5$) as well as an output layer ($\ell = 6$). Depending on whether only equilibrium flow rates or also additional data from earlier time steps (recall Figure 7.3) were used, the *width* of the input layer was either $n_0 = 4$ or $n_0 = 44$. The widths of the hidden layers were $n_1 = \cdots = n_5 = 1024$ throughout, and the width of the output layer was $n_6 = k^2$ depending on the lattice fineness (recall Figure 7.5). These values were fixed and other factors varied. This FCNN is large enough to cope with the complexity of the task and rather oversized which bears the risk of over fitting. This risk was counteracted with the help of regularisation. In all hidden layers, the SELU activation function has been used, see Section 2.6 and Equation 2.20. In the

output layer the logistic (or sigmoid) function, see Equation 2.21 has been used. The logistic function is particularly well-suited to this specific application because it maps to the range $(0, 1)$ and hence, each output $f_{\boldsymbol{\theta}}(\boldsymbol{x})_j$ can directly be interpreted as the probability for the presence of a leakage in the respective subregion.

The entirety of weight matrices and bias vectors in Equation 2.19 constitute the parameters of the networks that shall be tweaked, i.e.,

$$\boldsymbol{\theta} := (\boldsymbol{W}^{[1]}, \boldsymbol{b}^{[1]}, \dots, \boldsymbol{W}^{[L]}, \boldsymbol{b}^{[L]}) . \tag{7.1}$$

To that end, an objective function consisting of two terms is minimised:

$$\mathcal{L}(\boldsymbol{\theta}) := \underbrace{\frac{1}{m_e} \sum_{i=1}^{m_e} \ell(\boldsymbol{y}^{(i)}, \hat{\boldsymbol{y}}^{(i)})}_{\text{data fit}} + \underbrace{\frac{\rho_{reg}}{m_e} \sum_{i=1}^{m_e} \sum_{j=1}^{k^2} |\hat{y}_j^{(i)}|}_{\text{regularisation}} \tag{7.2}$$

*First*, there is a term to ensure a good fit of the resulting model to the data. Therein, $\hat{\boldsymbol{y}}^{(i)} = f_{\boldsymbol{\theta}}(\boldsymbol{x}^{(i)})$ denotes a model prediction and each tuple $(\boldsymbol{x}^{(i)}, \boldsymbol{y}^{(i)})$ of flow rates and associated ground truth labels comes from an $m_e$-element subset of our training data. $10\%$ of the training data has been reserved for validation purposes (see Subsection 7.2.7) so that $m_e = 6480$ out of $7200$ examples remain for the minimisation of Equation 7.2. The *loss function* $\ell$ can be considered a distance function that would return a small positive value in case $\hat{\boldsymbol{y}}^{(i)} \approx \boldsymbol{y}^{(i)}$ and that would vice versa penalise larger discrepancies between model predictions and ground truths by returning respectively larger positive values.

*Second*, the objective function includes a regularisation term that is weighted by a regularisation strength $\rho_{reg}$. In machine learning, regularisation can be defined as the collection of strategies that are designed to reduce the test error, i.e., that cause models to perform well not only on training data but especially on new and unseen inputs. Here, the $\ell_1$-norm of the model predictions

$$\|\hat{\boldsymbol{y}}^{(i)}\|_1 = \sum_{j=1}^{k^2} |\hat{y}_j^{(i)}| \tag{7.3}$$

is used to incorporate a specific kind of prior knowledge into the model. Namely, it is known that only a small fraction of ground truth labels $y_j^{(i)}$ is equal to one because in each case, most quadratic subregions of the workpiece will not contain a leakage (see, e.g., Figure 7.5). This knowledge has been be integrated in terms of the $\ell_1$-norm as the latter is well-known to induce sparsity (see, e.g., [3]). In the end, penalising the network outputs in this way imposed of course an indirect penalty on the model parameters.

It remains to specify the loss function used in Equation 7.2. A *weighted binary cross-entropy loss* [5] is used where the discrepancy $\ell(\boldsymbol{y}^{(i)}, \hat{\boldsymbol{y}}^{(i)})$ is equal to

$$\sum_{j=1}^{k^2} -w_p y_j^{(i)} \ln(\hat{y}_j^{(i)}) - w_n (1 - y_j^{(i)}) \ln(1 - \hat{y}_j^{(i)}) . \tag{7.4}$$

The weights $w_p$ and $w_n$ shall account for the fact that the label $1$ (leakage) is under-represented in the training data and to force the models to pay more attention to this class during training. To understand that, recall from Subsection 7.2.1 that among the original data recordings, there were $100$ examples without leakage as well as $300$ examples for each case of one, two and three leakages. Hence, if a lattice fineness $k$ was fixed, then the probability $p_k$ for a particular subregion of the workpiece (i.e., a cell on the lattice) to contain a leakage was

$$p_k = 0.1 \cdot 0 + 0.3 \cdot \frac{1}{k^2} + 0.3 \cdot \frac{2}{k^2} + 0.3 \cdot \frac{3}{k^2} = \frac{9}{5k^2} \ . \tag{7.5}$$

Consequently, this probability decreases when $k$ was increased. By using

$$w_n = \frac{9}{5k^2} \quad \text{and} \quad w_p = 1 - w_n \tag{7.6}$$

in Equation 7.4 models have been forced to pay more attention to the under-represented class during training. Vice versa, both weights were simply chosen equal to one in order to turn off class weighting.

### 7.2.5. Test data

As mentioned above, $10\%$ of the original recordings (i.e., $100$ examples) are used as test data whose purpose it has been to estimate the ability of trained models to generalise to new data. To that end, the $100$ test examples were chosen such that they constitute a preferably representative sample from the entire data. A specific discrete optimisation problem formulation and the solver Python MIP [6] has been used to determine a test set containing $4$ examples without leakage, $32$ examples containing $1$ leakage, $32$ examples containing $2$ leakages and $32$ examples containing $3$ leakages subject to the constraint that in each case, every square in a $4 \times 4$ subdivision of the workpiece contained an equal number of leakages. Figure 7.4f shows the resulting subset of the test data for the case of one leakage while Figure 7.6 shows the two remaining cases with two and three leakages per recording. Importantly, the test data have not been augmented with synthetic data because in the final analysis, the performance of the models should be reported only on real data.

### 7.2.6. Experimental variables

In the course of the numerical experiments FCNNs have been applied to the classification task of predicting leakage-prone areas from volumetric flow rates, see Section 2.6). While the network architecture was kept essentially fixed (depth $6$, width $1024$ in hidden layers, SELU activation in hidden layers, sigmoid output activation), the aim is to investigate the impact of the following factors on the predictive performance of the resulting models:

- Data augmentation (see Subsection 7.2.2)
- Time series data (see Subsection 7.2.3)
- Lattice Fineness (see Subsection 7.2.3)
- Regularisation (see Subsection 7.2.4)

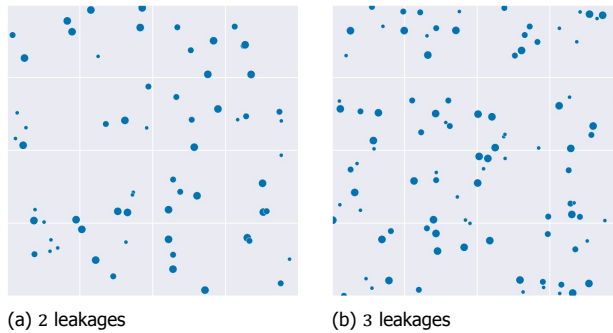(a) 2 leakages         (b) 3 leakages

Figure 7.6: Test data with 2 and 3 leakages per recording. The blue dots indicate the individual leakage positions and the different different sizes correspond to the three different diameters used in the experiments.

- Weighted loss (see Subsection 7.2.4)

Although it would have of course been possible to fine-tune the network architecture, use substantially different machine learning models (e.g. regression model, logistic regression or support vector machines), and make use of further techniques to potentially enhance the training procedure, within this thesis only one network architecture presented in Subsection 7.2.4 and the above-mentioned experimental variables have been used. In this way a differentiated view is possible and performance variations can be attributed as clearly as possible to single factors.

### 7.2.7. Evaluation metrics

The MAE, the precision, the recall and the F-score (see Section 2.6) have been used to assess and compare the performance of the different models with the variables presented in Subsection 7.2.6.

The purpose of the discussed metrics is manifold. *First* of all, as already mentioned in Subsection 7.2.4, 10% of the training data are reserved for validation purposes during training, i.e., these 10% are not directly used in the minimisation of Equation 7.2. Instead, the validation data are used to compute a weighted average of mean absolute error and precision/recall for different thresholds (the area under the so-called precision-recall curve to be exact) in regular intervals during training. The minimisation procedure for Equation 7.2 on the remaining training data is stopped as soon as this weighted average of metrics on the validation data stops improving. This technique shall prevent over-fitting of a model to the training data and is often referred to as early stopping. [3] *Second*, for each readily trained model, the F-score is evaluated on the union of training and validation data with respect to 1000 equally spaced thresholds between zero and one so as to fix one final threshold. *Third*, using this final threshold, the machine learing model is ultimately evaluated on unseen test data in terms of mean absolute error, precision, recall and F-score.

### 7.2.8. Experimental procedure

The aim of the performed experiments has been to isolate the impact of the experimental variables listed in Subsection 7.2.6 on the predictive performance of the model architecture introduced in Subsection 7.2.4 in terms of the metrics introduced in Subsection 7.2.7. All models were implemented, trained and evaluated using TensorFlow [7] and all experiments were conducted on a NVIDIA GeForce RTX 2080 Ti GPU. To accomplish the minimisation of the training loss Equation 7.2 the Adam optimiser [8] with standard settings in combination with *one-cycle* learning rate scheduling was used. The optimisation procedure was stopped after a maximum of $100$ epochs (i.e., passes of the optimiser through the training data), eventually interrupted prematurely due to early stopping (see Subsection 7.2.7). The training data was shuffled prior to each iteration and subdivided into batches of size $32$. Each configuration of experimental variables was applied repeatedly five times and the respective results were averaged in order to account for random effects at training time (random parameter initialisation and data shuffling).

## 7.3. Experimental results

In this Section the results of our numerical experiments are reported and discussed. Figure 7.7 illustrates the relation between ground truth, model prediction and hypothesis prediction. Figure 7.7a shows a ground truth, i.e., a randomly generated experimental setup established to generate flow rate measurements as described in Subsection 7.2.1. Note that Figures 7.2 and 7.3 refer to exactly this same setup. Now, Figure 7.7b shows the output $\hat{y} = f_\theta(x)$ of a readily trained neural network where the input $x$ is equal to the equilibrium flow rates depicted in Figure 7.3. Finally, Figure 7.7c shows the output of a hypothesis that results when an arbitrary threshold $0.1819 < \tau \le 0.2567$ is used. Here, the hypothesis prediction $\hat{h}$ features two TP, one FP, 13 *True Negative* (TN) and no FN.



(a) $y$    (b) $\hat{y}$    (c) $\hat{h}$
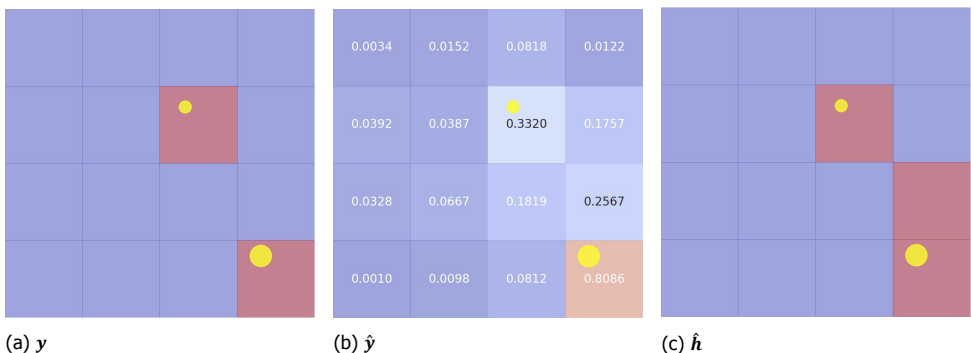
Figure 7.7: Exemplary comparison of ground truth (left), model prediction (middle, with annotated leakage probabilities) and hypothesis (right); the size of the yellow markers represents the size of the leakages that were introduced at the respective positions.

The overall results of the experiments are illustrated in Figures 7.8–7.11. Throughout, results for $k = 1, \dots, 8$ (lattice fineness) are plotted on the horizontal axis while

the value of a respective metric evaluated on the test data is plotted on the verti-
cal axis. The configuration of all remaining factors of variation can in each case be
seen from the title and the legend in the most right figure, respectively.
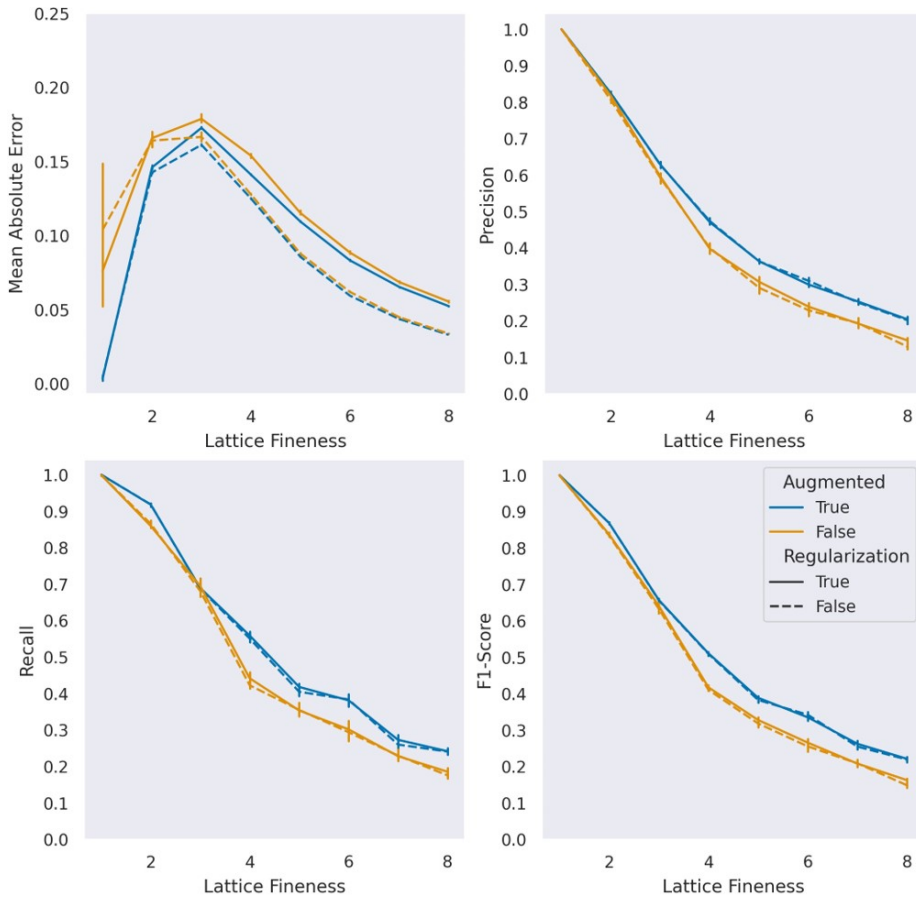


Figure 7.8: Impact of data augmentation and regularisation (equilibrium data, *Binary Cross-Entropy*
(BCE) loss, max. 3 leakages)

Figure 7.8 illustrates the impact of data augmentation and regularisation. Here,
two effects become apparent. First, data augmentation has a clear positive effect
in terms of all considered metrics. The mean performance gain depends on the
lattice fineness and ranges between $0.05\%$ ($k = 1$) and $9.34\%$ ($k = 8$) in terms of
the F1-score, and between $0.31\%$ ($k = 8$) and $7.27\%$ ($k = 1$) in terms of the mean
absolute error. Second, regularisation mostly decreases the mean absolute error
while its impact on the remaining metrics is negligible. The mean performance gain
(with data augmentation at the same time) ranges between $0.07\%$ ($k = 1$) and
$2.39\%$ ($k = 6$).
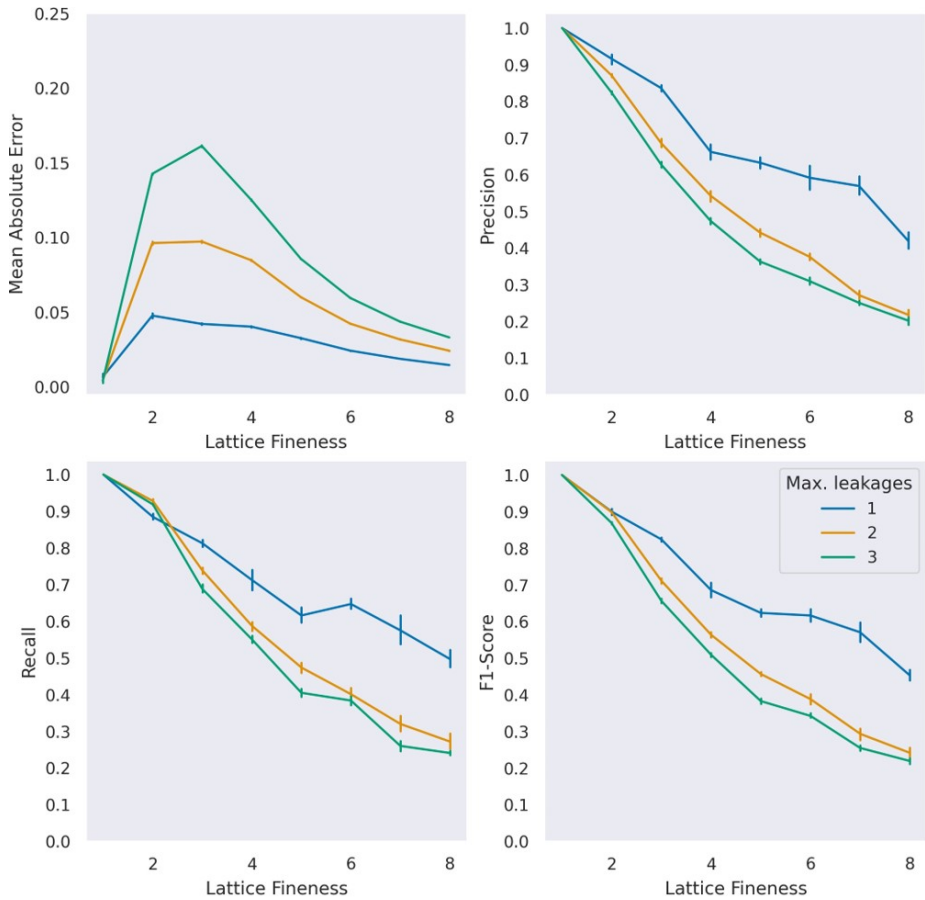
Figure 7.9: Impact of number of leakages (equilibrium data, BCE loss, with data augmentation and regularisation)

Figure 7.9 depicts the relation between model performance and number of leakages. In each case, the maximum number of leakages considered at training and testing time is the same. Hence, models that are evaluated on test data with maximally one leakage have also been trained on the subset of data with maximally one leakage, and so on. As might be expected, we can observe a drop in performance when the number of leakages is increased. Again, the magnitude of the gap between the respective curves depends on the lattice fineness. However, a look at the F1-score reveals that the performance loss is stronger between one and two leakages (up to 27.71% for $k = 7$) than between two and three leakages (maximally 7.39% for $k = 6$). The reason for this observation is the increases task complexity with more leakages. Even though an equal number of samples for each number of leakages has been taken, the possible location combinations increase exponential with increasing leakage number.
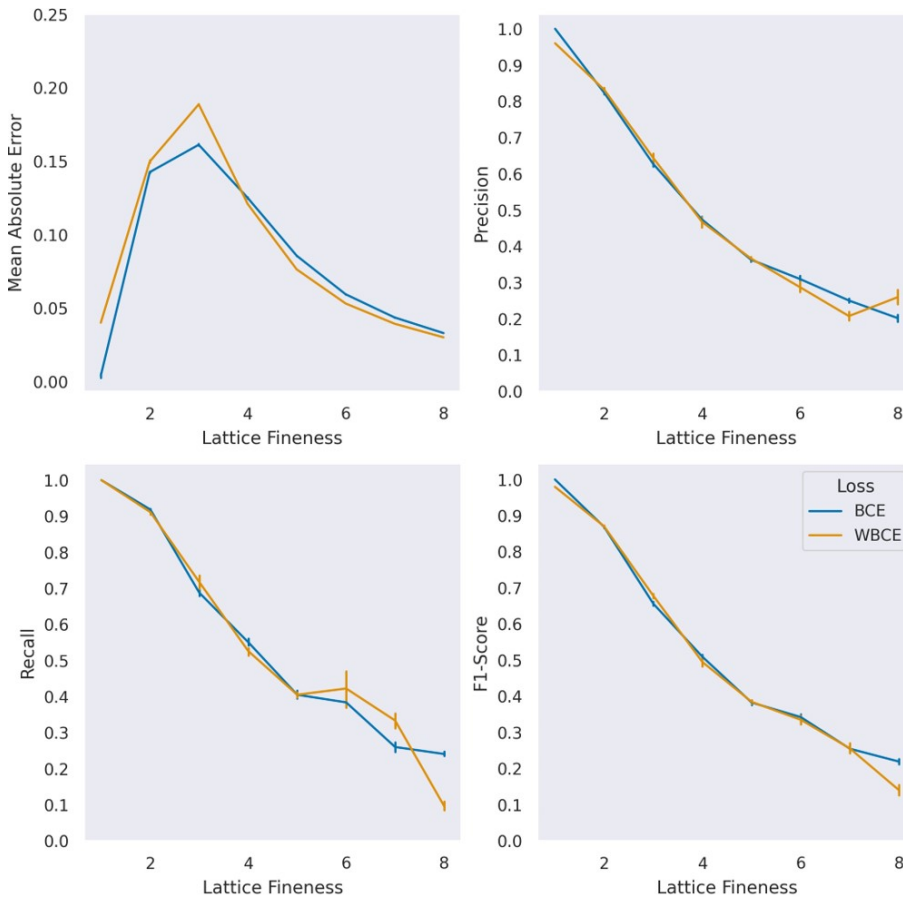
Figure 7.10: Impact of weighted loss (equilibrium data, with data augmentation and regularisation, max. 3 leakages)

Figure 7.10 illustrates the effect of using the *Weighted Binary Cross-Entropy* (WBCE) loss from Equation 7.4 instead of the standard BCE loss. The depicted results indicate that the use of a weighted loss function is slightly beneficial in terms of the mean absolute error when the lattice fineness is small. However, a significant performance gain due to the use of a weighted loss function cannot be claimed in general.

Finally, Figure 7.11 illustrates the impact of using flow rates from early time steps (see Figure 7.3) as additional input data. In short, it can be seen that the additional inputs enhanced nor the mean absolute error neither the F-score in our experiments. However, this holds true for this specific setting with a fixed network architecture and training algorithm. Generally, additional inputs of the same quality do at least not decrease the information content in the data, although they can potentially complicate training. Hence, the results cannot rule out that flow rate
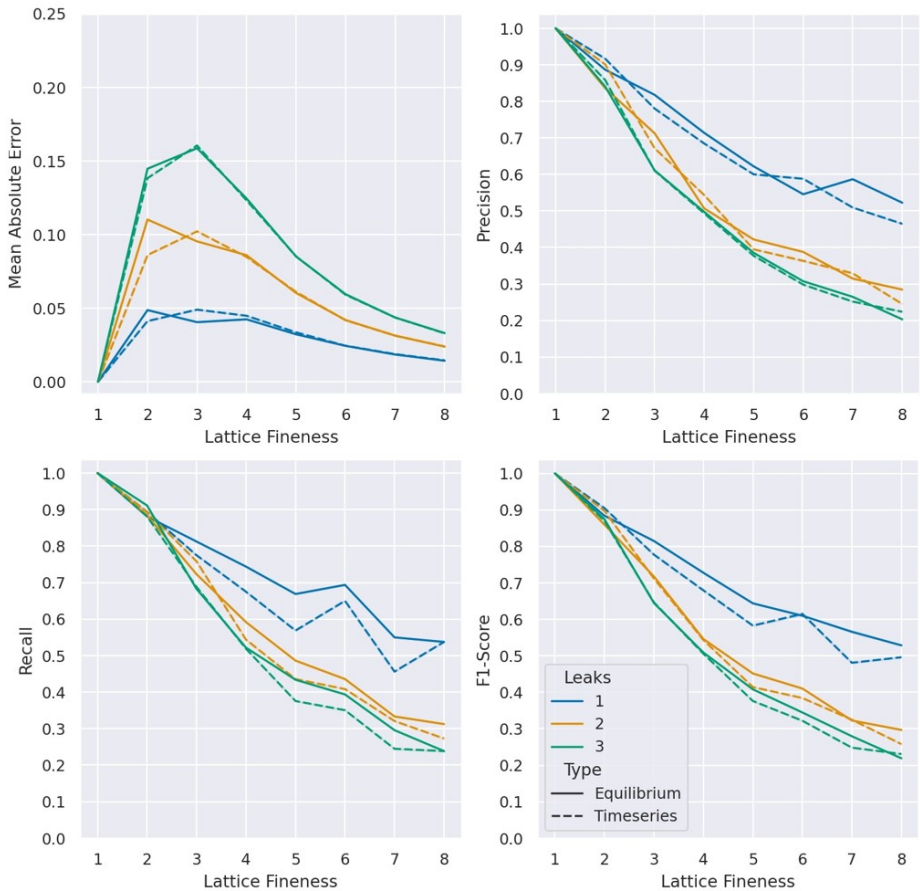
Figure 7.11: Impact of additional time series data (BCE loss only, with data augmentation and regularisation)

time series hold a potential that can be seen or leveraged by means of different approaches. This has not been the main focus in this thesis, but will be the subject of future work.

Altogether is can be seen, that the MAE first increases ($k \leq 3$) and then decrease again in all configurations (see Figures 7.8-7.11). This may be related to the fact, that with increasing lattice fineness fewer areas include a leakage, whereas before a lattice fineness of $k = 4$ it is possible, that multiple leakages are included in one quadrant.

## 7.4. Discussion of hypothesis addressed

The results show that leakage detection and localisation by deep learning is feasible. The established method works not only for single leaks but also in the presence of multiple leaks, although the prediction performance in such cases is still limited.

Examination of various factors shows that data augmentation and regularisation improve the performance of the machine learning model, while weighted loss does not. The use of time series data also does not seem to be very helpful in improving localisation. More data and/or other data is needed to further improve the prediction performance, especially in cases with multiple leaks. In addition, the impact of noisy or inconsistent data on potential performance loss needs to be investigated, as imperfect sensor data from similar measurements could indicate different leakage points in the data.

For further investigation, synthetic data should be used through simulations as discussed in subsection 4.3.1. These synthetic sensors can be used in combination with the superposition principle, which states that the flow rate of each sensor adds up when there are multiple leaks in the vacuum bag. Using the simulated data, it is also possible to study the noise-free distribution and determine if it is possible to get close to zero error in a noise-free world. The uncertainty of the machine learning model must be quantified in a confidence interval. Instead of extending the training data, the rotation and flipping equivariance could be explicitly incorporated into the network architecture of the deep learning model.

Additionally, it needs to be investigated whether the task of predicting multiple leakage positions is still feasible when the leakage is not limited to three values, as in this experiment. It could be that mapping leakage positions and areas to flow measurements is not injective. If this is the case, other methods and models such as regression models, logistic regression or support vector machines need to be developed to determine multiple leakage positions. This thesis and the introduced dataset can be seen as the basis for a larger body of work so that further investigations are likely to take place in near future.

The results of the investigations in this chapter show that there is great potential in leakage localisation using machine learning. Even if further investigations have to be carried out, the data-based approach shows significantly better results and higher precision than the naive model-based approach, especially for multiple leakages. Hypothesis 5 *"With the help of machine learning and Neural Networks it is possible to achieve higher precision when identifying leak prone areas with flow measurement compared to a naive model based approach."* is therefore confirmed.

**7**

# References

[1] C. Brauer and A. Haschenburger, *Localization of leakages in vacuum bagging withvolumetric flow meters and recurrent neural networks,* in *ISCM , Stade, Germany* (2021).

[2] Y. LeCun, Y. Bengio, and G. Hinton, *Deep learning,* nature **521**, 436 (2015).

[3] I. Goodfellow, Y. Bengio, and A. Courville, *Deep Learning*, Adaptive Computation and Machine Learning series (MIT Press, 2016).

[4] B. Alexe, T. Deselaers, and V. Ferrari, *Measuring the objectness of image windows,* IEEE transactions on pattern analysis and machine intelligence **34**, 2189 (2012).

[5] Y. S. Aurelio, G. M. de Almeida, C. L. de Castro, and A. P. Braga, *Learning from imbalanced data sets with weighted cross-entropy function,* Neural Processing Letters **50**, 1937 (2019).

[6] H. G. Santos and T. Toffolo, *Mixed integer linear programming with python,* (2020).

[7] M. Abadi, A. Agarwal, P. Barham, E. Brevdo, Z. Chen, C. Citro, G. S. Corrado, A. Davis, J. Dean, M. Devin, S. Ghemawat, I. Goodfellow, A. Harp, G. Irving, M. Isard, Y. Jia, R. Jozefowicz, L. Kaiser, M. Kudlur, J. Levenberg, D. Mané, R. Monga, S. Moore, D. Murray, C. Olah, M. Schuster, J. Shlens, B. Steiner, I. Sutskever, K. Talwar, P. Tucker, V. Vanhoucke, V. Vasudevan, F. Viégas, O. Vinyals, P. Warden, M. Wattenberg, M. Wicke, Y. Yu, and X. Zheng, *TensorFlow: Large-scale machine learning on heterogeneous systems,* (2015), software available from tensorflow.org.

[8] D. P. Kingma and J. Ba, *Adam: A method for stochastic optimization,* arXiv preprint arXiv:1412.6980 (2014).

**7**

# 8

# Industrial impact

*In order to understand the relevance of leakage detection in industrial composite manufacturing, it is important to assess the costs that occur in production with respect to leakages. It will be worked out how these can be reduced by implementing the methods developed in the thesis, and what additional added value the extended data availability can bring to companies with regard to Industry 4.0.*

## **8.1.** Introduction

As described in Subsection 2.4.4 as motivation and example, significant additional costs can arise due to leakages. In order to provide a better overview of the composition of the costs, this chapter uses a specific example to illustrate the costs more closely. Since the costs for leakages in vacuum bags during the manufacturing of fibre-reinforced composite components are not explicitly stated, it is difficult to obtain a clear statement on the exact amount. The costs considered in this chapter are explained on the basis of a $7\ m^2$ aerospace component, which have been evaluated with an European aircraft component manufacturer. The following overview provides a summary of the costs associated with leakages:

- Costs for vacuum test (Personal resources)
- Costs for potential leakage detection (Personal resources and material costs)
- Repair (Personal resources and material costs)
- Scrap (Part costs)

In the following sections, firstly, the cost of leakage for a composite aerospace component with a size of $7\ m^2$ is explained using the state of the art methods for vacuum leakage detection. The benefits of the improved leakage detection process are then shown and the potential savings are illustrated using this example. Finally, in order to demonstrate the entire added value for industry, the aspects related to Industry 4.0 are discussed.

## **8.2.** Cost modelling

There are several cost models available for evaluating the costs of CFRP manufacturing processes. The approaches can be split into qualitative and quantitative techniques. [1] An overview of the different classifications of the several available models is given by Zhao et al. [2] dividing them into estimation process, estimation model, calculation model and additional techniques.

An actual reference part is needed, as most of the models need specific design and process information for an accurate cost estimation. [2] For this purpose, the chosen typical aircraft composite example part of $7\ m^2$ is used. Other approaches include top-down breakdown methods that can be used before detailed design and process information is available. [3, 4] The first cost estimation models have been developed in 1976 by LeBlanc et al. [5] known as the *Advanced Composite Cost Estimation Manual* (ACCEM). Gutowski et al. [6] developed a 'first-order' model that is very general for estimating production times by evaluating the individual times for labour and machining of each process step for the manufacturing of composite parts. The costs of quality assurance and *Non Destructive Inspection* (NDI) are added by Shehab et al. [7]. The costs for rework and rejection, which are also relevant for evaluating the costs of leakages are mentioned in some models but need explicit calculation.

Figure 8.1 shows the major components and contributors for evaluating the costs of composite parts in traditional cost models. The major process steps are

shown on top. The light blue shows the specific process steps required for the production of the example part.
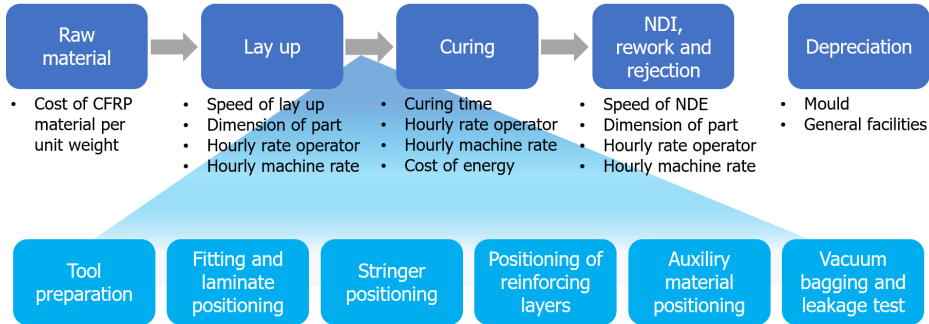


Figure 8.1: Process break down for cost modelling with the major contributors as well as breakdown for the process steps required for the example part. Each of the light blue process steps has a cycle time of 90 minutes.

Equation 8.1 shows a breakdown of the sums for the variable and fixed costs relevant to the manufacture of composite parts.

$$\sum \text{Variable costs} + \sum \text{Fixed costs} = \sum \text{Raw material cost} + \sum \text{Lay up cost} +$$
$$\sum \text{Curing cost} + \sum \text{NDI cost} + \sum \text{Rework \& rejection costs} + \sum \text{Depreciation}$$
(8.1)

As most of these costs are unaffected by the leakage detection, they are not part of the investigation of this thesis. The relevant costs are hidden in the lay up costs within the vacuum bagging and leakage test process step and in the rework and rejection costs. These costs are investigated in more depth in the following section.

## 8.3. Cost of leakages

In order to determine the overall costs associated with leakages, all costs listed in Section 8.1 must be taken into account. Since these are not explicitly shown, it is difficult to obtain clear values. The figures listed here have been agreed with a European manufacturer of aerospace components and have been determined explicitly for a series component of 7 $m^2$ in size. The component is manufactured at a rate of 120 pieces per month, resulting in 1440 components per year. The production of the component is divided into six process steps between the lay-up and the subsequent autoclave cycle, which are shown in Figure 8.1 in light blue. The cycle time is 1.5 hours per step, which results in a total of 9 hours plus the subsequent autoclave cycle of 6 hours. In addition to component, material and personnel costs, lead time and the associated indirect costs also play a role when

calculating the costs of leakages. All relevant input variables are listed in Table 8.1 and have been validated by the aerospace manufacturer.

Table 8.1: Overview of input variables relevant for the leakage cost estimation of the example component from a European aircraft manufacturer

| Variable | Value | Unit |
|---|---|---|
| Component size | 7 | $m^2$ |
| Component weight | 50 | $kg$ |
| Production rate | 1440 | $parts/year$ |
| Component cost (after autoclave) | 40,000 | € |
| Component cost (final) | 70,000 | € |
| Hourly rate operator | 120 | € |
| Time pressure increase test | 15 | $min$ |
| Rate of vacuum bags with leakages | 20 | % |
| Average time for leak detection | 20 | $min$ |
| Ratio renewal of vacuum bag | 1/10 | |
| Renewal of vacuum bag time | 1 | $hr$ |
| Rework rate due to leakages | 8 | % |
| Ratio big/small flaws | 1/10 | |
| Small flaw operator rework time | 2 | $hr$ |
| Big flaw operator rework time | 5 | $hr$ |
| Rejection rate due to leakage | 0.069 | % |
| Vacuum bag material | 1 | $€/m^2$ |
| Vacuum bagging operator time | 8.57 | $min/m^2$ |
| Vacuum bag evacuation time | 2 | $min/m^2$ |
| Leak search time with US microphone | 8.5 | $min/m^2$ |
| Two stage leakage detection time | 1.5 | $min/m^2$ |
| Two stage leakage detection system | 20,000 | € |
| Additional flow sensors | 1,500 | $€/sensor$ |

**Cost for vacuum test**   The cost of the standard vacuum test, as it is performed on each part after the vacuum bagging and before the autoclave process, is estimated at € 30-150 per part. A pressure increase test is performed in the standard series process and lasts 15 minutes. The costs of this test depend on how many employees perform the test, as their resources are tied up accordingly for this period, and can be calculated as:

$$\sum \text{Cost vacuum test} = \text{Hourly rate operator } (€/hr)) \cdot \text{Number of operators} \cdot \frac{\text{Time pressure increase test } (hr)}{60(min/hr))} \quad (8.2)$$

Since the vacuum setup in this example is relatively small, only one employee is needed for the test and thus only a smaller amount is estimated. If the component is correspondingly larger and more complex, several employees are needed to create the vacuum setup and thus more resources are tied up for the vacuum test, which takes the same amount of time. Lead time remains the same, but labour costs increase as the size of the part increases.

For the example component, the costs are estimated at € 30 per component. At the rate of 120 parts per month, the cost is € 43,200 per year for the vacuum test only. These costs are unavoidable without process improvement, as the test is performed as standard procedure on each component.

**Cost for potential leakage detection**   If the pressure increase test exceeds a certain limit, the leakage must be searched for in the vacuum bag. According to the component manufacturer, this is the case for every fifth component in the series production process. In most cases, the leaks can be found and repaired after a more or less complex search of about $10 - 60\ min$. As in most cases the leak is found before the whole part is searched $20\ min$ are used for the calculations. To estimate the costs for leakage localisation following equation is used:

$$\sum \text{Cost leakage localisation } = \text{Hourly rate operator } (\text{€}/hr) \cdot$$

$$\text{Number of operators} \cdot \frac{\text{Average time leak detection } (min)}{60 min/hr} + \sum \text{Cost vacuum test}$$

$$(8.3)$$

Every two to three weeks, or every 40-60 parts, it happens that a leak cannot be found and the vacuum assembly on the component has to be completely replaced. If leak detection takes too long or the vacuum bag has to be renewed, the affected component must be clocked out so that it does not block subsequent components and the clocked cycle can be maintained. The costs for vacuum bag renewal are calculated with the following equation:

$$\sum \text{Cost renewal of vacuum bag } = \text{Hourly rate operator } (\text{€}/hr)) \cdot$$

$$\text{Number of operators } \cdot \text{Renewal of vacuum bag time } (hr) +$$

$$\text{Vacuum bag material } (\text{€}) \cdot \text{Component size } (m^2) \quad (8.4)$$

These costs need to be corrected with the rate of vacuum bags with leakages and the ratio for vacuum bag renewal as not every part is affected by these:

$$\sum \text{Cost leakage detection } = \text{Rate of vacuum bags with leakages } (\%) \cdot$$

$$\left[ \sum \text{Cost leakage localisation } + \text{Ratio vacuum bag renewal } \cdot \right.$$

$$\left. \sum \text{Cost renewal of vacuum bag} \right]$$

<div align="right">(8.5)</div>

The result is the hidden cost of leakage detection in the part manufacturing. When using the input variables this results in € 16.54 per part.

The costs incurred per year for the additional search for leaks as well as the renewal of vacuum bags amount to an estimated € 23,800 per year for the component listed here. These costs include both personnel and material costs, and can be reduced or avoided through improved and automated leakage detection. For the new procedure, a pessimistic and optimistic estimate is made in Subsection 8.4 of how much these current figures can be reduced.

**Repair**   The rework or repairs caused by leaks are mainly due to surface porosity or, in more serious cases, defects in the component. It is estimated that of all the components produced, one in five needs to be reworked. This amounts to 288 components per year. The current rework time is estimated at an average of two hours per component, whereby it is mostly only a matter of closing the surface porosity. About every tenth rework is a more serious defect, where layers have to be removed and rebuilt and the repair is correspondingly more extensive. Of all the rework and repairs that occur for the component, approximately 40% are due to leaks in the vacuum assembly or tool. The costs for leakage rework included in each part can be calculated as follows:

$$\sum \text{Cost rework due to leakages } = \text{Rework rate due to leakages } (\%) \cdot$$

$$\left[ (1 - \text{Ratio big/small flaws}) \cdot \sum \text{Cost rework small flaws } + \right.$$

$$\left. \text{Ratio big/small flaws } \cdot \sum \text{Cost rework large flaws} \right]$$

<div align="right">(8.6)</div>

For the costs of the individual flaw sizes following equation is used:

$$\sum \text{Cost rework flaws } = \text{Hourly rate operator } (\text{€}/hr) \cdot$$

$$\text{Repair time per flaw size} (hr) \quad (8.7)$$

It should be noted that only labour costs are considered in this simplified approach. Normally, the cost of the non-conformity report, the cost for the engineer

or operator to assess the defect, as well as the cost of materials and a possible re-
peat of the autoclave cycle must also be considered. As this is beyond the scope of
this thesis and the labour costs are the major cost driver, a simplified cost approach
is used to provide an initial estimate of the repair costs associated with leakage.

Using the input variables from Table 8.1, the cost of rework due to leakage
hidden in the manufacturing costs is € 22.08 per part. This results in approximately
€ 31,800 per year for the example component. For the new procedure, a pessimistic
and optimistic estimate is made in Subsection 8.4 of how much these current figures
can be reduced.

**Scrap**   If a leak in the vacuum bag is not recognised or occurred during the auto-
clave process and exceeds a critical size, the component may no longer be salvage-
able and must be scrapped. It is estimated that this occurs approximately once a
year. With 1440 components per year, this corresponds to a scrapping rate due to
leakage of 0.069%. This rate is very low and yet the cost of scrapping is a large
part of the total cost of leakage. The example component has a final value of ap-
proximately € 70,000. This amount already includes the costs for machining, lac-
quering and subsequent assembly preparations. Since the defects caused by leak-
ages already occur in the autoclave step and are detected at the latest in the subse-
quent quality inspection, the component can already be scrapped before the costly
subsequent processing steps. This reduces the costs for a scrapped component to
€ 40,000. To calculating the hidden costs of rejection due to leakages per compo-
nent following Equation is used:

$$\sum \text{Cost rejection due to leakages} = \text{Rejection rate due to leakages} (\%) \cdot$$
$$\text{Component cost (after autoclave)} (\text{€}) \quad (8.8)$$

This results in € 27.60 per part. These costs can also be reduced if leakage
detection is automated and improved. For the new procedure, a pessimistic and
optimistic estimate is made in Subsection 8.4 of how much these current figures can
be reduced. In addition, it can be advantageous to integrate the leakage detection
into the autoclave and to be able to detect and evaluate leaks at an early stage.
In this way, defined limit values can be set at which the autoclave cycle can be
interrupted and the component possibly saved.

As can be seen in Table 8.2 all costs above for the example component amount
to € 138,800 per year and are thus significantly higher than the costs for leakages
listed by Haschenburger et al. [8] and in Chaper 2.

This again shows that it is difficult to estimate and assess the exact extent of
leakages. Figure 8.2 shows the percentage of the various cost types on the total
costs of leakages. Although there are no huge differences between the different
types it can be seen that the vacuum test and scrapping are the main cost drivers.

Furthermore, it can be concluded, that the hidden costs of leakages make up
0.14 % of the final part costs of € 70,000.

Table 8.2: Overview of input variables relevant for the leakage cost estimation of the example component from a European aircraft manufacturer

| Cost type | per part (€) | per year(€) |
|---|---|---|
| Cost vacuum test | 30.00 | 43,200 |
| Cost leakage localisation | 16.54 | 23,800 |
| Cost rework due to leakages | 22.08 | 31,800 |
| Cost rejection due to leakages | 27.60 | 40,000 |
| Total | 96.22 | 138,800 |
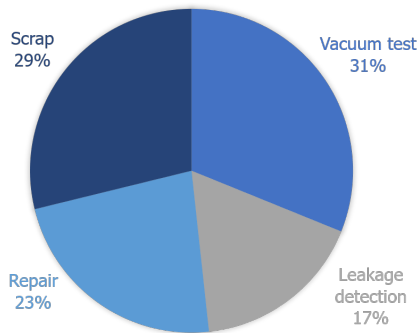


Figure 8.2: Percentage of the current various costs on the total cost associated with leakages

## 8.4. Improvement through advanced leakage detection

The methods for advanced leakage detection presented in this thesis can make an important contribution to reduce the above-mentioned costs. It has been shown that one of the biggest cost drivers is vacuum testing during production. This takes a standard time of 15 minutes for each manufactured component, a time during which the employees do not perform any effective work, but have to wait for the result of the pressure increase test. Figure 8.3 shows the standard leakage detection process compared to advanced leakage detection investigated in this thesis. First of all, it can be seen that the vacuum test can be omitted after completion of the vacuum setup, as the air tightness of the vacuum bag is already assessed by the flow measurement during evacuation. The waiting time of 15 minutes for the employees is eliminated. The personal costs for the hole process step are reduced from € 180 to € 150 per component. Furthermore, the process for detecting and localising a possible leakage can be significantly reduced by the systems, which are not only connected in sequence but also linked to each other. This eliminates the time and cost of vacuum testing and reduces the maximum leak detection time delay from $60\,min$ to $10\,min$, conservatively calculated, and corresponds to a personnel cost saving of about € 100 per component with leakage

in vacuum bag. The amortisation of the system and the costs after implementation are broken down in the Discussion, Subsection 8.6.
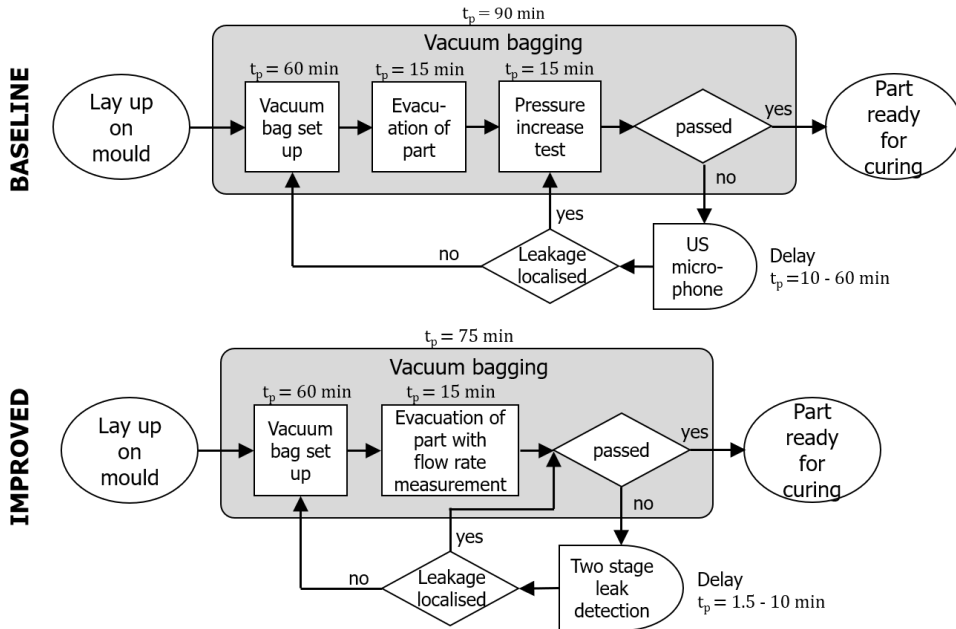


Figure 8.3: Baseline and proposed improved process flow chart for vacuum bagging and leakage detection. Flow chart in accordance to [9]

In view of the costs associated with leakages and their reduction under the improved process, some estimates need to be made in terms of the renewal of bag ratio, repair and scrap rate. As all predicted improvements are given in ranges it is possible to calculate an optimistic and pessimistic development of the costs for the proposed improved process. The values are listed in Table 8.3.

Table 8.3: Predicted development of renewal of bag ratio, repair and scrap rate in the new improved process for an optimistic and pessimistic scenario

|  | Optimistic | Pessimistic |
|---|---|---|
| Ratio renewal of vacuum bag | 1/15 | 1/10 |
| Leakage localisation time | $5\ min$ | $10\ min$ |
| Rework rate due to leakages | 4 % | 6 % |
| Ratio big/small flaws | 1/20 | 1/10 |
| Rejection rate due to leakage | 0.035 % | 0.05 % |

In the table it can be seen, that for an optimistic scenario the renewal of a vacuum bag can be reduced to every 15th part as with the new system more leakages can be detected. Furthermore the leakage detection time can be drastically

reduced from $10 - 60\ min$ to $1.5 - 10\ min$. For the optimistic calculation a average time of $5\ min$ until the leakage is found was predicted, whereas in the pessimistic scenario the maximum of $10\ min$ was used for the calculations with Equation 8.3 and 8.5. The rework is reduced to $4 - 6$ %, as more leakages are detected and repaired. Furthermore it is possible, that the ratio of big/small flaw is reduced, as bigger and more critical leakages are found and in consequence the big flaws are reduced in the optimistic scenario to $1/20$. The same can be applied for the rejection rate that is reduced by $25 - 50$ % using the improved leakage detection. The results for the calculations can be found in Figure 8.4 where the baseline costs per part are compared with the improved pessimistic and optimistic scenario.
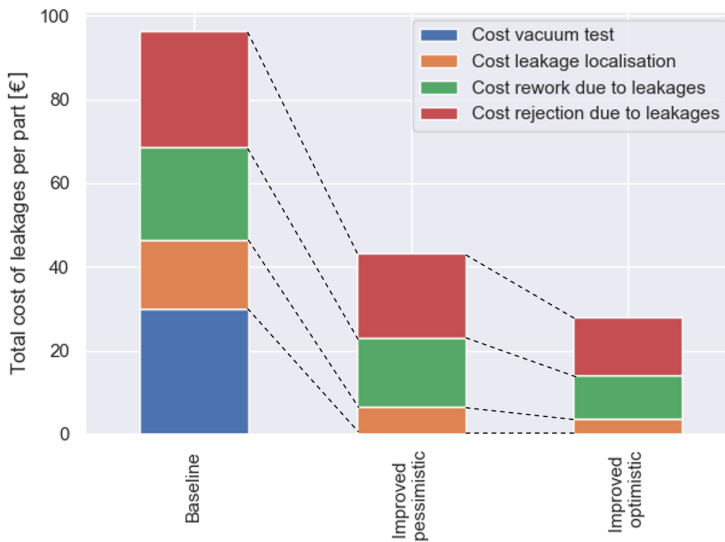


Figure 8.4: Leakage cost per part for baseline, improved pessimistic and optimistic scenario

As can be seen from Figure 8.4 the total costs per part can be reduced by half even in the pessimistic scenario. Most of the cost reduction is related to the elimination of the pressure increase test which is responsible for almost $1/3$ of the total costs of leakages per part. With the elimination of the vacuum test the production time per part is reduced by $15\ min$. At a production rate of $1440$ parts per year, this translates to $360$ hours per year. With a production time of $9$ hours per part this represents a potential increase in the production rate of approximately $3$ %. By reducing the renewal of bag rate from every $10^{th}$ to every $20^{th}$ part with leakages around $50\ m^2$ of vacuum film per year can be saved and with the reduced rejection rate around $12.5 - 25\ kg$ composite scrap per year can be avoided, reducing the ecological footprint.

Although quality inspection is critical in the manufacturing process of CFRP components, it is an avoidable process step if no rejection or rework of the product is required after the curing phase. [4] If leaks can already be identified during the process and both the position and the size are known, this offers several advan-

tages. Since the flow measurement can also be carried out during the autoclave process, it is possible to determine exactly at which point in time and in which area a leak has occurred.

The quality check can be minimised or eliminated if the leakage size, position and time of occurrence are known. The normal process step of non-destructive testing after the autoclave process can be skipped and the component can go to the repair shop immediately after completion of the autoclave cycle. This reduces the lead time of the parts and reduces the effort in the quality inspection. Quality control and rework can be planned at an early stage before the component reaches these process steps. Furthermore, if an irreparable defect due to a leakage is detected during the process (e.g. in the fitting area), the component can be rejected at an early stage and production capacities can be saved. The prerequisite for this is a good collection of data and a good data basis, in which a comparison of the flow values and the subsequent quality findings has taken place. This correlation must be validated in order to guarantee a reliable prediction of the quality of the components on the basis of the flow values.

Another advantage of advanced leakage detection is that recurring errors can be identified more quickly and the manufacturing process can be improved and adjusted through root cause analysis. For example, recurring vacuum breaks at the same stringer edge can be detected more quickly thanks to a statistical evaluation and the vacuum setup can be adjusted accordingly. At present, such faults are rarely analysed and are difficult to identify due to the lack of data.

## 8.5. Industry 4.0

When it comes to Industry 4.0, flow measurement offers considerable advantages compared to the current approach. This is not only about improved leakage detection; the flow measurement that is carried out before and during the autoclave process continuously collects data about the condition of the vacuum bag and the component inside.

If the flow measurement is used during the autoclave process, this leads to an increased gain in knowledge about a process in which previously only few data was monitored selectively. With the help of flow measurement, it is not only possible to detect leaks during the autoclave process, the sensor can also be used to monitor the outgassing of the materials during curing. This enables the monitoring of holding stages that are specifically set up to achieve outgassing of the materials. If the outgassing is completed beforehand, process time can be saved. Setting paths and compaction stages can also be monitored. All in all, this leads to increased process knowledge and inline quality assurance. However, the models and assumptions presented in this thesis must be extended in the case of autoclave use and adapted to the changed conditions. Nevertheless, the flow measurement also gives a quick feedback in the autoclave environment whether the vacuum bag has leaks or is airtight. If a leak occurs during the autoclave process, the question is whether the autoclave cycle must be interrupted or not. With the previous pressure values, this question is difficult to answer. With the help of the flow measurement values, a safe abort criterion can be defined and the employee has a precisely defined limit value.

The tools can also be checked with the help of the recorded data. Leaks can occur not only in the vacuum bags but also in the tools. A common reason for this is damage to the tool surface, screwed sensors or welded areas. These can lead to microporosities and thus leaks, especially at elevated temperatures. With the volumetric flow rate sensors the tools are continuously monitored and the maintenance cycles can be adjusted according to the data. Small deviations in the air tightness can be quickly identified and the tools can be specifically maintained. The vacuum connections and hoses can also be checked using the flow sensors before the autoclave cycles, so that faults in the periphery can be ruled out.

Continuous data collection improves the process understanding and it is the prerequisite for data analyses and statistical evaluations. With the help of these analyses, predictive values and fixed process windows can be defined. More sensors in the components and tools also mean more data, and if these can be processed centrally, it is possible to move closer and closer to self-controlled production. AI-based prediction models, together with the evaluation of sensor data, can lead to significantly improved and increased process robustness. The goal is to achieve predictable maintenance and quality in order to minimise downtime, reduce repair costs and process times. Self-learning systems also enable a transfer of the results to other components.

## 8.6. Discussion and conclusion

The study shows that the industrial value is difficult to assess unequivocally. The elaboration on the basis of an example component with values that were agreed with a manufacturer of aerospace components are higher than previously determined values in Subsection 2.4.4 and by Haschenburger et al. in [8]. This shows how difficult it is to obtain a clear statement about the costs and effects of leakage. It is however clear that fixed costs are incurred for the standard testing of the components, which can be significantly minimised with the help of the advanced leakage detection developed in the thesis.

The costs that arise from the search for leaks are difficult to measure, as they disappear in the overall additional work involved in manufacturing the components and are not explicitly recorded. With the new process leaks can be located more quickly and automatically. Even in a pessimistic scenario all costs for leakages can be reduced by half and an increase of the production rate of $3$ % can be achieved.

The investment for the two stage leakage detection system is around € 20,000. This includes the cost for one volumetric flow rate sensor and the evaluation unit. The price for additional volumetric flow rate sensors would be approximately € 1,500 per sensor. For the example component these costs would be amortised within around 6 month only taking into account the reduced standard process time of $15\ min$. With regard to the reduced delay time in case of a leakage the amortisation takes place even earlier. Within this process, the developed localisation methods like multilatertion (Chapter 6) and machine learning (Chapter 7) are used. Furthermore the simulation developed in Chapter 4 not only supports the machine learning but may be helpful when assessing the criticality of a leakage in combination with the findings from Chapter 5.

It showed that it is also important to reduce the costs arising from undetected leaks, as these account for $52\%$ of the costs associated with leaks and are, in the best case, completely avoidable. With the help of flow measurement, it is possible to monitor the entire process from vacuum build-up to curing and collect data continuously to increase process understanding and enable big data analysis.

All the presented methods and improvements to the process have been secured in various patents, especially in [10] and [11] as methods and devices for detecting a leakage. With the help of the proposed processes in this thesis and the resulting patents, it is not only possible to improve leakage detection, they also help to drastically reduce the occurrence of leaks during curing. The connections, hoses and tools are continuously checked and can be repaired or replaced at an early stage if necessary. If the flow measurement is used during the autoclave process, leaks that occur at this stage can also be detected and evaluated quickly. The availability of this information enables data-based decisions that can be made to save the component and reduce repair costs.

The chapter at hand shows the industrial value of introducing advanced leakage detection in production, not only in terms of cost savings but also in the area of Industry 4.0. It shows the potential to bring leakage detection and flow measurement to the next technology readiness level and its applicability in the industrial environment.

8

# References

[1] A. Niazi, J. Dai, S. Balabani, and L. Seneviratne, *Product Cost Estimation: Technique Classification and Methodology Review,* Journal of Manufacturing Science and Engineering-transactions of The Asme - J MANUF SCI ENG **128** (2006), 10.1115/1.2137750.

[2] X. Zhao, W. J. Verhagen, and R. Curran, *Estimation of aircraft component production cost using knowledge based engineering techniques,* Advanced Engineering Informatics **29**, 616 (2015).

[3] P. G. Pugh, *Working Top-Down: Cost Estimating before Development Begins,* Proceedings of the Institution of Mechanical Engineers, Part G: Journal of Aerospace Engineering **206**, 143 (1992).

[4] N. Miesen, *In-situ non-destructive evaluation process monitoring for CFRP manufacturing*, Ph.D. thesis, Delft University of Technology (2018).

[5] D. J. LeBlanc, J. Lorenzana, A. Kokawa, T. Bettner, F. Timson, and N. C. H. C. A. DIV., *Advanced Composite Cost Estimating Manual. Volume I.* (Defense Technical Information Center, 1976).

[6] T. Gutowski, D. Hoult, G. Dillon, E.-T. Neoh, S. Muter, E. Kim, and M. Tse, *Development of a theoretical cost model for advanced composite fabrication,* Composites Manufacturing **5**, 231 (1994).

[7] E. Shehab, W. Ma, and A. Wasim, *Manufacturing cost modelling for aerospace composite applications,* in *Concurrent Engineering Approaches for Sustainable Product Development in a Multi-Disciplinary Environment - Proceedings of the 19th ISPE International Conference on Concurrent Engineering*, Advanced Concurrent Engineering (Springer-Verlag London Ltd, 2013) pp. 425–433, 19th ISPE International Conference on Concurrent Engineering, CE 2012 ; Conference date: 03-09-2012 Through 07-09-2012.

[8] A. Haschenburger and C. Heim, *Two-stage leak detection in vacuum bags for the production of fibre-reinforced composite components,* CEAS Aeronautical Journal **10**, 885 (2019).

[9] N. Hebb, *Flowchart symbols defined,* BreezeTree Software (2012).

[10] H. Uçan, A. Haschenburger, C. Heim, and J.-T. Hesse, *Method and device for detecting a leak,* (2019).

[11] A. Al-Lami and A. Haschenburger, *Method and device for detecting a leak,* (2018).

**8**

# 9

# Conclusion and outlook

*In this thesis, leaky vacuum bags in composites manufacturing have been investigated. Novel approaches in leakage detection and localisation have been designed and different trials and methods have been developed to test the following principle hypothesis step-by-step:*

*'There is a method to characterise the influence of leakages in vacuum bagging on component quality in terms of size, type and location.'*

The present work investigates leakages in vacuum bags, their influence and their detection methods. The original aim of the thesis was to develop a method to characterise the influence of leakage. This requires a better understanding of the mechanisms within a vacuum bag and the development of detection methods suitable for industrial applications.

Chapter 4 deals with phenomena which can occur within a vacuum bag as soon as a leakage is present. The findings show, that the orifice plate equation is successfully applied to calculate the exact flow rate for leakages of different sizes. The phenomena that occur due to the changed pressure state are represented using a spring damper model. With the help of selected test procedures and CFD simulations, the conditions are successfully simulated and verified on the basis of the test results. Furthermore, with the help of simulation a possibility of data synthesis is created.

In order to check the influence of these changed pressure conditions on the final component quality, a series of tests is carried out with leaky vacuum bags in the autoclave in Chapter 5. The results show that two types of leaks can be distinguished, those that are purely in the film and those that have a direct connection to the laminate. The latter proved to be considerably more critical and leads to clear defects in the laminate from a leak size of $0.3\ mm$. Larger leaks that have no direct contact with the laminate, on the other hand, proved to be hardly critical and only led to slight local changes in thickness, even if the pressure increase is well above the aircraft manufacturers regulations. The mechanical properties of this results and the influence of resin richer areas needs to be investigated in more depth to fully exploit the potential.

To develop an appropriate leakage detection with the previous results taken into account, a comparison of leakage detection technologies is performed in Chapter 6. The results show, that a combination of volumetric flow rate measurement and infrared thermography is the most suitable method to find and locate leakages. With the help of the developed two stage leakage detection, leaks can potentially be found quickly, repeatable and automatically in the future.

In Chapter 7, the possible use of machine learning to further improve leakage detection is discussed. It is shown that this approach produces promising results for the detection and localisation, especially in the case of multiple leaks. However, this requires a large amount of training data, which is difficult to generate, especially for new components. In the future, the simulation from Chapter 4 can make a decisive contribution to the generation of synthetic data for model training.

The industrial value is presented in Chapter 8. It shows that advanced leakage detection can save process time in the standard evaluation of the vacuum bag tightness. At the same time, when leakages need to be found and located the delay of extra work can be reduced significantly by $83\%$. The permanent data collection contributes an additional benefit, especially with regard to Industry 4.0, but this is difficult to quantify and further investigation is needed.

In summary, it can be stated that the principle hypothesis *"There is a method to characterise the influence of leakages in vacuum bagging on component quality in terms of size, type and location."* is correct as an overall result of the individual studies. Leakages can be characterised by the various methods presented. More-

over, conclusions can be drawn about the influence on the resulting component quality. Reliable detection and localisation is enabled with the help of the volumetric flow measurement and infrared thermography and can be further optimised with the help of machine learning. In further tests, the transferability of the machine learning model to other geometries must be checked. The simulation can be used to support this transfer and to avoid lengthy test data acquisition through synthetic data generation.

When considering the societal value of this work, various aspects can be examined. First, there is the aspect of sustainability. In this field, the work makes a contribution to the resource-efficient production of aircraft components. The open mould process and the vacuum bagging involve a lot of waste, since a new bag has to be applied for each component. If a leakage in a vacuum bag cannot be found, it must be completely replaced, resulting in additional waste and costs. If the component is scrapped due to an undetected leak, more waste is generated and unnecessary resources are consumed. The methods presented in this thesis help to keep the required resources to a minimum. If the flow meters are also used during the autoclave process, they can additionally contribute to process shortening, and thus energy savings, as they can indicate when all volatiles have been evacuated from the component.

Another aspect that must be considered in the context of societal value is the higher automation of the process steps. On the one hand, this leads to increased process reliability, but can also contribute to the fact that fewer employees are needed in this area. Like stated in Chapter 8 the omitted task include mainly waiting for a pressure increase test or tedious manual leak detection, which might not be the most desirable types of work. Furthermore, when jobs are lost due to automation new job opportunities are created elsewhere and the continuity of the company is ensured. Thus, automation - if used correctly - is always an engine for growth in a company, through which it remains competitive. A decision against automation, out of false consideration for employees, is neither beneficial for the company nor its employees. If the competition uses automation for their own benefit, all companies that do not do so will eventually fall behind.

Future work in the area of leakage detection in vacuum bags should focus on the combination of simulation and machine learning, as well as on supporting the implementation of advanced leakage detection in industrial series production. Additionally, as the work within this thesis was technology driven further investigations should be carried out regarding the influence of leakages on the component quality, especially the mechanical values and the compaction of the laminate and fibre bed. When a leakage is present inside the vacuum bag the main focus should be to ensure that the compaction is still intact and no pressure gradient is formed. Here it could be important to take a closer look at the role of material and the influence of different material properties on the compaction behaviour under different pressure levels. The results of this work show that the current specifications for leakage detection could allow a greater margin, especially for leakages that do not have a direct connection to the laminate. Even though the investigations within this thesis are carried out on prepreg and autoclave processes, since this is where

**9**

the problems are greatest within the aerospace industry, the results can easily be transferred to other open mould processes. The extent of the defects in the various processes can vary and should be investigated in subsequent work. As this is of secondary importance for the sole detection of leaks, out-of-autoclave processes can also directly benefit from advanced leakage detection developed within this thesis.

Even though the open mould process is the oldest manufacturing method for fibre composite components, it will continue to be used primarily for large components. The results of this thesis help to ensure that the open mould process can remain successful, reliable, and become more sustainable in the future.

9

# Acknowledgements

**9**

# A

## Appendix

Table A.1: FMEA for leakages in vacuum bagging from an European aircraft manufacturer 2016

| ID | Functions or Process steps | Parts or Sub Process | SEV | OCC | DET | RPN |
|---|---|---|---|---|---|---|
| 1 | Leakage in sealent tape | | 6 | 2 | 5 | 60 |
| 2 | Selective leak | from 0,5 to 1,5  or bigger | 3 | 2 | 9 | 54 |
| 3 | Leakage under film fold | " | 3 | 2 | 9 | 54 |
| 4 | Leakage in stringer area | " | 3 | 2 | 9 | 54 |
| 5 | Slot in film | " | 3 | 2 | 9 | 54 |
| 6 | Leakage at sheet weld | " | 3 | 2 | 9 | 54 |
| 7 | Leakage under mold | Direct Bagging,      " | 3 | 2 | 9 | 54 |
| 8 | Perforation of film | | 6 | 2 | 10 | 120 |
| 9 | Leakge in tooling | Weld, etc | 6 | 2 | 10 | 120 |
| 10 | Vacuum valves | on tooling or on vacuum bagging | 6 | 2 | 10 | 120 |

**A**

Table A.2: Test matrix for leakage detection method comparison

| Experiment Method | Selective leak (diff. diameter) | Several leaks (diff. diameter) | Leakage in vacuum sealing tape | Leakage at sheet weld | Leakage under mold (direct bagging) | Perforation of the foil |
|---|---|---|---|---|---|---|
| Piezosensors (iNDTact) | 8 | 5 | 8 | 8 | 7 | 8 |
| Infrared thermography | 10 | 10 | 7 | 6 | 3 | 7 |
| Pressure increase test | 5 | 5 | 5 | 5 | 5 | 5 |
| Ink (EpoDye) | 8 | 8 | 0 | 0 | 0 | 8 |
| Gas detectors | 6 | 6 | 4 | 3 | 0 | 6 |
| Ultrasonic sensor (HuK) | 8 | 5 | 5 | 2 | 0 | 6 |
| Volumetric flow rate measurement | 10 | 10 | 10 | 10 | 10 | 10 |
| *Ratings key* | *10* | *10* | *10* | *5* | *5* | *5* |

| Experiment Method | Slot in foil | Leakage under Vacuum bag fold | Leakage at stiffeners | Automatic or manual | Duration | Handling |
|---|---|---|---|---|---|---|
| Piezosensors (iNDTact) | 8 | 8 | 7 | 10 | 10 | 7 |
| Infrared thermography | 9 | 7 | 5 | 10 | 9 | 8 |
| Pressure increase test | 5 | 5 | 5 | 10 | 8 | 7 |
| Ink (EpoDye) | 8 | 7 | 6 | 4 | 4 | 1 |
| Gas detectors | 7 | 5 | 6 | 7 | 3 | 5 |
| Ultrasonic sensor (HuK) | 7 | 4 | 5 | 4 | 3 | 2 |
| Volumetric flow rate measurement | 10 | 10 | 9 | 10 | 10 | 10 |
| *Ratings key* | *8* | *12* | *10* | *5* | *2* | *2* |

| Experiment Method | Available in autoclave | Leakage minimum size | Maximum size ( component ) | Costs | Overall evaluation (1-10) |
|---|---|---|---|---|---|
| Piezosensors (iNDTact) | 7 | 9 | 9 | 5 | 7.61 |
| Infrared thermography | 6 | 7 | 7 | 5 | 7.41 |
| Pressure increase test | 5 | 6 | 8 | 8 | 5.56 |
| Ink (EpoDye) | 0 | 8 | 3 | 8 | 4.90 |
| Gas detectors | 0 | 6 | 7 | 4 | 4.86 |
| Ultrasonic sensor (HuK) | 0 | 2 | 4 | 9 | 4.44 |
| Volumetric flow rate measurement | 10 | 10 | 10 | 10 | 9.90 |
| *Ratings key* | *7* | *3* | *4* | *2* | *100* |

Figure A.1: Compilation of equilibrium flows across all vacuum bags for selected hypodermic needle diameters. Error bars for readings below $1\ \ell_n/min$ are not large enough to be displayable in the graph due to the small error of the used high precision flow meters (max. $\pm 0.007\ \ell_n/min$)
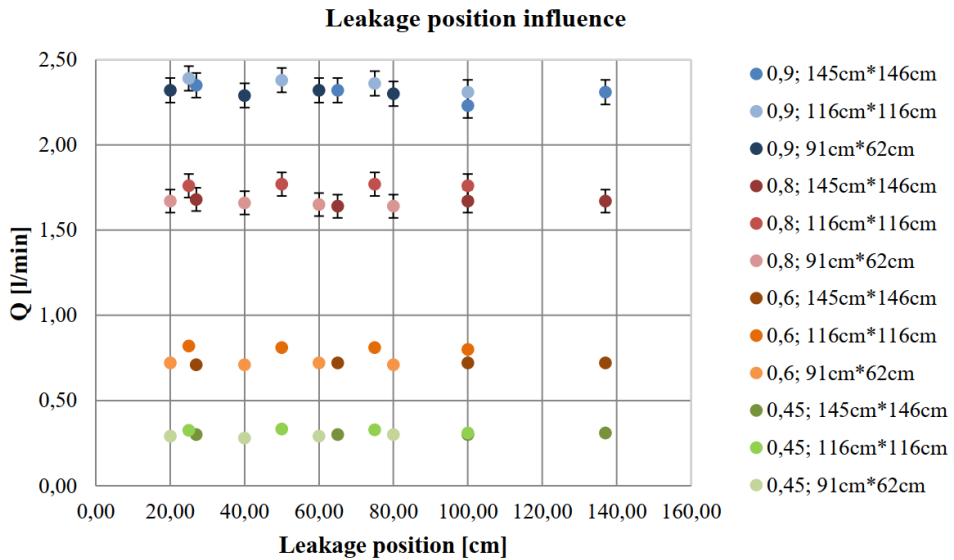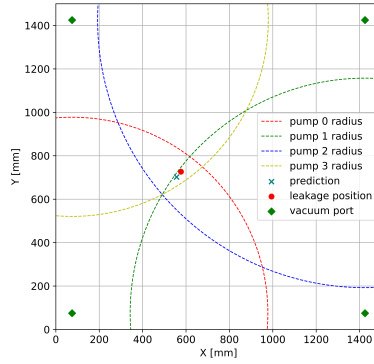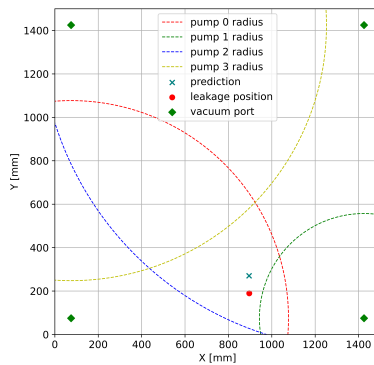
(a) General case far away from boundary
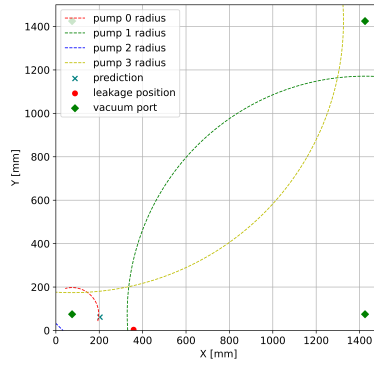


(b) General case on the boundary



(c) General case close to boundary

Figure A.2: Application of the numerical regression and trilateration method to three different examples of leakage position. As can be seen, the results become worse when the leakage location approaches the corners and/or boundary of the vacuum bag

# B

## Appendix

### Estimation of accuracy

Based on the accuracy of the available measurement technology, a first estimate of the achievable precision of the vacuum loss model was calculated. The estimate would be used to decide whether prediction of vacuum loss or calculation of volumetric flow rate thresholds would be possible within an acceptable margin of error and thereby reasonable in the first place.

The uncertainty of the flow rate which, according to the vacuum loss model, is calculated from several measured values could be evaluated according to Equation B.1.

$$u_Q = \sqrt{\left(\frac{\partial Q}{\partial (\Delta p/\Delta t)} \cdot u_{(\Delta p/\Delta t)}\right)^2 + \left(\frac{\partial Q}{\partial V_A} \cdot u_{V_A}\right)^2 + \left(\frac{\partial Q}{\partial T} \cdot u_T\right)^2 + \left(\frac{\partial Q}{\partial \rho} \cdot u_\rho\right)^2} \quad \text{(B.1)}$$

Since the pressure increase over time was a calculated value based on taken pressure logs it was considered as afflicted by only a single error. Being natural constants, the molar mass of air $M$ and the universal gas constant $R$ were not considered within the estimation of accuracy.

Partial derivation according to Equation B.1 yields

$$u_Q = \sqrt{\left(\frac{VM}{RT\rho} \cdot u_{(\Delta p/\Delta t)}\right)^2 + \left(\frac{M\Delta p}{RT\rho\Delta t} \cdot u_{V_A}\right)^2 + \left(-\frac{1}{T^2}\frac{MV\Delta p}{R\rho\Delta t} \cdot u_T\right)^2 + \left(-\frac{1}{\rho^2}\frac{MV\Delta p}{RT\Delta t} \cdot u_\rho\right)^2}$$
$$\text{(B.2)}$$

Expanding the fractions in each summand of Equation B.2 by the value with respect to which it was derivated beforehand results in

$$u_Q = \sqrt{\left(Q \cdot \frac{u_{(\Delta p/\Delta t)}}{\Delta p/\Delta t}\right)^2 + \left(Q \cdot \frac{u_{V_A}}{V_A}\right)^2 + \left(Q \cdot \frac{u_T}{T}\right)^2 + \left(Q \cdot \frac{u_\rho}{\rho}\right)^2} \qquad \text{(B.3)}$$

$Q$ can be factored out to finally get

$$f_Q = \sqrt{f_{(\Delta p/\Delta t)}^2 + f_{V_A}^2 + f_T^2 + f_\rho^2} \qquad \text{(B.4)}$$

The respective relative errors of all measured values are discussed in the following.

**Vacuum gauge**   The accuracy of the digital vacuum gauge that was used for all subsequently elaborated experiments was specified by the manufacturer as $u = \pm0.3\%$ of full scale for readings above $10\ mbar$ and as $f = \pm10\%$ of reading for values below $10\ mbar$. With a full scale value of $1200\ mbar$, a measured value included an uncertainty of

$$u_{(\Delta p/\Delta t)} = \pm0.003 \cdot 1200\ mbar = 3.6\ mbar \qquad \text{(B.5)}$$

The relative error of a measured value is determined by division of the uncertainty by the true value. Two extremes for the relative error of measured pressure had to be distinguished because an uncertainty of $\pm3.6\ mbar$ had a varying significance based on the numeric value of the reading. The highest measured pressure value was $950\ mbar$ after which every measurement was stopped. An absolute error of $\pm3.6\ mbar$ for a reading of $950\ mbar$ is a relative error of

$$f_{(\Delta p/\Delta t),1} = \frac{\pm3.6\ mbar}{950\ mbar} = \pm0.0037 = \pm0.37\% \qquad \text{(B.6)}$$

The second extreme occurred for a pressure reading of $10\ mbar$ for which an absolute error of $\pm3.6\ mbar$ is a relative error of

$$f_{(\Delta p/\Delta t),2} = \frac{\pm3.6\ mbar}{10\ mbar} = \pm0.36 = \pm36\% \qquad \text{(B.7)}$$

However, the relative error only took a maximum value of $\pm36\%$ for a reading of $10\ mbar$ and rapidly decreased as depicted in Figure B.1.

Readings below $10\ mbar$ had a relative error of $\pm10\%$ according to the manufacturer. Due to the complex nature of the uncertainty of pressure readings, both a worst-case scenario and a best-case scenario were considered for the overall estimation of accuracy. For future applications, a more consistent vacuum gauge should be used.

**Flow meters**   The volumetric flow meters are used to measure the air volume of a vacuum bag. The flow meters featured a built-in totaliser which integrated the measured volumetric flow rate over the process time to measure the total outflowing volume. The volume measurements accordingly are as accurate as the measured
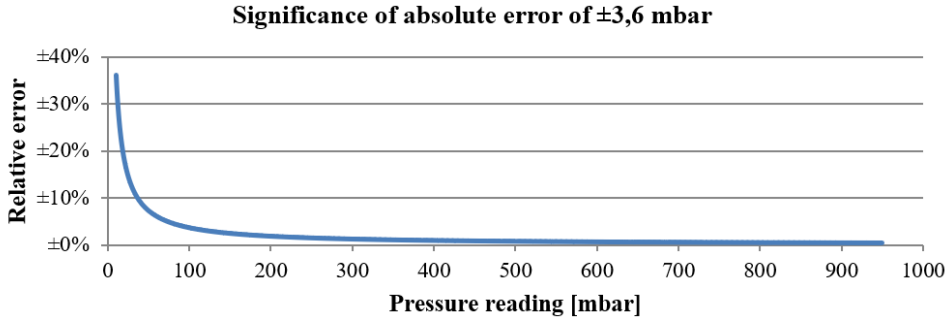
Figure B.1: Significance of absolute error of $\pm 3.6$ $mbar$

flow rates. A worst-case scenario had to be considered for the flow meters because the total error was composed of $\pm 0.3\%$ of the upper measurement limit and $\pm 0.5\%$ of the reading value. Two volumetric flow meters were used; thus, the worse accuracy was used for the overall estimation of accuracy. The first flow meter had an upper measurement limit of 20 $\ell$n/min and was used to measure flow rates down to $1$ $\ell_n/min$. The largest error occurred at the lowest reading value with a magnitude of

$$f_{V_A,1} = \frac{\pm \left( 0.003 \cdot 20 \frac{\ell_n}{min} + 0.005 \cdot 1 \frac{\ell_n}{min} \right)}{1 \frac{\ell_n}{min}} = \pm 0.065 = \pm 6.5\% \qquad \text{(B.8)}$$

The upper measurement limit of the second flow meter was $1$ $\ell_n/min$ while the lowest measured value was $0.09$ $\ell_n/min$ for the hypodermic needle of nominal diameter $0.3$ $mm$. Accordingly, the largest possible error was

$$f_{V_A,2} = \frac{\pm \left( 0.003 \cdot 1 \frac{\ell_n}{min} + 0.005 \cdot 0.09 \frac{\ell_n}{min} \right)}{0.09 \frac{\ell_n}{min}} = \pm 0.0383 = \pm 3.83\% \qquad \text{(B.9)}$$

For the purpose of a conservative assumption, the larger error of $f_{(V_A,1)} = \pm 6.5\%$ was used as the accuracy of the flow meters.

**Temperature and air density**   All experiments were conducted inside an air-conditioned environment of $22°C$. Allowing for temperature fluctuations of $u_T = \pm 1°C$ around this preset value results in a relative error of

$$f_T = \frac{\pm 1K}{295,15K} = \pm 0.00338 = \pm 0.34\% \qquad \text{(B.10)}$$

With fluctuating temperature, the air density changes too. Interpolation for air density at $22°C$ yields

**B**

$$\rho_{22°C} = \rho_{20°C} + \frac{\rho_{25°C} - \rho_{20°C}}{25°C - 20°C} \cdot (22°C - 20°C) = 1.19602 \frac{kg}{m^3} \tag{B.11}$$

with

$$\rho_{20°C} = 1.2041 \frac{kg}{m^3}; \rho_{25°C} = 1.1839 \frac{kg}{m^3} \tag{B.12}$$

Analogously, air densities for $21°C$ and $23°C$ are calculated.

$$\rho_{21°C} = 1.20006 \frac{kg}{m^3}; \rho_{23°C} = 1.19198 \frac{kg}{m^3} \tag{B.13}$$

The relative error of air density results to $f_\rho \approx \pm 0.34\%$.

$$f_{\rho,1} = \frac{\rho_{21°C} - \rho_{22°C}}{\rho_{22°C}} = -0.00338 \approx -3.34\% \tag{B.14}$$

$$f_{\rho,2} = \frac{\rho_{23°C} - \rho_{22°C}}{\rho_{22°C}} = +0.00338 \approx +3.34\% \tag{B.15}$$

**Total error**   Finally, using all calculated relative errors and the best and worst-case scenarios of the pressure gauge accuracy, an upper and lower limit for the achievable accuracy for the calculation of volumetric flow rate from a specified pressure increase per time can be calculated according to Equation B.4.

$$f_{Q,best} = \pm\sqrt{0.0037^2 + 0.065^2 + 0.0034^2 + 0.0034^2} = 0.0653 = 6.53 \tag{B.16}$$

$$f_{Q,worst} = \pm\sqrt{0.36^2 + 0.065^2 + 0.0034^2 + 0.0034^2} = 0.3658 = 36.58 \tag{B.17}$$

The significant deviation between upper and lower limit estimate was due to the unfavorable method with which the error of the vacuum gauge was specified. When plotting the total error of $Q$ dependent on the vacuum gauge reading and thus the relative error of the pressure readings, it becomes evident that the total error rapidly drops below $\pm 10\%$ and converges towards $f_{Q,best} = 6.53\%$. This is shown in Figure B.2.

The accuracy of the vacuum loss prediction could be assessed in analogy to Equation B.4.

$$f_{\Delta p/\Delta t} = \sqrt{f_Q^2 + f_T^2 + f_\rho^2 + f_{V_A}^2} \tag{B.18}$$

$$f_{\Delta p/\Delta t} = \pm\sqrt{0.065^2 + 0.0034^2 + 0.0034^2 + 0.065^2} = 0.092 = \pm 9.2\% \tag{B.19}$$

Considering additional sources of error and comparing the accuracies of vacuum loss prediction and volumetric flow rate calculation, an error of $f_{aim} = \pm 10\%$ was a reasonable assumption for the achievable accuracy of the model, thus confirming the meaningfulness of the endeavour. Additional possible errors that were not accounted for were:
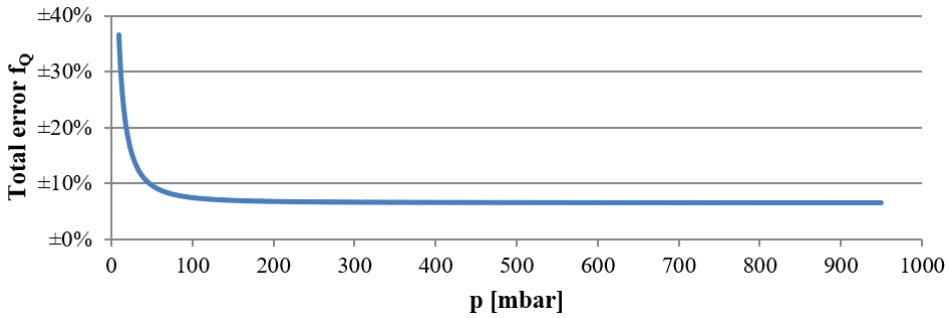
Figure B.2: Total error in dependence of vacuum gauge reading

- Deviations in breather quality and permeability
- Additionally occurring, unintended leakages
- Deviations in vacuum line diameter
- Flow resistance of the vacuum port
- Flow resistance inside the vacuum system
- Fluctuations of ambient pressure due to weather
- Deviations in vacuum bag dimensions
- Differences in tooling surface quality
- Discrepancies during leakage puncture

An estimate of the mean variation was not possible since not enough measurements could be repeated due to the high number of parameters that were changed in the course of all conducted experiments.

# Curriculum Vitæ

## Anja Haschenburger

28-05-1987     Born in Stade, Germany as Anja Imke Tripmaker.

## Education

2007–2010     *Apprenticeship* as Process Mechanic for Plastics and Rubber
Technology
Airbus Operations GmbH Stade

2007–2011     *Bachelor of Engineering* Composites
PFH University of Applied Sciences Göttingen

2013–2015     *Master of Arts* General Management
FOM University of Applied Sciences Hamburg

## Career

2011–2015     *Engineer* at Airbus Operations GmbH Stade
Manufacturing Engineering Department

since 2015     *Research Engineer* at DLR German Aerospace Center
Composite Process Technologies Department

since 2019     *PhD Candidate* at Delft University of Technology
Faculty Aerospace Engineering
Department Aerospace Materials and Structures

since 2021     *Lecturer* at FH Wedel
University of Applied Sciences

# List of Publications

## Journal Publications

7. **A. Haschenburger**, J. Stüve, and C. Dransfeld *Analytical and numerical calculation of leakages in vacuum bagging*, Applied Composite Materials (2022) (To be submitted for review).

6. **A. Haschenburger**, C. Brauer, J. Stüve, C. Dransfeld, and A. Kothari, *Potential use of machine learning for automated leakage detection*, Journal of Intelligent Manufacturing (2022) (To be submitted for review).

5. **A. Haschenburger**, L. Onorato, M.S. Sujahudeen, D.S. Taraczky, A. Osis, A.R.S. Bracke, M.D. Byelov, F.I. Vermeulen, E.H.Q. Oosthoek, *Computational methods for leakage localisation in a vacuum bag using volumetric flow rate measurements*, Production Engineering (2022).

4. **A. Haschenburger**, and J. Stüve, *Influence of leaky vacuum bags on the quality of composite parts made from prepreg material*, The Journal of Plastics Technology **4**, 204-229 (2021).

3. **A. Haschenburger**, N. Menke, and J. Stüve, *Sensor based leakage detection in vacuum bagging*, The International Journal of Advanced Manufacturing Technology **116**, 2413–2424 (2021).

2. **A. Haschenburger**, and C. Heim, *Two-stage leak detection in vacuum bags for the production of fibre-reinforced composite components*, CEAS Aeronautical Journal **10**, 885-892 (2019).

1. **A. Tripmaker**, and H. Uçan, *Detection of leakages on composite high performance structure parts*, Lightweight Design worldwide **10**, 46-49 (2017).

## Conference Contributions

6. C. Brauer, and **A. Haschenburger**, *Localization of leakages in vacuum bagging with volumetric flow meters and recurrent neural networks*, ISCM 2021, Stade, Germany.

5. **A. Haschenburger**, and N. Menke, *Sensor based analysis and identification of leak-prone areas in vacuum bagging for high performance composite components*, SAMPE Europe 2018, Southampton, England.

4. **A. Haschenburger**, and C. Heim, *Zweistufige Leckagedetektion an Vakuumaufbauten für die Herstellung von Faserverbundbauteilen*, Deutscher Luft- und Raumfahrtkongress (DLRK) 2017, München, Germany.

3. H. Apmann, M. Mayer, K. Fortkamp, **A. Haschenburger**, C. Krombholz, S. Meister, H. Ucan, and P. Zapp, *Verfahren der INLINE-Qualitätssicherung und der zerstörungsfreien Prüfung innerhalb der Fertigungslinie von Faser-Metall-Laminaten*, Deutscher Luft- und Raumfahrtkongress (DLRK) 2017, München, Germany.

2. **A. Tripmaker**, W. Fröhlingsdorf, H. Uçan, and M. Bludszuweit, *Einsatzmöglichkeiten von simulationsunterstützten Autoklavprozessen*, 5. Fachkongress Composite Simulation (2016), Hamburg, Germany.

1. H. Uçan, D. Akin, and **A. Tripmaker**, *Einsatzmöglichkeiten von Thermographiemessungen im Autoklaven zur Prozessüberwachung und Qualitätskontrolle*, Deutscher Luft- und Raumfahrtkongress (DLRK) 2015, Rostock, Germany.

## Patents

4. A. Al-Lami, and **A. Haschenburger**, *Method and device for detecting a leak*, DE102018 105889B4 (2018).

3. H. Uçan, **A. Haschenburger**, C. Heim, and J. T. Hesse, *Method and device for detecting a leakage*, WO2019043227A1 (2018).

2. **A. Haschenburger**, A. Kolbe, M. Schreiber, and S. Steffen, *Method and device for displaying component documentation*, WO2018185077A1 (2018).

1. H. Uçan, P. Zapp, D. Akin, and **A. Haschenburger**, *Method for producing a component*, EP3354444B1 (2017).